



HAL
open science

Mathematical modeling of antibody nanoconjugates transport in tumors

Cristina Vaghi

► **To cite this version:**

Cristina Vaghi. Mathematical modeling of antibody nanoconjugates transport in tumors. Numerical Analysis [math.NA]. Université de Bordeaux, 2020. English. NNT : 2020BORD0326 . tel-03157478

HAL Id: tel-03157478

<https://theses.hal.science/tel-03157478v1>

Submitted on 3 Mar 2021

HAL is a multi-disciplinary open access archive for the deposit and dissemination of scientific research documents, whether they are published or not. The documents may come from teaching and research institutions in France or abroad, or from public or private research centers.

L'archive ouverte pluridisciplinaire **HAL**, est destinée au dépôt et à la diffusion de documents scientifiques de niveau recherche, publiés ou non, émanant des établissements d'enseignement et de recherche français ou étrangers, des laboratoires publics ou privés.

Thèse présentée pour obtenir le grade de

DOCTEUR DE L'UNIVERSITÉ DE BORDEAUX

École doctorale de Mathématiques et Informatique

Specialité: MATHÉMATIQUES APPLIQUÉES ET CALCUL SCIENTIFIQUE

CRISTINA VAGHI

sous la direction de Sébastien Benzekry, Raphaëlle Fanciullino et Clair Poignard

Mathematical modeling of antibody nanoconjugates transport in tumors

Soutenue le 16 décembre 2020 devant le jury composé de :

Sébastien Benzekry	CR, HDR, Inria Bordeaux-Sud-Ouest, MONC	Directeur de thèse
Helen Byrne	Pr, University of Oxford	Rapportrice
Raphaëlle Fanciullino	MCU, HDR, Université d'Aix-Marseille	Directrice de thèse
Florence Gattacceca	MCU, HDR, Université d'Aix-Marseille	Examinatrice
Hans Peter Grimm	PhD, Roche Innovation Center Basel	Examineur
Jonathan P. Mochel	Associate Professor, Iowa State University	Invité
Roberto Natalini	DR, CNR Roma	Rapporteur
Clair Poignard	DR, Inria Bordeaux-Sud-Ouest, MONC	Directeur de thèse
Rebecca Shipley	Pr, University College of London	Président

ABSTRACT

Title: Mathematical modeling of antibody nanoconjugates transport in tumors

Abstract: Nanomedicine offers promising and innovative tools to treat cancer. Recently, liposomes conjugated with an antibody were developed to target breast cancer cells while sparing healthy tissues from the toxicity of the chemotherapy. These nanoparticles are called antibody-nanoconjugates (ANCs) and are currently tested in a preclinical trial. However, the pharmacokinetics, biodistribution, and efficacy of these nanoparticles are not well known and could be improved. Mathematical modeling can help in understanding the intratumor penetration of the nanoparticles and in quantifying the treatment efficacy.

Pharmacokinetic-pharmacodynamic modeling evaluates the dose-response relationship *in vivo* and can be used to optimize the therapy schedule. Here, we described several biological processes using ordinary differential equations: (i) the untreated tumor growth with a novel reduced Gompertz model, (ii) the nanoparticle biodistribution using a two-compartment pharmacokinetic model, and (iii) the therapeutic response with a resistance model. All the models were validated against experimental data in the statistical framework of nonlinear mixed-effects modeling, which models simultaneously the dynamic of the population and the inter-individual variability.

Furthermore, we derived a spatial mathematical model with the two-scale asymptotic expansion method to describe the fluid and nanoparticle transport within the tumor tissue. This approach allowed us to evaluate the barriers that impair a homogeneous distribution of nanoparticles at the tumor site. Moreover, we propose a computational framework to predict tumor accumulation of nanoparticles using individual imaging data.

Keywords: antibody-nanoconjugates, nonlinear mixed-effects modeling, two-scale asymptotic expansion

Titre: Modélisation mathématique du transport des nanoparticules dans les tumeurs

Résumé: La nanomédecine offre des perspectives ambitieuses pour le traitement du cancer. Récemment, des liposomes conjugués à des anticorps spécifiques ont été développés pour cibler les cellules tumorales du cancer au sein, en réduisant la toxicité de la chimiothérapie dans les tissus sains. Ces nanoparticules, appelées ANC (pour antibody nano-conjugate), sont actuellement testées dans une phase préclinique. Cependant, la pharmacocinétique, la biodistribution et l'efficacité de ces nanoparticules ne sont pas bien caractérisées quantitativement et pourrait être améliorées. La modélisation mathématique peut aider à mieux comprendre la dynamique de la pénétration des ANC dans la tumeur et à améliorer l'efficacité du traitement.

La modélisation pharmacocinétique-pharmacodynamique permet d'évaluer la réponse du traitement *in vivo* en fonction de la dose injectée. Dans ce travail, nous avons décrit plusieurs phénomènes biologiques avec des équations différentielles ordinaires : (i) la croissance tumorale avec un nouveau modèle réduit de Gompertz, (ii) la biodistribution des nanoparticules avec un modèle pharmacocinétique à deux compartiments, et (iii) la réponse au traitement avec un modèle de résistance. Tous les modèles ont été calibrés dans le cadre des modèles non linéaires à effets mixtes, qui décrivent la dynamique globale de la population ainsi que la variabilité individuelle.

De plus, nous avons dérivé un modèle mathématique spatial avec la technique de développement asymptotique double-échelle pour décrire le transport des fluides et des nanoparticules dans le tissu tumoral. Cette méthodologie nous permet d'évaluer les barrières microscopiques qui empêchent une distribution homogène des ANC dans la tumeur. Finalement, nous proposons un schéma computationnel pour prédire l'accumulation des nanoparticules à partir des données individuels d'imagerie.

Keywords: nanoparticules, modèles non linéaires à effets mixtes, pharmacocinétique, pharmacodynamique, développement asymptotique double-échelle

RÉSUMÉ

Le cancer du sein est le plus diagnostiqué chez les femmes au monde. Les progrès faits par la science dans le cadre des traitements médicaux et chirurgicaux ont permis d'améliorer les perspectives de survie ainsi que la qualité de vie des personnes affectées par cette maladie. Néanmoins, beaucoup reste à faire pour améliorer les médicaments. La toxicité des chimiothérapies est notamment un grand problème. Pour limiter ces effets secondaires, une approche innovante consiste à appliquer des nanotechnologies pour encapsuler l'agent cytotoxique dans des nanoparticules, afin de cibler les cellules tumorales et de préserver les tissus sains. Cependant, la dynamique de pénétration de ces nanoparticules dans le tissu tumoral n'est pas bien caractérisée quantitativement. L'objectif de ce projet de recherche est d'utiliser la modélisation mathématique pour décrire le transport des nanoparticules dans la tumeur, afin de mieux comprendre leurs propriétés et en optimiser l'efficacité.

Cette thèse se base sur une collaboration interdisciplinaire avec des pharmaciens de l'équipe SMARTc de l'université d'Aix-Marseille, qui ont développé des immunoliposomes, aussi appelés ANC (pour antibody nano-conjugate). Ces nanoparticules à base lipidique contiennent un agent cytotoxique (docétaxel) et présentent sur leur surface un anticorps (trastuzumab) qui se lie aux récepteurs Her2 des cellules du cancer au sein. Elles sont actuellement évaluées dans une phase préclinique. Les questions auxquelles nous nous sommes intéressés sont les suivantes: Comment est-il possible de prévoir la taille de la tumeur et l'efficacité des nanoparticules ? Quelle est la programmation optimale du traitement ? Comment le microenvironnement de la tumeur (comme la pression du fluide interstitiel, la densité des vaisseaux, la taille de la tumeur ou l'expression de Her2) affecte-t-il le transport des nanoparticules ? Comment est-il possible de personnaliser la dose et le protocole d'administration des médicaments à partir de données histologiques sur le microenvironnement de la tumeur ?

Les résultats de ce travail apportent une contribution directe au développement des anticorps-nanoconjugués dans le traitement du cancer du sein.

La modélisation mathématique peut permettre de mieux comprendre la dynamique sous-jacente au processus de transport des nanoparticules dans la tumeur, ce qui est la première étape pour évaluer l'efficacité et adapter la posologie. Quand les ANC sont injectées par voie intraveineuse, elles doivent traverser différentes barrières: le transport vasculaire jusqu'au site de la tumeur, le transport trans-épithélial pour passer des capillaires au tissu tumoral, la pénétration dans le com-

partiment interstitiel et l'absorption par les cellules (endocytose). La complexité liée au transport des nanoparticules jusqu'au tissu tumoral rend difficile de quantifier la concentration de nanoparticules qui va réellement agir sur les cellules cancéreuses à partir de la dose injectée. Des modèles biophysiques peuvent décrire ce processus et déterminer la portion de médicament qui arrive aux cellules tumorales ainsi que leur efficacité.

Ce manuscrit se divise en deux parties: dans la première partie, nous étudions un modèle pharmacocinétique-pharmacodynamique afin de caractériser la biodistribution des nanoparticules ainsi que l'efficacité *in vivo* ; dans la deuxième partie, un modèle spatial de transport de fluide et de nanoparticules dans la tumeur est dérivé avec la méthode du développement asymptotique double-échelle.

La modélisation pharmacocinétique-pharmacodynamique permet d'évaluer la réponse du traitement *in vivo* en fonction de la dose injectée. Dans ce travail, nous avons décrit plusieurs phénomènes biologiques avec des équations différentielles ordinaires: (i) la croissance tumorale avec un nouveau modèle réduit de Gompertz, (ii) la biodistribution des nanoparticules avec un modèle pharmacocinétique à deux compartiments, et (iii) la réponse au traitement avec un modèle de résistance. Tous les modèles ont été calibrés dans le cadre des modèles non linéaires à effets mixtes, qui décrivent la dynamique globale de la population ainsi que la variabilité inter-individuelle.

Nous avons dérivé un modèle de Gompertz réduit dans le cadre statistique des modèles non linéaires à effets mixtes pour décrire la croissance des tumeurs non traitées. Ce modèle, qui comporte un paramètre au niveau de la population et un paramètre spécifique à l'individu, a montré un bon pouvoir descriptif (similaire au modèle de Gompertz) et a amélioré les prédictions du temps d'initiation de la tumeur. En outre, grâce à l'interprétation biologique des paramètres du modèle, nous avons pu valider le modèle sur un nouvel ensemble de données en estimant les paramètres à partir d'expériences indépendantes. Notre modèle devrait être testé afin de prédire la taille des tumeurs individuelles (c'est-à-dire pour les prévisions dans le futur). En effet, une bonne caractérisation de la croissance de la tumeur est d'une importance fondamentale pour faire des prédictions sur la réponse individuelle aux traitements. Bien que notre méthode reste à étendre à des données cliniques, ces résultats sont prometteurs pour l'estimation personnalisée de l'âge d'une tumeur à partir de mesures limitées au moment de la détection. L'estimation de l'âge de la tumeur d'un patient pourrait en effet être instructive pour la pratique clinique, par exemple pour contribuer à l'élaboration de modèles informatiques personnalisés de métastases.

La biodistribution des ANC et leur efficacité ont été évaluées à l'aide d'un modèle pharmacocinétique-pharmacodynamique. Un modèle pharmacocinétique (PK) à deux compartiments basé sur un système d'équations différentielles ordinaires a été utilisé pour décrire l'échange de nanoparticules entre les compartiments systémique et tumoral. Le modèle PK a été calibré sur quatre ensembles différents de données, ce qui nous a permis de comparer la distribution des anticorps-nanoconjugués et des liposomes (sans trastuzumab greffé en surface) dans les compartiments central

et tumoral. Un modèle pharmacodynamique (PD) de résistance a été utilisé pour évaluer l'efficacité des nanoparticules. La comparaison entre les liposomes et les ANC n'a pas montré de différences significatives en termes d'activité cytotoxique, bien que la résistance acquise aux ANC soit légèrement inférieure à la résistance aux liposomes. Les mécanismes d'action des liposomes et des immunoliposomes devraient être davantage mis en évidence, même si la plus grande efficacité globale des ANC pourrait être due à une internalisation plus efficace grâce à l'anticorps greffé à la surface. De plus, l'efficacité des deux nanoparticules était supérieure à celle des médicaments libres grâce à l'amélioration de la pharmacocinétique des deux formulations liposomales. Toutefois, la PK des ANC et des liposomes pourrait être évaluée plus en détail. La mesure de la concentration plasmatique du médicament nous permettrait d'estimer le volume de distribution et la clairance systémique des deux formulations liposomales. En effet, les immunoliposomes pourraient être reconnus et éliminés plus rapidement par le système des macrophages ou ils pourraient être absorbés par d'autres organes en raison du trastuzumab greffé. Dans une perspective d'avenir, un modèle pharmacocinétique physiologique (PBPK) pourrait permettre de mieux comprendre les phénomènes impliqués dans les processus d'absorption, de distribution, de métabolisme et d'excrétion. En outre, l'efficacité *in vivo* des nanoparticules pourrait être modélisée en tenant compte du docétaxel et du trastuzumab dans le processus de la croissance tumorale.

La modélisation pharmacocinétique-pharmacodynamique est fondamentale dans le processus de développement des médicaments: la pharmacocinétique permet d'évaluer l'exposition au site d'action en fonction de la dose injectée, tandis que la pharmacodynamique décrit la réponse au traitement. De nouveaux schémas de traitement pourraient être testés expérimentalement en fonction des prédictions de notre modèle. Il est important de noter que la modélisation de la PKPD permet de traduire la PK en applications cliniques en quantifiant la dose initiale requise chez l'homme.

La grande hétérogénéité des tissus tumoraux ainsi que les propriétés des nanomédicaments ont un impact sur l'administration des médicaments au niveau du site de la tumeur. Pour comprendre les principaux facteurs qui affectent la distribution des nanoparticules, nous avons dérivé un modèle spatial de transport de médicaments qui prend en compte les caractéristiques microscopiques de la tumeur sur la dynamique globale. L'étude de la distribution des ANC dans la tumeur se base sur trois points : (i) l'élaboration d'un modèle théorique avec des équations mathématiques pour la description des phénomènes biologiques, (ii) la simulation numérique des modèles dérivés et (iii) leur validation avec des données expérimentales. On propose un modèle théorique de concentration des ANC dans les vaisseaux et dans le compartiment interstitiel couplé avec l'écoulement des fluides dans le tissu tumoral. La pénétration des nanoparticules dans la tumeur se produit par diffusion et convection. Il faut donc d'abord caractériser l'environnement tumoral, c'est-à-dire le transport des fluides interstitiel et sanguin. Le tissu tumoral peut être vu comme un milieu poreux hétérogène irrigué par des capillaires très irréguliers et perméables. Avec la méthode d'homogénéisation nous avons construit un modèle asymptotique qui décrit l'écoulement des fluides au niveau macroscopique, en

tenant compte de la microstructure du tissu tumoral (i.e., le réseau des capillaires). Le modèle est un couplage d'équations de Darcy et présente des comportements différents selon la perméabilité et la structure capillaire paramétrée. Ainsi, le modèle prend en considération l'hétérogénéité et la porosité du tissu tumoral. Enfin, nous avons développé un modèle asymptotique de diffusion, convection et réaction des nanoparticules avec la méthode d'homogénéisation pour décrire la concentration des ANC dans les capillaires et dans le compartiment interstitiel. Le terme de réaction prend en compte l'interaction des nanoparticules avec les cellules tumorales. Après avoir fait une analyse mathématique du modèle dérivé, nous avons obtenu des résultats numériques en utilisant la méthode des différences finies. Les simulations numériques ont montré que l'environnement tumoral (i.e., la structure des capillaires et leur perméabilité) a un fort impact sur la pénétration des ANC, en accord avec les observations biologiques. Ce résultat qualitatif est une étape essentielle pour garantir la validité du modèle. La calibration du modèle a été effectuée empiriquement ou à l'aide des différentes données à disposition: des données *in vitro* qui permettent d'analyser le mécanisme d'absorption par les cellules (pour déterminer le terme de réaction) ; les données *in vivo* donnent des informations sur la perméabilité des vaisseaux et sur la clairance des nanoparticules dans le plasma.

Enfin, nous avons proposé une méthodologie pour intégrer les données d'imagerie individuelles dans le modèle mathématique spatial. En particulier, nous avons utilisé des données *ex vivo* pour récupérer les tenseurs de perméabilité et avons effectué des simulations individuelles de la pénétration des nanoparticules dans le compartiment interstitiel de la tumeur. Ces prédictions ont été comparées aux résultats du modèle pharmacocinétique calibré à partir de mesures macroscopiques. Ces résultats sont prometteurs pour la personnalisation des traitements. Les technologies émergentes d'acquisition d'images permettent de quantifier les propriétés microscopiques de la tumeur *in vivo*. Ces données peuvent être intégrées dans le modèle afin de prédire l'accumulation de nanoparticules et de programmer la dose optimale pour améliorer l'efficacité thérapeutique.

Plusieurs stratégies pourraient être employées pour améliorer la délivrance des médicaments par les nanoparticules au niveau du site de la tumeur. Selon notre analyse, la pression du fluide interstitiel est la principale barrière d'une pénétration inefficace dans le tissu tumoral. Pour diminuer la pression du fluide interstitiel, la normalisation vasculaire pourrait être une solution possible. La diminution de la surface vasculaire et de la conductivité hydraulique des parois des vaisseaux réduirait la filtration du fluide et la pression du fluide interstitiel. Cependant, elle entraînerait également une perte de filtration des nanoparticules en raison de la perte de perméabilité des parois des vaisseaux. Une deuxième stratégie possible pourrait être la normalisation de la matrice interstitielle. L'augmentation de la conductivité hydraulique interstitielle permettrait de réduire la pression du fluide interstitiel. De plus, la normalisation de la matrice interstitielle pourrait améliorer la diffusion des nanoparticules, qui est affectée par le collagène. En outre, les propriétés des immunoliposomes pourraient être optimisées. Dans ce travail, nous avons observé que la taille des nanoparticules joue un rôle important dans leur transport. En effet, les grosses particules sont moins susceptibles d'être extravasées dans l'interstitium de la tumeur que les petites particules et leur diffusion est entravée. Par conséquent, la réduction de la taille pourrait favoriser une pénétration homogène dans le tissu

tumoral. En outre, le taux de greffe du trastuzumab pourrait affecter l'affinité de liaison des nanoparticules avec les cellules et les taux d'internalisation. Les expériences *in vitro* pourraient fournir des informations sur cette propriété des immunoliposomes. De plus, le médicament encapsulé dans les nanoparticules pourrait être modulé pour optimiser la quantité de médicament qui atteint le site de la tumeur. Une étude récente a montré qu'il pourrait y avoir une dose seuil du nombre de NP qui pourrait améliorer la délivrance du médicament (à savoir, 1 trillion de nanoparticules chez la souris). En outre, nous avons observé que les ANC pourraient améliorer la vascularisation. L'impact des immunoliposomes sur la vascularisation de la tumeur pourrait être étudié afin d'évaluer les effets sur la perméabilité des parois des vaisseaux. En particulier, la couronne de protéines qui se forme à la surface des nanoparticules pourrait apporter de l'oxygène à la tumeur, améliorant ainsi sa perméabilité. En outre, la couronne protéique pourrait être différente selon la composition chimique de la nanoparticule, ce qui pourrait mettre en évidence les différences d'accumulation de la tumeur entre les liposomes et les immunoliposomes.

ACKNOWLEDGEMENTS

Je tiens d'abord à remercier mes directeurs de thèse Sébastien Benzekry, Clair Poignard et Raphaëlle Fanciullino. Merci à Sébastien Benzekry pour avoir transmis sa passion pour les mathématiques appliquées à l'oncologie, et à Clair Poignard pour les enseignements en analyse mathématique et numérique. J'ai apprécié de travailler avec vous, tant d'un point de vue scientifique qu'humain. Je vous remercie pour l'estime et la confiance réciproques. Merci à Raphaëlle Fanciullino pour la connaissance en biologie et pharmacie qui ont apporté une grande contribution à mon travail de recherche.

Thanks to Helen Byrne and Roberto Natalini for having read this thesis and for the nice and encouraging comments. Thanks to Florence Gattacceca, Hans Peter Grimm, Jonathan P. Mochel and Rebecca Shipley for being part of the jury.

Merci à toute l'équipe SMARTc pour les discussions scientifiques et pour votre accueil à Marseille. Un grand merci en particulier à Anne Rodallec pour les données expérimentales et pour sa disponibilité infinie à répondre à toutes mes questions, et à Joseph Ciccolini pour les conseils scientifiques.

Je suis très fier d'avoir fait partie de l'équipe MONC. Merci à toutes et tous pour vos enseignements et pour la bonne atmosphère qui règne dans l'équipe. En particulier, merci à Olivier Saut pour toute la disponibilité et le soutien, Annabelle Collin pour les précieux conseils sur les simulations numériques, Christèle Etchegaray pour les inestimables conseils sur mon travail. Merci aussi à Sylvie Embolla pour sa gentillesse et disponibilité. Merci à tous les doctorants, postdocs et membres des équipes MONC et MEMPHIS pour les beaux moments passés ensemble, qui ont rendu ces trois années très agréables : Sergio, Pedro, Cédric, Arturo, Antoine, Guillaume, Giulia, Gwladys, Sébastien, Tommaso, Costanza et tous ceux qui sont partis au fil des ans. Merci en particulier à mes « co-bureau » Thibaut, Remi, Cécile, Floriane, Océane et Anne-Sophie pour votre disponibilité et soutien.

Ces trois années ont été très intenses et pleines des belles surprises. D'abord, merci à Bordeaux pour l'accueil, le bon vin et la bonne cuisine. Un très grand merci au Chœur Voyageur pour m'avoir fait découvrir la beauté du chant, pour m'avoir portée autour de la Nouvelle Aquitaine (mais pas seulement), pour son esprit et son bonheur qui m'ont accompagnée pendant ces dernières années. Merci à tous mes amis de Bordeaux pour les beaux moments passés ensemble.

Vorrei ringraziare in modo particolare i miei grandi compagni di viaggio, Silvia e Giuliano. Grazie a Silvia, con cui ho condiviso ogni avventura - e anche disavventura - dal primo giorno in cui sono arrivata a Bordeaux: grazie per avermi fatto sentire a casa e in famiglia, per essere sempre stata presente e per il sostegno reciproco. Grazie a Giuliano, che ho avuto la fortuna di incontrare a Bordeaux dopo esser stati compagni di università: grazie per essere stato un punto di riferimento per ogni mio dubbio matematico (e culturale) e per l'amicizia che ci lega da così tanti anni.

Grazie a tutti i miei amici in Italia per la loro costante presenza. Grazie in particolare a Mary, Marta, Lucrezia, Eleonora e Arianna per essere fonte di ispirazione dai tempi del liceo. Grazie a Elisa, Manuela, Annagiulia, Maria Laura, Claudia e Roberta per il forte legame che abbiamo dall'università.

Grazie alla mia famiglia che mi ha sempre sostenuto anche a distanza. Grazie a tutti i miei zii e cugini, a cui sono molto affezionata. Grazie ai miei fratelli, Stefano ed Emanuela, per essere sempre disponibili ad aiutarmi e consigliarmi. Un immenso grazie ai miei genitori, Bruna e Massimo, per aver sempre alimentato la mia curiosità e per il supporto incondizionato.

Infine, grazie a te, Giorgio, per tutto quello che abbiamo vissuto e che vivremo insieme. Grazie per essere sempre presente ad ascoltarmi, sostenermi, consigliarmi e per darmi ogni giorno una marcia in più.

ACRONYMS

NP	Nanoparticle
ANC	Antibody-nanoconjugate
NLMEM	Nonlinear mixed effects modeling
IFP	Interstitial fluid pressure
IFV	Interstitial fluid velocity
MVP	Microvascular pressure
EPR	Enhanced permeability retention
PK	Pharmacokinetics
PD	Pharmacodynamics

CONTENTS

Abstract	iv
Resumé	v
Acknowledgements	xi
Acronyms	xiii
1 Introduction	1
1.1 Biological background	3
1.2 State of the art	11
1.3 Experimental data	16
1.4 Main contributions and outline of the thesis	18
I PHARMACOKINETIC-PHARMACODYNAMIC MODELING	25
2 Untreated tumor growth analysis	27
2.1 Overview on tumor growth	29
2.2 Introduction	32
2.3 Material and methods	33
2.4 Results	38
2.5 Discussion	46
2.6 Validation of the reduced Gompertz model	52
2.7 Further applications of the reduced Gompertz model: assessing the differences in tumor growth kinetics	54
2.8 Conclusion	56
3 Evaluation of the nanoparticle dose-response relationship: <i>in vitro</i> studies	57
3.1 Introduction	59
3.2 Material and methods	60
3.3 Results	63
3.4 Discussion	63

4	<i>In vivo</i> pharmacokinetic-pharmacodynamic modeling of liposomes and immunoliposomes	67
4.1	Introduction	69
4.2	Biodistribution and tumor growth data	70
4.3	Mathematical modeling and calibration	72
4.4	Results	75
4.5	Discussion	81
II	SPATIAL MATHEMATICAL MODELING OF NANOPARTICLE TRANSPORT IN TUMOR TISSUES	87
5	Macro-scale models for fluid flow in tumor tissues: impact of the microstructure properties	89
5.1	Introduction	91
5.2	Microscale model of fluid transport in tumors	94
5.3	Continuum macroscale models using two scale asymptotic analysis	98
5.4	Derivation of the macro-scale models	104
5.5	Numerical convergence of the multiscale model to the homogenized models (2D) . .	109
5.6	Numerical simulations	112
5.7	Discussion	118
6	Macro-scale model of nanoparticle and drug transport in the tumor interstitium	121
6.1	Introduction	123
6.2	A microscopic model of nanoparticle transport in the tumor interstitium	124
6.3	Derivation of a macroscale model of nanoparticle concentration in the tumor tissue .	125
6.4	Numerical simulations	128
6.5	Discussion	137
7	A computational framework to predict individual tumor nanoparticle accumulation	141
7.1	Introduction	143
7.2	<i>Ex vivo</i> data: microscopy fluorescence imaging	144
7.3	Methods	144
7.4	Results	150
7.5	Discussion	154
	Conclusion and perspectives	157
	Appendices	161

A	Cell doubling time	161
B	Supplementary figures and tables to Chapter 2	169
C	Supplementary material to Chapter 3	180
	Bibliography	203

INTRODUCTION

Breast cancer is the most common malignant tumor diagnosed in women worldwide [1]. In the last decades, several innovative treatments have improved life expectancies and the quality of life of people who are affected by this disease. Indeed, the majority of early-stage breast malignancies is curable with currently available therapeutical options. However, advanced metastatic breast cancer is still an incurable disease and the goals of therapies are to control symptoms and prolong survival with low-toxic treatments [2].

Toxicity associated with cytotoxic drugs is a challenging problem in breast cancer therapy. To overcome this issue, nanoparticles (NPs) can be developed to target the tumor site and to spare healthy tissues. In this thesis, we focus on liposomes conjugated with cancer cell-specific antibodies [3], which are called antibody-nanoconjugates (ANCs). Mathematical modeling can help in better understanding the properties of these nanoparticles, enabling us to quantify the intra-tumor penetration and their efficacy. Importantly, it provides a link between different kinds of data (such as *in vitro*, *in vivo* and *ex vivo* data) that can be used to understand the nanoparticle contribution in the tumor growth kinetics. This can be applied to make predictions of the individual NPs accumulation and response to the therapy and potentially schedule personalized treatments.

This thesis is the result of a three year research project in the INRIA team MONC at the Institut de Mathématiques de Bordeaux (University of Bordeaux). The study has been carried out in collaboration with the SMARTc team¹ in Marseille, who realized the experiments and provided the data to analyze.

The document is divided into two parts: in the first part, the pharmacokinetic-pharmacodynamic of the nanoparticles is investigated to assess the nanoparticles dose-response relationship; in the second part, a spatio-temporal model of ANC transport in the tumor tissue is introduced to quantify the intra-tumor penetration of the nanoparticles according to the characteristics of the tumor architecture. This chapter introduces the biological background and relevant questions that were addressed, as well as the methodology that has been applied.

¹SMARTc, CRCM Inserm UMR1068, CNRS UMR7258, Aix Marseille University, France

Contents

1.1 Biological background	3
1.1.1 Breast cancer overview	3
1.1.2 Nanomedicine	4
1.1.2.1 Liposomes: mechanism of drug delivery in cancer treatment . .	5
1.1.3 Development of antibody-nanoconjugates against breast cancer	8
1.1.4 Open questions	10
1.2 State of the art	11
1.2.1 Overview of mathematical models in cancer nanomedicine	11
1.2.2 The journey of nanoparticles to solid tumors: determinants and barriers .	12
1.2.3 Techniques to improve nanoparticle delivery	15
1.3 Experimental data	16
1.3.1 <i>In vitro</i> data	16
1.3.2 <i>In vivo</i> data	17
1.3.3 <i>Ex vivo</i> data	17
1.4 Main contributions and outline of the thesis	18

1.1 Biological background

1.1.1 Breast cancer overview

Breast cancer is a disease that develops primarily in the breast tissue, typically in the lobules or the ducts of the breast. It occurs when mutations of genes that regulate cell growth let cells proliferate in an uncontrolled way. Therapies and prognosis strongly depend on the histological and molecular characteristics and several classifications of breast cancer have been made (see Figure 1.1). Here, we shortly explain the major features of breast cancer and its treatment and we invite the reader to read [2] and [4] for further details.

Histology. Invasive ductal carcinoma is the most common breast cancer (50%-70% of patients) followed by invasive lobular carcinoma (5%-15% of cases) [4].

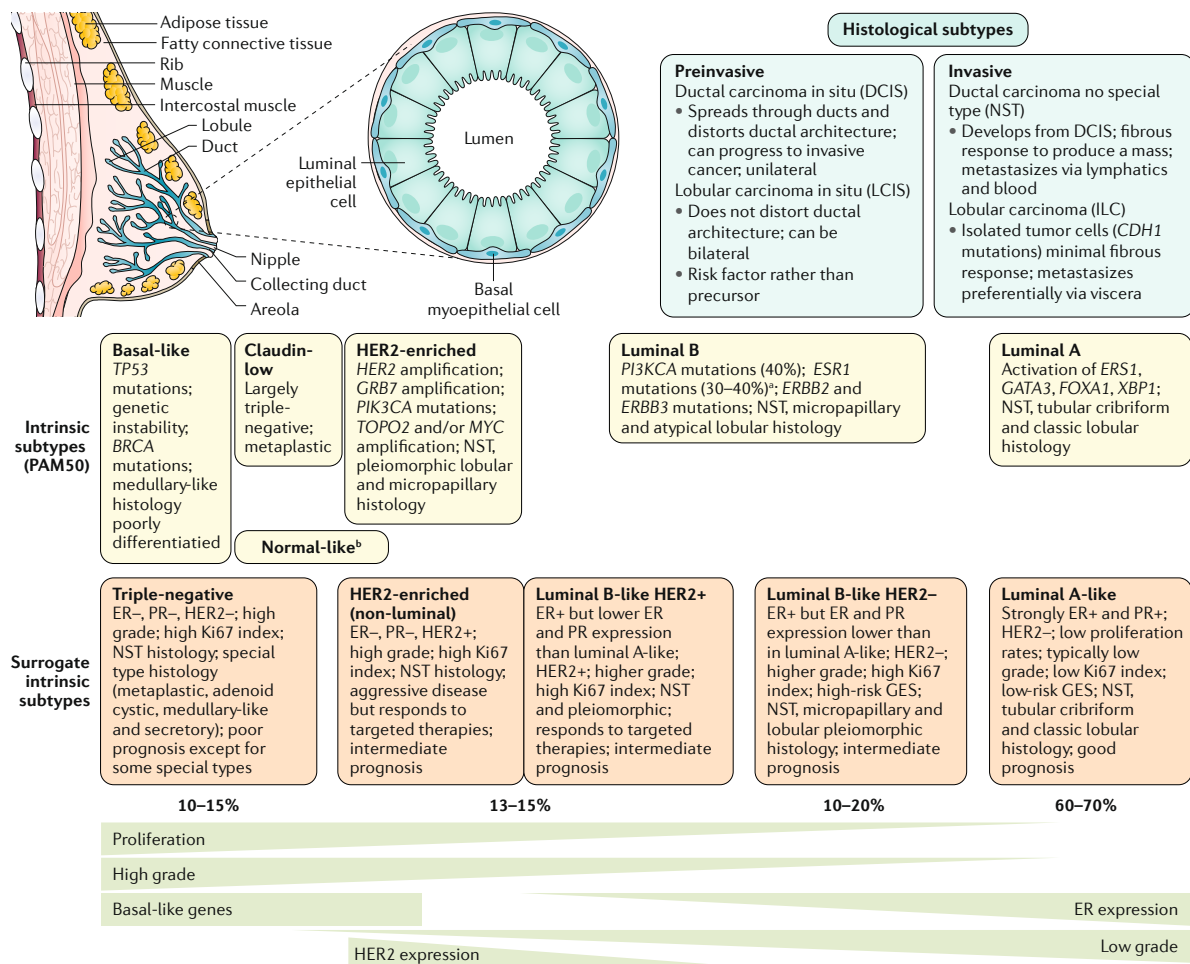


Figure 1.1. Classification of breast cancer according to the histology and the molecular alterations (from [2]).

Molecular alterations. Two major molecular alterations affect the prognosis and the treatment of breast cancer: the hormone receptors and the epidermal growth factor receptor. The estrogen re-

ceptor alpha ($ER\alpha$) is overexpressed in over half of all breast cancers [5]. $ER\alpha$ is a ligand-activated transcription factor that stimulates cell proliferation in the breast tissue when activated by estrogens. A further marker of $ER\alpha$ signaling is the progesterone receptor (PR). Breast cancers with overexpression of one of these two steroid hormone receptors are classified as HR^+ . The second main molecular alteration concerns the epidermal growth factor (ERBB2, also known as Her2 or Her2/neu). Breast cancer with overexpression of **Her2 receptors** are classified as Her2-positive. Amplification of this oncogene plays an important role in the development of certain types of aggressive breast tumors. However, this receptor has recently become an important biomarker since drugs targeting Her2 receptors have drastically improved the prognosis of Her2-positive breast cancer [6].

Breast cancers that don't express $ER\alpha$, PR and Her2 receptors are called **triple-negative** and lack targeted therapies, implying a worse prognosis. It represents approximately 15% of all breast tumors [7].

Stages. Breast cancer stage is usually denoted by a number on a scale from I to IV based on the extent of the disease (tumor size, skin or chest invasion, lymph nodes involvement and metastatic spread). Stage I is associated to non-invasive breast cancers, while stage IV describes distant metastatic diseases. Recently, molecular alterations have been included in the determination of breast cancer stage [4].

Standard treatments. Therapies for early-stage breast cancer usually include local intervention and systemic treatments to eliminate the tumor and to prevent metastatic spread. The goal of advanced breast cancer treatments is rather to prolong life and control symptoms with palliative care. Local treatment consists of surgical intervention with the removal of the tumor possibly followed by radiotherapy. Systemic treatments can be adjuvant (before surgery), neo-adjuvant (after surgery) or both. They can involve chemotherapy, targeted therapies or a combination of them according to the molecular alteration of the cancer cells. Among the targeted therapies, the introduction of **trastuzumab (Herceptin[®]) has revolutionized the treatment of Her2-positive breast cancer.** Moreover, trastuzumab emtansine (T-DM1, Kadcyla[®]) is an antibody-drug conjugate consisting of trastuzumab covalently linked to the microtubule inhibitory drug DM1 and has recently been approved to treat Her2-positive advanced breast cancer [8].

The toxicity of chemotherapy drugs remains a major issue in breast cancer treatment. Nanotechnology offers potential and hopes to breast cancer research with the development of innovative nano-formulations of chemotherapy [9]. With a deeper understanding of the molecular properties of breast cancer, the nano-carriers can indeed better target the tumor cells while sparing healthy tissues [10]. The next sections provide an overview of nanomedicine and its role in breast cancer therapy.

1.1.2 Nanomedicine

Nanomedicine is an emerging branch of medicine that applies tools and knowledge of nanotechnology, involving the use of materials at the nanoscale (1-100 nm). Research in this field spans from

nanoscience to chemistry, physics, biology and pharmacology. Early and rapid diagnosis, targeted drug delivery, innovative ways to provide tissue and organ replacement and personalized medicines are the main challenges of nanomedicine [11]. Here, we provide a short overview of the major applications of nanomedicine and refer to [12] for an exhaustive review. Then, we focus on the mechanism of drug delivery in tumors by liposomes.

Nanoparticles for **drug delivery** can improve the pharmacokinetics (*i.e.*, the absorption, distribution, metabolism, and excretion) of the drug. Nanoengineered devices can indeed increase the bioavailability of a drug in a specific part of the body over a period of time. For example, in anti-cancer therapy, they can easily circulate in the blood vessel network and target the tumor thanks to the leaky neoplastic vasculature. Moreover, nanocarriers might regulate drug release, reduce drug clearance rate and lower the side effects on non-target tissues [13]. Furthermore, their ability to interact with molecules can overcome biological barriers and improve the uptake across the cell membrane. Nanosized formulations include liposomes, polymeric nanoparticles, dendrimers, inorganic nanoparticles and nanocrystals and are mainly applied in the treatment of cardiovascular diseases [14], brain diseases and disorders [15], and cancer. Doxil[®] and Abraxane[®] are two examples of FDA-approved nanodrugs used to treat advanced metastatic breast cancer [10].

Nanotechnologies also provide alternative approaches for medical **diagnosis**. Nanoparticle contrast agents can be used for ultrasound or magnetic resonance imaging (MRI) to improve contrast [16]. They are mainly used to detect cardiovascular diseases and tumors. Nanosensors can be engineered to label specific structures or microorganisms to monitor physical parameters or detect the presence of chemical species [17]. **Theranostic nanoparticles** are biomedical devices that combine diagnostic and therapeutic agents in a single platform and are designed for specific and personalized disease management [18].

Furthermore, nanomedicine offers promises to **tissue and organ engineering**. The primary goal is to create devices that can substitute tissues. Nanomaterials can be synthesized to provide new functions and properties to implants. For example, carbon nanostructures are integrated in bone tissue engineering as they provide mechanical strength and useful electronic properties [19].

1.1.2.1 Liposomes: mechanism of drug delivery in cancer treatment

Liposomes are spherical vesicles with a membrane composed of a lipid bilayer that can encapsulate drugs and imaging agents. They are currently used for cancer treatment and diagnosis. In the last three decades, efforts have been made to improve their efficiency, biocompatibility, biodegradability, toxicity profile, capability to incorporate multiple agents (both hydrophilic and hydrophobic drugs) and, finally, actively target the tumor site [20].

The original liposome preparation dates back to 1965 by Bangham *et al.* [21], who established the basis for model membrane systems. Liposomes were first studied as drug delivery systems in the 70s [22, 23, 24]. However, when intravenously administered, the **conventional liposomes** were rapidly captured by the mononuclear phagocyte system (MPS) and removed from blood circulation, leading

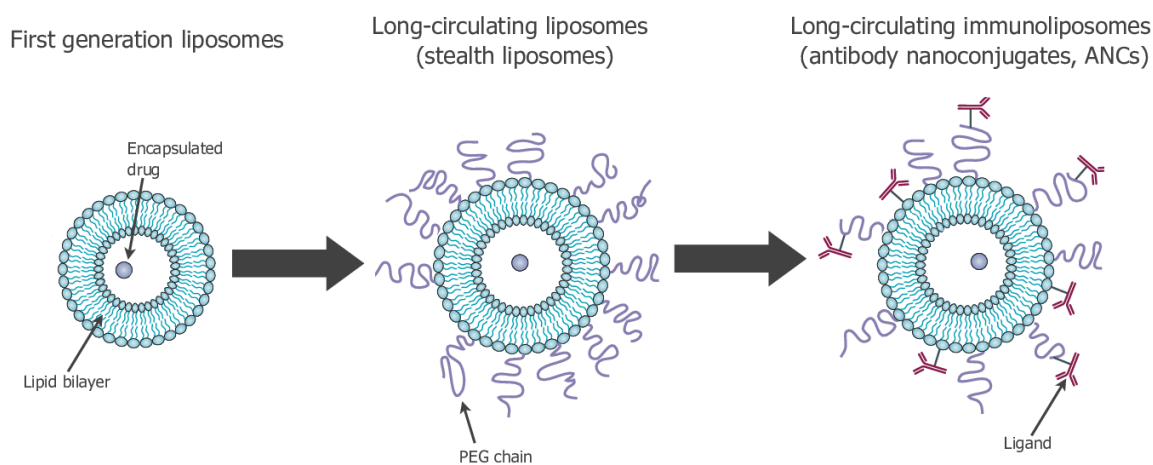


Figure 1.2. History of the development of liposomes for drug delivery: conventional liposomes (*left*); stealth liposomes (*center*); immunoliposomes (*right*). Images adapted from [30].

to inefficient drug delivery (Figure 1.2, left). Therefore, at the end of the 80s, a second formulation of long-circulating liposomes has been developed to reduce the interactions between the MPS macrophages and the nanoparticles. Among these long-circulating liposomes, there are **stealth liposomes**, which are nanocarriers obtained by modifying the surface with hydrophilic polymers such as polyethylene glycol (PEG) [25, 26] (see Figure 1.2, center). The hydrophilic polymers possess a flexible chain that occupies the space around the liposome surface and excludes other macromolecules from this space, inhibiting the interaction between the macrophages and the liposomes. As a result, long-circulating liposomes can passively accumulate inside other tissues and organs, taking advantage of the leaky vasculature in correspondence of the tumor. This phenomenon, called *passive targeting*, is particularly evident in tumors undergoing angiogenesis [27]. Finally, starting from the 90s, efforts have been focused on developing stealth-liposomes that *actively target* tumor sites [28]. These **stealth-immunoliposomes** are obtained by coupling specific ligands to the liposomal surface that bind tumor cell-specific receptors (Figure 1.2, right). For instance, anti-Her2 monoclonal antibodies can be used as ligands to target Her2 receptors [29, 3].

Doxil[®] (pegylated liposomal doxorubicin) is the first FDA approved nanodrug (1995) [31]. It is used in the treatment of some types of cancer, such as metastatic ovarian cancer, metastatic breast cancer and AIDS-related Kaposi's sarcoma.

As stated before, passive and active targeting are the main strategies that allow intravenously injected liposomes to reach the tumor site (Figure 1.3). Here below, we explain the main features of these two mechanisms.

Passive targeting

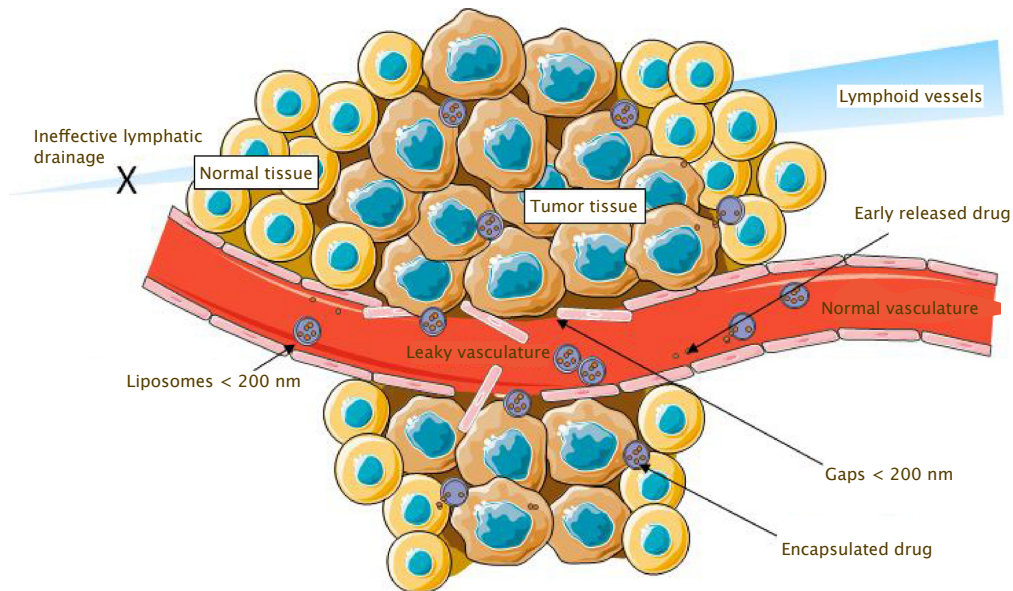
Big molecules, such as nanoparticles, liposomes or macromolecular drugs, tend to accumulate in tumor tissues much more than they do in healthy tissues. This phenomenon is called Enhanced Permeability Retention (EPR) effect [27]. Solid tumors are characterized by leaky vasculature that is necessary for the development of the tumor (angiogenesis). In addition, solid tumors lack of an adequate lymphatic drainage, leading to a limited circulatory recovery of the molecules that go through the vasculature gaps. As a results, macromolecules and nanoparticles accumulate in the tumor microenvironment. Long circulating liposomes improve the EPR effect, since they have longer interaction with the target and are more likely to pass through the vasculature gaps.

Important parameters that affect passive targeting through the EPR effect, apart from the PEGylated liposomes, are the size of the liposomes, the composition and the charge on the surface of the nanoparticles [32]. In particular, the permeation of the nanoparticles within the tumor is highly influenced by the size of the nanoparticles. Small nanoparticles (~10 nm) rapidly diffuse throughout the tumor matrix, while large nanoparticles (~100 nm) stay close to the vasculature [32]. Physical and chemical properties of the nanoparticles affect their pharmacokinetics and, therefore, their tumor accumulation capacity [32]. The process involving cell internalization of liposomes is mainly endocytosis [33]. Depending on their physical attributes, such as particle size, shape and surface charge and on the cell line, they are subject to a particular cellular internalization route or a combination of processes. These include, for example, phagocytosis, clathrin-mediated endocytosis (or receptor-mediated endocytosis), clathrin-independent endocytosis, caveolae and macropinocytosis.

Active targeting

Actively targeted liposomes have been designed to improve tumor specificity. They are prepared by grafting targeting moieties, such as molecule ligands, peptides or monoclonal antibodies, on the liposomal surface. When liposomes accumulate in the tumor microenvironment, they are endocytosed into the cells by interacting with specific cell surface receptors (*receptor-mediated endocytosis*) [34]. However, a comparison between passive and active targeting reveals a lack of significant difference in tumor accumulation [35, 36].

Passive targeting



Active targeting

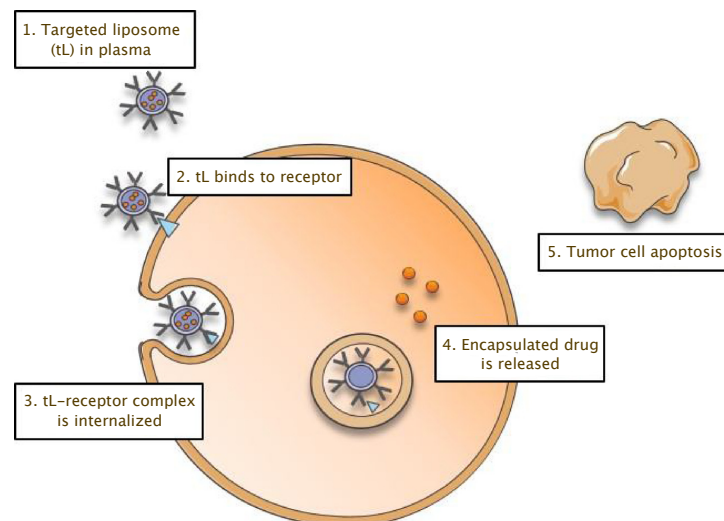


Figure 1.3. Passive targeting (*top*) and active targeting (*bottom*): mechanisms of drug delivery of the immunoliposomes. Images adapted from [37].

1.1.3 Development of antibody-nanoconjugates against breast cancer

Several efforts have been made to reduce the toxicity and improve the specificity of chemotherapy treatments of breast cancer. The research group SMARTc has developed a liposomal formulation that combines docetaxel and trastuzumab to target breast cancer cells [3]. These nanocarriers are

currently in a preclinical trial. In this section, we explain the main characteristics of this kind of nanoparticles and how they are obtained.

Docetaxel is a chemotherapy drug belonging to the family of taxanes. It is an anti-mitotic drug that arrests the mitosis cycle at the metaphase/anaphase stabilizing the microtubules. Then, since the microtubules don't disassemble in presence of docetaxel, they accumulate inside the cell leading to cell apoptosis. **Trastuzumab** is a monoclonal antibody that binds Her2 receptors, inducing an immune-mediated response that causes internalization and downregulation of Her2. Docetaxel combined with trastuzumab is widely used to treat Her2 positive breast cancers, (neoadjuvant and/or adjuvant [38], both for advanced and early-stage diseases).

The high cytotoxicity of docetaxel affects all dividing cells in the human body, leading to severe adverse effects. To overcome this issue, the chemotherapy drug has been incorporated into *stealth* liposomes engrafted with trastuzumab on the surface to target better tumor cells and to spare healthy tissues. These immunoliposomes are called **antibody-nanoconjugates (ANCs)**. A schematic of ANCs is shown in Figure 1.4.

The ANCs developed by Rodallec *et al.* are made of natural lipids [39] and the diameter of the nanoparticle is 140 nm. Other details on the encapsulation of docetaxel and the trastuzumab engraftment on the liposome surface are detailed in [39].

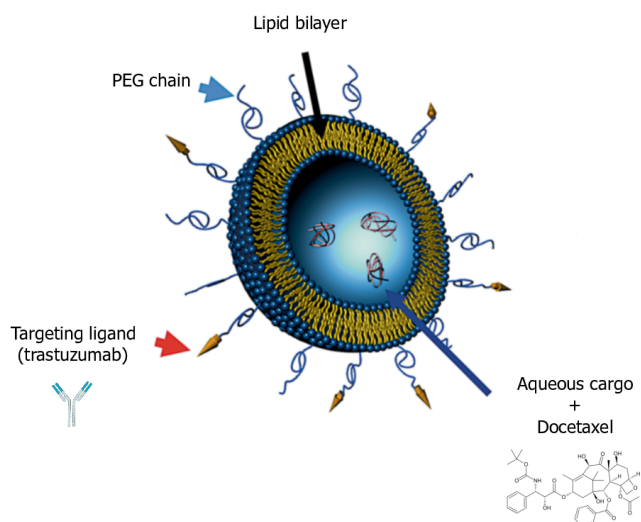


Figure 1.4. Stealth liposome with targeting ligand: the liposome is composed by a lipid bilayer and it contains the chemotherapy drug (docetaxel). On the surface, the PEGylated chain impairs the interactions with the macrophages and the ligand (trastuzumab) targets Her2 receptors on breast cancer cells. Figure adapted from [40].

1.1.4 Open questions

The main challenge of nanoparticles for drug delivery is to enhance the drug efficacy at the site of action while reducing toxicity. The quantification of the efficacy of ANCs is not a trivial task due to the higher complexity associated with the nanoformulation compared with the standard treatments. Indeed, several parameters might affect the journey of the nanoparticles as well as the cellular uptake. Furthermore, the characteristics of the tumor tissue - such as interstitial fluid pressure, the permeability of the vessel walls, and tumor size - can impact the absorption of the nanoparticles. Moreover, the heterogeneity of the tumor microenvironment impairs a homogeneous distribution of the NP (e.g., some regions of the tumor might have high enhanced permeability retention, while others might show a limited vascular permeability), implying also a heterogeneous response in the *in vivo* experiments.

The quantification of the biodistribution properties of the nanoparticle is of fundamental importance to ameliorate the **ANC design**. Moreover, efficacy studies allow **patient-specific therapy scheduling**.

The following points are the main questions that we want to address in this study:

- How is it possible to predict the tumor size and the NP efficacy? Which is the optimal treatment scheduling? Which is the dose for first clinical studies?
- How does the tumor microenvironment (such as interstitial fluid pressure, vessel density, tumor size or Her2 expression) affect the transport of nanoparticles? How could it be possible to personalize the drug dose and scheduling from histology data about the tumor microenvironment?
- Which is the optimal design of ANCs (size, trastuzumab graft rate) to increase their concentration in the tumor tissue?

Mathematical modeling is a powerful tool to (i) improve our understanding of biological processes of cancer and (ii) to help physicians and experimental design. For the first purpose, mechanistic models are built under given assumptions and tested against experimental data. On the one hand, this methodology allows us to strengthen or reject the initial theory and helps in formulating new hypotheses. On the other hand, the quantification of the treatment efficacy and predictions of the tumor progression are necessary for clinical decision management. Furthermore, in a preclinical context, they provide insights of new therapeutic options including optimal scheduling that can eventually be translated into clinical applications.

In this thesis, we focus on the two purposes: (i) we investigate the efficacy of the nanoparticles as function of the concentration to schedule an optimal treatment and (ii) we develop a continuum model to understand how nanoparticles penetrate into the tumor tissue.

1.2 State of the art

1.2.1 Overview of mathematical models in cancer nanomedicine

Nanomedicine offers promising therapeutical and diagnostic options, but there are several challenges that need to be investigated. Low and heterogeneous nanoparticle accumulation are the major limitations of nanomedicine [35]. NP physicochemical parameters, tumor models and cancer types affect the low delivery efficiency. Therefore, it is necessary to define techniques and tools for a quantitative analysis. For example, computational tools and mathematical modeling can help in understanding tumor interactions and response to drugs and nanoparticles, coupling models of the physical microenvironment of the tumor with convection-diffusion equations for drug transport [41]. Several challenges must nevertheless be addressed to have a successful fruition of nanomedicine [42]: improving loading efficacy and on-command release, modulating recognition and sequestration by immune cells and maximizing accumulation at biological targets. This can be achieved with a joint collaboration between experimental and computational scientists.

Several mathematical modeling approaches can be employed according to the nanoparticle properties that have to be investigated [43]. Different time and length scale models can be considered to address questions about the biochemical interactions of the nanoparticle in the organism and the tumor deliverability [43] (Figure 1.5). Molecular simulations, such as Monte Carlo, molecular dynamics and coarse-grained simulations, can be employed to maximize the loading efficiency, namely the ratio between the mass of encapsulated drug and the total mass, while controlling the release (see, for example, [44, 45]). Molecular simulations can be also applied to analyze the interaction of blood proteins with nanoparticles in order to optimize the surface features [46]. Indeed, it has been noted that nanoparticles exposed to blood tend to be covered by different molecules forming a protein corona, affecting the bioavailability and the therapeutic performances of nanomedicines [47]. Discrete modeling has been adopted to investigate the nanoparticle internalization, highlighting the process of endocytosis by the cells [48, 49]. At the tissue scale, continuum models highlight the macroscopic behavior of nanoparticles. Gentile et al. [50] investigated how the vessel permeability and blood rheology impact the nanoparticle diffusion in the blood vessels using a diffusion-convection equation. Importantly, continuum models are increasingly validated against imaging data [51]. Continuum models of spheroids have been employed to determine the diffusion coefficient of the nanoparticles and the cellular uptake [52, 53]. Several studies have analyzed the diffusion coefficient according to the properties of the nanoparticles. Size, shape, and density were found to impact the nanoparticle wall-deposition in the blood vessels [54, 55]. In particular, small nanoparticles improve the margination rates; lighter particles marginate significantly more compared to NP with larger density; non-spherical nanoparticles showed higher margination compared to spherical particles. Moreover, intratumoral pharmacokinetics of nanoparticle has been studied using intravital imaging and linked to the treatment efficacy [56]. Furthermore, the transport of nanoparticles in tumor tissues can be modeled with continuum mechanics approaches and particle based systems [57].

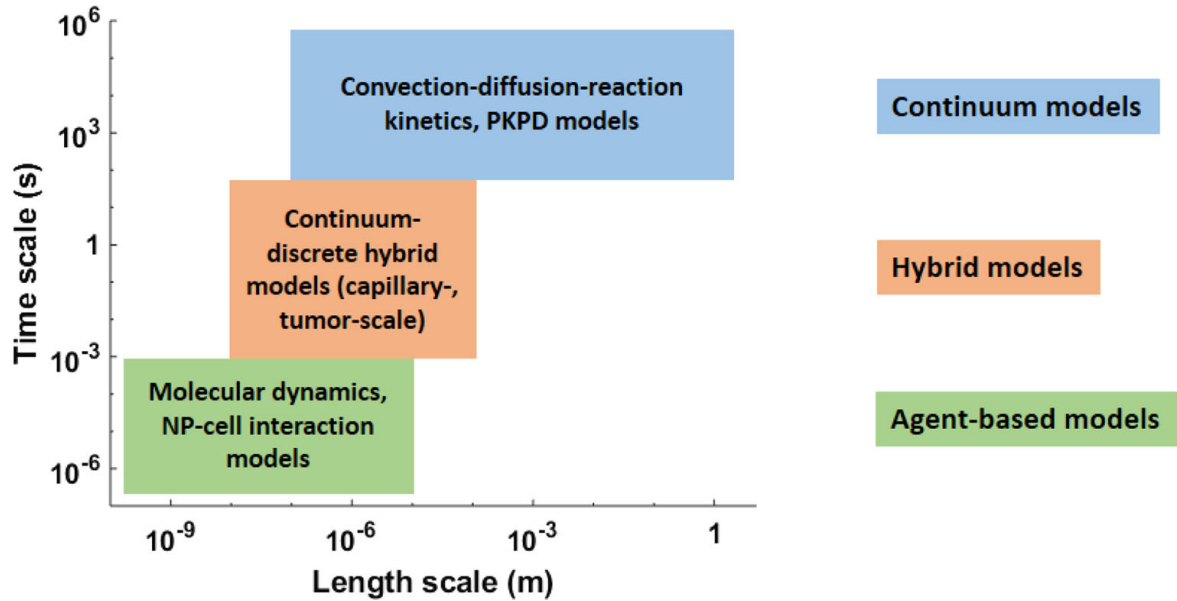


Figure 1.5. Classification of the mathematical models used to study nanoparticles for cancer treatment according to the length and time scales. NP = nanoparticle. Image from [43].

1.2.2 The journey of nanoparticles to solid tumors: determinants and barriers

Most tissues (both healthy or neoplastic) are composed of three subcompartments: vascular, interstitial and cellular. When drugs or nanoparticles are intravenously injected, they have to go through several barriers to reach the tumor tissue, such as the distribution through vascular space, transport across microvascular walls, transport through interstitial space and transport across the cell membrane [58] (see Figure 1.6). All these processes may involve either convection or diffusion. Tumors have an abnormal microenvironment that is characterized by (i) accumulated solid stress, (ii) abnormal blood vessels network, (iii) elevated interstitial fluid pressure and (iv) dense interstitial structure [59]. These peculiarities, that distinguish a neoplastic tissue from a normal one, cause barriers to drug delivery. Moreover, heterogeneity in the microenvironment results in poor drug delivery. Here below, we list the main determinants and barriers that drugs and nanoparticles have to encounter during their path to the tumor tissue [60].

- **Blood transport.** The heterogeneous spatial distribution of tumor vessels and poor lymphatic drainage hinder a uniform delivery and efficacy of therapeutic agents in tumors. Indeed, blood vessels are heterogeneously distributed, leaving avascular spaces. Moreover, their walls are leaky and hyperpermeable in some places while not in other [62]. Vessel collapse can also occur, due to the solid stress exerted by proliferating tumor cells and stromal cells. Blood flow velocity is also compromised by the elevated viscous and geometrical resistance offered by the tumor vasculature. Finally, the lack of an efficient lymphatic network inside the tumor coupled with leaky tumor vessels increases the interstitial fluid pressure.

Blood transport in tumor capillaries is quantified based on the perfusion rate of blood q [63],

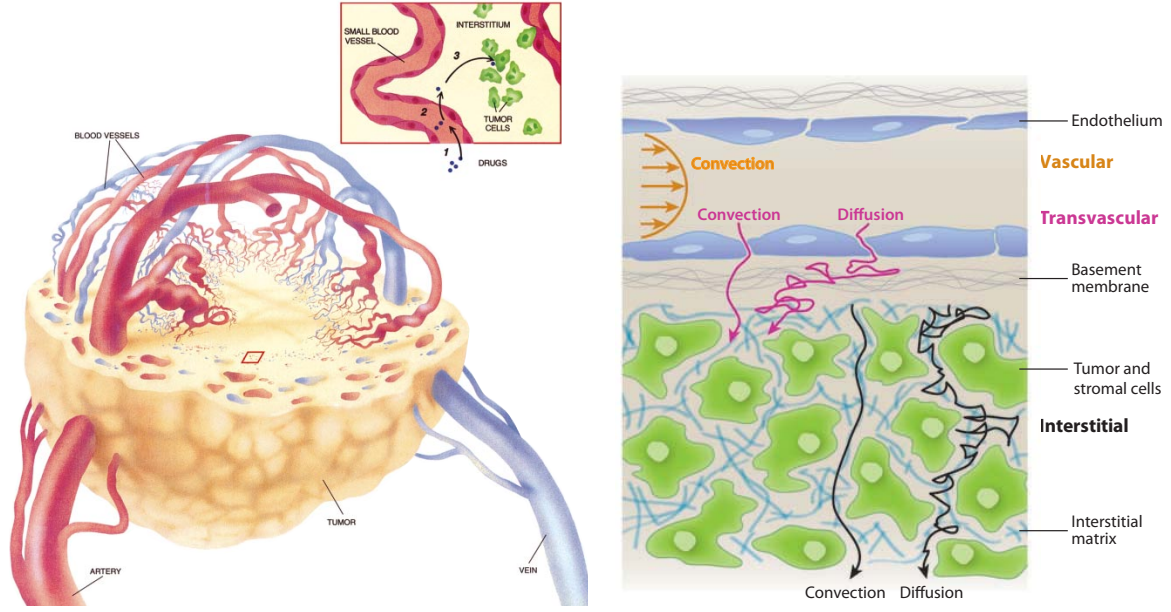


Figure 1.6. *Left:* scheme of solid tumor (from [61]): blood vessels, interstitium and cancer cells. *Right:* determinants of particle transport in a tumor composed by blood vessels and the surrounding tissue. Figure from [59].

defined as:

$$q = \frac{Q}{V}, \quad (1.1)$$

where Q is the volumetric flow rate and V is the tissue volume. The flow rate Q is equal to the pressure drop Δp_c divided by the resistance R :

$$Q = \frac{\Delta p_c}{R}. \quad (1.2)$$

The flow resistance R is a function of the vascular morphology (i.e., the number of vessels of various types, their branching pattern, their diameter, length and volume) and of the blood rheology (i.e., their viscosity). Under the assumption of a laminar flow through a circular rigid vessel of radius r and length L , the flow resistance is given by the Hagen-Poiseuille equation [63]:

$$R = \frac{8\eta L}{\pi r^4} = \eta Z, \quad (1.3)$$

where η is the viscosity and Z is the geometrical resistance (hindrance).

The drug supply to tumor tissue is determined by the flux of drug J_v into a tissue region by blood vessels. Denoting by c_c the drug concentration in the feeding blood vessels, J_c is defined by

$$J_c = Qc_c. \quad (1.4)$$

The heterogeneity in vascular distribution and flow rates can be taken into account by considering the distribution of perfusion rates calculated as the volumetric flow rate for each vessel Q_j multiplied by the volume of tissue it feeds V_j . Note that the parameters Q_j , $c_{c,j}$ and V_j can be

measured in real time using different techniques [59], such as standard intravital microscopy [64], multiphoton microscopy (e.g. [65]) and optical frequency domain imaging (e.g., [66]).

- **Transvascular transport.** Nanoparticles are transported across the vascular endothelium through intracellular junctions. They take advantage of the leaky vasculature characterizing the tumor microenvironment (EPR effect) [27]. However, vascular permeability depends on both the properties of the particles and the physiological characteristics of the vasculature. Indeed, it decreases when the size of the particles increases. Moreover, the heterogeneity of the tumor vessels impairs a homogeneous extravasation and delivery of particles.

Tumors are characterized by high interstitial fluid pressure [67]. The interstitial hypertension is caused by the high permeability of tumor vessels in combination with the lack of functional lymphatic vessels in the tumor interstitial space. On the one hand, this results in high IFP inside the tumor that becomes almost equal to the microvascular pressure. On the other hand, close to the tumor surface the IFP decreases rapidly causing a sharp pressure gradient. When the IFP inside the tumor exceeds the microvascular fluid pressure, it causes intravasation of materials back to the blood vessels. A direct consequence of the high IFP is that the main mechanism of mass transport across vessels is diffusion.

The flux of drugs across the vessel walls and their basement membranes is due to a combination of diffusive and convective transport. The diffusive flux $J_{t,d}$ depends on the difference between the plasma concentration c_c and the interstitial concentration c_t , the vascular surface area S_v and the vascular permeability P :

$$J_{t,d} = PS_v(c_c - c_t). \quad (1.5)$$

The advective flux $J_{t,a}$ is defined as follows

$$J_{t,a} = c_c L_p S_v (1 - \sigma)(p_c - p_t), \quad (1.6)$$

where L_p is the hydraulic conductivity of the vessel walls, σ is the solute reflection coefficient, and $p_c - p_t$ is the transmural hydrostatic pressure gradient.

The transvascular flux J_t is equal to the sum of (1.5) and (1.6):

$$J_t = PS_v(c_c - c_t) + L_p S_v (1 - \sigma)(p_c - p_t)c_c \quad (1.7)$$

Moreover, the transvascular flux J_t can be measured experimentally [59].

- **Interstitial transport.** It has been demonstrated that the IFP in tumors strictly depends on the hydrostatic microvascular pressure [68]. Due to the elevated IFP, tumor interstitium is characterized by no pressure gradient. Therefore, the main mechanism of transport in the tumor interstitium is diffusion. The tumor interstitial matrix consists of collagen fibers that interact with other molecules such as proteoglycans and glycosaminoglycans. The movement of a diffusing nanoparticle depends on the size, charge and configuration of the particle, and on the properties of the interstitium, such as the collagen content, the site of tumor growth and

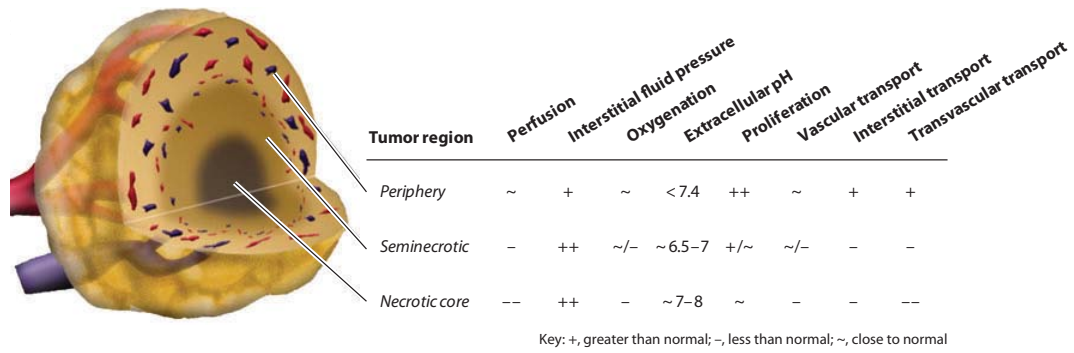


Figure 1.7. Properties of the three regions in the tumor microenvironment: periphery, seminecrotic region and necrotic core. Figure from [59]

the sulfate glycosaminoglycan content. Moreover, the interstitial matrix in tumor is characterized by a heterogeneous distribution of the components. It can be divided into two phases: a viscous phase, characterized by high collagen-fiber concentration, and an aqueous phase, characterized by low fiber concentration. This results in a two components diffusion.

In [58], the transport of molecules through the interstitial matrix is described as a diffusion-convection equation on the variable c_t (i.e., the interstitial concentration of particles):

$$\frac{\partial c_t}{\partial t} = D_t \nabla^2 c_t + \mathbf{u}_t \cdot \nabla c_t, \quad (1.8)$$

where D_t is the diffusion coefficient and \mathbf{u}_t is the interstitial fluid velocity. Diffusion is caused by concentration gradients while convection is due to the motion of interstitial fluid. Moreover, diffusion and convection coefficients depend on the tumor type and on the molecules that are transported inside the tumor interstitium. In [69] the authors underline that the elevated interstitial pressure plays a significant role in the transport of macromolecules in tumors: the poor penetration of macromolecules into tumors is due to heterogeneous blood perfusion, hindered diffusion in the interstitium, high interstitial fluid pressure and, in case of binding molecules such as monoclonal antibodies, rapid and heterogeneous extravascular binding.

- **Cell transport and metabolism.** The cellular uptake depends on the drug interaction with the cell membrane and membrane molecules. A mathematical model based on statistical thermodynamic theory has been developed in [70] to define the ligand density and the particle size that optimally yield cellular uptake. The results agree with the experimental data in [71].

1.2.3 Techniques to improve nanoparticle delivery

Tumor normalization strategies might be adopted to overcome the biological barriers that characterize malignant tissues, enhancing nanoparticle delivery [60]. For this purpose, mathematical modeling is a powerful tool to test *in silico* the combination of several treatments and at different regimes. Results can guide the formulation of new hypotheses and the planning of new experiments.

Antiangiogenic drugs normalize the tumor vasculature reducing the permeability of the vessel walls, hence improving a homogeneous drug perfusion in the tumor tissue [60]. Trastuzumab has an indirect antiangiogenic effect [72]. It was observed that it decreases diameter, volume and permeability of blood vessels in experimental human breast tumour that overexpress receptor Her2 in mice. However, vascular normalization leads to a decreased permeability of the vessel walls that might represent a disadvantage in nanomedicine. Indeed, nanoparticles might not take advantage of large pores to accumulate in tumors [60]. Yonucu *et al.* introduced a mathematical model to study whether antiangiogenic therapy could increase liposome delivery due to normalization of tumor vessels [73]. They assessed the improvement of liposomal drug delivery by experimenting different drug regimens.

The dense structure of the interstitial matrix hinders the penetration of nanoparticles in the tumor. Enhanced NPs interstitial diffusion coefficient has been found with multiphase nanoparticles that decrease their size from 100 nm to 10 nm when extravasated in the tumor interstitium [74]. Furthermore, extracellular matrix normalization might increase the volume fraction assessible to the molecules. Mathematical models can describe the combined effects of chemotherapy and matrix degrading drugs [75].

1.3 Experimental data

All the experimental data were provided by the SMARTc in Marseille and include *in vitro*, *in vivo* and *ex vivo* data. Animal tumor model studies were performed in strict accordance with guidelines for animal welfare in experimental oncology and were approved by local ethics committees. Mainly, three human cell lines were considered in the studies according to the expression of Her2 receptor: SKBR3 (Her2++), MDA-MB-453 (Her2+) and MDA-MB-231 (Her2-). The latter is also known as triple negative breast cancer and it is therefore more challenging as it is the most resistant cell line to trastuzumab.

1.3.1 *In vitro* data

In vitro data were used to assess the *in vitro* cytotoxicity, namely to build the dose-response relationship with a cell culture. 2D experiments performed to study the efficacy of different types of drugs as a function of the concentration [39]. 3D *in vitro* cytotoxicity was studied with different dose regimens [76].

Cell viability: 2D MTT assay

The MTT assay (3-(4,5-dimethylthiazol-2-yl)-2,5-diphenyltetrazolium bromide) is applied to measure the cell viability. It is a colorimetric assay that reflects the metabolic activity of the cells: after adding a solubilization solution, the live cells become pink and the dead ones become blue.

Then, a spectrophotometer measures the wavelength of the absorbance of the solution. Finally, the wavelength relative to each concentration is normalized with respect to the control cells.

1.3.2 *In vivo* data

Female nude mice with an orthotopically implanted tumor were considered for *in vivo* studies. In this thesis, we will focus on the MDA-MB-231 cell line to test the efficacy of the treatment as well as the penetration of nanoparticles in the tumor. Tumor growth, angiogenesis and liposomal distribution in the body were tracked *in vivo* using different techniques that are listed below (such as caliper, fluorescence and bioluminescence).

Tumor growth: caliper

Traditionally, caliper measurements are used to compute tumor volume. Two perpendicular diameters ($d_1 \leq d_2$) of the tumors are measured using a caliper and the tumor volume is obtained as follows:

$$V = \frac{1}{6} \pi d_1^2 d_2. \quad (1.9)$$

However, the measurement of the diameters of the tumors is not always of easy access, especially when tumors are orthotopically implanted. Therefore, non-invasive *in vivo* imaging techniques have been developed to quantify the tumor development.

Tumor growth and nanoparticles biodistribution: fluorescence and bioluminescence imaging

The most common reporter genes are green fluorescent proteins (GFP) and red fluorescent proteins, in case of fluorescence imaging, and luciferase, for bioluminescence imaging. Fluorescence imaging is based on the acquisition of GFP signal resulting from the excitation by an external light source. Bioluminescence imaging is based on the endogeneous production of light by the expression of luciferase. This enzyme produces light when it reacts with the substrate luciferin in the presence of oxygen and ATP. An advantage of bioluminescence is that there is a low background, since it does not require an excitation light source. Fluorescent imaging suffers from the problem of autofluorescence. However, GFP fluorescent images can be acquired in real-time, while bioluminescent images are acquired in the minute timescale [77].

Fluorescence imaging was used to track tumor growth and nanoparticle distribution in the body.

1.3.3 *Ex vivo* data

CD31 antibody staining and fluorescence imaging have been employed to have the distribution of the blood vessels and the cell density *ex vivo*. CD31 (acronym of cluster of differentiation 31) is a membrane protein that is expressed on endothelial cells. It is primarily used to demonstrate the

presence of endothelial cells in histological tissue sections to evaluate the degree of angiogenesis. Specific antibodies bind the CD31 proteins and can be conjugated with dyes to make neoplastic vessels fluorescent.

1.4 Main contributions and outline of the thesis

In this section, the main results of the thesis are summarized and the organization of the document is described.

Unperturbed tumor growth analysis

Published in [78, 79].

For several decades, mathematical models have been used to quantify tumor growth kinetics, but mostly fitted to individual or average growth curves. In Chapter 2, we compared three classical models (exponential, logistic and Gompertz) using a population approach (nonlinear mixed-effects modeling), which accounts for inter-animal variability. **The exponential and the logistic models failed to fit the experimental data while the Gompertz model showed excellent descriptive power.** Indeed, the Gompertz model might catch the drop-off of the specific growth rate:

$$V(t) = V_{\text{inj}} \exp\left(\frac{\alpha^i}{\beta^i} (1 - \exp(-\beta^i t))\right),$$

where V_{inj} is the initial tumor size at $t = 0$, while α^i and β^i are the two individual parameters to estimate. The strong correlation observed between these two parameters within the population motivated a simplification of the model. Assuming a linear relationship between α^i and β^i ($\alpha^i = k\beta^i$), we defined the **reduced Gompertz model**:

$$V(t) = V_{\text{inj}} \exp(k(1 - \exp(-\beta^i t))).$$

with a single individual-specific parameter β^i and a population-specific parameter k within the population.

The reduced Gompertz model and the Gompertz model showed equal descriptive power.

Combining the mixed-effects approach with Bayesian inference, we predicted the age of individual tumors with only few late measurements. Thanks to its simplicity, **the reduced Gompertz model showed superior predictive power.** Furthermore, we tested the ability of the reduced Gompertz model to capture differences in tumor growth dynamics within subgroups of the same population, obtaining good results.

Although our method remains to be extended to clinical data, these results are promising for the personalized estimation of the age of a tumor from limited measurements at diagnosis.

Pharmacokinetic-pharmacodynamic modeling of liposomes and immunoliposomes

In Chapter 3 we conducted a statistical analysis using *in vitro* data to compare the efficacy of liposomes, immunoliposomes and standard drugs on monolayer cell cultures. In particular, we found that the efficacy of ANCs was equal or higher than normal drugs and estimated some parameters that provide information on the interactions between nanoparticles and cells (such as the dissociation constant).

In Chapter 4 we introduce a mathematical model to investigate the pharmacokinetics-pharmacodynamics (PKPD) of nanoparticles.

We used a two-compartment pharmacokinetic (PK) model to describe the NPs exchange between the blood vessels (central or systemic compartment) and the tumor compartment. Denoting by A_c and A_t the nanoparticle amount in the blood and in the tumor, respectively, the model reads as:

$$\begin{aligned}\frac{dA_c}{dt} &= -k_c A_c - k_{c,t} A_c, \\ \frac{dA_t}{dt} &= k_{c,t} A_c - k_e A_t,\end{aligned}$$

where k_c is the clearance rate of the systemic compartment, k_e is the elimination rate of the tumor, and $k_{c,t}$ is the parameter that drives the exchange of nanoparticles between the tumor and the capillaries, which depends on the properties of the nanoparticle and on the permeability and surface of the vessel walls.

Several biodistribution datasets were used to estimate the parameters employing nonlinear mixed-effects modeling. In particular, we compared the PK of liposomes and ANCs at different doses.

High inter-individual variability was recognized in the results, confirming previous observations. Indeed, individual tumor architecture might have peculiar barriers that affect the tumor accumulation of nanoparticles. Importantly, **we estimated a larger exchange rate for the immunoliposomes than for the liposomes**. This result was found in accordance with the observation that immunoliposomes might improve the vascularization of the tumor.

Furthermore, the nanoparticle-induced decay was described by a resistance model. The two liposomal formulation did not show a significant difference in terms of efficacy, although liposomes had larger resistance compared to ANCs. Moreover, we analyze the pharmacodynamic to the free drugs (free docetaxel plus free trastuzumab), which efficacy was lower with respect to the nanodrugs. Moreover, ANCs and liposomes showed improved pharmacokinetics with respect to the free drugs.

Mathematical modeling of fluid and nanoparticle transport in malignant tissues

Submitted [80].

Tumor architecture is highly heterogeneous and develops barriers that impair a homogeneous distribution of therapeutics. New technologies permit to acquire highly detailed imaging data that

could be integrated into mathematical models to investigate the properties of particles and make predictions on their accumulation. However, the resolution of discrete models that take into account the entire complexity of the tumor microstructure is infeasible due to the high computational costs. In Chapters 5 and 6, macroscopic models of fluid and nanoparticle transport are investigated using formal two-scale asymptotic expansion. This technique allows us to take into account the microscopic features of the tumor environment on the global dynamic at the tissue scale. We assumed that a generic variable $v^\varepsilon(\mathbf{x})$, as function of the macroscopic spatial variable \mathbf{x} and of the microscopic parameter ε , could be approximated as

$$v^\varepsilon(\mathbf{x}) = v(\mathbf{x}) + \varepsilon \phi\left(\frac{\mathbf{x}}{\varepsilon}\right) \nabla_{\mathbf{x}} v(\mathbf{x}),$$

where $v(\mathbf{x})$ is the macroscopic variable and $\phi\left(\frac{\mathbf{x}}{\varepsilon}\right)$ is the corrector that takes into account oscillations at the microscopic scale.

The main drivers of nanoparticle transport in the tumor tissue are diffusion and convection. Therefore, fluid transport must be first described using mathematical modeling.

In Chapter 5 we studied macroscale models of fluid transport in tumor tissues using the two-scale asymptotic expansion method. These models consisted of a system of Darcy's law that describes the fluid transport in a double porous medium (i.e., capillaries and interstitium). Starting from a micro-scale model of interstitial fluid transport and blood transport, we motivated the interface conditions between the interstitial compartment and the capillaries using an asymptotic expansion technique. We derived a Starling's law type equation to describe the flux through the vessel walls. Moreover, we considered the Joseph-Beavers-Saffman slip condition at the boundary between the capillary lumen and the vessel wall. This condition states that the slip velocity along the vessel wall is proportional to the shear stress.

Then, using the two scale homogenization technique, we derived three different macroscale models to describe the fluid transport in tumor tissues according to the magnitude of the permeability of the vessel walls and of the interstitial hydraulic conductivity. In particular, the following regimens were derived for the interstitial fluid pressure p_t and the capillary pressure p_c in the domain Ω :

- **Model 1:** highly permeable walls and large interstitial hydraulic conductivity

$$\nabla \cdot \left(\left(\mathbf{K} + \frac{C_t}{C_c} \mathbf{E} \right) \nabla p_c \right) = 0 \quad p_t = p_c \quad \text{in } \Omega. \quad (1.10)$$

- **Model 2:** weakly permeable walls and large interstitial hydraulic conductivity

$$\nabla \cdot (\mathbf{K} \nabla p_t) = C_t (p_t - p_c), \quad \nabla \cdot (\mathbf{E} \nabla p_c) = C_c (p_c - p_t) \quad \text{in } \Omega. \quad (1.11)$$

- **Model 3:** weakly permeable walls and small interstitial hydraulic conductivity

$$\nabla \cdot (\mathbf{K} \nabla p_t) = C_t (p_t - p_c), \quad \nabla \cdot (\mathbf{E} \nabla p_c) = 0 \quad \text{in } \Omega. \quad (1.12)$$

In the three models, \mathbf{K} and \mathbf{E} are the permeability tensors of the interstitium and of the capillaries, respectively, and C_t, C_c are constant parameters that will be defined later on. The definition of these tensors involves the so-called correctors, as usual in homogenization. It characterizes the impact of the microstructure on the effective properties of the tissue at the macroscale. Model 2 has been derived assuming a small magnitude of the capillary permeability and confirms previous results of Shipley and Chapman [81] and Penta *et al.* [82].

The interstitial fluid flow \mathbf{u}_t and the blood velocity \mathbf{u}_c are given in the first two cases by the average quantities

$$\mathbf{u}_t = -\mathbf{K}\nabla p_t, \quad \mathbf{u}_c = -\mathbf{E}\nabla p_c \quad \text{in } \Omega,$$

while for the third model they are given by

$$\mathbf{u}_t = -\varepsilon\mathbf{K}\nabla p_t, \quad \mathbf{u}_c = -\mathbf{E}\nabla p_c \quad \text{in } \Omega.$$

Boundary conditions must be added to guarantee well-posedness. Dirichlet-Dirichlet boundary conditions can be imposed to p_t and p_c if the pressures in the surrounding tissue are known. Mixed Dirichlet and Neumann boundary conditions can be chosen to ensure the continuity of \mathbf{u}_t or \mathbf{u}_c .

We compared the different asymptotic regimes with some models given in the literature and showed the links between the different models.

Furthermore, mathematical and numerical analysis on the homogenized tensors was performed to assess their properties according to the geometric microstructure. Eventually, numerical simulations on the macroscopic models were performed and the results were compared to the literature.

The nanoparticle accumulation depends on the tumor microstructure and nanoparticle design. In Chapter 6, a mathematical model of nanoparticle transport in the tumor interstitium was derived using formal two-scale asymptotic expansion. Since the nanoparticle concentration in the capillaries c_c was considered to be saturated, we neglected spatial variations of c_c and modeled the nanoparticle concentration in the interstitium c_t and the NP concentration that binds the cells c_b . The diffusion tensor \mathbf{D}_t was defined according to the correctors that arose from homogenization. The nanoparticle-cell interactions were driven by the parameters λ_t and λ_b that depend on the association and dissociation rates, and on the concentration of the Her2 receptors c_e . The decay rate of the drugs was denoted by λ_d . The homogenized model reads as:

$$\begin{aligned} \frac{\partial c_t}{\partial t} + \nabla \cdot (\mathbf{u}_t c_t) &= \nabla \cdot (\mathbf{D}_t \nabla c_t) - \lambda_t c_t (c_e - c_b) + \lambda_b c_b - \lambda_d c_t + \mathcal{J}_v[c_c, c_t], \quad \text{in } \Omega, \\ \frac{dc_b}{dt} &= \lambda_t c_t (c_e - c_b) - \lambda_b c_b - \lambda_d c_b, \quad \text{in } \Omega, \end{aligned}$$

where $\mathcal{J}_v[c_c, \phi_t c_t]$ is a term that drives the exchange between the capillaries and the interstitium.

The model was **calibrated with nanoparticle-specific parameters** that were estimated empirically or with experimental data. *In vitro* data were used to quantify the cellular uptake; *in vivo* pharmacokinetic data provided information on the permeability of the vessel walls and the nanopar-

ticle concentration in the tumor vessels. Comparison of ANCs, liposomes and docetaxel as a free drug showed improved accumulation of nanoparticles with respect to the free drugs, thanks to the better pharmacokinetics of NP (such as low clearance rates). Qualitative simulations were performed to investigate several properties of the nanoparticles and of the tumor architecture to assess their impact on the global accumulation.

A computational framework to predict individual tumor liposome accumulation

Chapters 5 and 6 provide a theoretical and qualitative analysis of the mathematical models of fluid and NPs transport.

In Chapter 7, we used *ex vivo* microscopy fluorescence images to recover the individual vascular structure and interstitial porosity. This allowed making individual predictions on the tumor accumulation of nanoparticles. To this end, we introduced the interstitial porosity of the interstitium ϕ_t , i.e. the interstitial volume fraction available to the nanoparticles:

$$\begin{aligned} \frac{\partial (\phi_t c_t)}{\partial t} + \nabla \cdot (\mathbf{u}_t \phi_t c_t) &= \nabla \cdot (\phi_t \mathbf{D}_t \nabla c_t) - \lambda_t \phi_t c_t (c_e - c_b) + \lambda_b \phi_t c_b + \mathcal{J}_v[c_c, \phi_t c_t] - \lambda_d \phi_t c_t, & \text{in } \Omega, \\ \frac{d(\phi_t c_b)}{dt} &= \lambda_t \phi_t c_t (c_e - c_b) - \lambda_b \phi_t c_b - \lambda_d \phi_t c_b, & \text{in } \Omega. \end{aligned}$$

Results were in agreement with the pharmacokinetic model found in Chapter 4. We remarked high inter-individual variability based on the tumor characteristics. Indeed, large tumors improved the total accumulation of nanoparticles. Moreover, the vascular and interstitial volume fractions affected the global accumulation of nanoparticles.

This approach is promising for treatment personalization. *In vivo* image acquisition modalities or biopsies might provide the data to integrate into mathematical models to predict therapeutic accumulation in the tumor.

Code development

Several codes have been implemented to simulate the different mathematical models.

The `m1x_py` module was written using both Python and R to analyze tumor growth with nonlinear mixed effects modeling. Given a dataset with measurements and a tumor growth model as inputs, the module calibrates the mathematical model running Monolix 2018 R2 [83] thanks to the Monolix API for R. The outputs of the module are the same as Monolix: a folder containing the estimates, standard errors, graphics and several diagnostic tools is created. Moreover, a function was written to compare different tumor growth models. It creates a .pdf file with a summary of the models ranked in ascending order of Akaike information criteria.

The library PLUMKY (Population modeling of tumor growth kinetics and Bayesian predictions) was implemented to run predictions of tumor kinetics with Bayesian inference and likelihood maxi-

mization. This code is publicly available at <https://github.com/cristinavaghi/plumky> and is specifically designed to perform backward extrapolation of initiation time. The library contains `mlx_py` to learn the population parameters from the learning dataset. Moreover, the a posteriori distributions of the parameters were estimated using `PyStan`, which is a Python interface to the software `Stan` [84] for Bayesian inference based on the No-U-Turn sampler, a variant of Hamiltonian Monte Carlo [85].

Simulations of the fluid transport model were performed using `FreeFem++` [86] and visualization was done thanks to the `ffmatlib.idp` library (https://github.com/samplemaker/freefem_matlab_octave_plot). The code was implemented to perform 2D and 3D simulations. For 3D simulations, the geometry of the domain and the triangulation were defined with `Gmsh` [87]. For the time-dependent nanoparticle transport model, we used a model in radial coordinates assuming an axisymmetric domain. A finite difference scheme was implemented in `Matlab`.

Part I

**PHARMACOKINETIC-PHARMACODYNAMIC
MODELING**

UNTREATED TUMOR GROWTH ANALYSIS

Abstract. Tumor growth curves are classically modeled by means of ordinary differential equations. In analyzing the Gompertz model several studies have reported a striking correlation between the two parameters of the model, which could be used to reduce the dimensionality and improve predictive power. We analyzed tumor growth kinetics within the statistical framework of nonlinear mixed-effects (population approach). This allowed the simultaneous modeling of tumor dynamics and inter-animal variability. Experimental data comprised three animal models of breast and lung cancers, with 833 measurements in 94 animals. Candidate models of tumor growth included the exponential, logistic and Gompertz models. The exponential and – more notably – logistic models failed to describe the experimental data whereas the Gompertz model generated very good fits. The previously reported population-level correlation between the Gompertz parameters was further confirmed in our analysis ($R^2 > 0.92$ in all groups). Combining this structural correlation with rigorous population parameter estimation, we propose a reduced Gompertz function consisting of a single individual parameter (and one population parameter). Leveraging the population approach using Bayesian inference, we estimated times of tumor initiation using three late measurement timepoints. The reduced Gompertz model was found to exhibit the best results, with drastic improvements when using Bayesian inference as compared to likelihood maximization alone, for both accuracy and precision. Specifically, mean accuracy (prediction error) was 12.2% versus 78% and mean precision (width of the 95% prediction interval) was 15.6 days versus 210 days, for the breast cancer cell line. These results demonstrate the superior predictive power of the reduced Gompertz model, especially when combined with Bayesian estimation. They offer possible clinical perspectives for personalized prediction of the age of a tumor from limited data at diagnosis. The code and data used in our analysis are publicly available at <https://github.com/cristinavaghi/plumky>. [79]

Part of this chapter has been published in [79, 78].

Contents

2.1 Overview on tumor growth	29
2.1.1 The mechanisms of tumor growth	29
2.1.2 Techniques to monitor tumor growth	30
2.2 Introduction	32
2.3 Material and methods	33
2.3.1 Ethics statement	33
2.3.2 Mice experiments.	34
2.3.3 Tumor growth models.	35
2.3.4 Population approach.	35
2.3.5 Individual predictions	36
2.4 Results	38
2.4.1 Population analysis of tumor growth curves	38
2.4.2 The reduced Gompertz model	40
2.4.3 Prediction of the age of a tumor	44
2.5 Discussion	46
2.6 Validation of the reduced Gompertz model	52
2.7 Further applications of the reduced Gompertz model: assessing the differences in tumor growth kinetics	54
2.8 Conclusion	56

2.1 Overview on tumor growth

Cancer can be viewed as the result of abnormal proliferation of any of the different kinds of cells in the body. A tumor can be either benign, if it remains confined to its original location mostly, or malignant if it can invade the surrounding tissues and spread to distant body sites throughout the circulatory or lymphatic systems, creating metastasis [88].

Moreover, both benign and malignant tumors can be classified according to the type of cells that are involved. A carcinoma is a type of cancer that involves epithelial cells; sarcoma is a solid tumor of connective tissues (e.g., muscle, bone or cartilage); leukemia and lymphoma are tumors of the blood-forming cells and of the immune system, respectively.

Since we deal with breast cancer data, we will focus on the process of tumor growth relative to carcinomas.

2.1.1 The mechanisms of tumor growth

At the cell scale, tumor initiation arises from a genetic mutation that leads to abnormal cell proliferation of a single cell [89]. Then, tumor progression is a multistep process that results from a progressive alteration of the cells that become gradually malignant.

Not all the cells in a tumor proliferate: only a small percentage of cells in a tumor duplicates, while the majority is composed of quiescent cells (i.e. that do not proliferate) and dead cells, that are due to necrosis.

The steps characterizing tumor growth can be summarized as follows [89]:

- carcinoma generation: cells start to proliferate abnormally, pushing away the surrounding tissues including vasculature;
- cell necrosis: when the tumor grows (more than 1 mm^3), the cells in the center miss nutrients and die without control (cell *necrosis*; this is in contrast to apoptosis that is an active, programmed process of cell death);
- angiogenesis: large tumors require new vessels network to receive oxygen and nutrients. Tumors release VEGF (Vasculature Endothelial Growth Factor) proteins that induce the formation of vasculature;
- metastasis: it refers to the growth of secondary tumors at sites distant from the primary tumor. Metastatic spread is linked to the dissemination of tumor cells via the blood or lymphatics.

Figure 2.1 shows the main steps of tumor growth.

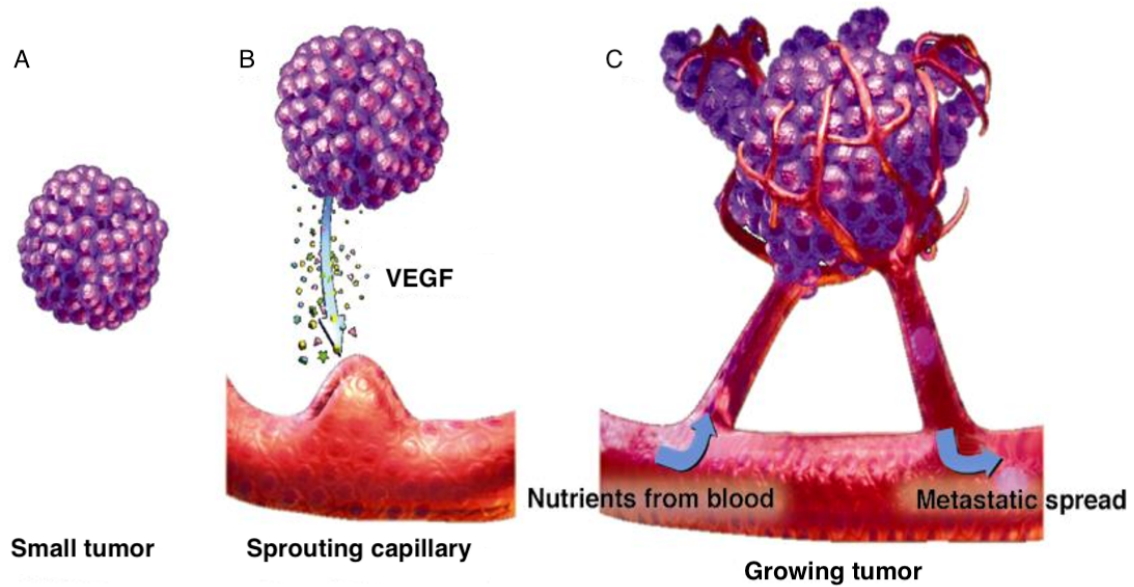


Figure 2.1. Tumor growth: proliferating cells (A); when the tumor size is greater than 1 mm^3 angiogenesis occurs (B); metastatic spread (C). Figure from [90].

2.1.2 Techniques to monitor tumor growth

In vivo studies are fundamental to analyze the effects of potential anti-cancer treatments. Tumor cell lines can be implanted orthotopically or ectopically in mice or, alternatively, oncogene-driven or chemically induced models can be adopted in order to better simulate human diseases. Several techniques have been adopted to study solid tumor growth and cancer progression in living animals [91]. Traditionally, caliper measurements are used to compute tumor volume. Two perpendicular diameters ($d_1 \leq d_2$) of the tumors are measured using a caliper and then the tumor volume is obtained as follows:

$$V = \frac{1}{6} \pi d_1^2 d_2. \quad (2.1)$$

However, the measurement of the diameters of the tumors is not always of easy access, especially when tumors are orthotopically implanted. Therefore non-invasive *in vivo* imaging is necessary in order to quantify the tumor development. Non-invasive imaging techniques are promising in order to make longitudinal studies possible (indeed the measurement of tumor development does not require to sacrifice the animal), reducing the number of animals needed and producing more robust data. These techniques for small animals include, for example optical imaging, such as bioluminescence imaging (BLI) [92] and fluorescence imaging (FLI) [93], that are widely used in the preclinical applications (for both *in vitro* and *in vivo* experiments). Puaux *et al.* [91] provide a detailed comparison between the various techniques according to the quantities of interest (detection of small tumors, tumor burden measurement and tumor identification).

The most common reporter genes are green fluorescent proteins (GFP) and red fluorescent proteins, in case of fluorescence imaging, and luciferase, for bioluminescence imaging. Fluorescence imaging is based on the acquisition of GFP signal resulting from the excitation by an external light source.

Method	Bioluminescence imaging	Fluorescence imaging
Physical basis	Visible light emitted during chemical reaction	Visible light emitted after fluorochrome excitation
Reagent used	D-luciferin substrate	None
Spatial resolution	1 to 10 mm dependant on tissue depth	1 to 10 mm dependant on tissue depth
Reporter gene needed	Yes	Yes
Smallest detectable tumor (diameter)	< 1 mm	2 mm
Analysis time	1 hour/mouse; 2 hours/10 mice	30 min/mouse; 1 hour/10 mice
Main advantages	Detection of nonpalpable tumors; low background; relative measure of tumor size; high throughput	High throughput
Main disadvantages	Light emission dependant on tissue depth and on local availability of substrate reagents (such as luciferin)	Light emission dependant on tissue depth; high background due to tissue fluorescence

Table 2.1. Summary of optical imaging methods used for detection of tumors in living animals (from [91]).

Bioluminescence imaging is based on the endogeneous production of light by the expression of luciferase. This enzyme produces light when it reacts with the substrate luciferin in the presence of oxygen and ATP. An advantage of bioluminescence is that there is a low background, since it does not require an excitation light source. Fluorescent imaging suffers from the problem of autofluorescence. On the other hand, GFP fluorescent images can be acquired in real-time, while bioluminescent images are acquired in the minute timescale [77]. Table 2.1 provides a comparison between the two optical imaging techniques. As found in [77, 92], there is a significant correlation between tumor volume and the fluorescent signal, as well as between tumor volume and bioluminescent imaging [94]. This proves that both optical techniques can be applied to study tumor growth over time.

2.2 Introduction

In the era of personalized oncology, mathematical modeling is a valuable tool for quantitative description of physiopathological phenomena [95, 96]. It allows for a better understanding of biological processes and generates useful individual clinical predictions, for instance for personalized dose adaptation in cancer therapeutic management [97]. Tumor growth kinetics have been studied since several decades both clinically [98] and experimentally [99]. One of the main findings of these early studies is that tumor growth is not entirely exponential, provided it is observed over a long timeframe (100 to 1000 folds of increase) [100]. The specific growth rate slows down and this deceleration can be particularly well captured by the Gompertz model [101, 100, 102]:

$$V(t) = V_{\text{inj}} e^{\frac{\alpha}{\beta}(1-e^{-\beta t})}, \quad (2.2)$$

where V_{inj} is the initial tumor size at $t_{\text{inj}} = 0$ and α and β are two parameters.

While the etiology of the Gompertz model has been long debated [103], several independent studies have reported a strong and significant correlation between the parameters α and β in either experimental systems [100, 104, 105], or human data [105, 106, 107]. While some authors suggested this would imply a constant maximal tumor size (given by $V_{\text{inj}} e^{\frac{\alpha}{\beta}}$ in (2.2)) across tumor types within a given species [105], others argued that because of the presence of the exponential function, this so called 'carrying capacity' could vary over several orders of magnitude [108].

Mathematical models for tumor growth have been previously studied and compared at the level of individual kinetics and for prediction of future tumor growth [109, 110]. However, detailed studies of statistical properties of tumor growth models using a population approach (i.e. integrating structural dynamics with inter-subject variability [111]) are rare [112]. Nonlinear mixed effects modeling of the Gompertz model has been applied to several fields in biology, e.g. to model growth in Japanese quails [113] or broiler chicken growth [114]. In the field of tumor growth modeling, studies using a population approach have mostly been conducted for perturbed tumor growth under the action of therapeutics (see e.g. [115] for a clinical study and [116] for a review). In a previous publication, our group has used a mixed-effects framework to compare the descriptive power of several unperturbed tumor growth models, yet without reporting visual predictive checks, analysis of residuals nor values of the population parameters (typical values and standard deviations of the random effects) [109]. Other related works include the coupling of tumor growth models with metastatic spreading [117, 118], or an analysis of tumor growth kinetics from different cell lines using the Simeoni model only [119, 112]. A calibrated model of lymphoma tumor growth has also been introduced and used for predictions in [120]. More complex mechanistic models have been proposed to investigate the link between biological processes and tumor growth dynamics and perform predictions, including angiogenesis [121] and solid stress [122]. A model for tumor-immune interactions has been developed and validated in [123, 124], demonstrating its ability to predict future prostate specific antigen dynamics based on several pre- and post-treatment initiation data points. Mathematical models of tumor growth inhibition were presented to assess tumor size dynamics in colorectal cancer [125] and adult diffuse low-grade gliomas [126]. Spatial models have also been widely proposed in a the-

oretical context but few of them have been compared to data (see [127] for an example on thyroidal lung nodules and [128, 129] for gliomas).

Here we provide a detailed and comparative analysis of statistical properties of multiple classical tumor growth models within a population framework, applied to a data set of 94 animals, including three animal models and two methods of tumor size quantification (versus 54 animals in [109]). The main focus and novelty of the work reported here is to analyze the above-mentioned correlation between Gompertz parameters using a population approach, in order to improve model-derived predictions. This led us to a simplified model with only one subject-specific parameter (and one population-specific), the "reduced Gompertz" model [105].

Using population distributions as priors allows to make predictions on new subjects by means of Bayesian algorithms [85, 130, 84]. The added value of the latter method is that only few measurements per individual are necessary to obtain reliable predictions. In contrast with previous work focusing on the *forward* prediction of the size of a tumor [109], the present study addresses the *backward* problem, i.e. the estimation of the age of a tumor [131]. This question is of fundamental importance in the clinic since the age of a tumor can be used as a proxy for determination of the invisible metastatic burden at diagnosis [118]. In turn, this estimation has critical implications for decision of the extent of adjuvant therapy [132]. Since predictions of the initiation time of clinical tumors are hardly possible to verify for clinical cases, we developed and validated our method using experimental data from multiple data sets in several animal models. This setting allowed to have enough measurements, on a large enough time frame in order to assess the predictive power of the methods.

2.3 Material and methods

The python code and the data used in our analysis are available at <https://github.com/cristinavaghi/plumky>.

2.3.1 Ethics statement

Animal tumor model studies were performed in strict accordance with the recommendations in the Guide for the Care and Use of Laboratory Animals of the National Institutes of Health. Protocols used were approved by the Institutional Animal Care and Use Committee (IACUC) at Tufts University School of Medicine for studies using murine Lewis lung carcinoma (LLC) cells (Protocol: #P11-324) and at Roswell Park Cancer Institute (RPCI) for studies using human LM2-4^{LUC+} breast carcinoma cells (Protocol: 1227M). Institutions are AAALAC accredited and every effort was made to minimize animal distress [109].

For the breast data measured by fluorescence, guidelines for animal welfare in experimental oncology as recommended by European regulations (decree 2013-118 of February 1, 2013) were fol-

lowed. All animal experiments were approved by the Animal Ethic Committee of the Aix-Marseille Université (CE14). The protocol was registered as #2017031717108767 at the French Ministry of Research. Mice were monitored daily for signs of distress, pain, decreased physical activity, or any behavioral change and weighted thrice a week. Water was supplemented with paracetamol (80 mg/kg/day) to prevent any metastasis-related pain [76].

2.3.2 Mice experiments.

The experimental data comprised three data sets. Animal tumor model studies were performed in strict accordance with guidelines for animal welfare in experimental oncology and were approved by local ethics committees. Precise description of experimental protocols was reported elsewhere (see [109] for the volume measurements and [76] for the fluorescence measurements).

Breast data measured by volume ($N = 66$) This dataset is publicly available at the following repository [133]. It consisted of human LM2-4^{LUC+} triple negative breast carcinoma cells originally derived from MDA-MB-231 cells. Animal studies were performed as described previously under Roswell Park Comprehensive Cancer Center (RPCCC) Institutional Animal Care and Use Committee (IACUC) protocol number 1227M [109, 118]. Briefly, animals were orthotopically implanted with LM2-4^{LUC+} cells (10^6 cells at injection) into the right inguinal mammary fat pads of 6- to 8-week-old female severe combined immunodeficient (SCID) mice. Tumor size was measured regularly with calipers to a maximum volume of 2 cm^3 , calculated by the formula $V = \pi/6w^2L$ (ellipsoid) where L is the largest and w is the smallest tumor diameter. The data were pooled from eight experiments conducted with a total of 581 observations. All LM2-4^{LUC+} implanted animals used in this study are vehicle-treated animals from published studies [109, 118]. Vehicle formulation was carboxymethylcellulose sodium (USP, 0.5% w/v), NaCl (USP, 1.8% w/v), Tween-80 (NF, 0.4% w/v), benzyl alcohol (NF, 0.9% w/v), and reverse osmosis deionized water (added to final volume) and adjusted to pH 6 (see [134]) and was given at 10ml/kg/day for 7-14 days prior tumor resection.

Breast data measured by fluorescence ($N = 8$). This dataset is publicly available at the following repository [135]. It consisted of human MDA-MB-231 cells stably transfected with dTomato lentivirus. Animals were orthotopically implanted (80,000 cells at injection) into the mammary fat pads of 6-week-old female nude mice. Tumor size was monitored regularly with fluorescence imaging. The data comprised a total of 64 observations. To recover the fluorescence value corresponding to the injected cells, we computed the ratio between the fluorescence signal and the volume measured in mm^3 . We used linear regression considering the volume data of a different data set with same experimental setup (mice, tumor type and number of injected cells). The estimated ratio was $1.52 \cdot 10^9 \text{ photons}/(\text{s} \cdot \text{mm}^3)$ with relative standard error of 11.3%, therefore the initial fluorescence signal was $1.22 \cdot 10^7 \text{ photons/s}$.

Lung data measured by volume ($N = 20$). This dataset is publicly available at the following repository [136]. It consisted of murine Lewis lung carcinoma cells originally derived from a spontaneous tumor in a C57BL/6 mouse [137]. Animals were implanted subcutaneously (10^6 cells at injection)

on the caudal half of the back in anesthetized 6- to 8-week-old C57BL/6 mice. Tumor size was measured as described for the breast data to a maximum volume of 1.5 cm^3 . The data was pooled from two experiments with a total of 188 observations.

2.3.3 Tumor growth models.

We denote by t_I and V_I the initial conditions of the equation. At time of injection ($t = 0$), we assumed that all tumors within a group had the same size/volume V_{inj} (equal to the number of injected cells converted into the appropriate unit) and denoted by α the specific growth rate (i.e. $\frac{1}{V} \frac{dV}{dt}$) at this time and size.

We considered the exponential, logistic and Gompertz models [109]. The first two are respectively defined by the following equations

$$\begin{cases} \frac{dV}{dt} = \alpha V, \\ V(t_I) = V_I, \end{cases} \quad \text{and} \quad \begin{cases} \frac{dV}{dt} = \rho \left(1 - \frac{V}{K}\right) V, \\ V(t_I) = V_I. \end{cases} \quad (2.3)$$

In the logistic equation, K is a carrying capacity parameter. It expresses a maximal reachable size due to competition between the cells (e.g. for space or nutrients). The quantity $\rho = \alpha \left(\frac{K}{K - V_{\text{inj}}}\right)$ is a coefficient related to the growth rate. For small values of V_{inj} , ρ tends to α .

The Gompertz model is characterized by an exponential decrease of the specific growth rate with rate denoted here by β . Although multiple expressions and parameterizations coexist in the literature, the definition we adopted here reads as follows:

$$\begin{cases} \frac{dV}{dt} = \left(\alpha - \beta \left(\frac{V}{V_{\text{inj}}}\right)\right) V, \\ V(t_I) = V_I. \end{cases} \quad (2.4)$$

Note that the injected volume V_{inj} appears in the differential equation defining V . This is a natural consequence of our assumption of α as being the specific growth rate at $V = V_{\text{inj}}$. This model exhibits sigmoidal growth up to a saturating value given by $K = V_{\text{inj}} e^{\frac{\alpha}{\beta}}$. Note also that the value of K in the Gompertz model is independent of the initial data (t_I, V_I). The latter was considered to be $(0, V_{\text{inj}})$ when performing population analysis, while it was set equal to the observation $y_{n^i-2}^i$ of an animal i for backward prediction (see section Individual predictions).

2.3.4 Population approach.

Let N be the number of subjects within a population (group) and $\mathbf{Y}^i = \{y_1^i, \dots, y_{n^i}^i\}$ the vector of longitudinal measurements in animal i , where y_j^i is the observation of subject i at time t_j^i for $i = 1, \dots, N$ and $j = 1, \dots, n^i$ (n^i is the number of measurements of individual i). We assumed the following observation model

$$y_j^i = f(t_j^i; \boldsymbol{\theta}^i) + e_j^i, \quad j = 1, \dots, n^i, \quad i = 1, \dots, N, \quad (2.5)$$

where $f(t_j^i; \theta^i)$ is the evaluation of the tumor growth model at time t_j^i , $\theta^i \in \mathbb{R}^p$ is the vector of the parameters relative to the individual i and e_j^i the residual error model, to be defined later. An individual parameter vector θ^i depends on fixed effects μ , identical within the population, and on a random effect η^i , specific to each animal. Random effects follow a normal distribution with mean zero and variance matrix ω . Specifically:

$$\log(\theta^i) = \log(\mu) + \eta^i, \quad \eta^i \sim \mathcal{N}(0, \omega).$$

The choice of a log-normal distribution ensured the positivity of the parameters without adding any constraint. Moreover, the ratio of two log-normal distributions is a log-normal distribution.

We considered a combined residual error model e_j^i , defined as

$$e_j^i = (\sigma_1 + \sigma_2 f(t_j^i; \theta^i)) \varepsilon_j^i,$$

where $\varepsilon_j^i \sim \mathcal{N}(0, 1)$ are the residual errors and $\sigma = [\sigma_1, \sigma_2]$ is the vector of the residual error model parameters.

In order to compute the population parameters, we maximized the population likelihood, obtained by pooling all the data together. Usually, this likelihood cannot be computed explicitly for nonlinear mixed-effect models. We used the stochastic approximation expectation minimization algorithm (SAEM) [111], implemented in the Monolix 2018 R2 software [83]. This algorithm is a variation of the EM algorithm, where the expectation step is replaced by a stochastic approximation of the likelihood function [138]. This method has been proven to efficiently converge to the maximum likelihood estimator for nonlinear mixed effects models [111].

In the remainder of the manuscript we will denote by $\phi = \{\mu, \omega, \sigma\}$ the set of the population parameters containing the fixed effects μ , the covariance of the random effects ω and the error model parameters σ .

2.3.5 Individual predictions

For a given animal i , the backward prediction problem we considered was to predict the age of the tumor based on the three last measurements $\mathbf{y}^i = \{y_{n^i-2}^i, y_{n^i-1}^i, y_{n^i}^i\}$. Since we were in an experimental setting, we considered the injection time as the initiation time and thus the age was given by $a^i = t_{n^i-2}^i$. Then, we considered as model $f(t; \theta^i)$ the solution of the Cauchy problem (2.4) endowed with initial conditions $(t_I^i = t_{n^i-2}^i, V_I^i = y_{n^i-2}^i)$. For estimation of the parameters (estimate $\hat{\theta}^i$), we applied two different methods: likelihood maximization alone (no use of prior population information) and Bayesian inference (use of prior). The predicted age \hat{a}^i was then defined by

$$f(t_{n^i-2}^i - \hat{a}^i; \hat{\theta}^i) = V_{\text{inj}},$$

that is:

$$\hat{a}^i = \frac{1}{\hat{\beta}^i} \left(\log \left(\frac{\hat{\alpha}^i}{\hat{\beta}^i} \right) - \log \left(\frac{\hat{\alpha}^i}{\hat{\beta}^i} - \log \left(\frac{V_I^i}{V_{\text{inj}}} \right) \right) \right) \quad (2.6)$$

in case of the Gompertz model.

Likelihood maximization

For individual predictions with likelihood maximization, no prior information on the distribution of the parameters was used. Parameters of the error model were not re-estimated: values from the population analysis were used. The log-likelihood can be derived from (2.5):

$$\begin{aligned} l(\boldsymbol{\theta}^i) &= \ln \left(\prod_{j=n^i-2}^{n^i} \mathbb{P}(y_j^i | \boldsymbol{\theta}^i) \right) \\ &= -\frac{3}{2} \log(2\pi) - \frac{1}{2} \sum_{j=n^i-2}^{n^i} \left(\log(\sigma_1 + \sigma_2 f(t_j^i, \boldsymbol{\theta}^i)) + \left(\frac{y_j^i - f(t_j^i, \boldsymbol{\theta}^i)}{\sigma_1 + \sigma_2 f(t_j^i, \boldsymbol{\theta}^i)} \right)^2 \right), \end{aligned} \quad (2.7)$$

where $\mathbb{P}(y_j^i | \boldsymbol{\theta}^i)$ is the likelihood of the observation of the animal i at time t_j^i .

In order to guarantee the positivity of the parameters, we introduced the relation $\boldsymbol{\theta}^i = g(\boldsymbol{\gamma}^i) = e^{\boldsymbol{\gamma}^i}$ and substituted this in equation (2.7). The negative of equation (2.7) was minimized with respect to $\boldsymbol{\gamma}^i$ (yielding the maximum likelihood estimate $\hat{\boldsymbol{\gamma}}^i$) with the function `minimize` of the python module `scipy.optimize`, for which the Nelder-Mead algorithm was applied. Thanks to the invariance property, the maximum likelihood estimator of $\boldsymbol{\theta}^i$ was determined as $\hat{\boldsymbol{\theta}}^i = e^{\hat{\boldsymbol{\gamma}}^i}$. Individual prediction intervals were computed by sampling the parameters $\boldsymbol{\theta}^i$ from a gaussian distribution with variance-covariance matrix of the estimate defined as $\nabla g(\hat{\boldsymbol{\gamma}}^i)^T \cdot (\hat{s}^{2,i}(\mathbf{I}^{-1}(\hat{\boldsymbol{\gamma}}^i))) \cdot \nabla g(\hat{\boldsymbol{\gamma}}^i)$ where $\hat{s}^{2,i} = \frac{1}{3-p} \sum_{j=n^i-2}^{n^i} \left(\frac{y_j^i - f(t_j^i, \hat{\boldsymbol{\theta}}^i)}{\sigma_1 + \sigma_2 f(t_j^i, \hat{\boldsymbol{\theta}}^i)} \right)^2$, with p the number of parameters (and the factor 3 in the denominator because this is the number of observations), $\mathbf{I}(\hat{\boldsymbol{\gamma}}^i)$ the Fisher information matrix and $\nabla g(\hat{\boldsymbol{\gamma}}^i)$ the gradient of the function $g(\boldsymbol{\gamma})$ evaluated in the estimate $\hat{\boldsymbol{\gamma}}^i$. Denoting by $\mathbf{f}(\boldsymbol{\gamma}) = [f(t_j^i, e^{\boldsymbol{\gamma}})]_{j=n^i-2}^{n^i}$ and by $\boldsymbol{\Omega}(\boldsymbol{\gamma}) = \text{diag} \left(\sigma_1 + \sigma_2 [f(t_j^i, e^{\boldsymbol{\gamma}})]_{j=n^i-2}^{n^i} \right)$, the Fisher information matrix was defined by [139]:

$$[\mathbf{I}(\boldsymbol{\gamma})]_{l,m} = \left[\frac{\partial \mathbf{f}(\boldsymbol{\gamma})}{\partial \boldsymbol{\gamma}_l} \right]^T \boldsymbol{\Omega}^{-1}(\boldsymbol{\gamma}) \left[\frac{\partial \mathbf{f}(\boldsymbol{\gamma})}{\partial \boldsymbol{\gamma}_m} \right] + \frac{1}{2} \text{tr} \left[\boldsymbol{\Omega}^{-1}(\boldsymbol{\gamma}) \frac{\partial \boldsymbol{\Omega}(\boldsymbol{\gamma})}{\partial \boldsymbol{\gamma}_l} \boldsymbol{\Omega}^{-1}(\boldsymbol{\gamma}) \frac{\partial \boldsymbol{\Omega}(\boldsymbol{\gamma})}{\partial \boldsymbol{\gamma}_m} \right]. \quad (2.8)$$

Bayesian inference

When applying the Bayesian method, we considered *training sets* to learn the distribution of the parameters ϕ and *test sets* to derive individual predictions. For a given animal i of a *test set*, we predicted the age of the tumor based on the combination of: 1) population parameters ϕ identified on the *training set* using the population approach and 2) the three last measurements of animal i . We set as initial conditions $t_I = 0$ and $V_I^i \sim \mathcal{N}(y_{n^i-2}^i, \sigma_1 + \sigma_2 y_{n^i-2}^i)$. We considered the initial volume V_I to be a random variable to account for measurement uncertainty on $y_{n^i-2}^i$. We then estimated the

posterior distribution $\mathbb{P}(\boldsymbol{\theta}^i | \mathbf{y}^i)$ of the parameters $\boldsymbol{\theta}^i$ using a Bayesian approach [130]:

$$\mathbb{P}(\boldsymbol{\theta}^i | \mathbf{y}^i) = \frac{\mathbb{P}(\mathbf{y}^i | \boldsymbol{\theta}^i) \mathbb{P}(\boldsymbol{\theta}^i)}{\mathbb{P}(\mathbf{y}^i)}, \quad (2.9)$$

where $\mathbb{P}(\boldsymbol{\theta}^i)$ is the prior distribution of the parameters estimated through nonlinear mixed-effects modeling (i.e., the population parameters ϕ), $\mathbb{P}(\mathbf{y}^i | \boldsymbol{\theta}^i) = \int_{\mathbb{R}} \mathbb{P}(V_I^i) \mathbb{P}(\mathbf{y}^i | \boldsymbol{\theta}^i, V_I^i) dV_I^i$ is the likelihood, defined from equation (2.5), and $\mathbb{P}(\mathbf{y}^i) = \int_{\mathbb{R}^p} \mathbb{P}(\boldsymbol{\theta}^i) \mathbb{P}(\mathbf{y}^i | \boldsymbol{\theta}^i) d\boldsymbol{\theta}^i$ is a normalization factor. The predicted distributions of extrapolated growth curves and subsequent \hat{a}^i were computed by sampling $\boldsymbol{\theta}^i$ from its posterior distribution (2.9) using `Pystan`, a Python interface to the software `Stan` [84] for Bayesian inference based on the No-U-Turn sampler, a variant of Hamiltonian Monte Carlo [85]. The sampling procedure depends on the evaluation of the likelihood $\mathbb{P}(\mathbf{y}^i | \boldsymbol{\theta}^i)$, which relies itself on V_I^i . Therefore, V_I^i was sampled from its distribution for each realization of the posterior distribution. Predictions of \hat{a}^i were then obtained from (2.6), considering the median value of the distribution.

Different data sets were used for learning the priors (*training sets*) and prediction (*test sets*) by means of k -fold cross validation, with k equal to the total number of animals of the dataset ($k = N$, i.e. leave-one-out strategy). At each iteration we computed the parameters distribution of the population composed by $N-1$ individuals and used this as prior to predict the initiation time of the excluded subject i . The `Stan` software was used to draw 2000 realizations from the posterior distribution of the parameters of the individual i .

2.4 Results

Results were similar for the three data sets presented in the materials and methods. For conciseness, the results presented below are related to the largest dataset (breast cancer data measured by volume). Results relative to the other datasets are reported in Tables B1-B4 and Figures B1-B10.

2.4.1 Population analysis of tumor growth curves

The population approach was applied to test the descriptive power of the exponential, logistic and Gompertz models for tumor growth kinetics. The number of injected cells at time $t_{\text{inj}} = 0$ was 10^6 , therefore we fixed the initial volume $V_{\text{inj}} = 1 \text{ mm}^3$ in the whole dataset [109]. We set $(t_I, V_I) = (t_{\text{inj}}, V_{\text{inj}})$ as initial condition of the equations.

We ran the SAEM algorithm with the `Monolix` software to estimate the fixed and random effects [83]. Moreover, we evaluated different statistical indices in order to compare the different tumor growth models. This also allowed learning of the parameter population distributions that were used later as priors for individual predictions. Results are reported in Table 2.2, where the models are ranked according to their AIC (Akaike Information Criterion), a metrics combining parsimony and goodness-of-fit. The Gompertz model was the one with the lowest values, indicating superior goodness-of-fit. This was confirmed by diagnostic plots (Figure 2.2). The visual predictive checks

(VPCs) in Figure 2.2A compare the empirical percentiles with the theoretical percentiles, i.e. those obtained from simulations of the calibrated models. The VPC of the exponential and logistic models showed clear model misspecification. On the other hand, the VPC of the Gompertz model was excellent, with observed percentiles close to the predicted ones and small prediction intervals (indicative of correct identifiability of the parameters). Figure 2.2B shows the prediction distributions of the three models. This allowed to compare the observations with the theoretical distribution of the predictions. Only the prediction distribution of the Gompertz model covered the entire dataset. The logistic model exhibited a saturation of tumor dynamics at lower values than compatible with the data.

Moreover, the distribution of the residuals was symmetrical around a mean value of zero with the Gompertz model (Figure 2.2C), strengthening its good descriptive power, while the exponential and logistic models exhibited clear skewed distributions. The observations vs individual predictions in Figure 2.2D further confirmed these findings.

These observations at the population level were confirmed by individual fits, computed from the mode of the posterior conditional parameter distribution for each individual (Figure 2.3). Confirming previous results [109], the optimal fits of the exponential and logistic models were unable to give appropriate description of the data, suggesting that these models should not be used to describe tumor growth, at least in similar settings to ours. Fitting of late timepoints data forced the proliferation parameter of the exponential model to converge towards a rather low estimate, preventing reliable description of the early datapoints. The converse occurred for the logistic. Constrained by the early data points imposing to the model the pace of the growth deceleration, the resulting estimation of the carrying capacity K was biologically irrelevant (much too small, typical value 1303 mm^3 , see Table 2.3), preventing the model to give a good description of the late growth.

Table 2.3 provides the values of the population parameters. The relative standard error estimates associated to population parameters were all rather low ($<3.81\%$), indicating good practical identifiability of the model parameters. Standard error estimates of the constant error model parameters were found to be slightly larger ($<19.3\%$), suggesting that for some models a proportional error model might have been more appropriate - but not in case of the exponential model. Since our aim was to compare different tumor growth equations, we established a common error model parameter, i.e. a combined error model. Relative standard errors of the standard deviations of the random effects ω were all smaller than 9.6% (not shown).

These model findings in the breast cancer cell line were further validated with the other cell lines. For both the lung cancer and the fluorescence-breast cancer cell lines, the Gompertz model outperformed the other competing models (see Tables B1 and B2 for goodness-of-fit metrics, and Tables B3 and B4 for parameter values), as also shown by the diagnostic plots (Figures B1 and B2). Individual plots confirmed these observations and are provided in Figures B3 and B4. For the fluorescence-breast cancer cell line the constant part of the error model was found negligible and we used a proportional error model (i.e., we fixed $\sigma_1 = 0$). Value of σ_2 was found particularly high for the Exponential model (Table B4), which resulted in inappropriate fits (Figures B2 and B4), further

supporting rejection of this model. Estimated inter-individual variability for the other models was found small. This was probably due to the small number of animals in the data set.

Together, these results confirmed that the exponential and logistic models are not appropriate models of tumor growth while the Gompertz model has excellent descriptive properties, for both goodness-of-fit and parameter identifiability purposes.

Model	-2LL	AIC	BIC
Gompertz	7129	7143	7158
Reduced Gompertz*	7259	7269	7280
Logistic	7584	7596	7609
Exponential	8652	8660	8669

Table 2.2. Models ranked in ascending order of AIC (Akaike information criterion). Other statistical indices are the log-likelihood estimate (-2LL) and the Bayesian information criterion (BIC). *The reduced Gompertz model is introduced below.

Model	Par.	Unit	Fixed effects	ω	R.S.E. (%)
Gompertz	α	day ⁻¹	0.58	0.19	2.51
	β	day ⁻¹	0.072	0.26	3.42
	σ	-	[20.5, 0.11]	-	[16.9, 7.53]
Reduced Gompertz*	β	day ⁻¹	0.075	0.13	1.74
	k	-	7.87	-	0.21
	σ	-	[14.8, 0.17]	-	[19.3, 5.32]
Logistic	ρ	day ⁻¹	0.325	0.138	1.82
	K	mm ³	1303	0.25	3.81
	σ	-	[58.9, 0.12]	-	[8.97, 9.14]
Exponential	α	day ⁻¹	0.231	0.08	1.38
	σ	-	[272, 0.26]	-	[6.10, 15.1]

Table 2.3. Fixed effects (typical values) of the parameters of the different models. Par. = parameter. ω = standard deviation of the random effects. R.S.E. = relative standard errors of the estimates. σ = residual error model parameters. *The reduced Gompertz model is introduced below.

2.4.2 The reduced Gompertz model

Correlation between the Gompertz parameters.

During the estimation process of the Gompertz parameters, we found a high correlation between α and β within the population. At the population level, the SAEM algorithm estimated a correlation of the random effects equal to 0.981. At the individual level, α^i and β^i were also highly linearly correlated (Figure 2.4A, $R^2 = 0.968$), confirming previous results [100, 105, 104, 106, 140]. This

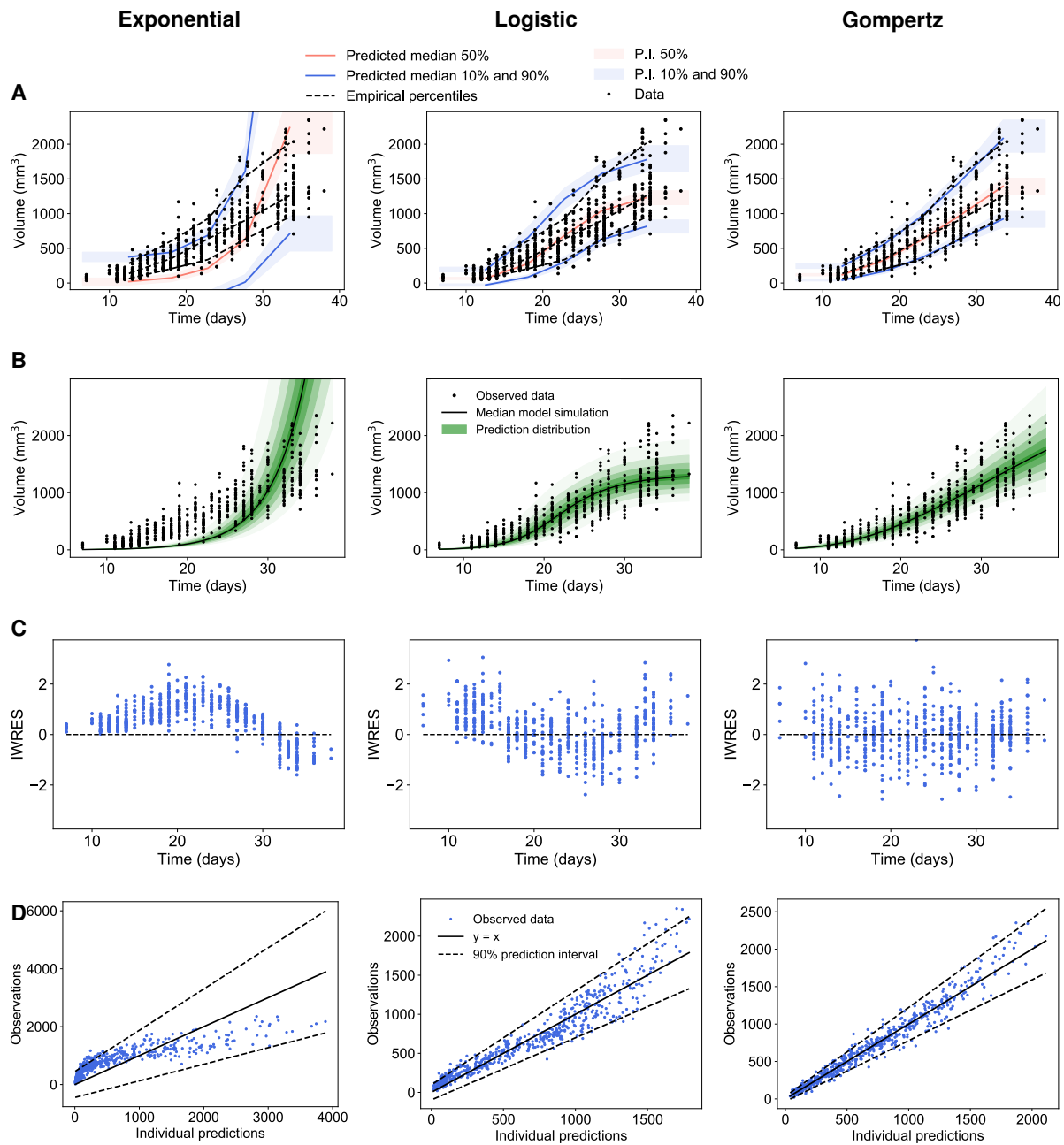


Figure 2.2. Population analysis of experimental tumor growth kinetics. (A) Visual predictive checks assess goodness-of-fit for both structural dynamics and inter-animal variability by reporting model-predicted percentiles (together with confidence prediction intervals (PI) in comparison to empirical ones. They were obtained by multiple simulations of each model. The time axis was then split into bins and in each interval the empirical percentiles of the observed data were compared with the respective predicted medians and intervals of the simulated data [83]. (B) Prediction distributions. They were obtained by multiple simulations of all individuals in the dataset, excluding the residual error [83]. (C) Individual weighted residuals (IWRES) with respect to time. (D) Observations vs predictions Left: exponential, Center: logistic, Right: Gompertz models.

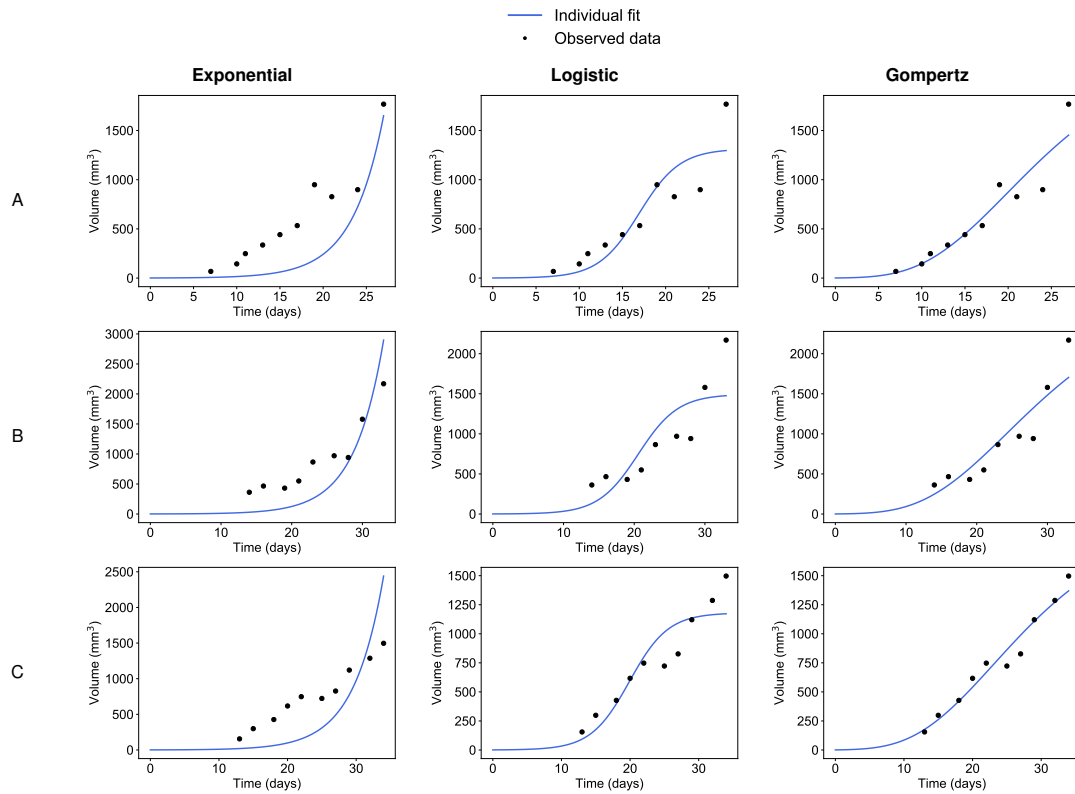


Figure 2.3. Individual fits from population analysis. Three representative examples of individual fits (animal (A), animal (B) and animal (C)) computed with the population approach relative to the exponential (left), the logistic (center) and the Gompertz (right) models.

motivated the reformulation of the alpha parameter as follows:

$$\alpha^i = k\beta^i + c, \quad (2.10)$$

where k and c are representing the slope and the intercept of the regression line, respectively. In our analysis we found c to be small ($c = 0.14$), thus we further assumed this term to be negligible and fixed it to 0. This suggests k as a constant of tumor growth within a given animal model with similar characteristics (note however that from (2.4), k depends on V_{inj}) [105, 141]. In turn, this implies an approximately constant limiting size

$$K^i = V_{inj} e^{\frac{\alpha^i}{\beta^i}} \simeq V_{inj} e^k \simeq 2600 \text{ mm}^3, \quad \forall i. \quad (2.11)$$

The other data sets gave analogous results in terms of goodness of fit and correlation between α and β , even if the constant limiting size was found different in the three cell lines. The estimated correlations of the random effects were 0.967 and 0.998 for the lung cancer and for the fluorescence-breast cancer, respectively. The correlation between the parameters was also confirmed at the individual level (see Figures B5 and B6, R^2 was 0.923 and 0.99 for the two data sets, respectively).

Biological interpretation in terms of the proliferation rate.

By definition, the parameter α^i is the specific growth rate (SGR) at the volume V_{inj} , simply assumed to be the volume corresponding to the number of injected cells within a given animal model (e.g. $V_{inj} = 1$ for the breast data measured by volume). Assuming that the cells don't change their proliferation kinetics when implanted, this value should thus in theory be equal to the *in vitro* proliferation rate (supposed to be the same for all the cells of the same cell line), denoted here by λ . The value of this biological parameter was assessed *in vitro* and estimated at 0.837 [118]. In support to our quantitative assumptions, we indeed found estimated values of α^i close to λ (fixed effects of 0.58, see Table 2.3).

However, most of the values of α^i were smaller than λ in the majority of the cases (Figure 2.4A). We postulated that this difference could be explained by the fact that not all the cells will be successfully grafted when injected in an animal. Under such assumption the SGR at the initial time, to be compared with λ , would not be given by α^i anymore. Instead, denoting by $\hat{V}_{inj}^i < V_{inj}$ the (unknown) volume of the successfully grafted cells, and assuming further that the SGR at initiation would be fixed and given by λ leads to the following reformulation of the Gompertz model

$$\begin{cases} \frac{dV^i}{dt} = \left(\lambda - \beta^i \log \left(\frac{V^i}{\hat{V}_{inj}^i} \right) \right) V^i \\ V^i(t_I = 0) = \hat{V}_{inj}^i \end{cases}$$

In turn, fitting this model to the data provides estimates of the percentage of successful engraftment of $7\% \pm 12.5\%$ (mean \pm standard deviation).

Alternatively, these results might also be explained by a time lag between the cell implantation and the initiation of tumor growth, due to the time needed by the cells to adapt to the new environment [142]. However, the two interpretations are indistinguishable in our case and might require a more

elaborate analysis with specific data.

Population analysis of the reduced Gompertz model.

The high correlation among the Gompertz parameters, suggested that a reduction of the degrees of freedom (number of parameters) in the Gompertz model could improve identifiability and yield a more parsimonious model. We considered the expression (2.10), assuming c to be negligible. We therefore propose the following reduced Gompertz model:

$$\left\{ \begin{array}{l} \frac{dV^i}{dt} = \left(\beta^i k - \beta^i \log \left(\frac{V^i}{V_{inj}^i} \right) \right) V^i \\ V^i(t_j^i) = V_I^i \\ \log(\beta^i) = \log(\beta_{pop}) + \eta_\beta^i, \quad \eta_\beta^i \sim \mathcal{N}(0, \omega_\beta) \\ k = k_{pop} \end{array} \right., \quad (2.12)$$

where β has mixed effects, while k has only fixed effects, i.e., is constant within the population.

Figure 2.4 shows the results relative to the population analysis of this reduced Gompertz model. Results of the diagnostic plots indicated no deterioration of the goodness-of-fit as compared with the Gompertz model (Figure 2.4B-D). Only on the last timepoint was the model slightly underestimating the data (Figure 2.4D), which might explain why the model performs slightly worse than the two-parameters Gompertz model in terms of strictly quantitative statistical indices (but still better than the logistic or exponential models, Table 2.2). Individual dynamics were also accurately described (Figure 2.4E). Parameter identifiability was also excellent (Table 2.3).

The other two data sets gave similar results (see Figures B5 and B6).

Together, these results demonstrated the accuracy of the reduced Gompertz model, with improved robustness as compared to previous models.

2.4.3 Prediction of the age of a tumor

Considering the increased robustness of the reduced Gompertz model (one individual parameter less than the Gompertz model), we further investigated its potential for improvement of predictive power. We considered the problem of estimating the age of a tumor, that is, the time elapsed between initiation (here the time of injection) and detection occurring at larger tumor size (Figure 2.5). For a given animal i , we considered as first observation $y_{n^i-2}^i$ and aimed to predict its age $a^i = t_{n^i-2}^i$ (see Methods). We compared the results given by the Bayesian inference with the ones computed with standard likelihood maximization method (see Methods). To that end, we did not consider any information on the distribution of the parameters. For the reduced Gompertz model however (likelihood maximization case), we used the value of k calculated in the previous section (Table 2.3), thus using information on the entire population. Importantly, for both prediction approaches, our methods allowed not only to generate a prediction of a^i for estimation of the model accuracy (i.e.

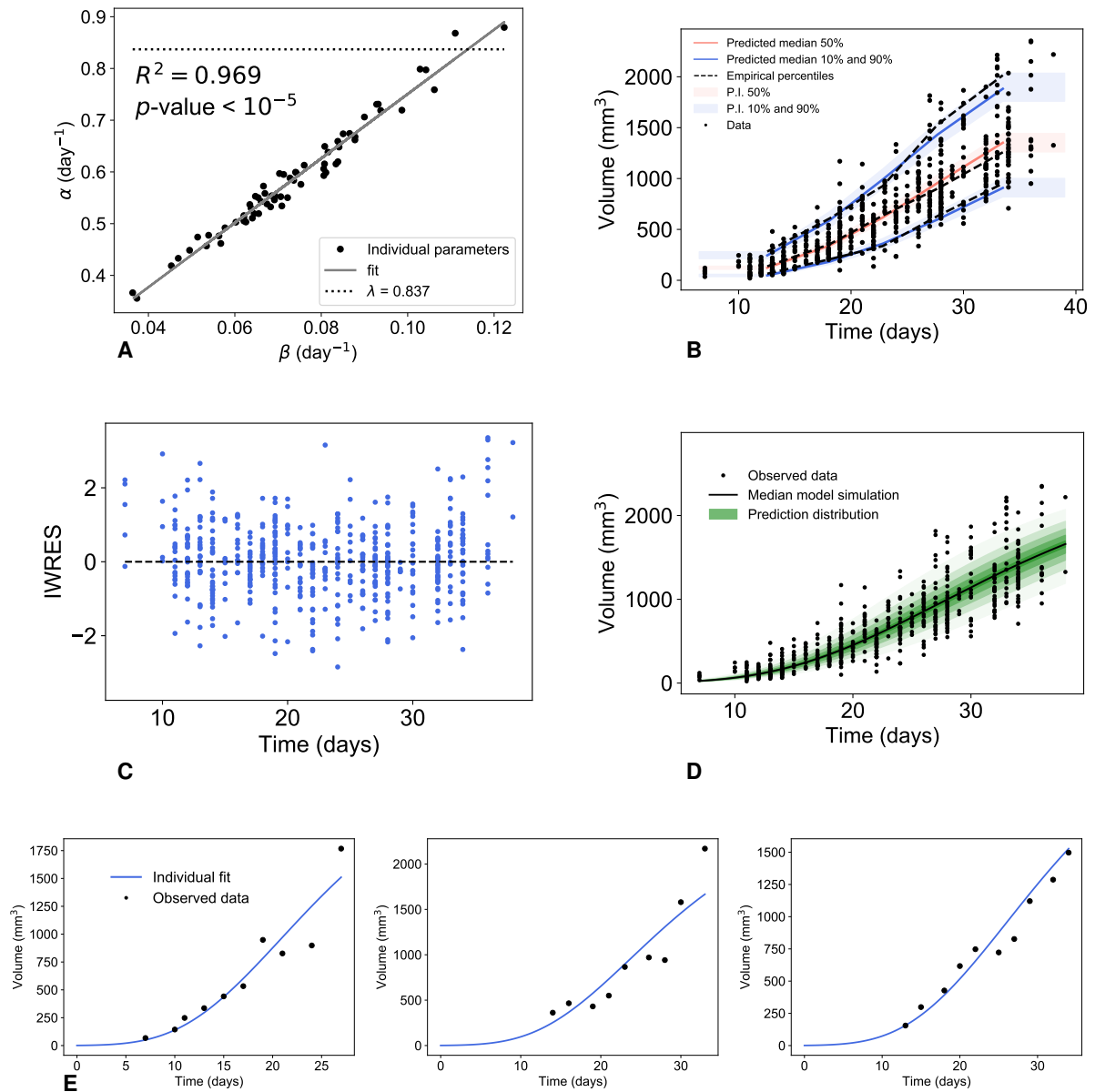


Figure 2.4. Correlation of the Gompertz parameters and diagnostic plots of the reduced Gompertz model from population analysis. Correlation between the individual parameters of the Gompertz model (A) and results of the population analysis of the reduced Gompertz model: visual predictive check (B), scatter plots of the residuals (C), prediction distribution (D) and examples of individual fits (E).

absolute relative error of prediction), but also to estimate the uncertainty of the predictions (i.e. precision, measured by the width of the 95% prediction interval (PI)).

Figure 2.5 presents a few examples of prediction of three individuals without (LM) and with (Bayesian inference) priors relative to the breast cancer measured by volume. The reduced Gompertz model combined to Bayesian inference (bottom row) was found to have the best accuracy in predicting the initiation time (mean error = 12.2%, 8.8% and 12.3% for the volume-breast cancer, lung cancer and fluorescence-breast cancer respectively) and to have the smallest uncertainty (precision = 15.6, 7.79 and 23.6 days for the three data sets, respectively). Table 2.4 gathers results of accuracy and precision for the Gompertz and reduced Gompertz models under LM and Bayesian inference relative to the three data sets. With only local information of the three last data points, the Gompertz model predictions were very inaccurate (mean error = 156%, 178% and 236%) and the Fisher information matrix was often singular, preventing standard errors to be adequately computed. With one degree of freedom less, the reduced Gompertz model had better performances with LM estimation but still large uncertainty (mean precision under LM = 210, 103 and 368 days) and poor accuracy using LM (mean error = 79%, 68.9% and 91.7%). Examples shown in Figure 2.5 were representative of the entire population relative to the breast cancer measured by volume. Eventually, for 97%, 95% and 87.5% of the individuals of the three data sets the actual value of the age fell in the respective prediction interval when Bayesian inference was applied in combination with the reduced Gompertz models. This means a good coverage of the prediction interval and indicates that our precision estimates were correct. On the other hand, this observation was not valid in case of likelihood maximization, where the actual value fell in the respective prediction interval for only 42.4%, 35% and 75% of the animals when the reduced Gompertz model was used.

Addition of *a priori* population information by means of Bayesian estimation resulted in drastic improvement of the prediction performances (Figure 2.6). This result was confirmed in the other data sets (see Figures B7 and B8 for the lung cell line and Figures B9 and B10 for the breast cell line measured by fluorescence). For the breast and lung cancer cell lines measured by volume, a Wilcoxon test was performed to analyze the different error distributions shown in Figures 2.6C and B8C. For the fluorescence-breast cancer cell line we could not report a significant difference in terms of accuracy between the Gompertz and the reduced Gompertz when applying Bayesian inference. This can be explained by the low number of individuals included in the data set.

Overall, the combination of the reduced Gompertz model with Bayesian inference clearly outperformed the other methods for prediction of the age of experimental tumors.

2.5 Discussion

We have analyzed tumor growth curves from multiple animal models and experimental techniques, using a population framework. This approach is ideally suited for experimental or clinical data of the same tumor type within a given group of subjects. Indeed, it allows for a description

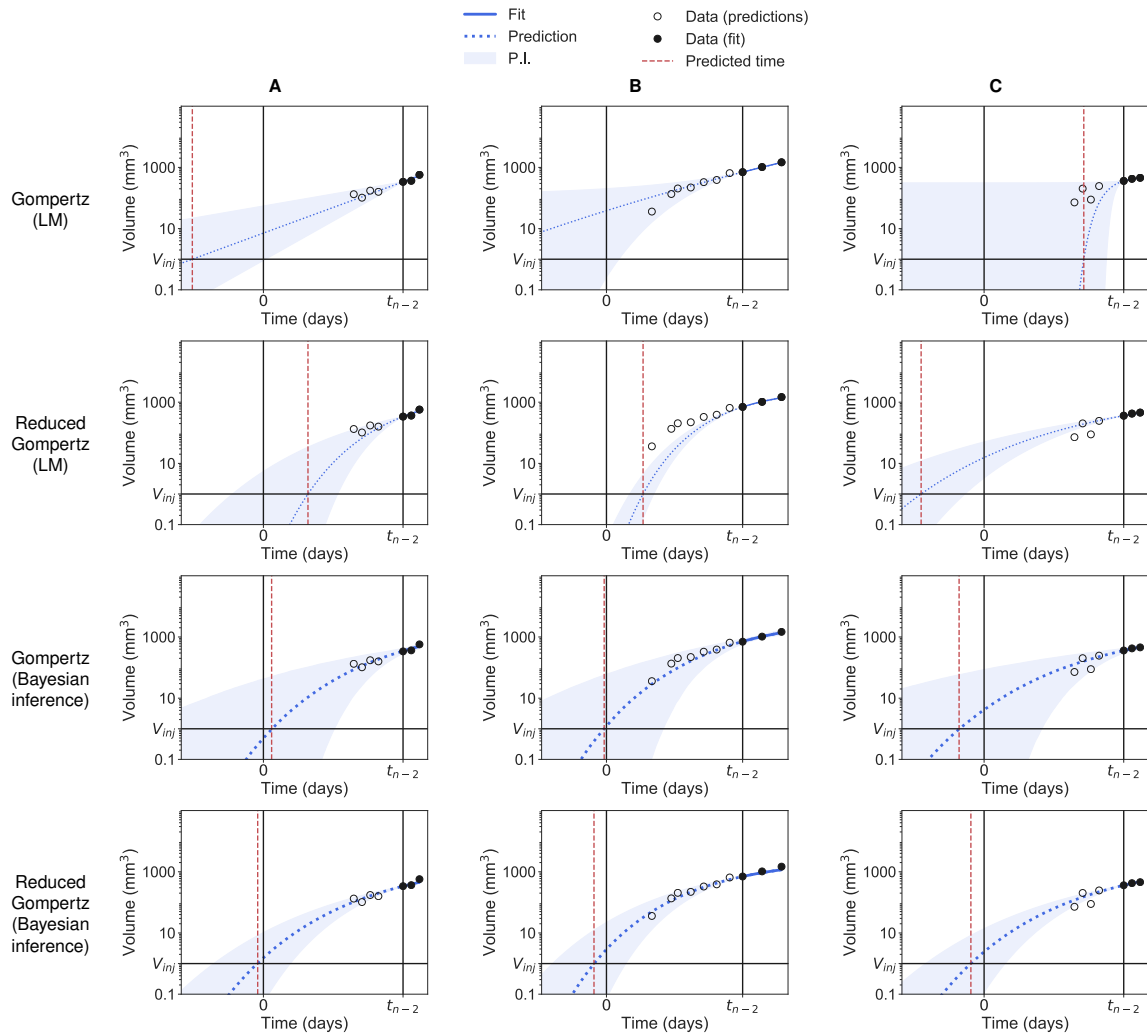


Figure 2.5. Backward predictions computed with likelihood maximization and with Bayesian inference. Examples of backward predictions of three individuals (A), (B) and (C) computed with likelihood maximization (LM) and Bayesian inference: Gompertz model with likelihood maximization (first row); reduced Gompertz with likelihood maximization (second row); Gompertz with Bayesian inference (third row) and reduced Gompertz with Bayesian inference (fourth row). Only the last three points are considered to estimate the parameters. The grey area is the 95% prediction interval (PI) and the dotted blue line is the median of the posterior predictive distribution. The red line is the predicted initiation time and the black vertical line the actual initiation time.

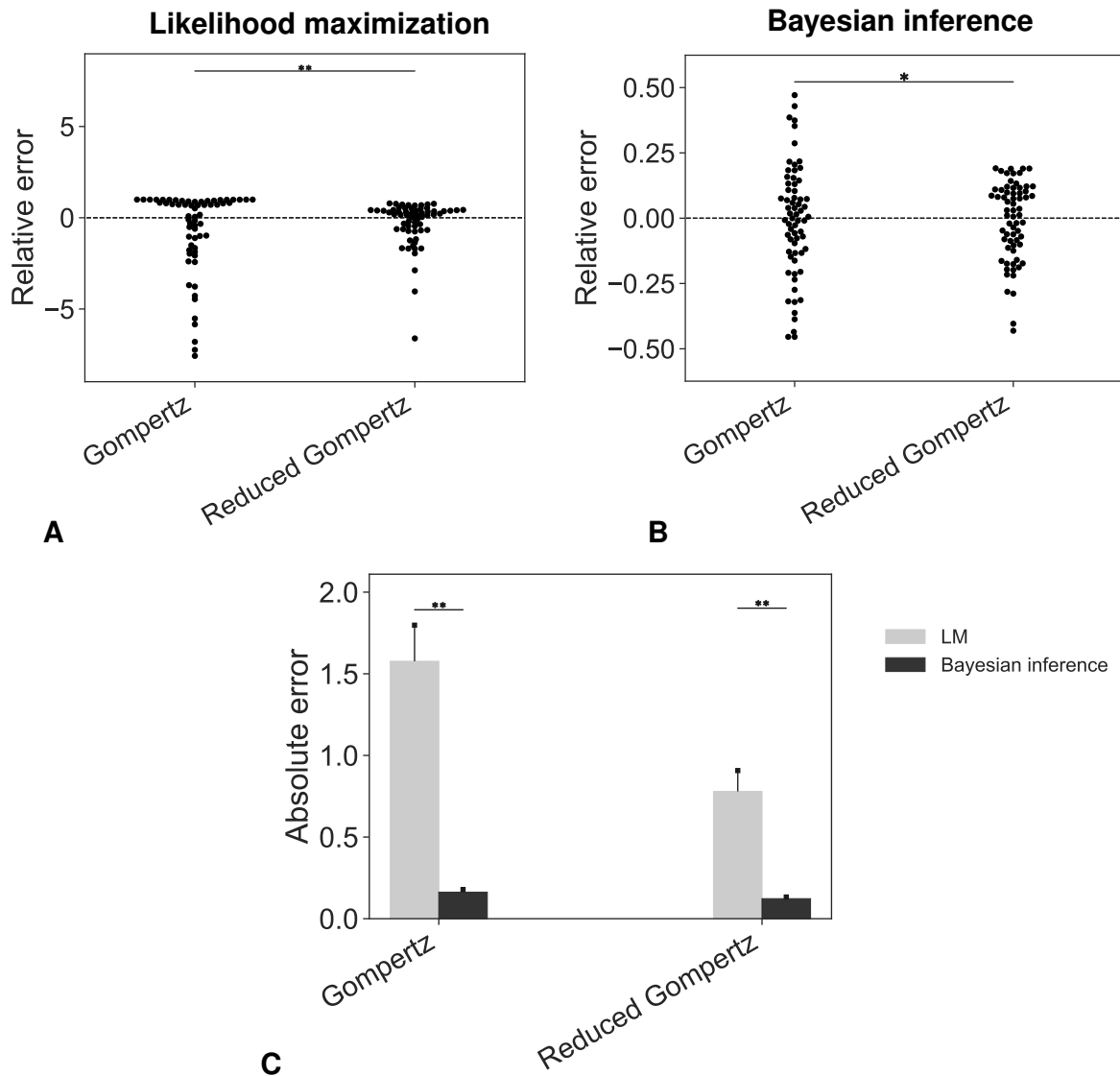


Figure 2.6. Accuracy of the prediction models. Swarmplots of relative errors obtained under likelihood maximization (A) or Bayesian inference (B) (* p -value < 0.05, ** p -value < 0.01, Levene's test). (C) Absolute errors: comparison between the different distributions (* p -value < 0.05, ** p -value < 0.01, Wilcoxon test). In (A) three extreme outliers were omitted (values of the relative error were greater than 20) for both the Gompertz and the reduced Gompertz in order to ensure readability. LM = Likelihood Maximization

Cell line	Model	Estimation method	Error	PI
Breast, volume	Reduced Gompertz	Bayesian	12.2 (1.05)	15.6 (0.509)
	Reduced Gompertz	LM	79 (13.2)	210 (58.6)
	Gompertz	Bayesian	16.4 (1.65)	41.1 (1.63)
	Gompertz	LM	156 (21.7)	-
Lung, volume	Reduced Gompertz	Bayesian	8.78 (1.43)	7.79 (0.275)
	Reduced Gompertz	LM	68.9 (33.1)	103 (92.6)
	Gompertz	Bayesian	18.9 (2.87)	19.7 (1.89)
	Gompertz	LM	178 (71.6)	-
Breast, fluores- cence	Reduced Gompertz	Bayesian	12.3 (2.9)	23.6 (5.15)
	Reduced Gompertz	LM	91.7 (21.1)	368 (223)
	Gompertz	Bayesian	13.5 (3.5)	45.4 (4.43)
	Gompertz	LM	236 (150)	-

Table 2.4. Accuracy and precision of methods for prediction of the age of experimental tumors of the three cell lines. Accuracy was defined as the absolute value of the relative error (in percent). Precision was defined as the width of the 95% prediction interval (PI column, in days). Reported are the means and standard errors (in parenthesis). LM = likelihood maximization

of the inter-subject variability that is impossible to obtain when fitting models to averaged data (as often done for tumor growth kinetics [143]), while enabling a robust population-level description that is strictly more informative than individual fits alone. As expected from the classical observation of decreasing specific growth rates [100, 144, 102, 145, 146], the exponential model generated very poor fits. More surprisingly given its popularity in the theoretical community (probably due to its ecological ground), the logistic model was also rejected, due to unrealistically small inferred value of the carrying capacity K . This finding confirms at the population level previous results obtained from individual fits [109, 147]. It suggests that the underlying theory (competition between the tumor cells for space or nutrients) is unable – at least when considered alone – to explain the decrease of the specific growth rate, suggesting that additional mechanisms need to be accounted for. Indeed, the logistic model relies on space-independent cellular interactions, which might be biologically unrealistic [148]. Few studies have previously compared the descriptive performances of growth models on the same data sets [109, 149, 110]. In contrast to our results, Vaidya and Alexandro [110] found admissible description of tumor growth data employing the logistic model. Beyond the difference of animal model, we believe that the major reason explaining this discrepancy is the type of error model that was employed, as also noticed by others [147]. Here we used a combined error model, in accordance to our previous study [109] that had examined repeated measurements of tumor size and concluded to rejection of a constant error model (used in [110]). Moreover, statistical goodness-of-fit metrics were substantially worse when using a constant error model (e.g AIC of 7362 versus 7129, for the Gompertz model, results not shown). To avoid overfitting, we also made the assumption to keep the initial value V_l fixed to V_{inj} . As noted before [109], releasing this constraint leads to ac-

ceptable fits by either the exponential or logistic models (to the price of deteriorated identifiability). However, the estimated values of V_I are in this case biologically inconsistent.

On the other hand, the Gompertz model demonstrated excellent goodness-of-fit in all the experimental systems that we investigated. This is in agreement with a large body of previous experimental and clinical research works using the Gompertz model to describe unaltered tumor growth in syngeneic [150, 100, 104, 147] and xenograft [151, 152] preclinical models, as well as human data [145, 107, 106, 102]. The poor performances of the logistic model compared to the Gompertz model can be related to the structural properties of the models. The two sigmoid functions lie between two asymptotes ($V = 0$ and $V = K$) and are characterized by an initial period of fast growth followed by a phase of decreasing growth. These two phases are symmetrical in the logistic model, which is characterized by a decrease of the specific growth rate $\frac{1}{V} \frac{dV}{dt}$ at constant speed. On the other hand, the Gompertz model exhibits a faster decrease of the specific growth rate, at speed $-\frac{\beta}{V}$, or $e^{-\beta t}$ as a function of t , and the sigmoidal curve is not symmetric around its inflexion point. The logistic and Gompertz models belong to the same family of tumor growth equations and can be seen as specific cases of the generalized logistic model $\frac{dV}{dt} = \rho V \left(1 - \left(\frac{V}{K}\right)^\nu\right)$ [146, 109]. We also analyzed the latter model, which demonstrated good descriptive power but lacked robustness of convergence. Indeed, the SAEM algorithm converged to different estimates starting from different initial guesses of the parameters. This might be explained by the larger number of parameters (3) that led to identifiability problems. In addition, we found that values of ν able to describe the data were often very small ($< 10^{-3}$), thus suggesting convergence to the Gompertz model.

Similarly to previous reports [100, 105, 106, 107], we also found a very strong linear correlation between the two parameters of the Gompertz model, i.e. α the proliferation rate at injection and β the rate of decrease of the specific growth rate. Importantly, this correlation is not due to a lack of identifiability of the parameters at the individual level, which we investigated and found to be excellent. Such finding motivated our choice to use a reduced Gompertz model, with only one individual-specific parameter, and one population-specific parameter. This model has been proposed before in the context of individual tumor growth curves [105, 141] but here we leveraged the population approach to ensure reliable estimation of the population-level parameter and statistical distribution of the individual-level parameter. Importantly, while previous studies had only investigated the resulting predictive power in only one animal [104] or using simulation data [141], here we rigorously demonstrated how the reduced Gompertz allows better backward (or forward, although not reported here) prediction of tumor size and time of initiation. This analysis was performed using state-of-the-art techniques from predictive modeling (e.g. cross-validation), on a large number of animals.

The descriptive power of the reduced Gompertz model was found similar to the two-parameters Gompertz model. Critically, while previous work had demonstrated that two individual parameters were sufficient to describe tumor growth curves [109], these results now show that this number can be reduced to one. Interestingly, we found different values of the carrying capacity K for the breast and the lung cancer cell lines measured by volume ($K = 2600 \text{ mm}^3$ and 12300 mm^3 , respectively), in

contrast with previous claims [105]. This suggests that there might not be a characteristic saturation point within a species [141] but the carrying capacity could be a typical feature of a tumor type in an animal model. From (2.12), the population constant k depends on the value of the parameter V_{inj} , therefore it cannot be viewed as a universal constant of tumor growth. However, it can be considered as a common trait within a species with similar characteristics (such as tumor type and value of V_{inj}). We used the formulations of the Gompertz (2.4) and reduced Gompertz (2.12) in order to define α as the specific growth rate at injection, which could be compared to the *in vitro* proliferation rate λ . This could be leveraged clinically to predict past or future tumor growth kinetics based on proliferation assays, derived from a patient's tumor sample.

The reduced Gompertz model, combined to Bayesian estimation from the population prior, allowed to reach good levels of accuracy and precision of the time elapsed between the injection of the tumor cells and late measurements, used as an experimental surrogate of the age of a given tumor. Importantly, performances obtained without using a prior were substantially worse. The method proposed herein remains to be extended to clinical data, although it will not be possible to have a firm confirmation since the natural history of neoplasms from their inception cannot be reported in a clinical setting. Nevertheless, the encouraging results obtained here could allow to give informative estimates, even if approximative. Importantly, the methods we developed also provide a measure of precision, which would give a quantitative assessment of the reliability of the predictions. For clinical translation, V_{inj} should be replaced by the volume of one cell $V_c = 10^{-6} \text{ mm}^3$. Moreover, since the Gompertz model has a specific growth rate that tends to infinity when V gets arbitrarily small, our results might have to be adapted with the Gomp-Exp model [153, 118].

Our methodology might face multiple challenges for future clinical applications. First, it is difficult to fully characterize unperturbed tumor kinetics in humans and only few studies support the evidence that it follows a gompertzian growth [102]. This is due to the limited number of available observations in the clinic and to the fact that saturation of human tumors is almost never reached, since it coincides with an advanced stage of the cancer where patients usually receive a treatment. Moreover, human tumor growth curves, even if limited to the same organ and histological type, exhibit a substantially larger variability than in *in vivo* experimental settings where immortalized cancer cell lines are injected in genetically identical mice. Here, we have proven that a given animal model (i.e. same mice, tumor type and number of injected cells) is characterized by a common tumor growth constant, that defines the saturation point. In the human setting, it could be interesting to analyze this constant as a function of some covariates (such as weight, sex, tumor type). Eventually, in the Gompertz model we haven't considered that the initial phase of tumor growth might be affected by intrinsic stochasticity. Our choice was motivated by the large number of injected cells (of the order of 10^6) that allowed us to consider the initial variability to be negligible. For accurate clinical translation, stochasticity should ideally be taken into account to model the initial stages of tumor growth.

Personalized estimations of the age of a given patient's tumor would yield important epidemiological insights and could also be informative for routine clinical practice [131]. By estimating

the period at which the cancer initiated, it could give clues on the possible causes (environmental or behavioral) of neoplastic formation. Moreover, reconstruction of the natural history of the pre-diagnosis tumor growth might inform the presence and extent of invisible metastasis at diagnosis. Indeed, an older tumor has a greater probability of having already spread than a younger one. Altogether, the present findings could contribute to the development of personalized computational models of metastasis [118, 154, 155].

2.6 Validation of the reduced Gompertz model

We validated the reduced Gompertz model on a new dataset of unperturbed tumor growth with a different V_{inj} . The experiment details are provided in [76]. 6-week-old female nude mice were orthotopically grafted (mammary fat pad) with 80,000 MDA-MB-231 cells in 60% Matrigel. Tumor growth was initially monitored using fluorescence imaging, while starting from day 44 caliper measurements were employed because of loss of dTomato expression *in vivo*.

Data and methods

We took into account the two types of observations. In particular, until day 30 tumor size was monitored with fluorescence imaging and starting from day 44 it was measured with caliper. Therefore, tumor growth data y_i^j of an individual i at time t_i^j is defined as

$$y_i^j = \begin{cases} y_{\text{fluo},i}^j, & t_i^j \leq 30, \\ y_{\text{cal},i}^j, & t_i^j \geq 44, \end{cases} \quad (2.13)$$

where $y_{\text{fluo},i}^j$ is the fluorescence signal and $y_{\text{cal},i}^j$ is the tumor volume measured with caliper. We denoted by K_{FV} the conversion rate from the fluorescence signal to the tumor volume (in $\text{mm}^3 \cdot (\text{phot.}/\text{s})^{-1}$). In the following sections, we will denote the evolution of the tumor volume V in time considering the two measurement types V_{fluo} (fluorescence) and V_{cal} (caliper) as follows

$$V(t) = \begin{cases} K_{FV} V_{\text{fluo}}(t), & t \leq 30, \\ V_{\text{cal}}(t), & t > 30. \end{cases} \quad (2.14)$$

The injected number of tumor cells was $V_{inj} = 0.08 \text{ mm}^3$.

The reduced Gompertz model was considered to describe the tumor growth kinetics in time:

$$\frac{dV_{\text{fluo}}}{dt} = \left(k\beta^i - \beta^i \log \left(\frac{V_{\text{fluo}}}{V_{inj}/K_{FV}^i} \right) \right) V_{\text{fluo}}, \quad V_{\text{fluo}}(0) = V_{inj}/K_{FV}^i, \quad (2.15)$$

$$\frac{dV_{\text{cal}}}{dt} = \left(k\beta^i - \beta^i \log \left(\frac{V_{\text{cal}}}{V_{inj}} \right) \right) V_{\text{cal}}, \quad V_{\text{cal}}(0) = V_{inj}, \quad (2.16)$$

where k has fixed effects, while K_{FV}^i and β^i have random effects within the population. The specific growth rate α^i at the injected volume V_{inj} satisfies $\alpha^i = k\beta^i$. The large number of degrees of freedom and the lack of data from day 30 to day 44 induced us to determine some parameters from other

experiments. Since we claim that the carrying capacity might be constant within a tumor type in a given species (see Section 2.4.2), we estimated the fixed-effects parameter k from equation (2.11), with $V_{\text{inj}} = 0.08 \text{ mm}^3$:

$$k = \log\left(\frac{K}{V_{\text{inj}}}\right) \approx 10.4. \quad (2.17)$$

Moreover, we observed that the specific growth rate α should be equal to the *in vitro* proliferation rate λ . Assuming this relationship, we were able to estimate the parameter β as follows:

$$\beta^i = \frac{\alpha^i}{k} = \frac{\lambda^i}{k}.$$

The cell doubling time was studied *in vitro* on MDA-MB-231 dTomato cells and results are provided in appendix A. From Table A3, we estimated the distribution of the proliferation rate (in h^{-1}):

$$\begin{aligned} \log(\lambda^i) &\sim \mathcal{N}(\log(\lambda_{\text{pop}}), \omega_\lambda^2) \\ &= \mathcal{N}\left(\log\left(\frac{K_{\text{pop}} - V_{0,\text{pop}}}{K_{\text{pop}}}\rho_{\text{pop}}\right), \left(\frac{K_{\text{pop}} - V_{0,\text{pop}}}{K_{\text{pop}}}\right)^2 \omega_\rho^2\right) \\ &= \mathcal{N}(\log(0.037), 0.004). \end{aligned}$$

Therefore, we obtained the distribution of the parameter β (converted in day^{-1}):

$$\log(\beta^i) \sim \mathcal{N}\left(\log\left(\frac{24}{k}\lambda_{\text{pop}}\right), \left(\frac{24}{k}\right)^2 \omega_\lambda^2\right) = \mathcal{N}(\log(0.086), 0.024). \quad (2.18)$$

We tested the reduced Gompertz model on the control data fixing k and β^i according to (2.17) and (2.18), respectively, using *Monolix 2019R2*. This was a real validation of the reduced Gompertz model, as the predictions were concordant with independent data. Moreover, we estimated the parameter K_{FV} and recovered the entire tumor growth kinetics.

Parameter estimation with nonlinear mixed effects modeling

We pooled together fluorescence and volume data to estimate tumor growth parameters. We employed a similar methodology to section 2.4.1. In this case, we assumed a proportional error model for both the fluorescence and the caliper measurements. Indeed, early observations of the caliper-measured tumor volume were not available. The observation model reads as follows:

$$\begin{cases} y_{\text{fluo},i}^j = V_{\text{fluo}}(t^j; \boldsymbol{\theta}) + \sigma_{\text{fluo}} V_{\text{fluo}}(t^j; \boldsymbol{\theta}) \varepsilon_j^i, \\ y_{\text{cal},i}^j = V_{\text{caluo}}(t^j; \boldsymbol{\theta}) + \sigma_{\text{cal}} V_{\text{cal}}(t^j; \boldsymbol{\theta}) \varepsilon_j^i, \end{cases} \quad (2.19)$$

where $\boldsymbol{\theta}$ is the set of parameters of the tumor growth model $V(t)$, σ_{fluo} and σ_{cal} are the error model parameters, and $\varepsilon_j^i \sim \mathcal{N}(0, 1)$ is the residual error.

Due to the large number of degrees of freedom, the error model parameter of caliper data σ_{cal} was fixed to 0.17, which was the estimated value for the reduced Gompertz model in Table 2.3.

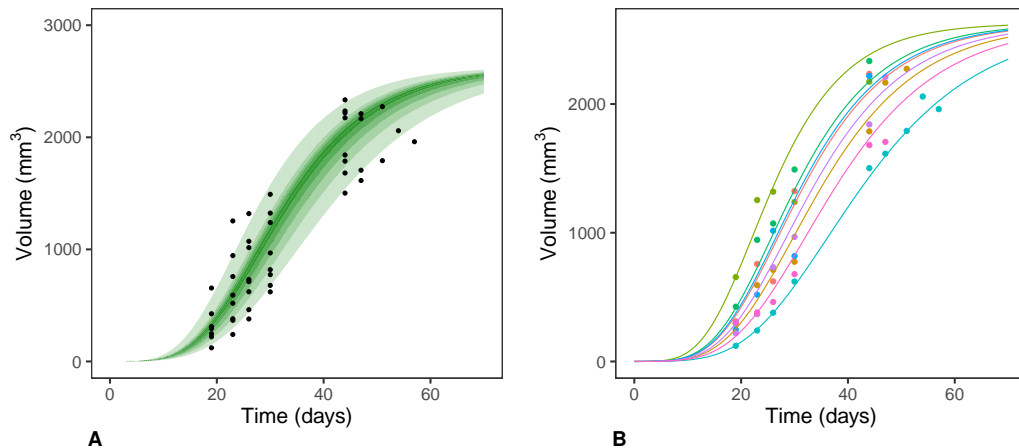


Figure 2.7. Validation of the reduced Gompertz model: prediction distributions (A) and individual fits (B) with the volume data (after day 44) and the rescaled fluorescence data (before day 30).

Results

We analyzed the control group to validate the hypotheses on the parameters k and β and to estimate the distribution of the parameter K_{FV} . We used Monolix 2019R2 [156] to perform the analysis. The visualization was done using the Simulx function of the mlxR R package [157], that allowed us to rescale fluorescence data to volume data. Results are shown in Figure 2.7 on the left. Good individual fits were found for the caliper data (after day 44) considering that k and the distribution of the parameter β were fixed. Moreover, the reduced Gompertz model was able to describe the rescaled fluorescence data (before day 30). The parameter K_{FV} was found to have fixed values of $2.11e-7 \text{ mm}^3 \cdot (\text{phot/s})^{-1}$ and standard deviation of the random effects equal to 0.54.

2.7 Further applications of the reduced Gompertz model: assessing the differences in tumor growth kinetics

An additional application of the reduced Gompertz model consists in the evaluation of the differences in tumor growth dynamics in different experimental groups. We performed an analysis on data provided by Melissa Dolan and John Ebos¹ to test if there were significant differences in tumor growth kinetics between groups (such as resistant vs sensitive cancer cell lines).

A classical approach to compare tumor growth curves of different experimental groups consists in determining if there are significant differences between the means at given time points using a t-test. However, this methodology is highly limited, as it requires that measurements are acquired at the same time and multiple p -values need to be compared. The evaluation of the specific growth rate using the exponential growth model could be a possible strategy to address this problem. However,

¹Department of Pharmacology and Therapeutics, Roswell Park Comprehensive Cancer Center

Group	Cell type	Strain	Treatment	V_{inj} [mm ³]	# of animals
1	+	BALB/c	None	0.04	40
2	-	BALB/c	None	0.04	40
3	+	SCID	None	0.04	5
4	-	SCID	None	0.04	5

Table 2.5. Summary of the different groups considered in the study. Cell type + means resistant cells, while cell type - means sensitive cells. V_{inj} is the volume of tumor cells that was initially injected into the animal.

the exponential model failed in fitting tumor growth data, as observed before. Here, we propose a novel strategy to compare tumor growth curves based on the parameter β of the reduced Gompertz model.

Tumor growth analysis was performed on each couple of groups using the Monolix software. The parameter k was considered to have fixed effects within the population - composed by the two groups - while β was assumed to have both fixed and random effects. Moreover, a combined error model was used. The population parameters were estimated by maximizing the population likelihood, obtained by pooling together the data of each pair of groups, adding a group covariate to the parameter β .

This methodology allowed us to estimate only one individual parameter β and to compare the distributions of this parameter in each pair of groups. Student's t-test was used to determine whether the mean of the estimated individual parameter β was the same for the two groups. If the calculated p -value was found lower than 0.05, then we rejected the null hypothesis that the distributions of β of the two groups were equal.

Here, we show some examples of this kind of test. We analyzed tumor growth kinetics on control groups, therefore no treatment was provided. Table 2.5 provides a summary of the different groups that we considered. The animals were classified according to the strain, cell type and treatment. The analysis was performed to assess differences in tumor growth kinetics in groups 1-2 and 3-4. Figure 2.8 shows the results of the test. The spaghetti plots provide a visualization of the dataset. Especially for the pair 3-4, the difference in tumor growth kinetics is noticeable from this plot. Using nonlinear mixed effects modeling, we estimated the parameter k (considered fixed in each couple of groups) and the distribution of the parameter β . The prediction distributions in Fig 2.8 assess the goodness of fit of the reduced Gompertz model. Eventually, the t-test was used to evaluate the differences in the distribution of the parameter β between the two groups. In the two cases, the estimated p -value was small, suggesting a significant difference within the subgroups in each pair.

These results are relevant for our collaborators to quantify difference in tumor growth kinetics.

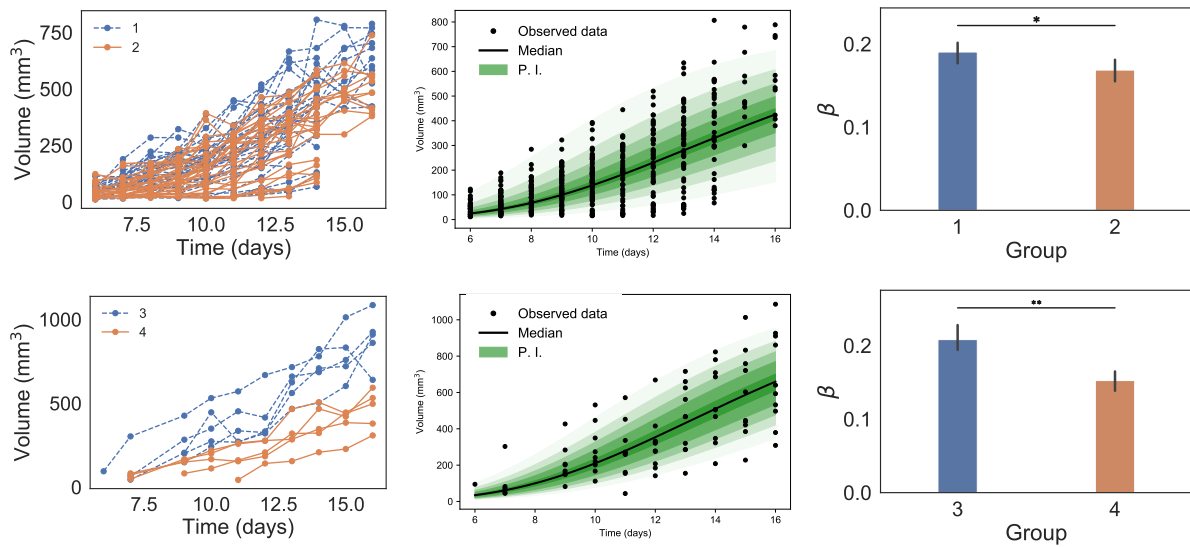


Figure 2.8. Test between groups 1-2 (first row) and groups 3-4 (second row): spaghetti plot (*left*) with the individual tumor growth data; prediction distribution (*middle*) obtained by the nonlinear mixed effects modeling analysis; distribution of the parameter β in the groups (*right*) with the result from the t-test. * means that the p-value was less than 0.05 and ** means that the p-value was less than 0.01.

2.8 Conclusion

To conclude this chapter, we have defined a novel reduced Gompertz model in the statistical framework of nonlinear mixed-effects modeling. It consists of a parameterization of the Gompertz model with one population-specific parameter and an animal-specific parameter. Besides the good performances in fitting tumor growth data of different cancer types, this new model has higher predictive power than the classical Gompertz model since it requires only one parameter to estimate. Moreover, it is a promising tool to assess differences in tumor growth kinetics between subgroups of a population. Indeed, models with only one individual-specific parameter are preferable for this type of analysis. Among these models, we have considered the exponential and the reduced Gompertz. The latter was found to have much superior descriptive power.

EVALUATION OF THE NANOPARTICLE DOSE-RESPONSE RELATIONSHIP: *in vitro* STUDIES

Abstract. *In vitro* experiments are the first step to evaluate the cellular response to a drug. In the case of nanoparticles, they are carried out on cell cultures that have been isolated from their usual biological context. These simplified systems - that exclude the complexity associated with all living organisms - permit to identify the interactions between components, such as drug molecules and cells. Here, we compare the *in vitro* efficacy of immunoliposomes, liposomes and free drugs on different breast cancer cell lines using mathematical modeling. In particular, we fitted experimental data to the Hill function, which describes the ligand-receptor interactions. Results obtained from this analysis provide important information that can be integrated into mathematical models to simulate the response of more complex systems.

Contents

3.1	Introduction	59
3.2	Material and methods	60
3.2.1	Experimental <i>in vitro</i> data	60
3.2.2	Derivation of the Hill function	61
3.2.3	Model calibration: nonlinear regression	63
3.3	Results	63
3.4	Discussion	63

3.1 Introduction

Nanoparticle antiproliferative efficacy depends on the biochemical behavior at the cellular level. However, the complexity related to all living organisms impairs to evaluate interactions of specific components *in vivo*. This is the reason why *in vitro* cell cultures are used to first investigate their response when they are subject to a drug.

Here, we used the Hill equation [158] to describe the biochemical behavior of 2D breast cancer cell cultures that were treated with different drugs [3]. In particular, we investigated the antiproliferative efficacy of docetaxel, docetaxel combined with trastuzumab and two kinds of liposomal formulations that differ by their chemical composition. Experiments were carried out on three different breast cancer cell lines, according to the expression of the Her2 receptor, namely SKBR3 (Her2++), MDA-MB-453 (Her2+) and MDA-MB-231 (Her2-).

The Hill equation has been extensively used to describe physicochemical reactions [159], such as enzyme kinetics [160] (Michaelis-Menten equation). In pharmacological modeling, it has been proposed first by Wagner to investigate the drug concentration-response relationship [161]. Later, it has been extensively used in pharmacokinetic-pharmacodynamic modeling to characterize the drug response when it is nonlinear and saturable [162, 163, 159].

The Hill function is widely accepted in the pharmacological community as it is simple and provides good fits to experimental data. However, other models present in the literature characterize the effect of a drug. The E_{\max} model, is the simplest model which describes the effect E of a drug as a function of the concentration c [164]:

$$E = E_0 \pm \frac{E_{\max}c}{Ec_{50} + c}, \quad (3.1)$$

where E_0 is the baseline, E_{\max} is the maximum effect of the drug and Ec_{50} is the concentration corresponding to the half of E_{\max} . However, the E_{\max} model is not able to describe the dose-response relationship of each drug. The Hill equation was then derived starting from the E_{\max} model and adding a new parameter γ that represents the number of binding molecules to a receptor [158]:

$$E = E_0 \pm \frac{E_{\max}c^\gamma}{Ec_{50}^\gamma + c^\gamma}. \quad (3.2)$$

The Hill model has been proven to describe a larger variety of drug responses. Indeed, when $\gamma = 1$, the equation reduces to the hyperbolic E_{\max} model, while if γ is different than one, the curve becomes sigmoid. More complex models can be defined to describe the effect of the combination of multiple drugs [159].

Nonlinear regression was used to calibrate the Hill function using *in vitro* data. This methodology allowed to estimate the parameters relative to the cytotoxic activity of different treatments and to compare them. In this Chapter, we focused on the *in vitro efficacy* of the ANCs, liposomes plus free trastuzumab and free drugs (free docetaxel plus free trastuzumab) on three cell lines that differ for the expression of the Her2 receptor expression. In section 3.2, we explain the material and methods. In particular, we derive the Hill function highlighting its mechanistic properties in section

3.2.2. Moreover, the different nonlinear regression techniques that have been adopted as well as their computation in sections C.1-C.2. Results of the data fit are shown in detailed in appendix C. Eventually, we draw the conclusions in section 3.4.

Importantly, the Hill model has been shown to have great descriptive power and to provide mechanistic insights in the setting of physicochemical equilibrium [159]. Data fit to the Hill equation specifies information on the nanoparticle-cell interactions that can be integrated in other models to make predictions of the drug response in complex organisms.

3.2 Material and methods

3.2.1 Experimental *in vitro* data

In vitro experimental details are provided in [3]. Here, we provide a concise description of the data and techniques. The *in vitro* experiments were carried out on the MDA-MB-231, SKBR3 and MDA-MB-453 cell lines. The cells were treated with different combination of drugs or nanoparticles:

- docetaxel: injection of the cytotoxic agent only,
- docetaxel + trastuzumab: injection of the chemotherapy combined with the monoclonal antibody,
- empty ANC-1: injection of the stealth immunoliposome without docetaxel,
- liposome 1 + free trastuzumab,
- ANC-1: injection of the stealth immunoliposome with trastuzumab engrafted on the surface,
- empty ANC-2,
- liposome 2 + free trastuzumab,
- ANC-2.

ANC-1 and liposome-1 differed from ANC-2 and liposome-2 for the chemical composition. The former were made of natural lipids and the latter were made of synthetic lipids.

The 2D *in vitro* experiments were conducted on a monolayer well plate for each treatment-group. Different concentrations of docetaxel and trastuzumab were tested and the efficacy was compared to the control. The MTT assay (3-(4,5-dimethylthiazol-2-yl)-2,5-diphenyltetrazolium bromide) was applied to measure the cell viability. This method is a colorimetric assay that reflects the metabolic activity of the cells: after adding a solubilization solution, the alive cells become pink and the dead ones become blue. Then, the spectrophotometer measures the wavelength of the absorbance of the solution. Finally the wavelength relative to each concentration is normalized with respect to the control cells.

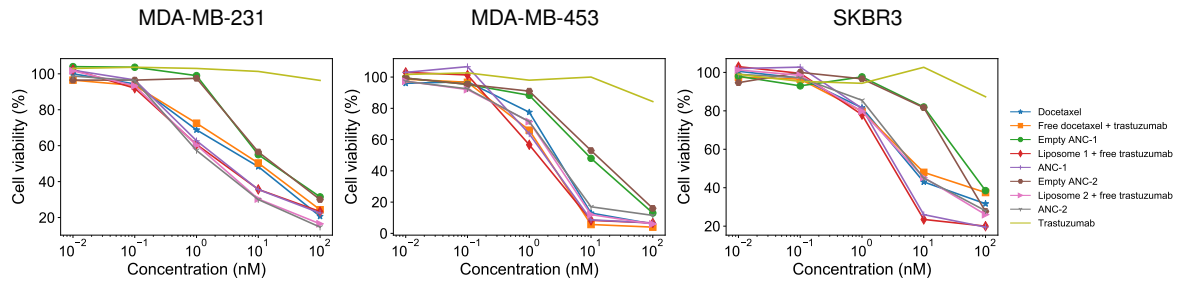


Figure 3.1. Cell viability as function of the docetaxel concentration with respect to the different treatments. Cell lines differ for the expression of the Her2 receptors: MDA-MB-231 cell line (left), MDA-MB-453 cell line (center), SKBR3 (right).

3.2.2 Derivation of the Hill function

We now consider the Hill function, that was introduced by Hill in 1910 to describe the binding of oxygen to hemoglobin [158]. Then, the theory has been extended to describe the interaction between ligands and receptors in the fields of biochemistry, physiology and pharmacology. The Hill function has been widely used in the context of pharmacodynamics in order to describe the drug effect on targeted receptors. We derive the model according to the occupancy theory, that states that the drug binds to the receptor and induces the receptor activation and that the pharmacological effect is proportional to the number of receptor sites occupied by drug [165, 166]. We make use of the following notation:

- R is the receptor; the receptor concentration is $r(t) = [R]$;
- C is the drug molecules; $c(t) = [C]$ is the drug concentration;
- γ is the number of drug molecules C binding to one receptor R ;
- $R_{\gamma C}$ is the drug-receptor complex; $v(t) = [R_{\gamma C}]$ is the drug-receptor complex concentration;
- E or $E(t)$ is the pharmacological effect;
- k_{on} , k_{off} are the association and dissociation rate constants, respectively, and k_2 is a proportionality constant.

The following equation describes the drug-receptor reaction:



where \rightleftharpoons denotes a reversible reaction, while \rightarrow indicates that the reaction goes in one way only. We are interested in determining an equation that describes the trend of the concentration of the drug-receptor complex with respect to the drug concentration.

In (3.3a) k_{on} and k_{off} are rate constants that characterize the association and dissociation of the complex, respectively. According to the law of mass action, the rate of a reaction is proportional to the product of the concentrations of the reactants. Therefore, the law of mass action applied to the reaction (3.3a) gives the following ordinary equation

$$\begin{cases} \frac{dv(t)}{dt} = k_{\text{on}}r(t)c^\gamma(t) - k_{\text{off}}v(t), \\ v(0) = 0. \end{cases} \quad (3.4)$$

Moreover, we assume that the total concentration of R , free plus combined, is constant. This conservation law implies that

$$\frac{dr}{dt} + \frac{dv}{dt} = 0 \quad \Rightarrow \quad r(t) + v(t) = r_0 \quad (3.5)$$

Combining (3.4) with (3.5) we obtain

$$\begin{cases} \frac{dv(t)}{dt} = k_{\text{on}}c^\gamma(t)[r_0 - v(t)] - k_{\text{off}}v(t), \\ v(0) = 0. \end{cases} \quad (3.6)$$

We now assume that the formation of the complex $R_\gamma C$ is very fast, so that it is at equilibrium, i.e. $dv/dt = 0$:

$$\bar{v} = \frac{r_0 \bar{c}^\gamma}{k_D + \bar{c}^\gamma}, \quad (3.7)$$

where \bar{v} and \bar{c} are, respectively, the drug and the drug-receptor complex concentrations at the equilibrium and $k_D = k_{\text{off}}/k_{\text{on}}$ is called dissociation constant of the complex.

In (3.3b), k_2 is a proportionality constant characterizing the pharmacological effect $E(t)$ with respect to the drug-receptor complex concentration $v(t)$:

$$E(t) = k_2 v(t). \quad (3.8)$$

When the total number of receptors is occupied, the effect is maximal:

$$E_{\text{max}} = k_2 r_0. \quad (3.9)$$

Combining equations (3.7) and (3.9) we obtain the sigmoid model, that describes the pharmacological effect at the equilibrium \bar{E} :

$$\bar{E} = \frac{E_{\text{max}} \bar{c}^\gamma}{k_D + \bar{c}^\gamma}. \quad (3.10)$$

In the pharmacodynamic models usually the constant k_D is substituted by Ec_{50}^γ , where Ec_{50} is the concentration at half the maximal effect.

Moreover, it is possible to introduce a baseline E_0 , obtaining

$$\bar{E} = E_0 \pm \frac{E_{\text{max}} \bar{c}^\gamma}{Ec_{50}^\gamma + \bar{c}^\gamma}. \quad (3.11)$$

Equation (3.11) is an empirical model that describes either stimulation or inhibition of the effect with respect to the concentration of the drug.

3.2.3 Model calibration: nonlinear regression

The methodology employed to calibrate the model with the *in vitro* data are detailed in Appendix C, in particular in Sections C.1 and C.2. In general, we used the Nelder-Mead algorithm to maximize the likelihood function and ran a Python code to obtain the best estimates. For each drug on each cell line, we tested the descriptive power of the Hill function with (i) two parameters to estimate (Ec_{50} and γ , with $E_{\max} = 1$) and (ii) three degrees of freedom (Ec_{50} , γ and E_{\max}) and compared the two formulations with the likelihood ratio test. This methodology allowed to understand which set of parameters could better describe the data.

3.3 Results

Results are detailed in Sections C.3, C.4 and C.5 for the MDA-MB-231, SKBR3 and MDA-MB-453 cell lines, respectively. All the liposomal formulations showed similar cytotoxic activity *in vitro* on the three cell lines. Here, we summarize the results relative to the *in vitro* antiproliferative efficacy of the ANC-1, liposome-1 plus free trastuzumab and free drugs.

Globally, the Hill function could describe the different treatments apart from trastuzumab when administered alone, which did not show antiproliferative activity. The model with three parameters to estimate (namely, Ec_{50} , γ and E_{\max}) provided the best description of the ANC-1 and liposome-1 plus free trastuzumab for the MDA-MB-231 and SKBR3 cell lines. The cytotoxicity of the free drugs was better described when fixing $E_{\max} = 1$. However, for the MDA-MB-453 cell line, results showed better estimates fixing $E_{\max} = 1$ when any of the three treatments was administered.

The comparison of the treatments is shown in Figure 3.2 on the different cell lines. In the three cell lines, the cell viability showed similar trends when ANC-1 or liposome-1 plus free trastuzumab were administered. Free drugs behaved differently compared to the nanoparticles in the MDA-MB-231 and SKBR3 cell lines. Indeed, the estimated Ec_{50} was larger for the free drugs than for the nanoparticles, as shown in Table 3.1.

3.4 Discussion

The Hill equation allowed us to quantify the nanoparticle efficacy *in vitro* and to compare it to the cytotoxic behavior of the traditional free drugs. We observed that the Hill function with three degrees of freedom described better the behavior of the liposomes, in particular of ANC-1 and liposome-1 plus free trastuzumab. Hence, the cell viability does not tend to zero when the concentration tends to infinite, but there is a plateau corresponding to E_{\max} . This could be due to several effects. First of all, there is uncertainty in the experimental evaluation for low values of cell viability (i.e. < 20%). Moreover, it is possible that the nanoparticles do not diffuse around the cells and, therefore, that the cell viability for high concentrations of the drug is lower when the drug is free than when it

Cell line	Drug	Parameter	Value	R.S.E.(%)
MDA-MB-231	ANC-1	Ec_{50}	1.188	18.456
		γ	0.983	15.585
		E_{max}	0.758	4.084
	Liposome-1 + free trastuzumab	Ec_{50}	1.031	25.488
		γ	0.867	19.144
		E_{max}	0.764	5.334
	Free drugs	Ec_{50}	9.528	31.903
		γ	0.490	14.987
		E_{max}	1	-
MDA-MB-453	ANC-1	Ec_{50}	1.543	14.494
		γ	1.433	21.543
		E_{max}	1	-
	Liposome-1 + free trastuzumab	Ec_{50}	1.274	12.131
		γ	1.318	19.396
		E_{max}	1	-
	Free drugs	Ec_{50}	1.547	10.830
		γ	1.433	11.504
		E_{max}	1	-
SKBR3	ANC-1	Ec_{50}	2.065	25.018
		γ	1.672	28.418
		E_{max}	0.800	5.154
	Liposome-1 + free trastuzumab	Ec_{50}	1.734	26.757
		γ	1.763	40.958
		E_{max}	0.800	5.261
	Free drugs	Ec_{50}	17.917	31.569
		γ	0.471	13.239
		E_{max}	1	-

Table 3.1. Best estimates of the Hill model parameters of the ANC-1, liposome-1 plus free trastuzumab and free drugs (free docetaxel plus trastuzumab) on the three different cell lines. Ec_{50} is expressed in nM, while γ and E_{max} are dimensionless parameters. R.S.E.= relative standard error.

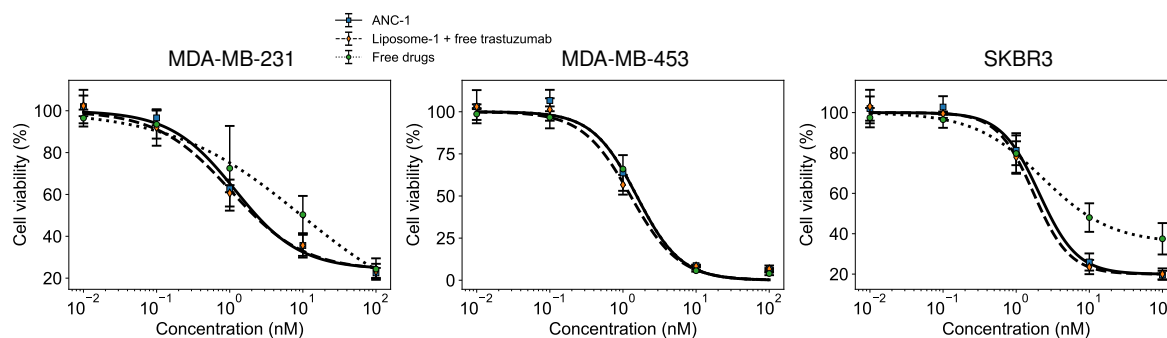


Figure 3.2. Best fit of the Hill function plotted against *in vitro* data as function of the docetaxel concentration: cell viability of the three different cell lines when treated with ANC-1, liposome-1 plus free trastuzumab or free drugs (free docetaxel + free trastuzumab).

is encapsulated into the immunoliposomes. In order to address this issue, 3D *in vitro* experiments might help in understanding the propagation of the nanoparticles in the tissue.

The *in vitro* analysis was performed to compare the cytotoxicity of the different drugs, as provided in Appendix C. No large difference was observed in efficacy between the liposomal formulations when administered *in vitro*. However, ANCs and liposomes showed equal or higher efficacy *in vitro* compared to the free drugs, regardless of the Her2 expression on the cell lines. Indeed, the estimated EC_{50} of the different nanoparticles was equal or lower than EC_{50} of the free drugs.

Although the efficacy of the two immunoliposomes was similar, ANC-1 showed larger encapsulation rate of docetaxel and stability (i.e., limited leakage of docetaxel, conservation of the original shape and trastuzumab engraftment) than ANC-2 [39]. Hence, ANCs-1 were further tested *in vivo* to evaluate the pharmacokinetics and pharmacodynamics. In the remaining part of the thesis, we denote by ANC the immunoliposomes that have the same composition of ANC-1. Furthermore, the liposomal formulation of docetaxel considered for the *in vivo* studies corresponds to liposome-1.

In vitro studies provide insights on the nanoparticle-cell interactions. For instance, the association, dissociation and internalization rates drive cell metabolism and drive the efficacy of the treatment. These parameters could be integrated into pharmacokinetic-pharmacodynamic models to analyze *in vivo* the drug cytotoxicity. Moreover, they can be used to calibrate models of nanoparticle transport in the tumor interstitium to describe the cellular binding and uptake of the nanoparticles. To this end, specific *in vitro* experiments could provide information on the binding sites of the nanoparticles, as well as the binding affinity of the drug [53, 52].

In vivo

PHARMACOKINETIC-PHARMACODYNAMIC MODELING OF LIPOSOMES AND IMMUNOLIPOSOMES

Abstract. Pharmacokinetic-pharmacodynamic modeling (PKPD) is based on mathematical expressions that allow a quantification of the dose-response relationship of drugs. Pharmacokinetic models describe at the macroscopic scale how the organs in the body affect the drug delivery to the tumor through the mechanisms of absorption, distribution, metabolism and excretion. Pharmacodynamics describes of the efficacy of the nanoparticles. In this chapter, we performed an analysis of ANCs and liposomes injected with free trastuzumab. A two-compartmental PK model allowed us to evaluate the biodistribution of the two nanoparticles. Furthermore, a resistance model was used to compare the efficacy of different treatments. The experimental data involved the MDA-MB-231 breast cancer cell line, which does not show overexpression of the Her2 receptor.

Contents

4.1	Introduction	69
4.2	Biodistribution and tumor growth data	70
4.3	Mathematical modeling and calibration	72
4.3.1	Two-compartment PK model	72
4.3.2	PKPD modeling	73
4.4	Results	75
4.4.1	PK modeling	75
4.4.2	PKPD modeling	79
4.4.3	Applications to dose optimization	79
4.5	Discussion	81

4.1 Introduction

Pharmacokinetic-pharmacodynamic modeling is fundamental in the drug delivery system development [167]. It permits to quantify the pharmacokinetics (PK), pharmacodynamics (PD) and their relationship using mathematical models [168]. PK describes the absorption and distribution of the drugs and PD evaluates the efficacy of the drugs.

Pharmacokinetic (PK) models can be noncompartmental or compartmental. The latter estimate the drug exposure by computing the area under the curve of the concentration as function of time, without providing a description of the drug kinetics. On the other hand, compartmental models are based on the empirical assumption that the body can be decomposed into compartments (i.e., organs or tissues), namely a central one that is connected to one or more peripheral compartments. A system of ordinary differential equations defines the nanoparticle concentration in each compartment and their coupling. The parameters of the model might include for example the clearance, the tumor uptake and the elimination and can be determined by fitting plasma concentration data. Nonlinear mixed-effects modeling is an ideal statistical framework to estimate the population parameters, as it provides a description of the global dynamics as well as the inter-individual variability within a dataset. Several mathematical models have been used to describe the bioavailability of nanoparticles at the tumor site. For exhaustive reviews, we refer to [37, 43]. A one-compartment model has been employed to evaluate differences between active and passive targeting of nanoparticles in tumor accumulation [169]. When intravenously injected, nanoparticle concentration in plasma might show a biphasic decrease [170], suggesting a two-compartment model. Three compartment models have also been considered to estimate tumor vascular permeability and nanoparticle retention in tumors [171].

Compartmental PK models are the most used to describe drug biodistribution, to estimate pharmacokinetic parameters and to test different dose and schedules [172]. They are fundamental to translate the preclinical studies into the clinics. A further class of more complex models is represented by physiologically based pharmacokinetic (PBPK) models. They take into account physiological mechanisms, providing a more realistic description of the impact of the whole body in the drug biodistribution. The first PBPK models of nanoparticles are quite recent [173, 174] and are based on models originally developed for free drugs. In [175] the authors investigate a compartmental PBPK model for nanoparticles. It is a mechanistic model that describes the whole-body nanoparticle biodistribution and the *in vivo* tumor uptake. Mechanistic models have been employed to study the PK of antibody-drug conjugates in breast cancer treatment, such as trastuzumab emtansine (T-DM1), that is a drug consisting in a chemical combination of a monoclonal antibody (trastuzumab) and a cytotoxic agent (maytansinoid antitubulin agent DM1) [176]. Singh *et al.* used a two-compartmental model with linear elimination from the central compartment to describe the biexponential profile of both trastuzumab and T-DM1. Importantly, Cilliers *et al.* developed a detailed PBPK model that was able to study the impact of the drug-antibody ratio on the tumor penetration [177].

Optical fluorescence imaging is a technique of rising interest to monitor *in vivo* nanoparticle

biodistribution. Kumar *et al.* conjugated silica nanoparticles with near-infrared fluorophore to analyze NP biodistribution, clearance and toxicity [178]. Furthermore, this methodology has been proven to be ideal to perform pharmacokinetic analysis of different nanoparticle designs, such as to investigate shape, size and active vs passive targeting [179, 169].

Pharmacokinetic-pharmacodynamic modeling is used to quantify the relationship between dose, drug exposure and response. The efficacy of the therapies can be described by ordinary differential equations that evaluate the net growth rate and the drug-induced decay [180].

Here, we investigated a two-compartmental model that describes the nanoparticle exchange between the systemic and the tumor compartments. Our model was tested on two datasets with two different administration schedules and on two nanoparticles, namely the ANCs and the liposomes injected with trastuzumab. *In vivo* biodistribution of nanoparticles was tracked with fluorescence imaging. Moreover, we employed a resistance model to describe the efficacy of nanoparticles. The model was calibrated against *in vivo* tumor growth data.

Further applications of PKPD modeling include the translation of preclinical studies to the clinics, optimization of therapeutic scheduling and clinical trials [181].

4.2 Biodistribution and tumor growth data

In vivo nanoparticle distribution was tracked in time using fluorescence imaging. Optical imaging is a fast and non-invasive approach that has been proved to be able to monitor nanoparticle amount in the tumor and in the body [179, 169].

Low dose

8-weeks old female nude mice (Charles River, France) were orthotopically grafted (mammary fat pad) with 80 000 MDA-MB-231 Luc+ dTomato+ cells in 60% matrigel. Here, we consider the group of animals treated with ANC (n = 12 mice) and the group that received liposomal docetaxel with free trastuzumab (n = 10 mice). Treatments started 13 days after tumor implantation. Docetaxel and trastuzumab were administered at 1.3 mg/kg and 0.5 mg/kg once a week for 5 consecutive weeks. Localization and quantification of DiR-fluorescent nanoparticles in tumors were tracked weakly using spectral unmixing.

Since the injected dose of drugs was low, no efficacy was observed on tumor growth. Therefore, this dataset was used only for the pharmacokinetic study.

High dose

All the experiment details are provided in [76]. Distribution studies were performed on MDA-MB-231 bearing mice. 6-week-old female nude mice were orthotopically grafted (mammary fat

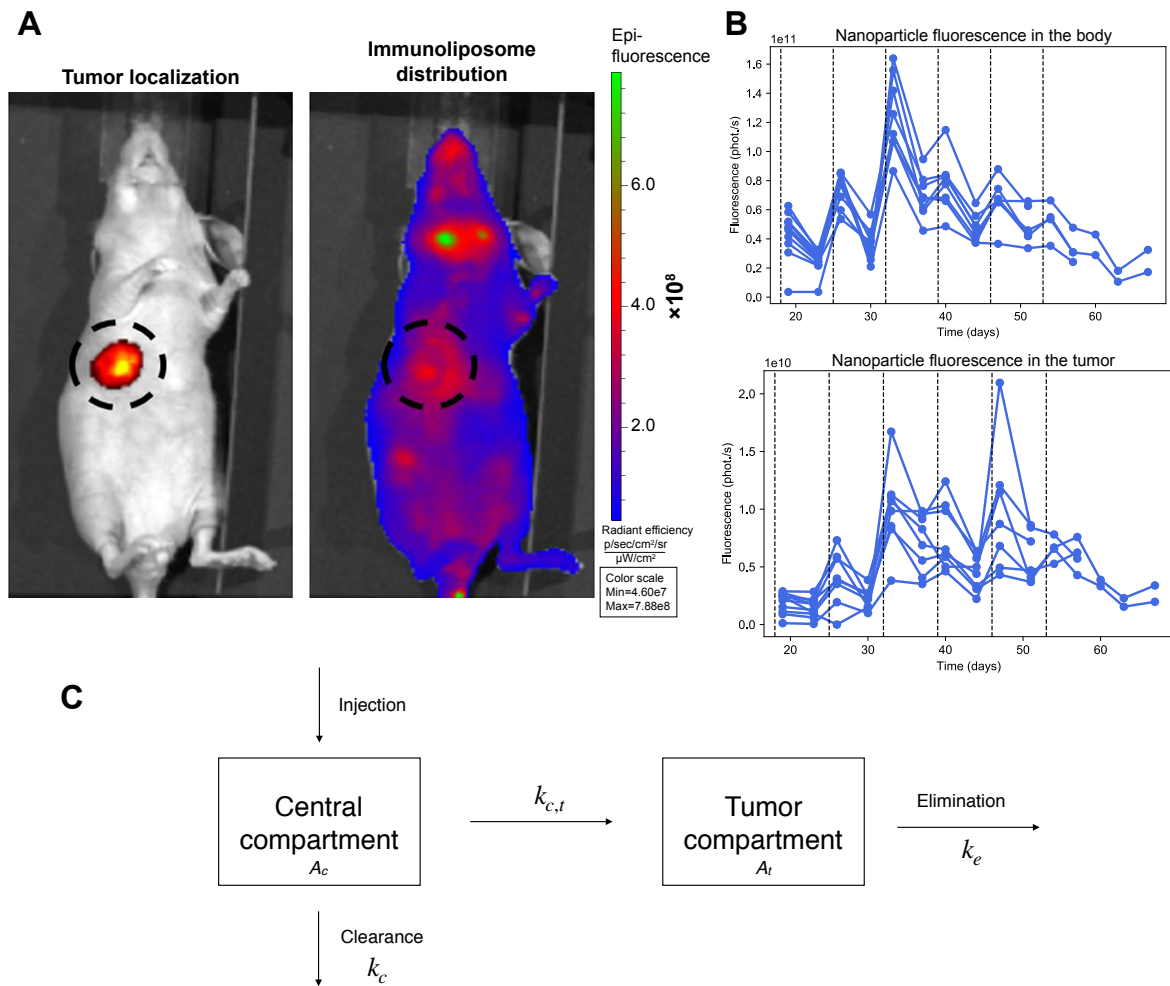


Figure 4.1. Pharmacokinetic analysis: data and model. (A) Example of fluorescence imaging to quantify immunoliposome accumulation in tumors: tumor localization and nanoparticle distribution in the entire body. Figure from [76]. (B) Example of the spaghetti plot of the nanoparticle distribution in the entire body (top) and in the tumor (bottom). Vertical black dotted lines correspond to the days of nanoparticle administration. The dataset corresponds to the ANC group with high dose of docetaxel. (C) Schematic of the two-compartment model used for the pharmacokinetic analysis: The nanoparticle amounts in the central and in the tumor compartments are denoted, respectively, by A_c and A_t . The injected dose enters into the central compartment. The parameter $k_{c,t}$ drive the nanoparticle exchange between the tumor compartment and the central compartment. Nanoparticles are eliminated by the body with a clearance rate k_c and by the tumor with a rate k_e .

Group	Drug	Day 18	Day 25	Day 32	Day 39	Day 46	Day 53
ANC	Docetaxel	3.3	5	5	5	5	3
	Trastuzumab	1.3	1.9	1.9	1.9	1.9	1.15
Liposome + free trastuzumab	Docetaxel	5	5	5	5	5	5
	Trastuzumab	1.9	1.9	1.9	1.9	1.9	1.9

Table 4.1. Treatment scheduling of ANCs and liposomes plus free trastuzumab in the high-dose experiment. Dose is given in (mg/kg).

pad) with 80,000 MDA-MB-231 cells in 60% Matrigel. After 18 days, mice were divided into groups according to the treatment. Here, we consider mice treated with ANC ($n = 10$ animals) and liposomal docetaxel + free trastuzumab ($n = 10$ animals) to analyze the both the pharmacokinetics and pharmacodynamics, and mice treated with free docetaxel plus free trastuzumab to compare the pharmacodynamics of three different therapies. Treatment administration occurred once a week over 6 consecutive weeks. Drug administration is detailed in Table 4.1. Localization and quantification of DiR-fluorescent nanoparticles in tumors were tracked weakly using spectral unmixing (see Figure 4.1A). Imaging was performed on an IVIS Spectrum imager equipped with Living Image 4.2.1 software. DiR-labeled nanoparticles were excited at 745 nm and emission was recorded from 780 to 840 nm. The spaghetti plot of the nanoparticle fluorescence of the ANC group is shown in Figure 4.1B.

Tumor growth was initially monitored using fluorescence imaging, while starting from day 44 caliper measurements were employed because of loss of dTomato expression *in vivo*.

4.3 Mathematical modeling and calibration

4.3.1 Two-compartment PK model

We grossly assumed that the body is composed of two compartments: the central compartment and the tumor. A schematic of the model is provided in Figure 4.1C. The injected dose D_i at day $t_{\text{adm},i}$ (for $i = 1, \dots, N_{\text{adm}}$, where N_{adm} is the total number of drug administration) enters into the systemic circulation, where nanoparticle amount is denoted by A_c . Here, nanoparticles are eliminated by the macrophages, liver, spleen and kidneys with a clearance rate k_c . Nanoparticle amount in the tumor is described by the variable A_t . The rate of nanoparticle tumor entry from the central compartment is denoted by $k_{c,t}$ and we assumed that NPs could not return in the vessels once they had extravasated into the malignant tissue. Moreover, nanoparticles might be cleared or uptaken by the tumor cells with a rate k_e . Denoting by K_F the conversion rate from mg/kg to fluorescence values, the system

of ordinary differential equations reads as

$$\frac{dA_c}{dt} = -k_c A_c - k_{c,t} A_c + \sum_i^{N_{\text{adm}}} \frac{D_i}{K_F} \delta_D(t - t_{\text{adm},i}), \quad A_c(0) = 0, \quad (4.1)$$

$$\frac{dA_t}{dt} = k_{c,t} A_c - k_e A_t, \quad A_t(0) = 0, \quad (4.2)$$

where δ_D is the Dirac delta function that satisfies $\delta_D(t \neq 0) = 0$ and $\int_{-\infty}^{\infty} \delta_D(t) dt = 1$.

Parameter estimation using nonlinear mixed effects modeling

The population approach is a particularly appropriate statistical framework to analyze pharmacokinetic data. Monolix 2019 R2 [156] was used to estimate the PK model parameter for each group of individuals.

Since docetaxel was the cytotoxic drug encapsulated in the nanoparticles, the injected dose D was calibrated based on the docetaxel administration. Trastuzumab dose was neglected in the PK model. Moreover, we assumed the conversion rate K_F and the tumor elimination rate k_e to have fixed values within the population, while all other parameters were assumed to have fixed and random effects within the population. Eventually, we assumed a proportional error model e_j^i for both observations in the central and tumor compartments, and denoted by σ_c and σ_t the error model parameters of the two compartments. Denoting by $\mathbf{Y}_j^i = [Y_{c,j}^i, Y_{t,j}^i]$ the vector of subject i at time t_j^i containing the observations of the nanoparticle fluorescence in the entire body $Y_{c,j}^i$ and in the tumor $Y_{t,j}^i$, we assumed the following observation model

$$\mathbf{Y}_j^i = \mathbf{A}(t_j^i; \boldsymbol{\theta}^i) + \mathbf{e}_j^i, \quad (4.3)$$

$$\mathbf{e}_j^i = \begin{bmatrix} \sigma_c A_c(t_j^i; \boldsymbol{\theta}^i) \varepsilon_j^i \\ \sigma_t A_t(t_j^i; \boldsymbol{\theta}^i) \varepsilon_j^i \end{bmatrix}, \quad (4.4)$$

where $\mathbf{A}(t_j^i; \boldsymbol{\theta}^i) = [A_c(t_j^i; \boldsymbol{\theta}^i) \varepsilon_j^i, A_t(t_j^i; \boldsymbol{\theta}^i) \varepsilon_j^i]$ is the vector of the solution of system (4.1)-(4.2) evaluated at time t_j^i , $\boldsymbol{\theta}^i$ is the vector of the parameters of individual i and $\varepsilon_j^i \sim \mathcal{N}(0, 1)$ is the residual error.

4.3.2 PKPD modeling

Two measurement types were used to monitor tumor growth. In particular, until day 30 tumor size was monitored with fluorescence imaging and starting from day 44 it was measured with caliper. Therefore, tumor growth data y_i^j of an individual i at time t_i^j is defined as

$$y_i^j = \begin{cases} y_{\text{fluo},i}^j, & t_i^j \leq 30, \\ y_{\text{cal},i}^j, & t_i^j \geq 44, \end{cases} \quad (4.5)$$

where $y_{\text{fluo},i}^j$ is the fluorescence signal and $y_{\text{cal},i}^j$ is the tumor volume measured with caliper. We denoted by K_{FV} the conversion rate from the fluorescence signal to the tumor volume (in $\text{mm}^3 \cdot (\text{phot./s})^{-1}$). In the following sections, we will denote the evolution of the tumor volume V in time

considering the two measurement types V_{fluo} (fluorescence) and V_{cal} (caliper) as follows

$$V(t) = \begin{cases} K_{FV} V_{\text{fluo}}(t), & t \leq 30, \\ V_{\text{cal}}(t), & t > 30. \end{cases} \quad (4.6)$$

The injected number of tumor cells was $V_{\text{inj}} = 0.08 \text{ mm}^3$.

Ordinary differential equations usually quantify the net growth and drug-induced decay process [180] and nonlinear mixed-effects modeling is used to calibrate the model. Here, we considered the reduced Gompertz model [79] to describe the unperturbed tumor growth and a first-order decay process to model the action of nanoparticles:

$$\frac{dV}{dt} = \left(k\beta^i - \beta^i \log\left(\frac{V}{V_{\text{inj}}}\right) \right) V - E(A_t(t))V, \quad (4.7)$$

where $E(A_t(t))$ is the NPs efficacy that is considered as a function of the drug exposure A_t (*i.e.*, the nanoparticle amount in the tumor interstitium). In (4.7), k is the population-level parameter and β^i is specific for each animal i . We used the parameters β , k and K_{FV} estimated in Section 2.6 to characterize the untreated tumor growth kinetics.

Drug-induced decay is often modeled as function of the drug exposure. The simplest model considers the drug efficacy e constant in time:

$$E(A_t(t)) = eK_F A_t(t), \quad (4.8)$$

where we considered the conversion of the fluorescence intensity of the nanoparticles $K_F A_t(t)$ in mg/kg.

To account for a progressive development of resistance, we assumed that the efficacy of the drug decreases exponentially in time according to λ_R [125]:

$$E(A_t(t)) = e_0 \exp\left(\frac{t - t_{0,\text{adm}}}{\lambda_R}\right) K_F A_t(t), \quad (4.9)$$

where e_0 is the initial drug effect (or drug potency) $t_{0,\text{adm}}$ is the day of the first administration.

The two models were calibrated using the tumor growth data of individuals treated with ANCs, liposomes plus free trastuzumab and free drugs. We used the two compartment PK model to evaluate the exposure A_t of the two nanoparticles, while we did not have data on the pharmacokinetic of free docetaxel. Hence, we assumed the exposure of free docetaxel to be equal to the plasma amount of docetaxel, which dynamic was described by a one compartment model:

$$\frac{dA_c}{dt} = -k_c A_c, \quad (4.10)$$

where the clearance rate k_c was fixed within the population to 2.24 days^{-1} [182].

Parameter estimation with nonlinear mixed effects modeling

We pooled together fluorescence and volume data to estimate tumor growth parameters. We employed a similar methodology to section 2.4.1. In this case, we assumed a proportional error model for both the fluorescence and the caliper measurements. Indeed, early observations of the caliper-

measured tumor volume were not available. The observation model reads as follows:

$$\begin{cases} y_{\text{fluo},i}^j = V_{\text{fluo}}(t^j; \boldsymbol{\theta}) + \sigma_{\text{fluo}} V_{\text{fluo}}(t^j; \boldsymbol{\theta}) \varepsilon_j^i, \\ y_{\text{cal},i}^j = V_{\text{caluo}}(t^j; \boldsymbol{\theta}) + \sigma_{\text{cal}} V_{\text{cal}}(t^j; \boldsymbol{\theta}) \varepsilon_j^i, \end{cases} \quad (4.11)$$

where $\boldsymbol{\theta}$ is the set of parameters of the tumor growth model $V(t)$, σ_{fluo} and σ_{cal} are the error model parameters, and $\varepsilon_j^i \sim \mathcal{N}(0, 1)$ is the residual error.

Due to the large number of degrees of freedom, the error model parameter of caliper data σ_{cal} was fixed to 0.17, which was the estimated value for the reduced Gompertz model in Table 2.3.

4.4 Results

4.4.1 PK modeling

We considered the data of the four groups of individuals (treated with ANC or liposomal docetaxel plus free trastuzumab, at low and high concentrations) and used `Monolix 2019 R2` to fit the PK model and estimate the parameters.

Diagnostic plots of the low-dose groups are shown in Figure 4.2. The visual predictive check (VPC) of the central compartment of the ANCs data set (Figure 4.2A, left) shows that the model provides good fits in the central compartment at the first three injections (until day 34). Indeed, the predicted percentiles in the central compartment overestimate the empirical percentiles after day 34. However, the predicted percentiles in the VPC of the tumor compartment (Figure 4.2B, left) were found to be close to the empirical percentiles. The prediction distributions of the two compartments (Figure 4.2A-B, center) covered the data set, apart from the latest data points. Moreover, the observations versus predictions (Figure 4.2A-B, right) were symmetrically distributed around the bisector. Liposomes plus free trastuzumab (Figure 4.2C-D) provided good fits until the last injection (day 34).

Diagnostic plots of the high-dose groups are shown in Figure 4.3. ANCs provided good fits apart from the third and the last injection (Figure 4.3 A-B). On the other hand, the model was not able to catch the liposomal PK, since data show an exponential decreasing profile starting from the second injection.

Parameter estimates are provided in Table 4.2. Good parameter identifiability was found in the analysis. We observed that the value of the parameter $k_{c,t}$ was similar in the ANC-low-dose and ANC-high-dose groups and larger in the ANC groups than in the liposome groups. Moreover, low values of the clearance rate k_c were found in the four groups. Eventually, the tumor clearance rate k_e was found slightly larger for ANCs than for liposomes, implying a more rapid elimination of the immunoliposomes by the tumor compartment.

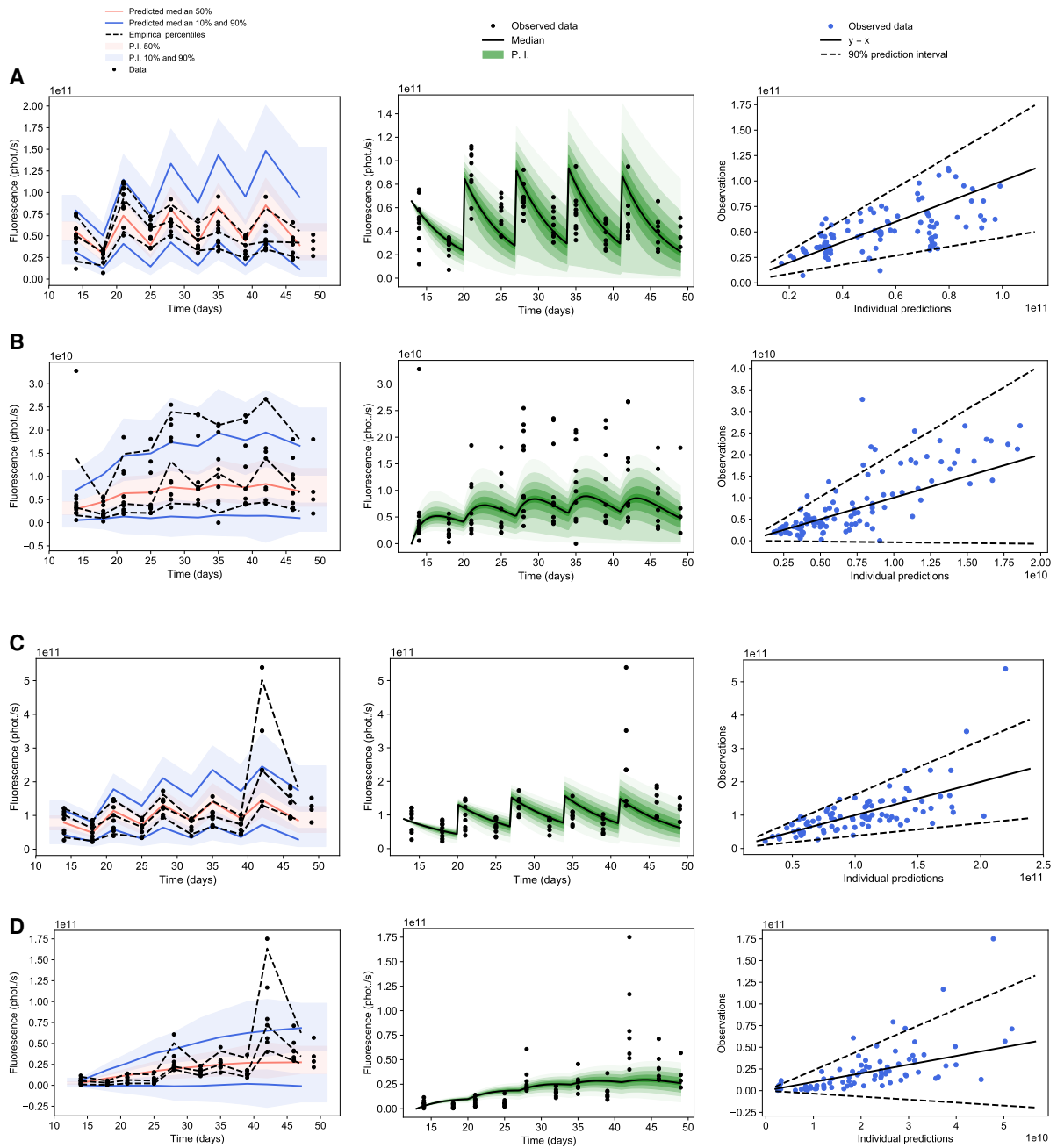


Figure 4.2. Low dose data sets - diagnostic plots obtained with Monolix: visual predictive checks (first column), prediction distribution (second column) and observations versus predictions (third column). (A) and (B) are the results of the ANC group in the central and tumor compartment, respectively. (C) and (D) are the results of the liposome + free trastuzumab in the central and tumor compartment, respectively.

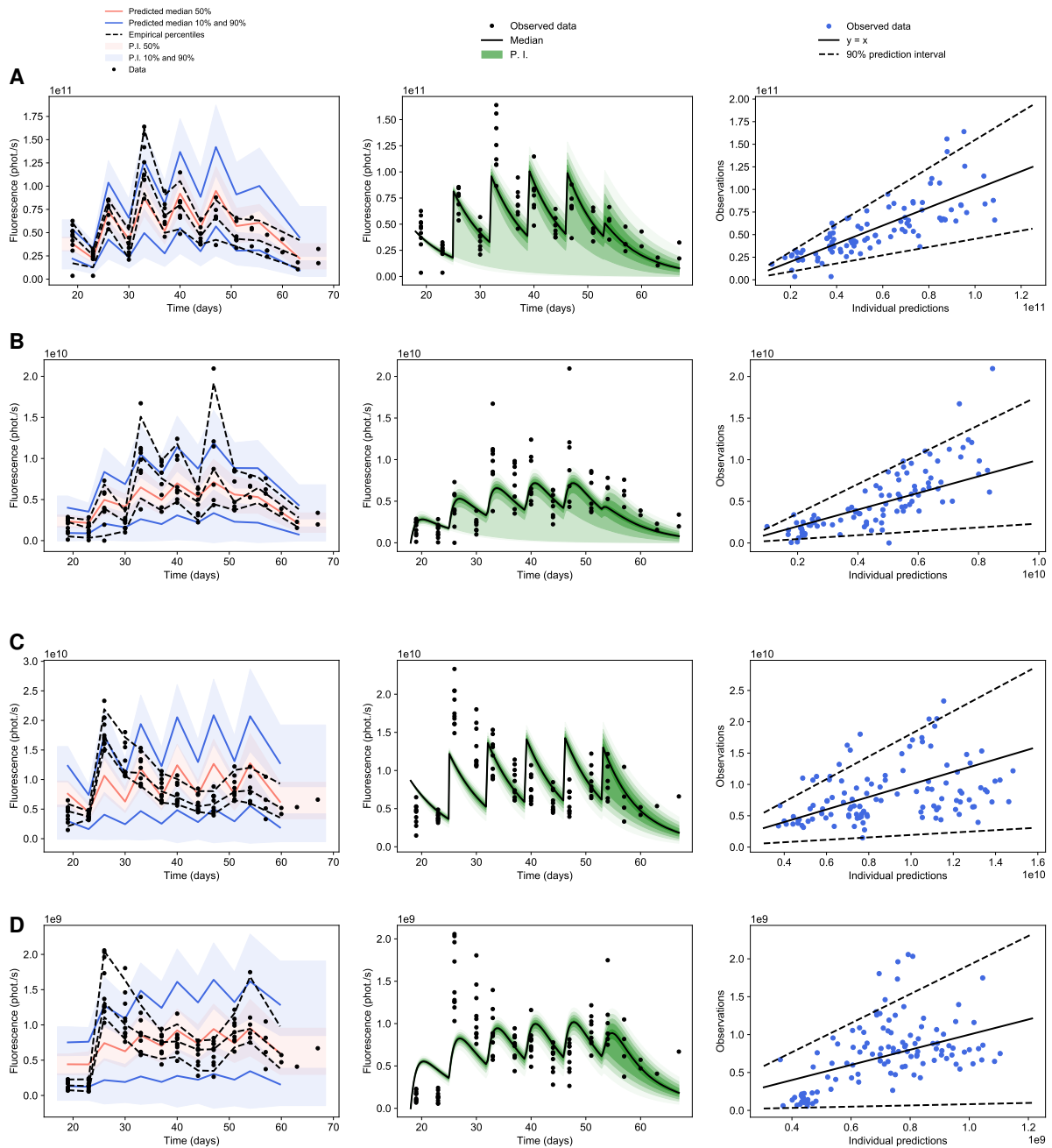


Figure 4.3. High dose data sets - diagnostic plots obtained with Monolix: visual predictive checks (first column), prediction distribution (second column) and observations versus predictions (third column). (A) and (B) are the results of the ANC group in the central and tumor compartment, respectively. (C) and (D) are the results of the liposome + free trastuzumab in the central and tumor compartment, respectively.

Data set	Parameter	Fixed effects	ω	R.S.E. (%)
ANC, low dose	K_F	1.98e-11	-	5.3
	$k_{c,t}$	0.0669	0.45	16.9
	k_c	0.0706	0.855	32.6
	k_e	0.489	-	11.2
	σ_c	0.337	-	8.04
	σ_t	0.63	-	10.3
Liposome, low dose	K_F	1.48e-11	-	7.71
	$k_{c,t}$	0.0363	0.142	20.8
	k_c	0.0648	0.72	31.6
	k_e	0.131	-	28.4
	σ_c	0.377	-	8.85
	σ_t	0.817	-	12.1
ANC, high dose	K_F	7.67e-11	-	5.1
	$k_{c,t}$	0.1	0.206	9.25
	k_c	0.0212	0.785	64.5
	k_e	1.17	-	2.37
	σ_c	0.333	-	8.17
	σ_t	0.466	-	9.22
Liposome, high dose	K_F	5.77e-10	-	7.82
	$k_{c,t}$	0.0867	0.067	7.15
	k_c	0.038	0.526	38.3
	k_e	1	-	0.085
	σ_c	0.49	-	8.14
	σ_t	0.558	-	8.56

Table 4.2. Parameter estimates of the PK model obtained with the nonlinear mixed effects modeling. K_F is expressed in $\text{mg}/\text{ks} \cdot (\text{phot.}/\text{s})^{-1}$, while $k_{c,t}$, k_c and k_e are all expressed in day^{-1} . σ_c and σ_t are the dimensionless error model parameters of the central and tumor compartments, respectively. ω = standard deviation of the random effects. R.S.E. = relative standard errors of the estimates.

Group	Parameter	Fixed Effects	ω	R.S.E (%)
ANC	e_0	0.27	1.12	15.8
	λ_R	19.5	0.698	42.7
	σ_{fluo}	0.383	-	21.6
Liposome + free trastuzumab	e_0	0.305	0.468	14.6
	λ_R	13.4	0.639	26
	σ_{fluo}	0.464	-	19
Free drugs	e_0	0.157	0.318	38.3
	λ_R	20.7	1.66	17.2
	σ_{fluo}	0.405	-	18.1

Table 4.3. Resistance model: estimated parameters of the ANCs, the liposomes plus free trastuzumab and free drugs (free docetaxel plus free trastuzumab). σ_{fluo} is the dimensionless error model parameter of the fluorescence data. ω = standard deviation of the random effects. R.S.E. = relative standard errors of the estimates.

4.4.2 PKPD modeling

Drug-induced decay of ANCs, liposome+free trastuzumab and free drugs (free docetaxel plus free trastuzumab) was studied fixing the distributions of the parameters relative to the net tumor growth (β and k) and the fluorescence conversion parameter K_{FV} .

First, the efficacy model in (4.8) was tested, but it failed in describing the dataset (results not shown). Indeed, constant efficacy might be not realistic. Then, the resistance model in (4.9) was considered and showed better fits than (4.8). Diagnostic plots are shown in Figure 4.4. Good individual fits of the caliper data were observed in the ANC, liposome and free drugs groups. Moreover, the resistance model could describe the rescaled fluorescence data. The tumor growth curves of individuals treated with free drugs showed a drop at each injection, since we assumed that the drug induced decay is proportional to the plasma exposure. However, smoother curves are expected in the biological process.

The estimates of the parameters of the resistance model are provided in Table 4.3. The large values of the standard deviations of the random effects ω for both e_0 and λ_R were indicative of a large inter-individual variability. No significant difference was found between ANCs and liposomes in terms of drug potency, although liposomes showed larger resistance than the immunoliposomes. Moreover, the estimated drug potency of the free drugs was significantly smaller than the other two groups.

4.4.3 Applications to dose optimization

The pharmacokinetic-pharmacodynamic model could be used to optimize the treatment scheduling. Here, we compared different administrations and simulated the PKPD model to predict the drug

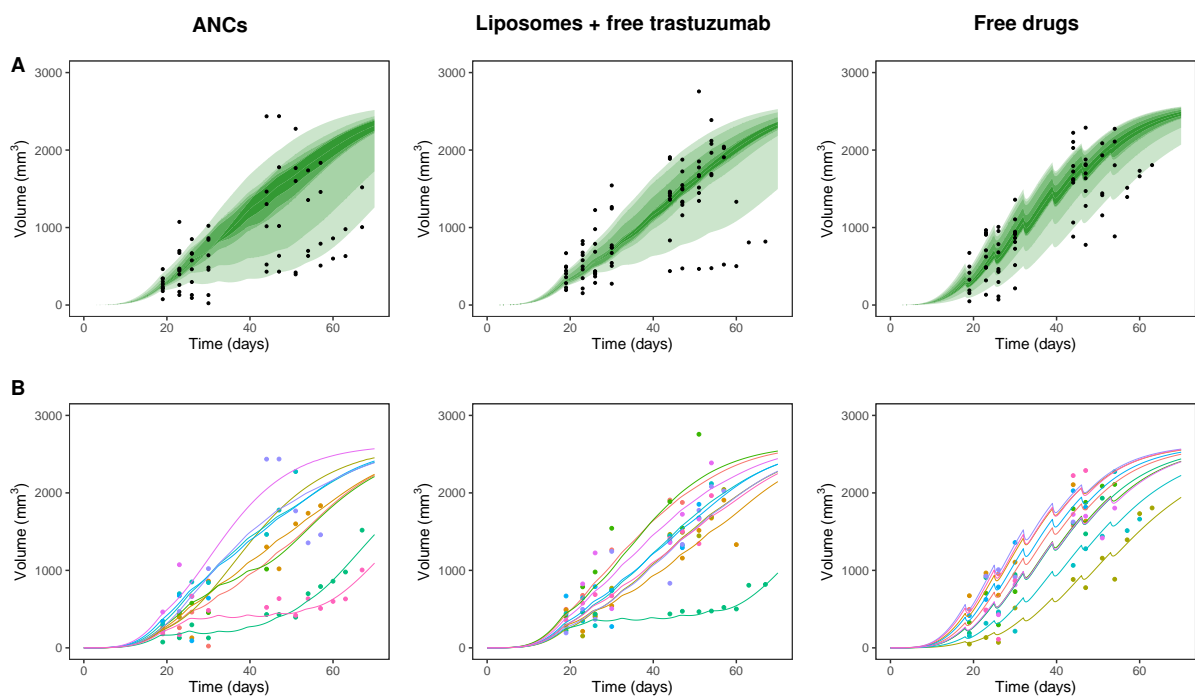


Figure 4.4. Pharmacodynamic modeling: prediction distributions (A) and individual fits (B) of the control group (left), ANC group (center) and liposome group (right).

exposure and the treatment efficacy. We compared ANCs, liposomes plus free trastuzumab and free drugs. Assuming that the drugs are administered within day 18 and 53 and that the total injected dose of docetaxel is 70 mg/kg, the following administrations were compared:

- Administration 1: 2 mg/kg every day,
- Administration 2: 14 mg/kg once a week,
- Administration 3: 10 mg/kg every 5 days,
- Administration 4: 35 mg/kg at day 18 and at day 53.

Simulations were performed with the `mlxR` package of `Simulx` [157] using the population parameters estimated in Tables 4.2 (high dose, for the two types of nanoparticles only) and 4.3. First, we compared the drug accumulation in the central and tumor compartments. The area under the curve (AUC) of the docetaxel amount delivered by the two nanoparticles is shown in Figure 4.5. Since parameters of the PK model of free drugs were fixed within the population, no inter-individual variability was shown in the simulations. The estimated AUCs of free docetaxel in the systemic compartment were 35.9, 41.9, 39.9 and 34.9 mg/kg for administration 1, 2, 3 and 4, respectively. In all cases, administration 2 led to a larger accumulation of the drug in the tumor compartment (Figure 4.5B). Moreover, Figure 4.6 shows the amount of nanoparticles in the tumor and systemic compartments as a function of time as well as the tumor growth inhibition relative to the four different treatment schedules. Globally, the groups of animals treated with one of the two nanoparticles showed large variability with any administrations. Lower variability was observed for the free drugs, where administration 2 significantly improved the treatment efficacy compared to administrations 1 and 4, while it showed a similar outcome as administration 3.

4.5 Discussion

PK modeling

We have analyzed the kinetics of nanoparticles in the body and tumor using a two-compartment model. The data were obtained with fluorescence imaging, that quantified the nanoparticle amount in the body and tumor. The goal of the PK model was to determine pharmacokinetic parameters for the ANCs and for the liposomal docetaxel injected with free trastuzumab.

We assumed that the nanoparticle fluorescence at the tumor site is proportional to the nanoparticle amount in the tumor interstitium, while the nanoparticle fluorescence in the entire body is proportional to the amount in the systemic circulation. This motivated our choice of the PK model, which describes the exchange between the central compartment (systemic circulation) and the tumor compartment thanks to a parameter that depends on the permeability and surface of the vessel walls. Moreover, nanoparticles might be cleared both in the central and tumor compartments. When

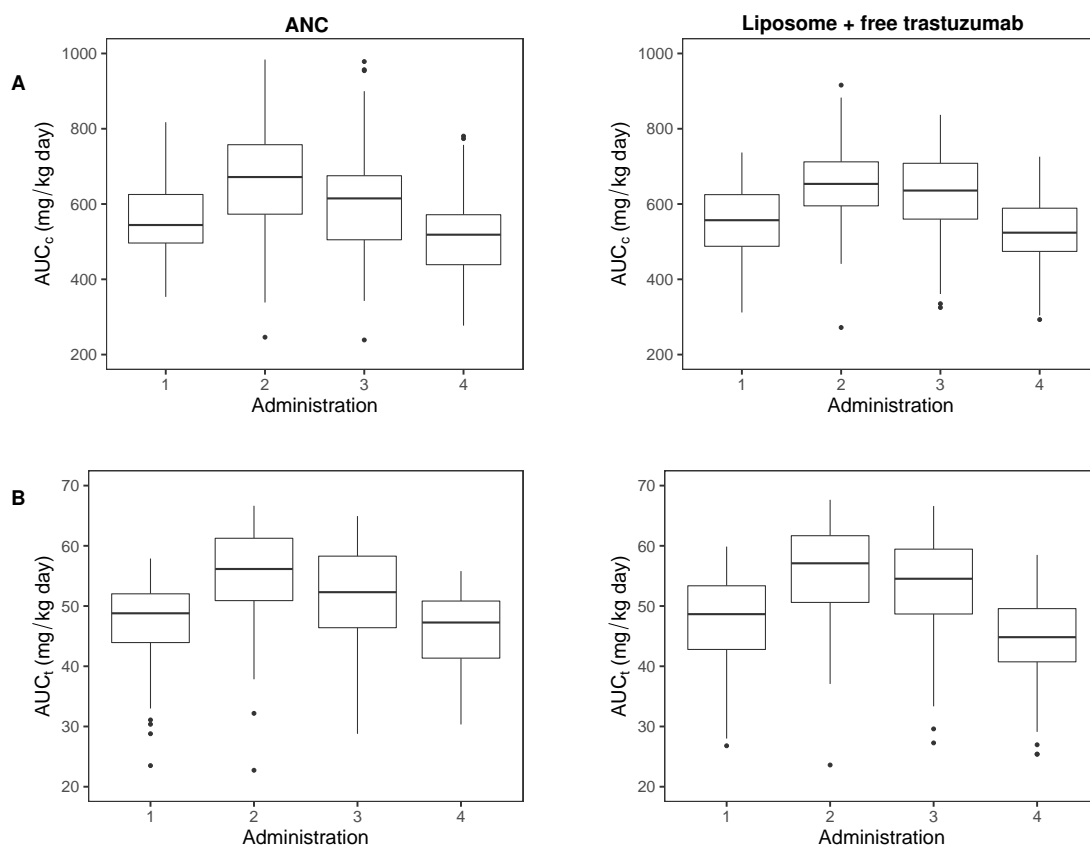


Figure 4.5. Estimated area under the curve (AUC) of ANCs (left) and liposomes (right) in (A) the central compartment (AUC_c) and (B) tumor compartment (AUC_t).

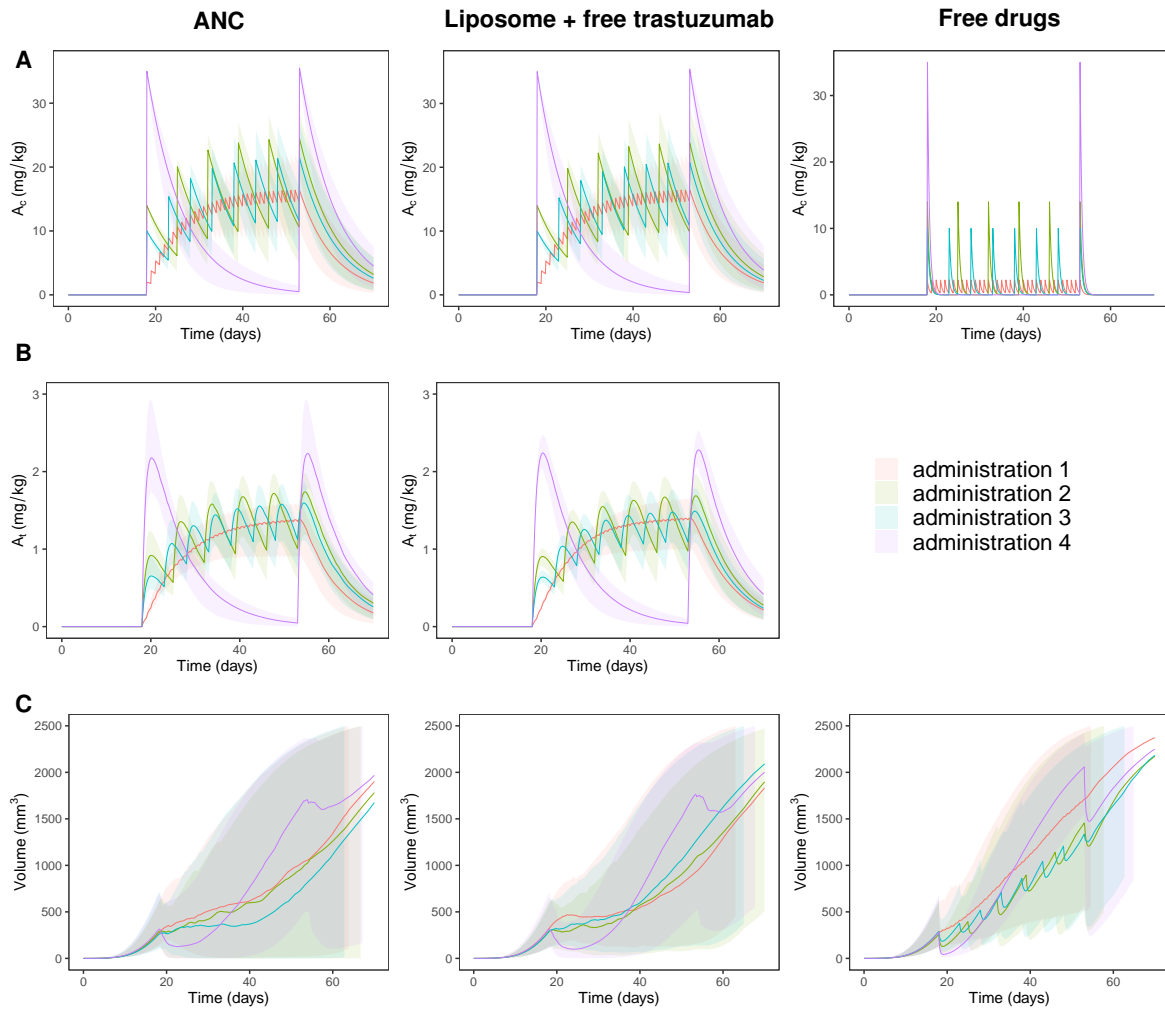


Figure 4.6. Tests of the different administrations: PK model simulations of the amount of drug in the systemic compartment (A), in the tumor compartment (B) and tumor growth inhibition simulations (C) of groups of animals treated with ANCs (left), liposomes + free trastuzumab (center) and free docetaxel + free trastuzumab (free drugs, right).

nanoparticles are in the systemic circulation, they might interact with the macrophage system, the liver or the kidneys, and are therefore eliminated. In the tumor compartment, nanoparticles might be expelled because of the high interstitial fluid velocity that drives particles out at the periphery of the tumor. Moreover, NPs might be drained by the lymphatic vessels.

Our model has some limitations. First of all, we considered the nanoparticle amount of the systemic compartment to be proportional to the nanoparticle fluorescence of the entire body. However, we did not take into account that liposomes might be absorbed by other organs (such as the liver, spleen, or kidneys) and remain fluorescent. This could explain the low values of the clearance rate k_c of the NPs, although it has been proven that stealth liposomes improve significantly drug pharmacokinetics [37]. We did not take into account temporal variations of the clearance rate, although it might be possible that the macrophage system recognizes and eliminates faster the nanoparticles after the first injections. Especially, ANCs might be cleared faster since they have an antibody coated on the surface. Indeed, we found that the clearance rate was larger for the ANCs than for the liposomes in the low-dose dataset. In the high-dose dataset, no difference in clearance rate was noticed between ANCs and liposomes because of the loss of fluorescence of the liposomes. Moreover, we assumed that the NP fluorescence at the tumor compartment is proportional to the amount of nanoparticle in the tumor interstitium, without considering the cell internalization. This was due to a lack of information on the internalization properties of the nanoparticles but could be integrated into future works. The parameter that drives the extravasation of liposomes from the vascular network to the tumor interstitium depends on the effective permeability of the vessel walls and the vascular surface per unit volume S/V . We have considered the parameter $k_{c,t}$ to be constant in time, while it has been observed that tumor vascularization evolves with tumor growth [183]. This could explain why the model was not able to describe the data at the earliest measurements. Interestingly, we found that the value of the parameter $k_{c,t}$ was significantly larger for the ANC than for liposomes. This could be explained by the fact that immunoliposomes might improve the vascularization of MDA-MB-231 tumors (as shown in Chapter 7).

We noticed that the high-dose liposome group showed a different trend compared to the other datasets after the second injection. This could be explained by a loss of fluorescence by the liposomes due to stability problems of these nanoparticles during the experiment.

As a future perspective, a physiologically-based pharmacokinetic (PBPK) model should be used to describe mechanistically the biodistribution of the nanoparticles in the body and could provide insights on the mechanisms of absorption and clearance.

PKPD modeling

Nanoparticle and free drugs efficacy was evaluated as a function of the drug concentration in the tumor. Due to a loss of fluorescence signal during the experiment, tumor size was monitored with fluorescence imaging in the first half of the experiment and with the caliper in the second part. The rescaling of fluorescence data to volume data was achieved by fitting untreated tumor growth to

the reduced Gompert model and estimating the parameters k and β from previous experiments, as detailed in Section 2.6. Although the distributions of the parameters K_{FV} and β were known from control data analysis, we observed that in some cases the large number of degrees of freedom of the efficacy models and the lack of observations from day 30 to day 44 led to poor fits on caliper data and to meaningless tumor growth curves obtained by rescaling fluorescence data. To overcome this problem, we fixed the error model parameter of the caliper measurements equal to 0.17, as previously estimated.

Drug-induced decay of ANCs, liposomes injected with free trastuzumab, and free drugs was described by a resistance model, assuming that the efficacy decreases exponentially in time. Good fits were observed for the three groups.

The two nanoparticles did not show significant differences in terms of drug potency. However, liposomes plus free trastuzumab exhibited slightly larger resistance than the immunoliposomes. Indeed, previous studies demonstrated that targeted-immunoliposomes improved overall therapeutic efficacy as a result of an efficient cell-internalization [184]. Furthermore, the two nanoparticles performed significantly better than the free drugs in terms of efficacy, thanks to the improved pharmacokinetic profiles of the two liposomal formulations. Tumor growth curves relative to the free drugs curves showed drops at each injection, due to the assumption that the drug-induced decay is proportional to the plasma amount of docetaxel (indeed, no data on the pharmacokinetics of the free drugs was available for this experiment). This trend is not usually observed in experimental data. Other models could be tested to describe the pharmacodynamic of the different drugs. For instance, the Simeoni model could be used to model the drug potency and the process of cell death, which could occur with a delay [185]. Moreover, the effect of trastuzumab should be considered in future works.

As future perspectives, *in vitro* studied could be integrated into the *in vivo* PKPD model to better understand the interactions between the drugs and the cells and how this is linked to the treatment efficacy. By integrating these data, it could be possible to understand the large inter-individual variability and to make more accurate individual predictions of the treatment response.

Optimization of the treatment scheduling and predictions of the clinical drug exposure-response relationship are examples of the applications of the pharmacokinetic-pharmacodynamic modeling.

Part II

SPATIAL MATHEMATICAL MODELING OF NANOPARTICLE TRANSPORT IN TUMOR TISSUES

MACRO-SCALE MODELS FOR FLUID FLOW IN TUMOR TISSUES: IMPACT OF THE MICROSTRUCTURE PROPERTIES

Abstract. Understanding the dynamics underlying fluid transport in tumor tissues is of fundamental importance to assess processes of drug delivery. Here, we analyze the impact of the tumor microscopic properties on the macroscopic dynamics of vascular and interstitial fluid flow by using formal asymptotic techniques.

Here, we obtained different macroscopic continuum models that couple vascular and interstitial flows. The homogenization technique allows us to derive two macroscale tissue models of fluid flow that take into account the microscopic structure of the vessels and the interstitial tissue. Different regimes were derived according to the magnitude of the vessel wall permeability and the interstitial hydraulic conductivity. Importantly, we provide an analysis of the properties of the models and show the link between them. Numerical simulations were eventually performed to test the models and to investigate the impact of the microstructure on the fluid transport.

Future applications of our models include their calibration with real imaging data to investigate the impact of the tumor microenvironment on drug delivery.

Part of this Chapter has been submitted in [80].

Contents

5.1	Introduction	91
5.2	Microscale model of fluid transport in tumors	94
5.3	Continuum macroscale models using two scale asymptotic analysis	98
5.3.1	Tensors properties	99
5.3.2	Limit problems	102
5.4	Derivation of the macro-scale models	104
5.5	Numerical convergence of the multiscale model to the homogenized models (2D)	109
5.6	Numerical simulations	112
5.6.1	Cell problems: tensor properties varying the microstructure	112
5.6.2	Macroscopic dynamic of fluid transport in tumors	112
5.7	Discussion	118

5.1 Introduction

Interstitial and capillary fluids are strongly connected in malignant tissues and are mainly involved in the transport of molecules in tumors. When drugs are intravenously injected, they have to overcome several barriers, including vascular transport, transvascular transfer, interstitial transport and finally cellular uptake [61]. The biological and physicochemical properties of the tumor microenvironment play a significant role in the drug delivery process [186]. The geometrical microstructure of the tumor also has an important impact on the fluid flow [187].

Neoplastic tissues are highly heterogeneous. They are generally characterized by [59] accumulated solid stress [188], abnormal blood vessels network [189], elevated interstitial fluid pressure (IFP) [68], that almost equals the microvessel pressure (MVP) and dense interstitial structure [190]. These traits, that distinguish tumor tissues from normal ones, cause barriers to drug delivery [61]. The heterogeneous spatial distribution of tumor vessels and poor lymphatic drainage impair a uniform delivery of therapeutic agents in tumors. Blood vessels are unevenly distributed, leaving avascular spaces. Moreover, their walls are leaky and hyperpermeable in some places while not in other [191]. Blood flow velocity is also compromised by the elevated viscous and geometrical resistance offered by the tumor vasculature [187]. Finally, the lack of an efficient lymphatic network inside the tumor coupled with leaky tumor vessels leads to a high IFP [67] almost equal to the microvascular pressure [68]. Due to elevated IFP, the tumor interstitium is characterized by no pressure gradient [192, 69].

Several mathematical models have been developed during the last decades to investigate the features of fluid transport in the tumor microenvironment. The porous medium theory has been employed to model interstitial fluid flow (IFF) relying on Darcy's law and using average field variables defined over the whole tissue [58, 193]. Fluid transport through the blood vessels has been exploited in both discrete and continuous manners, including spatial and temporal variations. In either discrete and continuous models, the IFF and microvascular fluid (MVF) are usually coupled by Starling's law [194], that describes the fluid filtration through the highly permeable vessels walls. Microscopic models of the flow patterns around an individual capillary and a network of blood vessels have been introduced relying on the Krogh cylinder model [195, 196, 197]. Poiseuille's law can be considered to describe the blood flow in a cylindrical domain [198, 199, 200]. Furthermore, Navier-Stokes equations have been adopted to model the spatio-temporal variations in blood flow [197, 193]. More detailed biophysical models have been developed to take into account the more realistic heterogeneity of the tumor vasculature [201]. Welter et al [202] introduced an exhaustive biophysical model that incorporates tumor growth, vascular network (including arteries and veins), angiogenesis, vascular remodeling, porous medium description for the extracellular matrix (ECM) and interstitial fluid, interstitial fluid pressure and velocity and chemical entities (such as oxygen, nutrients, drugs). On the other hand, continuous models based on mixture theory have been exploited to describe interstitial and vascular fluid flow, assuming that the two phases are present at each point of the tumor [203]. Multiscale models have further been employed to investigate the

coupling between tumor growth, angiogenesis, vascular remodeling and fluid transport [204] and the impact of collagen microstructure on interstitial fluid flow [205]. Imaging data have been integrated to both continuum and discrete models to quantify the effect of the heterogeneity on the fluid transport [206, 207].

The increasing amount of imaging data makes it possible to recover vascular networks in details. However, solving discrete models on the entire vessel tree might be computationally expensive. The formal two-scale homogenization technique allows to take into account microscopic features on the macroscopic dynamic of fluid flow. Two-scale asymptotic expansion has been previously applied to fluid and drug transport in tumors. A system of Darcy's equations has been derived in [81] to couple interstitial and vascular fluid flows in malignant tissues assuming a periodic medium. A higher complexity has been taken into account in [82], with the introduction of rheological effects in the blood flow and of local heterogeneity. A generalization of homogenized modeling for vascularized poroelastic materials has also been presented [208, 209]. More recently, higher complexity has been added to the homogenized models [210] considering three length scales for the vessel network (i.e., arteriole, venule and capillary scales).

The main novelty of this work is the study of the impact of the tumor microscopic properties on the global fluid dynamic. First, we describe a system of partial differential equations coupling interstitial, transvascular and capillary flows at the microscopic scale. While the interstitium and the capillary walls are assumed to be porous media where the fluid is governed by Darcy's law, the blood in the capillaries is considered a Newtonian fluid described by the Stokes equation. As the thickness of the capillary walls tends to zero, an asymptotic analysis similar to [211, 212] enables us to derive a Starling's law-type equation across the vessel wall for the transvascular transport of fluid flow. Then, we perform a two-scale analysis under periodic assumption [213] to derive formally effective macroscale tissue models of fluid flow for 3 asymptotic regimes depending on the magnitude of the permeability of the vessel wall and of the interstitial hydraulic conductivity. These models combine the effects of the interstitial compartment and the capillaries at the microscale, providing thus a link between the microstructure and the macroscopic fluid flow. Moreover, we compare the different asymptotic regimes with some models given in literature (namely, [186], [81], [82]) and show the links between the different models. In particular, we show that for the model initially derived by Shipley and Chapman [81] the difference between the capillary and the interstitium pressures decays exponentially fast from the boundary, making thus a link with the Baxter and Jain model [186]. Furthermore, we present the mathematical and numerical analysis on the homogenized tensors in order to assess their properties according to the geometric microstructure. Eventually, numerical simulations on the macroscopic models are performed and the results are compared to the literature.

This approach can be applied to study the impact of the tumor microscopic characteristics on drug delivery. Imaging data can provide the tissue microstructure that can be integrated in the homogenized model. This modeling technique prevents the resolution of the original micro-scale model that might be unfeasible as it requires the discretisation of the entire vessel network and porous medium. Moreover, the heterogeneities of malignant tissues can be taken into account by

considering the spatial variability of the micro-vessel features at the macroscopic scale.

Main results

First, we motivated the interface conditions between the interstitial compartment and the capillaries of the micro-scale model using an asymptotic expansion technique. We obtained a Starling's law type equation to describe the flux through the vessel walls. Moreover, we considered the Joseph-Beavers-Saffman slip condition at the boundary between the capillary lumen and the vessel wall. This condition states that the slip velocity along the vessel wall is proportional to the shear stress [214].

Then, using the two-scale asymptotic homogenization, we assumed that a generic variable $v^\varepsilon(\mathbf{x})$, as function of the macroscopic spatial variable \mathbf{x} and of the microscopic parameter ε , could be approximated as

$$v^\varepsilon(\mathbf{x}) = v(\mathbf{x}) + \varepsilon \phi\left(\frac{\mathbf{x}}{\varepsilon}\right) \nabla_{\mathbf{x}} v(\mathbf{x}),$$

where $v(\mathbf{x})$ is the macroscopic variable and $\phi\left(\frac{\mathbf{x}}{\varepsilon}\right)$ is the corrector that takes into account oscillations at the microscopic scale. Using this approach, we derived three different macroscale models to describe the fluid transport in tumor tissues according to the magnitude of the permeability of the vessel walls and of the interstitial hydraulic conductivity. In particular, the following regimens were derived for the interstitial fluid pressure p_t and the capillary pressure p_c :

- **Model 1:** highly permeable walls and large interstitial hydraulic conductivity

$$\nabla \cdot \left(\left(\mathbf{K} + \frac{C_t}{C_c} \mathbf{E} \right) \nabla p_c \right) = 0 \quad p_t = p_c. \quad (5.1)$$

- **Model 2:** weakly permeable walls and large interstitial hydraulic conductivity

$$\nabla \cdot (\mathbf{K} \nabla p_t) = C_t (p_t - p_c), \quad \nabla \cdot (\mathbf{E} \nabla p_c) = C_c (p_c - p_t). \quad (5.2)$$

- **Model 3:** weakly permeable walls and small interstitial hydraulic conductivity

$$\nabla \cdot (\mathbf{K} \nabla p_t) = C_t (p_t - p_c), \quad \nabla \cdot (\mathbf{E} \nabla p_c) = 0. \quad (5.3)$$

In the three models, \mathbf{K} and \mathbf{E} are the permeability tensors of the interstitium and the capillaries, respectively, and C_t, C_c are constant parameters that will be defined later on. The definition of these tensors involves the so-called correctors, as usual in homogenization. It characterises the impact of the microstructure on the effective properties of the tissue at the macroscale. Model (5.2) has been derived assuming a small magnitude of the capillary permeability and confirms previous results [81, 82].

The interstitial fluid flow \mathbf{u}_t and the blood velocity \mathbf{u}_c are given in the first two cases by the average quantities

$$\mathbf{u}_t = -\mathbf{K} \nabla p_t, \quad \mathbf{u}_c = -\mathbf{E} \nabla p_c,$$

while for the third model they are given by

$$\mathbf{u}_t = -\varepsilon \mathbf{K} \nabla p_t, \quad \mathbf{u}_c = -\mathbf{E} \nabla p_c.$$

Boundary conditions must be added in order to guarantee well-posedness. Dirichlet-Dirichlet boundary conditions can be imposed to p_t and p_c if the pressures in the surrounding tissue are known. Mixed Dirichlet and Neumann boundary conditions can be chosen to ensure the continuity of \mathbf{u}_t or \mathbf{u}_c .

5.2 Microscale model of fluid transport in tumors

At the microscale, the domain $\Omega \in \mathbb{R}^N$ (with $N = 2, 3$) is the medium that consists of the interstitium Ω_t , the vessel wall Ω_m and the capillary region Ω_c . The interface between the capillary and the vessel wall and the one between the interstitium and the vessel wall are denoted respectively by $\Gamma = \partial\Omega_c \cap \partial\Omega_m$ and $\Gamma_\delta = \partial\Omega_t \cap \partial\Omega_m$. Figure 5.1 shows the section of a capillary in the surrounding interstitium. In the three regions, the fluid flow is assumed to be incompressible.

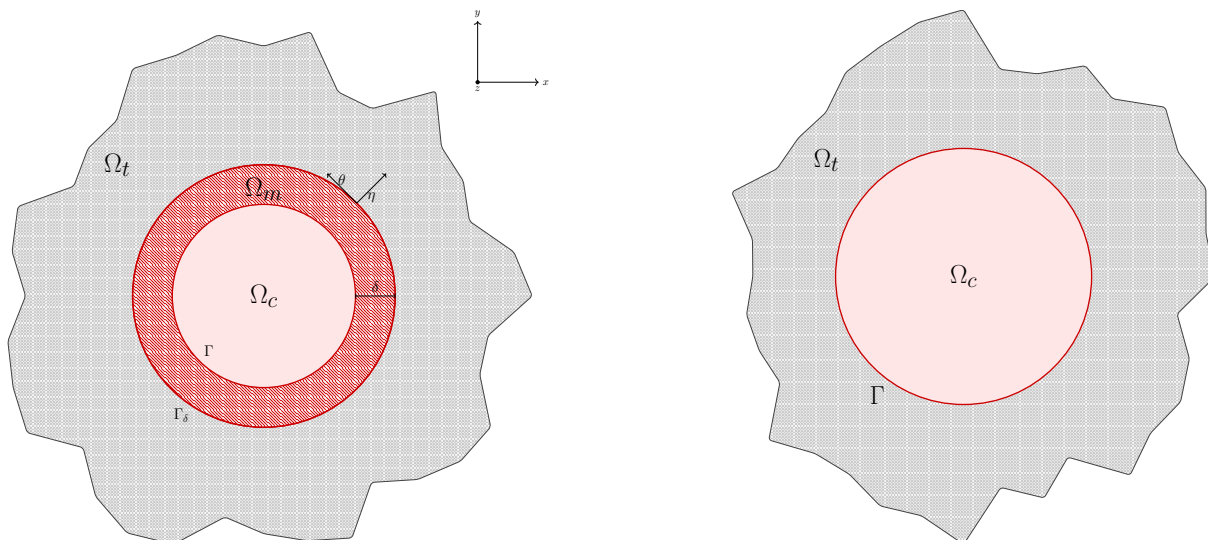


Figure 5.1. Schematic representation of the domain: section of the capillaries in the surrounding interstitial region.

The interstitium - composed by the cells and the extracellular matrix and collagen - is modeled as an isotropic porous medium, where the velocity \mathbf{u}_t and pressure p_t follow the Darcy's law:

$$\nabla \cdot \mathbf{u}_t = 0, \quad \mathbf{u}_t = -k_t \nabla p_t \quad \text{in } \Omega_t, \quad (5.4)$$

where k_t is the hydraulic conductivity in the interstitium. Vascular endothelial cells in tumors are highly disorganized and irregularly shaped [191]. Moreover, vessel walls are highly permeable. Similarly to the interstitium, the capillary walls - of thickness δ - are considered as a porous medium with hydraulic conductivity k_m , therefore the fluid flow velocity \mathbf{u}_m and pressure p_m in the capillary walls are described by

$$\nabla \cdot \mathbf{u}_m = 0, \quad \mathbf{u}_m = -k_m \nabla p_m \quad \text{in } \Omega_m.$$

In the capillaries, we assume that the fluid is Newtonian with a constant viscosity μ . Neglecting the

inertial effects and under the assumption of a laminar flow, we end up with the Stokes equation for the description of the vessel velocity \mathbf{u}_c and pressure p_c

$$\nabla \cdot \mathbf{u}_c = 0, \quad \mu \nabla^2 \mathbf{u}_c = \nabla p_c \quad \text{in } \Omega_c. \quad (5.5)$$

Interface conditions

At the two boundaries Γ and Γ_δ , we have to consider interface conditions in order to couple the different equations. We make the following choices, similarly to [215]:

1. Continuity of the normal velocity on both Γ and Γ_δ :

$$\mathbf{u}_c \cdot \mathbf{n} = \mathbf{u}_m \cdot \mathbf{n} \quad \text{on } \Gamma,$$

$$\mathbf{u}_t \cdot \mathbf{n} = \mathbf{u}_m \cdot \mathbf{n} \quad \text{on } \Gamma_\delta.$$

This condition guarantees the continuity of mass through the two interfaces and it is a natural choice since the fluid is assumed to be incompressible in the three regions.

2. Balance of the normal forces at the interfaces Γ, Γ_δ :

$$p_c - \mu[(\mathbf{n} \cdot \nabla)\mathbf{u}_c] \cdot \mathbf{n} = p_m \quad \text{on } \Gamma, \quad (5.6)$$

$$p_t = p_m \quad \text{on } \Gamma_\delta. \quad (5.7)$$

Condition (5.6) is due to the fact that the blood force in Ω_c acting on Γ is equal to the normal component of the Cauchy stress vector [216], while the only force in Ω_m acting on the interface is the Darcy pressure p_m . Analogously, equation (5.7) is motivated by the fact that the only forces acting on the interface Γ_δ are the Darcy's pressures p_m and p_t in the respective regions Ω_m and Ω_t .

3. Beavers-Joseph-Saffmann condition on the tangential component of the capillary velocity at the boundary with a porous medium Γ :

$$\mathbf{u}_c \cdot \boldsymbol{\tau} = -\frac{\sqrt{k_m \mu}}{\alpha_{BJ}} [(\mathbf{n} \cdot \nabla)\mathbf{u}_c] \cdot \boldsymbol{\tau} \quad \text{on } \Gamma, \quad (5.8)$$

where α_{BJ} is a constant depending on the properties of the interface. This condition comes from the experimental evidence shown by Beavers and Joseph [214] who observed that the slip velocity along Γ was proportional to the shear stress along Γ . Equation of the form (5.8) was derived by Saffmann using a statistical approach and the Brinkman approximation for non-homogeneous porous medium [217].

Non-dimensionalization

We perform a dimensional analysis in order to understand the relative amplitude of the different parameters involved. We rescale our fields as follows:

$$\mathbf{x} = L\mathbf{x}', \quad \mathbf{u} = U\mathbf{u}', \quad p = \frac{\mu LU}{d^2} p' + p_0,$$

where L is the characteristic domain length, d is the mean intercapillary distance and U is a characteristic velocity. The non-dimensional fluid transport problem reads (neglecting the primes for the sake of simplicity)

$$\nu \nabla^2 \mathbf{u}_c = \nabla p_c, \quad \nabla \cdot \mathbf{u}_c = 0, \quad \text{in } \Omega_c, \quad (5.9)$$

$$\mathbf{u}_t = -\kappa \nabla p_c, \quad \nabla \cdot \mathbf{u}_t = 0, \quad \text{in } \Omega_t, \quad (5.10)$$

$$\mathbf{u}_m = -\kappa_m \nabla p_m, \quad \nabla \cdot \mathbf{u}_m = 0, \quad \text{in } \Omega_m, \quad (5.11)$$

$$\mathbf{u}_c \cdot \mathbf{n} = \mathbf{u}_m \cdot \mathbf{n} \quad \text{on } \Gamma, \quad (5.12)$$

$$\mathbf{u}_t \cdot \mathbf{n} = \mathbf{u}_m \cdot \mathbf{n} \quad \text{on } \Gamma_\delta, \quad (5.13)$$

$$p_c - \nu[(\mathbf{n} \cdot \nabla) \mathbf{u}_c] \cdot \mathbf{n} = p_m \quad \text{on } \Gamma, \quad (5.14)$$

$$p_t = p_m \quad \text{on } \Gamma_\delta, \quad (5.15)$$

$$\mathbf{u}_c \cdot \boldsymbol{\tau} = -R_\tau [(\mathbf{n} \cdot \nabla) \mathbf{u}_c] \cdot \boldsymbol{\tau}, \quad \text{on } \Gamma. \quad (5.16)$$

where

$$\nu = \frac{d^2}{L^2}, \quad \kappa = \frac{k_t \mu}{d^2}, \quad \kappa_m = \frac{k_m \mu}{d^2}, \quad R_\tau = \frac{\sqrt{k_m \mu}}{\alpha_{BJ} L},$$

are dimensionless quantities.

Asymptotic expansion of the multi-scale model

We analyze the behaviour of the asymptotic system when the thickness of the capillary wall δ tends to 0, assuming that κ_m is proportional to δ with a proportionality coefficient R_n that will be defined later on:

$$\kappa_m = \delta R_n.$$

Let us denote by η the normal variable to the vessel membrane and by θ the tangential variable to the vessel wall. With these coordinates, the Laplacian is defined by

$$\nabla^2 : \frac{1}{\delta^2} \partial_\eta^2 + \frac{1}{\delta(1+\delta\zeta\eta)} \partial_\eta + \frac{1}{(1+\delta\zeta\eta)^2} \partial_\theta^2 + \partial_z^2,$$

where ζ is the curvature of the section. Therefore, the fluid transport equations in the capillary wall and the interface conditions are given by

$$\left(\partial_\eta^2 + \frac{\delta}{(1+\delta\zeta\eta)} \partial_\eta + \frac{\delta^2}{(1+\delta\zeta\eta)^2} \partial_\theta^2 + \delta^2 \partial_z^2 \right) p_m = 0 \quad \text{in } \Omega_m, \quad (5.17)$$

$$\mathbf{u}_c \cdot \mathbf{n} = -R_n \partial_\eta p_m \quad \text{on } \Gamma \quad (5.18)$$

$$\partial_\eta p_m = \frac{\kappa}{R_n} \nabla p_t \cdot \mathbf{n} \quad \text{on } \Gamma_\delta \quad (5.19)$$

$$p_c - \nu[(\mathbf{n} \cdot \nabla) \mathbf{u}_c] \cdot \mathbf{n} = p_m \quad \text{on } \Gamma, \quad (5.20)$$

$$p_t = p_m \quad \text{on } \Gamma_\delta, \quad (5.21)$$

$$\mathbf{u}_c \cdot \boldsymbol{\tau} = -R_\tau [(\mathbf{n} \cdot \nabla) \mathbf{u}_c] \cdot \boldsymbol{\tau} \quad \text{on } \Gamma \quad (5.22)$$

We perform an asymptotic expansion of the variables p_m, p_t, p_c and \mathbf{u}_c :

$$p_m = p_m^{(0)} + \delta p_m^{(1)} + \delta^2 p_m^{(2)} + \dots$$

$$p_t = p_t^{(0)} + \delta p_t^{(1)} + \delta^2 p_t^{(2)} + \dots$$

$$p_c = p_c^{(0)} + \delta p_c^{(1)} + \delta^2 p_c^{(2)} + \dots$$

$$\mathbf{u}_c = \mathbf{u}_c^{(0)} + \delta \mathbf{u}_c^{(1)} + \delta^2 \mathbf{u}_c^{(2)} + \dots$$

Equating coefficients of δ^0 in (5.17)-(5.22), we obtain the following system of equations

$$\partial_\eta^2 p_m^{(0)} = 0 \quad \text{in } \Omega_m \quad (5.23)$$

$$\mathbf{u}_c^{(0)} \cdot \mathbf{n} = -R_n \partial_\eta p_m^{(0)} \quad \text{on } \Gamma \quad (5.24)$$

$$\partial_\eta p_m^{(0)} = \frac{\kappa}{R_n} \nabla p_t^{(0)} \cdot \mathbf{n} \quad \text{on } \Gamma_\delta \quad (5.25)$$

$$p_c^{(0)} - \nu[(\mathbf{n} \cdot \nabla) \mathbf{u}_c^{(0)}] \cdot \mathbf{n} = p_m^{(0)} \quad \text{on } \Gamma \quad (5.26)$$

$$p_m^{(0)} = p_t^{(0)} \quad \text{on } \Gamma_\delta \quad (5.27)$$

$$\mathbf{u}_c^{(0)} \cdot \boldsymbol{\tau} = -R_\tau [(\mathbf{n} \cdot \nabla) \mathbf{u}_c^{(0)}] \cdot \boldsymbol{\tau} \quad \text{on } \Gamma \quad (5.28)$$

From (5.23) and (5.25) we infer

$$\partial_\eta p_m^{(0)} = \frac{\kappa}{R_n} \nabla p_t^{(0)} \cdot \mathbf{n} \quad \text{in } \Omega_m, \quad (5.29)$$

and then equations (5.29) and (5.26) leads to

$$p_m^{(0)} = \left(\frac{\kappa}{R_n} \nabla p_t^{(0)} \cdot \mathbf{n} \right) \eta + p_c^{(0)} - \nu[(\mathbf{n} \cdot \nabla) \mathbf{u}_c^{(0)}] \cdot \mathbf{n} \quad \text{in } \Omega_m. \quad (5.30)$$

Therefore from (5.27)

$$p_t^{(0)} = p_m^{(0)}(\eta = 1) = \frac{\kappa}{R_n} \nabla p_t^{(0)} \cdot \mathbf{n} + p_c^{(0)} - \nu[(\mathbf{n} \cdot \nabla) \mathbf{u}_c^{(0)}] \cdot \mathbf{n} \quad \text{on } \Gamma_\delta. \quad (5.31)$$

Let us define by $\Gamma \in \mathbb{R}^{N-1}$ the boundary when δ goes to 0, i.e. when the two interfaces Γ_δ and Γ are superimposed. From equations (5.31), (5.24) and (5.25) we derive formally the boundary conditions for small δ :

$$\kappa \nabla p_t^{(0)} \cdot \mathbf{n} = R_n \left(p_t^{(0)} - p_c^{(0)} + \nu[(\mathbf{n} \cdot \nabla) \mathbf{u}_c^{(0)}] \cdot \mathbf{n} \right) \quad \text{on } \Gamma, \quad (5.32)$$

$$\mathbf{u}_c^{(0)} \cdot \mathbf{n} = -\kappa \nabla p_t^{(0)} \cdot \mathbf{n} \quad \text{on } \Gamma, \quad (5.33)$$

$$\mathbf{u}_c^{(0)} \cdot \boldsymbol{\tau} = -R_\tau [(\mathbf{n} \cdot \nabla) \mathbf{u}_c^{(0)}] \cdot \boldsymbol{\tau} \quad \text{on } \Gamma. \quad (5.34)$$

Conditions (5.32)-(5.33) can be rewritten as

$$\mathbf{u}_t \cdot \mathbf{n} = \mathbf{u}_c \cdot \mathbf{n} = R_n (p_c - p_t - \nu[(\mathbf{n} \cdot \nabla) \mathbf{u}_c] \cdot \mathbf{n}) \quad \text{on } \Gamma. \quad (5.35)$$

Equation (5.35) is similar to Starling's law, that is the most widely used equation in literature to model flux transport across the vessel wall [69, 198] and reads

$$\mathbf{u}_c \cdot \mathbf{n} = L_p (p_c - p_t - \sigma (\pi_c - \pi_t)), \quad (5.36)$$

where L_p is the vascular permeability, σ is the osmotic reflection coefficient ($\sigma \in (0, 1)$) that expresses the glycocalyx filter function through the endothelial wall and $(\pi_c - \pi_t)$ is the oncotic pressure difference between the capillaries and the interstitium. However, the latter can be considered negligible compared to the interstitial fluid pressure difference in tumors [58, 218]. Moreover,

the viscous term in equation (5.35) is usually neglected but it is necessary to guarantee the well-posedness of the problem and does not change the physical meaning since it is based on the balance of the normal forces [82].

The relation between $R_{\mathbf{n}}$ and L_p is given thanks to the nondimensionalization of equation (5.36):

$$R_{\mathbf{n}} = \frac{L_p L \mu}{d^2}.$$

To conclude this section, our model is composed by equations (5.4), (5.5) in the respective regions of the domain Ω_t and Ω_c and by the interface conditions (5.32)-(5.34) on Γ .

5.3 Continuum macroscale models using two scale asymptotic analysis

This section is devoted to the derivation of a continuum macro-scale model using the two scale asymptotic expansion method [219, 220, 213]. We assume that d is the mean inter-capillary distance and L is the tissue characteristic length such that $\varepsilon = d/L \ll 1$. We denote by Y the reference periodic cell that is contained in $[0, 1]^N$ and is composed by the interstitium Y_t and the capillaries Y_c , i.e. $Y = Y_c \cup Y_t$ and the interface $\Gamma_Y = \partial Y_c \cap \Gamma_Y$. We assume that the interface is entirely contained in Y , i.e. $\Gamma_Y \cap \partial Y = \emptyset$. The normal vector \mathbf{n} to the interface Γ_Y is directed outward the vascular domain Y_c . The total domain Ω is divided periodically in each direction in identical squares Y_n^ε such that $Y_n^\varepsilon = \varepsilon n + \varepsilon Y$, $Y_{t,n}^\varepsilon = \varepsilon n + \varepsilon Y_t$, $Y_{c,n}^\varepsilon = \varepsilon n + \varepsilon Y_c$, $\Gamma_n^\varepsilon = \varepsilon n + \varepsilon \Gamma_Y$, $\forall n \in \{i \in \mathbb{Z}^N | Y_i^\varepsilon \cap \Omega \neq \emptyset\}$. Therefore, the domain Ω is composed of two subdomains $\Omega_t^\varepsilon = \cup_n Y_{t,n}^\varepsilon$ and $\Omega_c^\varepsilon = \cup_n Y_{c,n}^\varepsilon$ that depend on ε and are connected when $N = 3$. The interface between the two subdomains is $\Gamma^\varepsilon = \cup_n \Gamma_n^\varepsilon$. Figure 5.2 shows a schematic illustration of the periodic domain and of the unitary cell Y . According to the multiple scales theory, we introduce a spatial variation decoupling

$$\mathbf{y} = \frac{\mathbf{x}}{\varepsilon},$$

and assume that the macro and the micro spatial variables (\mathbf{x} and \mathbf{y} , respectively) are independent. Therefore, any field g that we have introduced before (such as \mathbf{u}_t , \mathbf{u}_c , p_t , p_c) depends on ε and is assumed to be written following an asymptotic expansion as:

$$g = g^\varepsilon(\mathbf{x}, \mathbf{y}) = \sum_{l=0}^{\infty} \varepsilon^l g^{(l)}(\mathbf{x}, \mathbf{y}),$$

where $g^{(l)}(\mathbf{x}, \mathbf{y})$ are Y -periodic functions.

Assuming that ν is of the same scale of ε^2 , that $R_{\mathbf{n}}$ is of the order of ε^γ (with $\gamma = 0, 1, 2$) and that κ is of the order of ε^η (with $\eta = 0, 1$), we rescale the three parameters as $\nu = \varepsilon^2 \bar{\nu}$, $R_{\mathbf{n}} = \varepsilon^\gamma \bar{R}_{\mathbf{n}}$ and $\kappa = \varepsilon^\eta \bar{\kappa}$ (so that $\bar{\nu} = \mathcal{O}(1)$, $\bar{R}_{\mathbf{n}} = \mathcal{O}(1)$ and $\bar{\kappa} = \mathcal{O}(1)$). The choice of the rescaling of the parameter ν is made in order to avoid trivial solution when ε goes to 0. We analyze the different regimens on varying the exponent γ .

We summarize here the main results relative to the leading order and derive formally the homogenized models in the Supporting Information S2. Let us denote by $|Y_c| = \int_{Y_c} d\mathbf{y}$, $|Y_t| = \int_{Y_t} d\mathbf{y}$ and $|\Gamma_Y| = \int_{\Gamma_Y} ds$ the measures of the subdomains Y_c and Y_t and of the interface Γ_Y , respectively. We in-

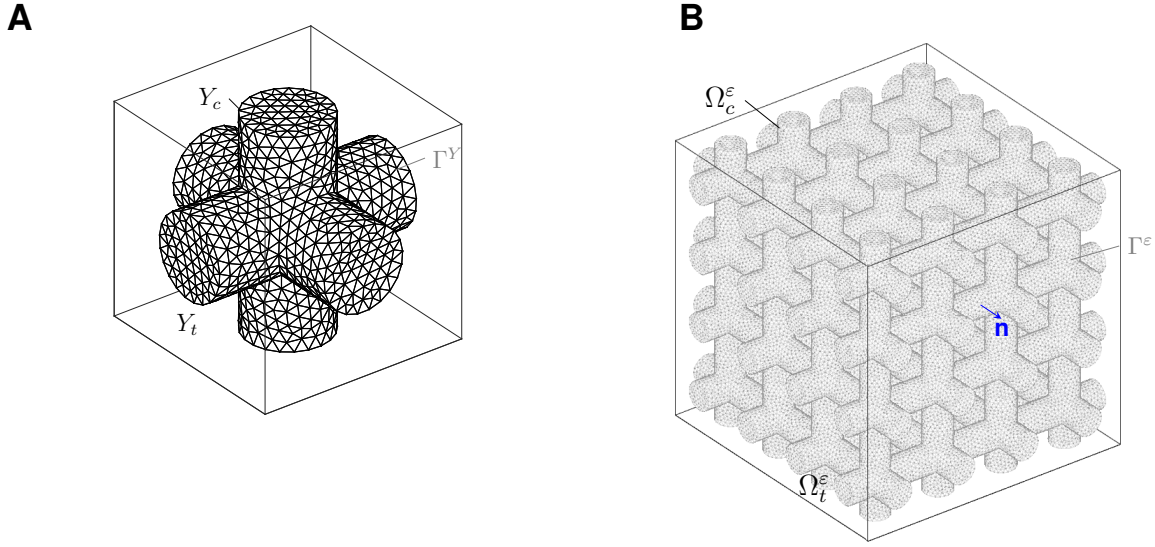


Figure 5.2. Unitary cell $Y = [0, 1]^3$ (left) composed by the capillary region Y_c and the interstitial compartment Y_t ; the interface between the two regions is denoted by Γ_Y . Periodic domain Ω (right): the tumor capillaries Ω_c^ϵ are assumed to be in the tubes, while the outer region corresponds to the interstitial compartment Ω_t^ϵ ; the interface between the two regions is denoted by Γ^ϵ and the normal \mathbf{n} is directed outward the vascular domain.

roduce the following two cell problems on the Y -periodic cell variables G^j , \mathbf{W}_j and P_j ($j = 1, \dots, N$):

$$\nabla_y^2 G^j = 0 \quad \text{in } Y_t \quad (5.37a)$$

$$\nabla_y G^j \cdot \mathbf{n} = \mathbf{n} \cdot \mathbf{e}_j \quad \text{on } \Gamma_Y. \quad (5.37b)$$

$$\bar{\nu} \nabla_y^2 \mathbf{W}^j + \mathbf{e}_j = \nabla_y P^j \quad \text{in } Y_c, \quad (5.38a)$$

$$\nabla_y \cdot \mathbf{W}^j = 0 \quad \text{in } Y_c, \quad (5.38b)$$

$$\mathbf{W}^j \cdot \mathbf{n} = 0 \quad \text{on } \Gamma_Y, \quad (5.38c)$$

$$[(\mathbf{n} \cdot \nabla_y) \mathbf{W}^j] \cdot \boldsymbol{\tau} = 0 \quad \text{on } \Gamma_Y. \quad (5.38d)$$

Let us define the following tensors:

$$[\mathbf{K}]_{ij} = \delta_{ij} - \frac{1}{|Y_t|} \int_{Y_t} \nabla_y G^j \cdot \mathbf{e}_i \, d\mathbf{y}, \quad [\mathbf{E}]_{ij} = \frac{1}{|Y_c|} \int_{Y_c} \mathbf{W}_j \cdot \mathbf{e}_i \, d\mathbf{y}. \quad (5.39)$$

The equations for the leading orders are summarized in Table 5.1. Boundary conditions need to be added, such as Dirichlet or Neumann conditions.

For the sake of simplicity, from now on we denote by (p_t, p_c) the leading orders of the interstitial and capillary pressures $(p_t^{(0)}, p_c^{(0)})$.

5.3.1 Tensors properties

In order to ensure the well-posedness of the models that we have derived, the permeability tensors \mathbf{K} and \mathbf{E} need to be positive definite. This section is devoted to the analysis of the tensor properties

Case	Convergence	Equation for the leading order in Ω
(1) $\gamma = 0, \eta = 0$	$p_t^\varepsilon(\mathbf{x}, \mathbf{y}) \rightarrow p_t^{(0)}(\mathbf{x})$	$\nabla \cdot \left(\left(\bar{\kappa} \mathbf{K} + \frac{ Y_c }{ Y_t } \mathbf{E} \right) \nabla p_t^{(0)} \right) = 0$
	$\mathbf{u}_t^\varepsilon(\mathbf{x}, \mathbf{y}) \rightarrow \mathbf{u}_t^{(0)}(\mathbf{x}, \mathbf{y})$	$\langle \mathbf{u}_t^{(0)} \rangle_{Y_t} = -\bar{\kappa} \mathbf{K} \nabla p_t^{(0)}$
	$p_c^\varepsilon(\mathbf{x}, \mathbf{y}) \rightarrow p_c^{(0)}(\mathbf{x})$	$p_c^{(0)} = p_t^{(0)}$
	$\mathbf{u}_c^\varepsilon(\mathbf{x}, \mathbf{y}) \rightarrow \mathbf{u}_c^{(0)}(\mathbf{x}, \mathbf{y})$	$\langle \mathbf{u}_c^{(0)} \rangle_{Y_c} = -\mathbf{E} \nabla p_c^{(0)}$
(2) $\gamma = 1, \eta = 0$	$p_t^\varepsilon(\mathbf{x}, \mathbf{y}) \rightarrow p_t^{(0)}(\mathbf{x})$	$\nabla \cdot \left(\bar{\kappa} \mathbf{K} \nabla p_t^{(0)} \right) = \frac{\bar{R}_n \Gamma_Y }{ Y_t } (p_t^{(0)} - p_c^{(0)})$
	$\mathbf{u}_t^\varepsilon(\mathbf{x}, \mathbf{y}) \rightarrow \mathbf{u}_t^{(0)}(\mathbf{x}, \mathbf{y})$	$\langle \mathbf{u}_t^{(0)} \rangle_{Y_t} = -\bar{\kappa} \mathbf{K} \nabla p_t^{(0)}$
	$p_c^\varepsilon(\mathbf{x}, \mathbf{y}) \rightarrow p_c^{(0)}(\mathbf{x})$	$\nabla \cdot \left(\mathbf{E} \nabla p_c^{(0)} \right) = \frac{\bar{R}_n \Gamma_Y }{ Y_c } (p_c^{(0)} - p_t^{(0)})$
	$\mathbf{u}_c^\varepsilon(\mathbf{x}, \mathbf{y}) \rightarrow \mathbf{u}_c^{(0)}(\mathbf{x}, \mathbf{y})$	$\langle \mathbf{u}_c^{(0)} \rangle_{Y_c} = -\mathbf{E} \nabla p_c^{(0)}$
(3) $\gamma = 2, \eta = 1$	$p_t^\varepsilon(\mathbf{x}, \mathbf{y}) \rightarrow p_t^{(0)}(\mathbf{x})$	$\nabla \cdot \left(\bar{\kappa} \mathbf{K} \nabla p_t^{(0)} \right) = \frac{\bar{R}_n \Gamma_Y }{ Y_t } (p_t^{(0)} - p_c^{(0)})$
	$\mathbf{u}_t^\varepsilon(\mathbf{x}, \mathbf{y}) \rightarrow \mathbf{u}_t^{(0)}(\mathbf{x}, \mathbf{y})$	$\langle \mathbf{u}_t^{(0)} \rangle_{Y_t} = -\varepsilon \bar{\kappa} \mathbf{K} \nabla p_t^{(0)}$
	$p_c^\varepsilon(\mathbf{x}, \mathbf{y}) \rightarrow p_c^{(0)}(\mathbf{x})$	$\nabla \cdot \left(\mathbf{E} \nabla p_c^{(0)} \right) = 0$
	$\mathbf{u}_c^\varepsilon(\mathbf{x}, \mathbf{y}) \rightarrow \mathbf{u}_c^{(0)}(\mathbf{x}, \mathbf{y})$	$\langle \mathbf{u}_c^{(0)} \rangle_{Y_c} = -\mathbf{E} \nabla p_c^{(0)}$

Table 5.1. Main results of the two-scale asymptotic analysis on varying the order of the parameters R_n and κ .

with respect to the periodic cell Y .

Lemma 5.3.1. *The tensor \mathbf{K} is symmetric and positive definite.*

Proof. Thanks to the Lax-Milgram theorem, problem (5.37) has a unique solution in $H^1(Y_t)/\mathbb{R}$. The variational formulation associated to (5.37) reads

$$\int_{Y_t} \nabla_y \mathbf{G}^j \cdot \nabla_y \varphi \, dy - \int_{\Gamma_Y} \mathbf{e}_j \cdot \mathbf{n}_{\text{out}} \varphi \, ds = 0,$$

for any periodic $\varphi \in H^1(Y_t)$ such that $\langle \varphi \rangle_{Y_t} = 0$. Considering $\varphi = G^i$ on Y_t , the following equations hold thanks to the divergence theorem

$$\begin{aligned} 0 &= \int_{Y_t} \nabla_y \mathbf{G}^j \cdot \nabla_y G^i \, dy - \int_{\Gamma_Y} \mathbf{e}_j \cdot \mathbf{n}_{\text{out}} G^i \, ds \\ &= \int_{Y_t} \nabla_y \mathbf{G}^j \cdot \nabla_y G^i \, dy - \int_{Y_t} \nabla_y \cdot (G^i \mathbf{e}_j) \, dy \\ &= \int_{Y_t} \nabla_y \mathbf{G}^j \cdot \nabla_y G^i \, dy - \int_{Y_t} \nabla_y G^i \cdot \mathbf{e}_j \, dy. \end{aligned}$$

Therefore, the tensor \mathbf{K} can be rewritten as

$$\begin{aligned} [\mathbf{K}]_{ij} &= \delta_{ij} - \frac{1}{|Y_t|} \int_{Y_t} \nabla_y \mathbf{G}^j \cdot \mathbf{e}_i \, dy, \\ &= \delta_{ij} - \frac{1}{|Y_t|} \int_{Y_t} \nabla_y \mathbf{G}^j \cdot \nabla_y G^i \, dy, \\ &= \frac{1}{|Y_t|} \int_{Y_t} \nabla_y (G^i - y_i) \nabla_y (G^j - y_j) \, dy. \end{aligned}$$

It follows that the tensor \mathbf{K} is symmetric. To prove that the tensor is positive definite, we consider any $\boldsymbol{\lambda} \in \mathbb{R}^N$ and define

$$\phi = \sum_{i=1}^N \lambda_i G^i.$$

The function ϕ is periodic and belongs to the space $H^1(Y_t)$. We prove that \mathbf{K} is semi-positive definite:

$$|Y_t| \boldsymbol{\lambda}^T \mathbf{K} \boldsymbol{\lambda} = \int_{Y_t} |\nabla_y (\phi - \mathbf{y} \cdot \boldsymbol{\lambda})|^2 \, dy \geq 0,$$

that is true for any $\nabla_y (\phi - \mathbf{y} \cdot \boldsymbol{\lambda})$. The equality holds if and only if

$$\nabla_y \phi = \boldsymbol{\lambda}.$$

However, under the assumption of periodicity in a connected domain, $\nabla_y \phi = \boldsymbol{\lambda}$ if and only if $\nabla_y \phi = \boldsymbol{\lambda} = \mathbf{0}$. Therefore, \mathbf{K} is positive definite. □

Remark 5.3.2. *The interstitial domain Y_t has to be connected to guarantee the positive definiteness of the tensor \mathbf{K} (otherwise, it is semi-positive definite).*

Lemma 5.3.3. *If the capillary domain Y_c is connected, then the tensor \mathbf{E} is symmetric and positive definite.*

Proof. We proceed analogously as [219]. Thanks to the Lax-Milgram lemma, there exist a unique weak solution to problem (5.38), which variational formulation reads as

$$\int_{Y_c} \nu \nabla_y \mathbf{W}^j : \nabla_y \mathbf{v} \, d\mathbf{y} - \int_{Y_c} \mathbf{e}_j \cdot \mathbf{v} \, d\mathbf{y} = 0,$$

for any periodic $\mathbf{v} \in H^1(Y_c)$ such that $\nabla_y \cdot \mathbf{v} = 0$ and $\mathbf{v} \cdot \mathbf{n} = 0$ on Γ_Y . Taking $\mathbf{v} = \mathbf{W}^i$ the following identity holds:

$$\begin{aligned} |Y_c| [\mathbf{E}]_{ij} &= \int_{Y_c} \mathbf{W}^j \cdot \mathbf{e}_i \, d\mathbf{y}, \\ &= \int_{Y_c} \nu \nabla_y \mathbf{W}^j : \nabla_y \mathbf{W}^i \, d\mathbf{y}. \end{aligned}$$

Therefore the tensor is symmetric. To prove that it is positive definite, we take any $\boldsymbol{\lambda} \in \mathbb{R}^N$ and define

$$\boldsymbol{\psi} = \sum_{i=1}^N \lambda_i \mathbf{W}^i.$$

We first prove that $\boldsymbol{\lambda}^T \mathbf{E} \boldsymbol{\lambda}$ is non-negative. Indeed,

$$|Y_c| \boldsymbol{\lambda}^T \mathbf{E} \boldsymbol{\lambda} = \int_{Y_c} \nu \nabla_y \boldsymbol{\psi} : \nabla_y \boldsymbol{\psi} \, d\mathbf{y} \geq 0.$$

The equality holds if and only if $\nabla_y \boldsymbol{\psi} = 0$. Then, the following equation must be satisfied

$$\begin{aligned} 0 = \int_{Y_c} \nu \nabla_y \boldsymbol{\psi} : \nabla_y \mathbf{v} \, d\mathbf{y} - \int_{\Gamma_Y} [(\mathbf{n} \cdot \nabla_y) \boldsymbol{\psi}] \cdot \mathbf{n} (\mathbf{v} \cdot \mathbf{n}) \, ds &= \int_{Y_c} \boldsymbol{\lambda} \cdot \mathbf{v} \, d\mathbf{y}, \\ \forall \mathbf{v} \in H^1(Y_c) : \nabla_y \cdot \mathbf{v} &= 0. \end{aligned} \quad (5.40)$$

Since (5.40) holds for any \mathbf{v} in the appropriate space defined above, it is valid also for $\mathbf{v} = \boldsymbol{\lambda}$. Therefore, we conclude that (5.40) is true if and only if $\boldsymbol{\lambda} = \mathbf{0}$ and state that \mathbf{E} is positive definite. \square

Remark 5.3.4. When the domain Y_c is not connected, then the unique solution to problem (5.38) is $\mathbf{W}^j = \mathbf{0}$ and $P^j = y_j$. In this case the tensor \mathbf{E} is zero.

Remark 5.3.5. The tensor $\bar{\kappa} \mathbf{K} + \frac{|Y_c|}{|Y_t|} \mathbf{E}$ is symmetric and positive definite since it is the sum of two symmetric and positive definite tensors.

Remark 5.3.6. If one of the two domains (Ω_c^ε or Ω_t^ε) is not connected, then $p_c = p_t$.

5.3.2 Limit problems

In this section, we show the link between the different models. We assume that both interstitium and capillary phases are connected so that the 3 models complemented with Dirichlet, Neumann or Robin conditions are well-posed.

Equivalence of model 2 and 3

First consider model (2) and (3) with Dirichlet conditions. Assuming that both \bar{R}_n and κ are of order of magnitude ε , model (3) reads as follows:

$$\varepsilon \nabla \cdot (\bar{\kappa} \mathbf{K} \nabla p_t) = \varepsilon \frac{\bar{R}_n |\Gamma_Y|}{|Y_t|} (p_t - p_c) \quad \text{in } \Omega, \quad (5.41a)$$

$$\nabla \cdot (\mathbf{E} \nabla p_c) = \varepsilon \frac{\bar{R}_n |\Gamma_Y|}{|Y_c|} (p_c - p_t) \quad \text{in } \Omega, \quad (5.41b)$$

$$p_t|_{\partial\Omega} = p_{t,\infty}, \quad p_c|_{\partial\Omega} = p_{c,\infty}, \quad \text{on } \partial\Omega. \quad (5.41c)$$

It is clear that (5.41b) is not a singular perturbation of the operator $\nabla \cdot (\mathbf{E} \nabla \cdot)$ in the sense of Kato [221] and thus the solution to problem (5.41) tends to the solution to the following problem, which is nothing that model (3):

$$\nabla \cdot (\bar{\kappa} \mathbf{K} \nabla p_t) = \frac{\bar{R}_n |\Gamma_Y|}{|Y_t|} (p_t - p_c) \quad \text{in } \Omega,$$

$$\nabla \cdot (\mathbf{E} \nabla p_c) = 0 \quad \text{in } \Omega,$$

$$p_t|_{\partial\Omega} = p_{t,\infty}, \quad p_c|_{\partial\Omega} = p_{c,\infty}, \quad \text{on } \partial\Omega.$$

Equivalence of model 1 and 2

Considering \bar{R}_n of the order of ε^{-1} and $\bar{\kappa}$ of the order of 1, model (2) of Table 5.1 reads then

$$\varepsilon \nabla \cdot (\bar{\kappa} \mathbf{K} \nabla p_t) = \frac{\bar{R}_n |\Gamma_Y|}{|Y_t|} (p_t - p_c) \quad \text{in } \Omega, \quad (5.42a)$$

$$\varepsilon \nabla \cdot (\mathbf{E} \nabla p_c) = \frac{\bar{R}_n |\Gamma_Y|}{|Y_c|} (p_c - p_t) \quad \text{in } \Omega \quad (5.42b)$$

$$p_t|_{\partial\Omega} = p_{t,\infty}, \quad p_c|_{\partial\Omega} = p_{c,\infty}, \quad \text{on } \partial\Omega. \quad (5.42c)$$

Here the asymptotic analysis is much trickier since both equations (5.42a)–(5.42b) are singular perturbation of the div-grad operator. In particular, a delicate asymptotic analysis makes appear a exponential decay of the $p_t - p_c$ from the boundary, showing that out of the vicinity of the tumor boundary, both pressures are equal. The details of this results are given in [222], however we expose here the main arguments in the simple case where $\bar{\kappa} \mathbf{K}$ and \mathbf{E} are colinear to the identity, that is for a $\lambda, \mu \neq 0$:

$$\bar{\kappa} \mathbf{K} = \frac{1}{\lambda} \mathbf{I}, \quad \mathbf{E} = \frac{1}{\mu} \mathbf{I}.$$

Then simple calculation shows that

$$\Delta(p_t - p_c) = \frac{\bar{R}_n}{\varepsilon} \left(\lambda \frac{|\Gamma_Y|}{|Y_t|} + \mu \frac{|\Gamma_Y|}{|Y_t|} \right) (p_t - p_c) \quad \text{in } \Omega, \quad (5.43a)$$

$$(p_t - p_c)|_{\partial\Omega} = p_{t,\infty} - p_{c,\infty}, \quad \text{on } \partial\Omega. \quad (5.43b)$$

It is well-known, especially in conduction theory [223] that problem (5.43) makes appear a so-called skin depth effect: the pressure difference $p_t - p_c$ decays exponentially fast from the boundary. More precisely, denoting by α the factor given by

$$\alpha = \sqrt{\bar{R}_n \left(\lambda \frac{|\Gamma_Y|}{|Y_t|} + \mu \frac{|\Gamma_Y|}{|Y_t|} \right)},$$

hence in the local coordinates near the boundary

$$p_t - p_c = (p_{t,\infty} - p_{c,\infty})e^{-\frac{\alpha}{\varepsilon}x_n} + O(\varepsilon),$$

where x_n is the normal variable with respect to the tumor boundary.

Interestingly, we thus obtain that in this asymptotic regime, the solution to model (2) with Dirichlet boundary conditions can be approached by the solution to model (1) with the following appropriate boundary condition

$$\begin{aligned} \nabla \cdot \left(\left(\lambda + \mu \frac{|Y_c|}{|Y_t|} \right) \nabla p \right) &= 0, & \text{in } \Omega \\ p|_{\partial\Omega} &= p_{t,\infty} - \frac{|\Gamma_Y|}{|Y_t|} / \left(\frac{|\Gamma_Y|}{|Y_t|} + \frac{|\Gamma_Y|}{|Y_c|} \right) (p_{t,\infty} - p_{c,\infty}), & \text{on } \partial\Omega. \end{aligned}$$

The generalisation to the case of symmetric definite positive tensors \mathbf{K} and \mathbf{E} is given in [222]. The result involves Riemannian geometry results which are far from the scope of this chapter, however the general idea of the exponential decay of the pressure difference remains.

5.4 Derivation of the macro-scale models

We derive the macroscopic models using formal two-scale homogenization according to the magnitude of the permeability of the vessel wall and of the interstitial hydraulic conductivity, namely

- Model 1: $\gamma = 0, \eta = 0$;
- Model 2: $\gamma = 1, \eta = 0$;
- Model 3: $\gamma = 2, \eta = 1$.

The differential operators are then

$$\nabla = \nabla_{\mathbf{x}} + \frac{1}{\varepsilon} \nabla_{\mathbf{y}}, \quad \nabla^2 = \nabla_{\mathbf{x}}^2 + \frac{2}{\varepsilon} \nabla_{\mathbf{x}} \cdot \nabla_{\mathbf{y}} + \frac{1}{\varepsilon^2} \nabla_{\mathbf{y}}^2.$$

The fluid transport in the tumor tissue can be then written as follows:

$$\varepsilon^3 \bar{\nu} \nabla_{\mathbf{x}}^2 \mathbf{u}_c + 2\varepsilon^2 \bar{\nu} \nabla_{\mathbf{y}} \cdot \nabla_{\mathbf{x}} \mathbf{u}_c + \varepsilon \bar{\nu} \nabla_{\mathbf{y}}^2 \mathbf{u}_c = \varepsilon \nabla_{\mathbf{x}} p_c + \nabla_{\mathbf{y}} p_c \quad \text{in } \Omega_c^\varepsilon \times Y_c, \quad (5.44)$$

$$\varepsilon \nabla_{\mathbf{x}} \cdot \mathbf{u}_c + \nabla_{\mathbf{y}} \cdot \mathbf{u}_c = 0 \quad \text{in } \Omega_c^\varepsilon \times Y_c, \quad (5.45)$$

$$\varepsilon^2 \nabla_{\mathbf{x}}^2 p_t + 2\varepsilon \nabla_{\mathbf{x}} \cdot \nabla_{\mathbf{y}} p_t + \nabla_{\mathbf{y}}^2 p_t = 0 \quad \text{in } \Omega_t^\varepsilon \times Y_t. \quad (5.46)$$

The interface conditions vary according to the value of γ and η :

$$-\varepsilon^2 \bar{\nu} [(\mathbf{n} \cdot \nabla_{\mathbf{x}}) \mathbf{u}_c] \cdot \mathbf{n} - \varepsilon \bar{\nu} [(\mathbf{n} \cdot \nabla_{\mathbf{y}}) \mathbf{u}_c] \cdot \mathbf{n} + p_c - p_t = \frac{1}{\varepsilon \gamma \bar{R}_{\mathbf{n}}} \mathbf{u}_c \cdot \mathbf{n} \quad \text{on } \Gamma^\varepsilon \times \Gamma_Y, \quad (5.47)$$

$$-\varepsilon \nu [(\mathbf{n} \cdot \nabla_{\mathbf{x}}) \mathbf{u}_c] \cdot \boldsymbol{\tau} - \nu [(\mathbf{n} \cdot \nabla_{\mathbf{y}}) \mathbf{u}_c] \cdot \boldsymbol{\tau} = \varepsilon \frac{\nu}{R_\tau} \mathbf{u}_c \cdot \boldsymbol{\tau} \quad \text{on } \Gamma^\varepsilon \times \Gamma_Y, \quad (5.48)$$

$$-\varepsilon^\eta \bar{\kappa} \nabla_{\mathbf{x}} p_t \cdot \mathbf{n} - \varepsilon^{\eta-1} \bar{\kappa} \nabla_{\mathbf{y}} p_t \cdot \mathbf{n} = \mathbf{u}_c \cdot \mathbf{n} \quad \text{on } \Gamma^\varepsilon \times \Gamma_Y. \quad (5.49)$$

Case 1: permeable vessel walls i.e. $\gamma = 0, \eta = 0$.

When $\gamma = 0$, equation (5.47) reads as

$$-\varepsilon^2 \bar{\nu}[(\mathbf{n} \cdot \nabla_{\mathbf{x}})\mathbf{u}_c] \cdot \mathbf{n} - \varepsilon \bar{\nu}[(\mathbf{n} \cdot \nabla_{\mathbf{y}})\mathbf{u}_c] \cdot \mathbf{n} + p_c - p_t = \frac{1}{\bar{R}_{\mathbf{n}}}\mathbf{u}_c \cdot \mathbf{n} \quad \text{on } \Gamma^\varepsilon \times \Gamma_Y$$

Identifying the terms of order ε^0 .

In the interstitium, equating coefficients of ε^0 in (5.46) and (5.49) gives

$$\nabla_{\mathbf{y}}^2 p_t^{(0)} = 0 \quad \text{in } \Omega_t^\varepsilon \times Y_t, \quad (5.50)$$

$$\bar{\kappa} \nabla_{\mathbf{y}} p_t^{(0)} \cdot \mathbf{n} = 0 \quad \text{on } \Gamma^\varepsilon \times \Gamma_Y, \quad (5.51)$$

with $p_t^{(0)}$ periodic in \mathbf{y} . Therefore $p_t^{(0)}$ does not depend on the local scale, i.e. $p_t^{(0)} = p_t^{(0)}(\mathbf{x})$.

Equating coefficients of ε^0 in the capillaries gives:

$$\nabla_{\mathbf{y}} p_c^{(0)} = 0 \quad \text{in } \Omega_c^\varepsilon \times Y_c, \quad (5.52)$$

$$\nabla_{\mathbf{y}} \cdot \mathbf{u}_c^{(0)} = 0 \quad \text{in } \Omega_c^\varepsilon \times Y_c, \quad (5.53)$$

$$\mathbf{u}_c^{(0)} \cdot \mathbf{n} = \bar{R}_{\mathbf{n}}(p_c^{(0)} - p_t^{(0)}) \quad \text{on } \Gamma^\varepsilon \times \Gamma_Y, \quad (5.54)$$

$$[(\mathbf{n} \cdot \nabla_{\mathbf{y}})\mathbf{u}_c^{(0)}] \cdot \boldsymbol{\tau} = 0 \quad \text{on } \Gamma^\varepsilon \times \Gamma_Y, \quad (5.55)$$

plus periodic boundary conditions on $p_c^{(0)}$ and $\mathbf{u}_c^{(0)}$ in \mathbf{y} . Integrating equation (5.53) we get the following condition on the pressure $p_c^{(0)}$:

$$\int_{Y_c} \nabla_{\mathbf{y}} \cdot \mathbf{u}_c^{(0)} dV = \int_{\Gamma_Y} \bar{R}_{\mathbf{n}}(p_c^{(0)} - p_t^{(0)}) dS = 0 \quad \Rightarrow \quad p_c^{(0)} = p_t^{(0)} \text{ on } \Gamma_Y,$$

since $p_t^{(0)}$ is a constant with respect to \mathbf{y} . Therefore, $p_c^{(0)}$ depends on the macroscale only and it is equal to $p_t^{(0)}(\mathbf{x})$. Moreover, condition (5.54) becomes

$$\mathbf{u}_c^{(0)} \cdot \mathbf{n} = 0 \quad \text{on } \Gamma^\varepsilon \times \Gamma_Y. \quad (5.56)$$

Identifying the terms of order ε^1 .

Equating coefficients of ε^1 in (5.46) and (5.49) yields

$$\nabla_{\mathbf{y}}^2 p_t^{(1)} = 0 \quad \text{in } \Omega_t^\varepsilon \times Y_t, \quad (5.57)$$

$$-\bar{\kappa} \nabla_{\mathbf{x}} p_t^{(0)} \cdot \mathbf{n} - \bar{\kappa} \nabla_{\mathbf{y}} p_t^{(1)} \cdot \mathbf{n} = \mathbf{u}_c^{(0)} \cdot \mathbf{n} \quad \text{on } \Gamma^\varepsilon \times \Gamma_Y, \quad (5.58)$$

where $\mathbf{u}_c^{(0)} \cdot \mathbf{n} = 0$. We exploit the linearity of system (5.57)-(5.58) and propose a solution of the form

$$p_t^{(1)} = - \sum_{j=1}^N G^j (\nabla_{\mathbf{x}} p_t^{(0)} \cdot \mathbf{e}_j) + \bar{p}_t^{(1)}, \quad (5.59)$$

where $G^j = G^j(\mathbf{y})$ satisfies the cell problem (5.37) for $j = 1, \dots, N$.

Equating coefficients of ε^1 in the capillaries yields:

$$\bar{\nu} \nabla_{\mathbf{y}}^2 \mathbf{u}_c^{(0)} = \nabla_{\mathbf{x}} p_c^{(0)} + \nabla_{\mathbf{y}} p_c^{(1)} \quad \text{in } \Omega_c^\varepsilon \times Y_c, \quad (5.60)$$

$$\nabla_{\mathbf{x}} \cdot \mathbf{u}_c^{(0)} + \nabla_{\mathbf{y}} \cdot \mathbf{u}_c^{(1)} = 0 \quad \text{in } \Omega_c^\varepsilon \times Y_c, \quad (5.61)$$

$$\mathbf{u}_c^{(1)} \cdot \mathbf{n} = \bar{R}_n(p_c^{(1)} - p_t^{(1)} - \bar{\nu}[(\mathbf{n} \cdot \nabla_{\mathbf{y}}) \cdot \mathbf{u}_c^{(0)}] \cdot \mathbf{n}) \quad \text{on } \Gamma^\varepsilon \times \Gamma_Y, \quad (5.62)$$

$$-R_\tau[(\mathbf{n} \cdot \nabla_{\mathbf{y}}) \mathbf{u}_c^{(1)}] \cdot \mathbf{n} \cdot \boldsymbol{\tau} = \mathbf{u}_c^{(0)} \cdot \boldsymbol{\tau} + R_\tau[(\mathbf{n} \cdot \nabla_{\mathbf{x}}) \mathbf{u}_c^{(0)}] \cdot \boldsymbol{\tau} \quad \text{on } \Gamma^\varepsilon \times \Gamma_Y. \quad (5.63)$$

We exploit the linearity of the system composed by (5.60)-(5.53)-(5.56)-(5.55) and propose a solution of the form:

$$\mathbf{u}_c^{(0)} = - \sum_{j=1}^N \mathbf{W}^j (\nabla_{\mathbf{x}} p_c^{(0)} \cdot \mathbf{e}_j) \quad (5.64)$$

$$p_c^{(1)} = - \sum_{j=1}^N P^j (\nabla_{\mathbf{x}} p_c^{(0)} \cdot \mathbf{e}_j) + \bar{p}^{(1)}(\mathbf{x}), \quad (5.65)$$

where (\mathbf{W}^j, P^j) solve the cell problem (5.38) for $j = 1, \dots, N$. Integrating (5.64) over Y_c , we find the leading order for the velocity $\mathbf{u}_c^{(0)}$:

$$\langle \mathbf{u}_c^{(0)} \rangle_{Y_c} = -\mathbf{E} \nabla_{\mathbf{x}} p_c^{(0)},$$

where \mathbf{E} is defined in (5.39).

Identifying the terms of order ε^2 .

Equating coefficients of ε^2 in (5.46) and (5.49) gives:

$$\nabla_{\mathbf{x}}^2 p_t^{(0)} + 2 \nabla_{\mathbf{x}} \cdot \nabla_{\mathbf{y}} p_t^{(1)} + \nabla_{\mathbf{y}}^2 p_t^{(2)} = 0 \quad \text{in } \Omega_t^\varepsilon \times Y_t, \quad (5.66)$$

$$-\bar{\kappa} \nabla_{\mathbf{x}} p_t^{(1)} \cdot \mathbf{n} - \bar{\kappa} \nabla_{\mathbf{y}} p_t^{(2)} \cdot \mathbf{n} = \mathbf{u}_c^{(1)} \cdot \mathbf{n} \quad \text{on } \Gamma^\varepsilon \times \Gamma_Y. \quad (5.67)$$

Integrating (5.66) we obtain the equation for the leading order of the interstitial pressure:

$$\nabla_{\mathbf{x}} \cdot \left(\left(\bar{\kappa} \mathbf{K} + \frac{|Y_c|}{|Y_t|} \mathbf{E} \right) \nabla_{\mathbf{x}} p_t^{(0)} \right) = 0, \quad (5.68)$$

where \mathbf{K} and \mathbf{E} are defined in (5.39).

Case 2: weakly permeable vessel walls *i.e.* $\gamma = 1, \eta = 0$.

When $\gamma = 1$, equation (5.47) becomes

$$-\varepsilon^2 \bar{\nu}[(\mathbf{n} \cdot \nabla_{\mathbf{x}}) \mathbf{u}_c] \cdot \mathbf{n} - \varepsilon \bar{\nu}[(\mathbf{n} \cdot \nabla_{\mathbf{y}}) \mathbf{u}_c] \cdot \mathbf{n} + p_c - p_t = \frac{1}{\varepsilon \bar{R}_n} \mathbf{u}_c \cdot \mathbf{n} \quad \text{on } \Gamma^\varepsilon \times \Gamma_Y.$$

This case has been previously addressed [81, 82]. We write here the formal derivation of the macroscale model for the sake of completeness. Equations in the interstitium are the same as the ones in the previous case, while equations (5.54) and (5.62) take a different form in the capillaries. Nevertheless, the cell problems defined in (5.37) and (5.38) hold.

Identifying the terms of order ε^0 .

As for the previous case, $p_t^{(0)}$ in the interstitium does not depend on the micro-scale, i.e. $p_t^{(0)} = p_t^{(0)}(\mathbf{x})$. The interface conditions for the variables $p_c^{(0)}$ and $\mathbf{u}_c^{(0)}$ read as follows:

$$\mathbf{u}_c^{(0)} \cdot \mathbf{n} = 0, \quad \text{on } \Gamma^\varepsilon \times \Gamma_Y, \quad (5.69)$$

$$[(\mathbf{n} \cdot \nabla_y) \mathbf{u}_c^{(0)}] \cdot \boldsymbol{\tau} = 0 \quad \text{on } \Gamma^\varepsilon \times \Gamma_Y. \quad (5.70)$$

Equating coefficients of ε^0 in the capillaries, equations (5.52)-(5.53)-(5.69)-(5.70) hold. Therefore, the leading order of the pressure in the capillaries depends only on the macro-scale $p_c^{(0)} = p_c^{(0)}(\mathbf{x})$.

Identifying the terms of order ε^1 .

In the interstitium, the same results found in the previous case hold.

Equating coefficients of ε^1 in the capillaries, yields

$$\bar{\nu} \nabla_y^2 \mathbf{u}_c^{(0)} = \nabla_x p_c^{(0)} + \nabla_y p_c^{(1)} \quad \text{in } \Omega_c^\varepsilon \times Y_c, \quad (5.71)$$

$$\nabla_x \cdot \mathbf{u}_c^{(0)} + \nabla_y \cdot \mathbf{u}_c^{(1)} = 0 \quad \text{in } \Omega_c^\varepsilon \times Y_c, \quad (5.72)$$

$$\mathbf{u}_c^{(1)} \cdot \mathbf{n} = \bar{R}_n (p_c^{(0)} - p_t^{(0)}) \quad \text{on } \Gamma^\varepsilon \times \Gamma_Y, \quad (5.73)$$

$$-R_\tau [(\mathbf{n} \cdot \nabla_y) \mathbf{u}_c^{(1)}] \cdot \mathbf{n} \cdot \boldsymbol{\tau} = \mathbf{u}_c^{(0)} \cdot \boldsymbol{\tau} + R_\tau [(\mathbf{n} \cdot \nabla_x) \mathbf{u}_c^{(0)}] \cdot \boldsymbol{\tau} \quad \text{on } \Gamma^\varepsilon \times \Gamma_Y. \quad (5.74)$$

Exploiting the linearity of this system, we propose a solution of the same type of (5.64) and (5.65) where (\mathbf{W}^j, P^j) solve the cell problem defined in (5.38).

Identifying the terms of order ε^2 .

In the interstitial domain, equating coefficients of ε^2 yields equations (5.66) and (5.67). We obtain the equations for the leading order by integrating (5.64), (5.73) in the capillaries, (5.66) and (5.67) in the interstitium:

$$\nabla_x \cdot (\bar{\kappa} \mathbf{K} \nabla_x p_t^{(0)}) = \frac{\bar{R}_n |\Gamma_Y|}{|Y_t|} (p_t^{(0)} - p_c^{(0)}), \quad (5.75a)$$

$$\nabla_x \cdot (\mathbf{E} \nabla_x p_c^{(0)}) = \frac{\bar{R}_n |\Gamma_Y|}{|Y_c|} (p_c^{(0)} - p_t^{(0)}). \quad (5.75b)$$

Case 3: weakly permeable walls and weakly interstitial hydraulic connectivity i.e.
 $\gamma = 2, \eta = 1$.

When $\gamma = 2$ and $\eta = 1$, equations (5.47)-(5.49) become

$$\begin{aligned} -\varepsilon^2 \bar{\nu}[(\mathbf{n} \cdot \nabla_{\mathbf{x}})\mathbf{u}_c] \cdot \mathbf{n} - \varepsilon \bar{\nu}[(\mathbf{n} \cdot \nabla_{\mathbf{y}})\mathbf{u}_c] \cdot \mathbf{n} + p_c - p_t &= \frac{1}{\varepsilon^2 \bar{R}_{\mathbf{n}}} \mathbf{u}_c \cdot \mathbf{n} && \text{on } \Gamma^\varepsilon \times \Gamma_Y, \\ -\varepsilon \bar{\kappa} \nabla_{\mathbf{x}} p_t \cdot \mathbf{n} - \bar{\kappa} \nabla_{\mathbf{y}} p_t \cdot \mathbf{n} &= \mathbf{u}_c \cdot \mathbf{n} && \text{on } \Gamma^\varepsilon \times \Gamma_Y. \end{aligned}$$

Identifying the terms of order ε^0 .

Equating the coefficients of $\varepsilon^{(0)}$, equation (5.50) holds in the interstitium and (5.52)-(5.53) hold in the capillaries.

The interface conditions for the variables $p_t^{(0)}$, $p_c^{(0)}$ and $\mathbf{u}_c^{(0)}$ read as follows:

$$-\bar{\kappa} \nabla_{\mathbf{y}} p_t^{(0)} \cdot \mathbf{n} = \mathbf{u}_c^{(0)} \cdot \mathbf{n}, \quad \text{on } \Gamma^\varepsilon \times \Gamma_Y, \quad (5.76)$$

$$\mathbf{u}_c^{(0)} \cdot \mathbf{n} = 0, \quad \text{on } \Gamma^\varepsilon \times \Gamma_Y, \quad (5.77)$$

$$[(\mathbf{n} \cdot \nabla_{\mathbf{y}})\mathbf{u}_c^{(0)}] \cdot \boldsymbol{\tau} = 0 \quad \text{on } \Gamma^\varepsilon \times \Gamma_Y. \quad (5.78)$$

Since $\mathbf{u}_c^{(0)} \cdot \mathbf{n} = 0$ on $\Gamma^\varepsilon \times \Gamma_Y$, $p_t^{(0)}$ in the interstitium does not depend on the micro-scale, i.e. $p_t^{(0)} = p_t^{(0)}(\mathbf{x})$.

Equating coefficients of ε^0 in the capillaries, equations (5.52)-(5.53)-(5.77)-(5.78) hold. Therefore, the leading order of the pressure in the capillaries depends only on the macro-scale $p_c^{(0)} = p_c^{(0)}(\mathbf{x})$.

Identifying the terms of order ε^1 .

Equating coefficients of ε^1 , equation (5.57) holds in the interstitium while equations (5.60)-(5.61) hold in the capillaries.

The interface conditions for the variables $p_t^{(1)}$, $p_c^{(1)}$ and $\mathbf{u}_c^{(1)}$ read as follows:

$$-\bar{\kappa} \nabla_{\mathbf{x}} p_t^{(0)} \cdot \mathbf{n} - \bar{\kappa} \nabla_{\mathbf{y}} p_t^{(1)} \cdot \mathbf{n} = \mathbf{u}_c^{(1)} \cdot \mathbf{n}, \quad \text{on } \Gamma^\varepsilon \times \Gamma_Y, \quad (5.79)$$

$$\mathbf{u}_c^{(1)} \cdot \mathbf{n} = 0, \quad \text{on } \Gamma^\varepsilon \times \Gamma_Y, \quad (5.80)$$

$$-R_\tau [(\mathbf{n} \cdot \nabla_{\mathbf{y}})\mathbf{u}_c^{(1)}] \cdot \mathbf{n} \cdot \boldsymbol{\tau} = \mathbf{u}_c^{(0)} \cdot \boldsymbol{\tau} + R_\tau [(\mathbf{n} \cdot \nabla_{\mathbf{x}})\mathbf{u}_c^{(0)}] \cdot \boldsymbol{\tau} \quad \text{on } \Gamma^\varepsilon \times \Gamma_Y. \quad (5.81)$$

In the interstitium, since $\mathbf{u}_c^{(1)} \cdot \mathbf{n} = 0$ on $\Gamma^\varepsilon \times \Gamma_Y$, the same results for $p_t^{(1)}$ found in the previous cases hold.

In the capillaries, we exploit the linearity of the system (5.60)-(5.53)-(5.77)-(5.78) and propose a solution for $\mathbf{u}_c^{(0)}$ and $p_c^{(1)}$ of the same type of (5.64) and (5.65) where (\mathbf{W}^j, P^j) solve the cell problem defined in (5.38).

Identifying the terms of order ε^2 .

Equating coefficients of ε^2 in the interstitium, we obtain (5.66) and the following interface condition:

$$-\bar{\kappa}\nabla_{\mathbf{x}}p_t^{(1)} \cdot \mathbf{n} - \bar{\kappa}\nabla_{\mathbf{y}}p_t^{(2)} \cdot \mathbf{n} = \mathbf{u}_c^{(2)} \cdot \mathbf{n}, \quad \text{on } \Gamma^\varepsilon \times \Gamma_Y. \quad (5.82)$$

Equating coefficients of ε^2 in (5.48), the following interface condition holds:

$$\mathbf{u}_c^{(2)} \cdot \mathbf{n} = \bar{R}_{\mathbf{n}} \left(p_c^{(0)} - p_t^{(0)} \right), \quad \text{on } \Gamma^\varepsilon \times \Gamma_Y. \quad (5.83)$$

Integrating equations (5.66) and (5.82) we obtain the equation for the leading order of the interstitial pressure:

$$\nabla_{\mathbf{x}} \cdot \left(\bar{\kappa} \mathbf{K} \nabla_{\mathbf{x}} p_t^{(0)} \right) = \frac{\bar{R}_{\mathbf{n}} |\Gamma_Y|}{|Y_t|} \left(p_t^{(0)} - p_c^{(0)} \right).$$

Integrating equation (5.64) and (5.80), we obtain the leading order for the pressure in the capillaries:

$$\nabla \cdot (\mathbf{E} \nabla p_c) = 0.$$

5.5 Numerical convergence of the multiscale model to the homogenized models (2D)

The purpose of 2D simulations is to prove the numerical convergence of the multiscale model to the homogenized ones, considering model 1 and model 2. Indeed, the large number of degrees of freedom required by the multiscale model makes the 3D simulations infeasible.

We ran the original multi-scale model for different values of ε , considering models 1 and 2 and compared the solutions to the two respective homogenized problems. In the two cases, the computational domain was set as the unitary square $(0, 1)^2$ and we assumed that it had a periodic structure with circular cells of radius $0.25 \cdot \varepsilon$. We considered values of ε in $\{\frac{1}{5}, \frac{1}{10}, \frac{1}{15}, \frac{1}{20}, \frac{1}{30}\}$. We denote by $(p_i^\varepsilon, \mathbf{u}_i^\varepsilon)$ the solution to the multi-scale model and by (p_i, \mathbf{u}_i) the solutions to the homogenized models ($i = t, c$). The multiscale model was solved using a subdomain iterative method based on a Dirichlet-Neumann domain decomposition technique [224, 215] as explained in algorithm 1. The equations were discretized using the Finite Elements Method, using linear polynomials (\mathbb{P}_1) for the pressures $p_t^\varepsilon, p_c^\varepsilon$ and quadratic polynomials (\mathbb{P}_2) for the blood velocity \mathbf{u}_c^ε . We set Dirichlet boundary conditions with $p_t^\varepsilon = p_t = p_c = p_\infty$ on $\partial\Omega$:

$$p_\infty = \begin{cases} \sin(\pi x) & \text{if } y = 1, 0 < x < 1, \\ -\sin(\pi x) & \text{if } y = 0, 0 < x < 1, \\ 0 & \text{if } x = 0, 0 < y < 1 \vee x = 1, 0 < y < 1. \end{cases}$$

Fig. 5.3 shows an example of the solutions to the multiscale model and to the homogenized models when $\varepsilon = 1/10$. The first and second columns provide the solution to the multiscale model (when $\gamma = 0$ and 1, respectively), where p_c^ε belongs to Ω_c^ε and p_t^ε belongs to Ω_t^ε . The homogenized solutions (in the third and fourth columns) have the same trend as the solution to the original mul-

Algorithm 1 Domain decomposition method for the resolution of the multiple scale model.

Input: Initial guess for λ , positive relaxation parameter θ .

1: **while** err > tol **do**

2: find the solution $p_t^{\varepsilon, n+1}$ to the interstitial problem:

$$\begin{aligned} \nabla^2 p_t^{\varepsilon, n+1} &= 0 && \text{in } \Omega_t^\varepsilon \\ -\kappa \nabla p_t^{\varepsilon, n+1} &= \lambda^n && \text{on } \Gamma^\varepsilon \\ p_t^{\varepsilon, n+1} &= p_\infty && \text{on } \Gamma_t^\varepsilon \end{aligned}$$

3: find the solution $(\mathbf{u}_c^{\varepsilon, n+1}, p_c^{\varepsilon, n+1})$ to the capillary problem:

$$\begin{aligned} \bar{\nu} \varepsilon^2 \nabla^2 \mathbf{u}_c^{\varepsilon, n+1} &= \nabla p_c^{\varepsilon, n+1}, & \nabla \cdot \mathbf{u}_c^{\varepsilon, n+1} &= 0 && \text{in } \Omega_c^\varepsilon \\ -\bar{\nu} \varepsilon^2 [(\mathbf{n} \cdot \nabla) \mathbf{u}_c^{\varepsilon, n+1}] \cdot \mathbf{n} + p_c^{\varepsilon, n+1} &= \frac{1}{\varepsilon \gamma \bar{R}_n} \mathbf{u}_c^{\varepsilon, n+1} \cdot \mathbf{n} + p_t^{\varepsilon, n+1} && \text{on } \Gamma^\varepsilon \\ -[(\mathbf{n} \cdot \nabla) \mathbf{u}_c^{\varepsilon, n+1}] \cdot \boldsymbol{\tau} &= R_\tau \mathbf{u}_c^{\varepsilon, n+1} \cdot \boldsymbol{\tau} && \text{on } \Gamma^\varepsilon \end{aligned}$$

4: compute λ^{n+1} and the error:

$$\begin{aligned} \lambda^{n+1} &= \theta (\mathbf{u}_c^{\varepsilon, n+1} \cdot \mathbf{n}) + (1 - \theta) \lambda^n \\ \text{err} &= \int_{\Gamma^\varepsilon} |\lambda^{n+1} - \lambda^n| \end{aligned}$$

5: **end while**

tiscale model in the entire domain Ω . In 2D, the solutions to the two homogenized models are equal because the tensor \mathbf{E} is null.

We showed numerically that p_t^ε converges to p_t strongly in $L^2(\Omega_t^\varepsilon)$ and that p_c^ε converges to p_c in $L^2(\Omega_c^\varepsilon)$, as proven in [219]. We noticed that the velocities converge weakly with respect to the L^2 -norms. To analyze convergence, we defined the following quantities:

$$e_{i, L^2}^\varepsilon = \frac{\|p_i^\varepsilon - p_i\|_{L^2(\Omega_i^\varepsilon)}}{\|p_i\|_{L^2(\Omega)}}, \quad e_{i, L^\infty}^\varepsilon = \|p_i^\varepsilon - p_i\|_{L^\infty(\Omega_i^\varepsilon)}, \quad \text{with } i = t, c.$$

Figure 5.4A shows the pattern of the errors. Indeed, the L^2 -errors decrease linearly with respect to $1/\varepsilon$. Figure 5.4B provides the pointwise differences between the solution to the multiscale model and the solution to the homogenized model, i.e. $|p_c - p_c^\varepsilon|$ in Ω_c^ε and $|p_t - p_t^\varepsilon|$ in Ω_t^ε . The peaks of the errors are in correspondence to the boundary between the two subdomains Γ^ε . The oscillations of the pointwise error can be smoothed thanks to the correctors.

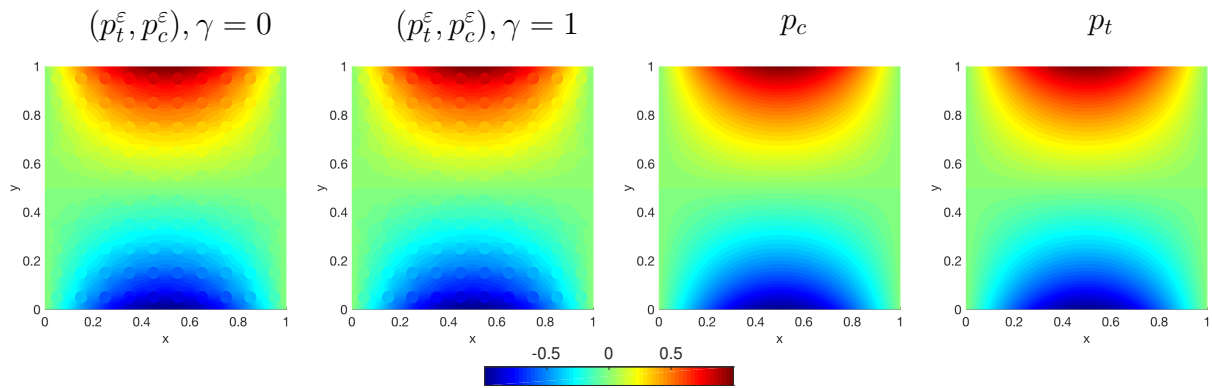


Figure 5.3. Example of the solutions to the multiscale model relative to model 1 (first column), and model 2 (second column) when $\varepsilon = 1/10$, compared with the solutions to the homogenized model (third and fourth columns). In the first two columns, p_c^ε belongs to the domain Ω_c^ε , corresponding to the circles, while p_t^ε belongs to the outer subdomain corresponding to Ω_t^ε .

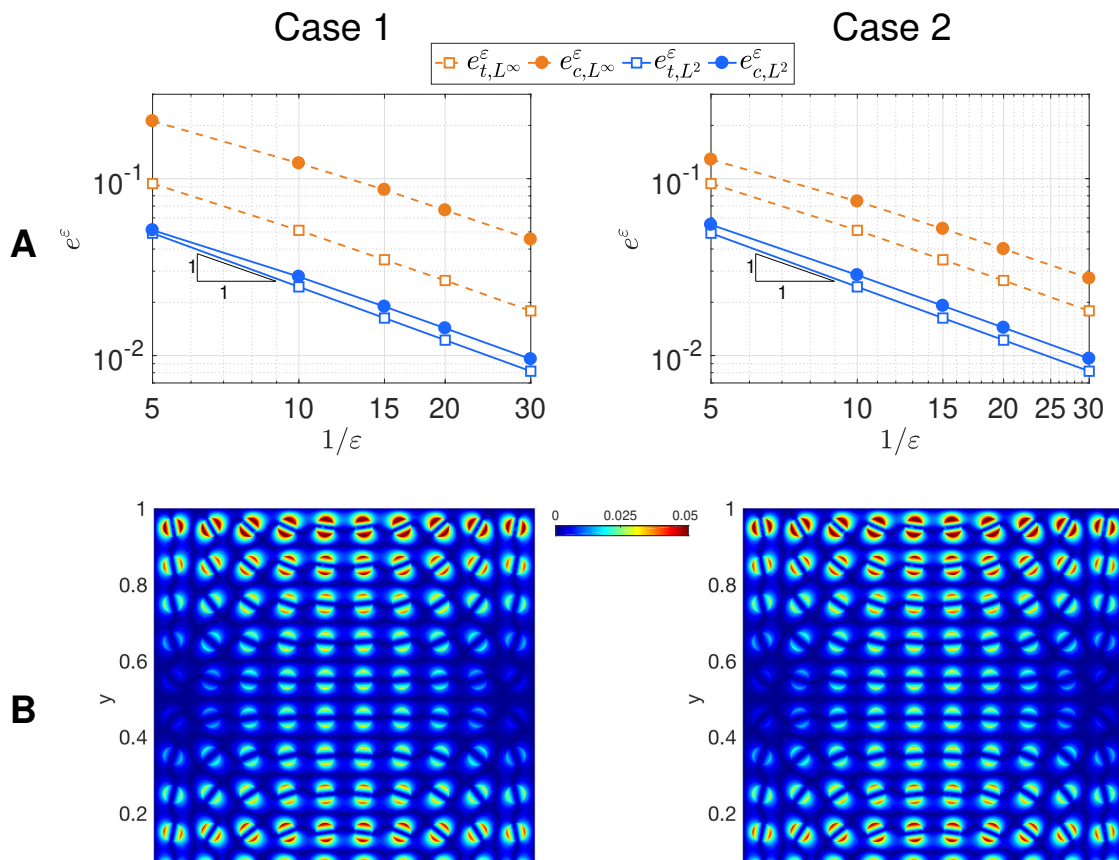


Figure 5.4. (A) numerical convergence of the multiscale problem to the homogenized model 1 (left) and homogenized model 2 (right). (B) example of pointwise differences of the capillary and interstitial pressures ($|p_c^\varepsilon - p_c|$ in the capillaries, $|p_t^\varepsilon - p_t|$ in the interstitial domain) between the multiscale problem and the respective homogenized models when $\varepsilon = 1/10$.

5.6 Numerical simulations

The Galerkin Finite Elements Method was used to discretize the equations in order to test the homogenized model 2. 3D simulations were run in order to analyze the impact of the micro-scale geometry on the homogenized solutions and the influence of the vessel permeability R_n on the fluid transport. Regarding the homogenized models, the following strategy has been adopted:

- The periodic cell was considered as the unit cube $(0,1)^3$ in \mathbb{R}^3 . The domain was divided in two regions (Y_t and Y_c) and the software Gmsh [87] was used to perform the triangulation \mathcal{T}_h . Problem (5.38) was discretized with the Galerkin Finite Elements Method using FreeFem++ [86]. Piecewise linear polynomials (\mathbb{P}_1) were used for the variable P^j . For the variable \mathbf{W}^j , we used piecewise linear polynomials with bubbles ($\mathbb{P}_{1b} = \{v \in H^1(\Omega) : \forall K \in \mathcal{T}_h \quad v|_K \in \mathbb{P}_1 \oplus \text{Span}\{\lambda_0^K \lambda_1^K \lambda_2^K \lambda_3^K\}\}$, where $\lambda_j^K, j = 0, \dots, N$ are the 4 barycentric coordinate functions of the element K). Problem (5.37) was solved on the domain Y_t using piecewise linear polynomials (\mathbb{P}_1) for the variable G^j .
- The tensors \mathbf{K} and \mathbf{E} were computed according to (5.39).
- The homogenized model was simulated on the normalized sphere of radius 0.5. Models in Table 5.1 were simulated using the Galerkin Finite Elements Method. Quadratic piecewise elements (\mathbb{P}_2) were used for both p_t and p_c .

5.6.1 Cell problems: tensor properties varying the microstructure

The tensors \mathbf{K} and \mathbf{E} defined in (5.39) have different properties according to the microstructure. To analyze them, we solved equations (5.37) and (5.38) in the unitary cell, i.e. the cube $(0,1)^3 \subset \mathbb{R}^3$. Different geometric configurations for the domains Y_t and Y_c were tested (Figure 5.5).

Table 5.2 provides the values of the elements in the two tensors \mathbf{K} and \mathbf{E} . These results confirm the analysis done in Section 5.3.1. Indeed, the tensors \mathbf{K} and \mathbf{E} are symmetric and positive definite when the two domains are connected (Fig. 5.5a, 5.5b and 5.5c). When the capillaries are not connected in all the directions (Fig. 5.5d, 5.5e), the tensor \mathbf{E} is semi-positive definite as the solution to the cell problems (5.37) is trivial: $\mathbf{W}^j = 0$ and $P^j = \mathbf{e}_j, j = 1, 2, 3$. Figure 5.5 provides the values of the interstitial and capillary volume fractions ($|Y_t|$ and $|Y_c|$, respectively) and of the vascular surface Γ_Y .

5.6.2 Macroscopic dynamic of fluid transport in tumors

We eventually considered realistic parameters to test model (2). The homogenized model was tested with a tumor considered as a sphere of normalized radius 0.5. Table 5.3 provides the values of the parameters of the model. Regarding the interstitial hydraulic conductivity k_t , the vascular permeability L_p and the tumor characteristic length L , we considered values relative to different tissues, as summarized in Tables 5.4, 5.5 and 5.6, respectively. Simulations were run considering

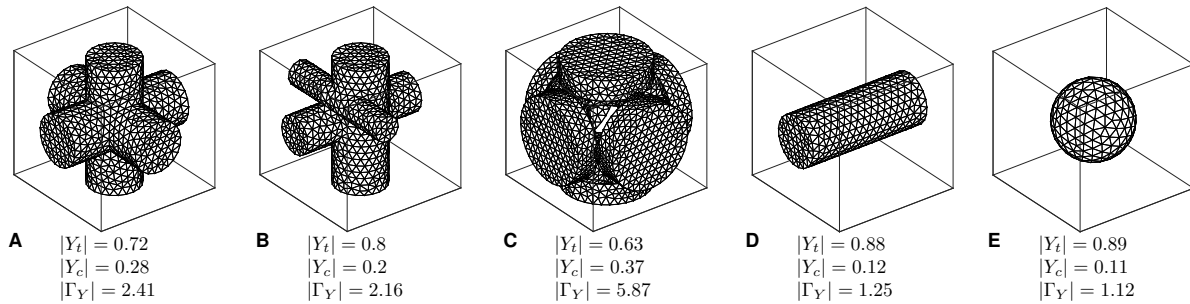


Figure 5.5. Different structures of the unit periodic cell with the respective volume and surface fractions. The mesh represents the capillary domain Y_c , while the difference between the box and the mesh is the interstitial compartment Y_t .

	K_{11}	K_{12}	K_{13}	K_{21}	K_{22}	K_{23}	K_{31}	K_{32}	K_{33}
A	0.808	7.5e-5	7.89e-6	7.5e-5	0.808	5.49e-5	7.89e-6	5.49e-5	0.808
B	0.877	-1.76e-3	3.91e-3	-1.76e-3	0.814	2.29e-3	3.91e-3	2.29e-3	0.933
C	0.72	-1.09e-4	1.03e-4	-1.09e-4	0.72	3.98e-5	1.03e-4	3.98e-5	0.72
D	1	-3.19e-8	-9.81e-8	-3.19e-8	0.895	1.01e-4	-9.81e-8	1.01e-4	0.895
E	0.954	-4.69e-5	5.2e-5	-4.69e-5	0.954	8.14e-5	5.2e-5	8.14e-5	0.954
	E_{11}	E_{12}	E_{13}	E_{21}	E_{22}	E_{23}	E_{31}	E_{32}	E_{33}
A	2.2e-3	8e-6	-1.1e-6	8e-6	2.2e-3	-1.3e-5	-1.1e-6	-1.3e-5	2.2e-3
B	9.5e-4	8.1e-7	2.3e-5	8.1e-7	1.8e-4	7.7e-6	2.3e-5	7.7e-6	2.9e-3
C	4.0e-4	-8.7e-7	-7.4e-7	-8.7e-7	4.0e-4	-2.7e-6	-7.4e-7	-2.7e-6	4.0e-4
D	4.7e-3	0	0	0	0	0	0	0	0
E	0	0	0	0	0	0	0	0	0

Table 5.2. Values of the tensors K and E for the different microstructures depicted in Fig. 5.5.

different microstructures, namely the ones shown in Figs 5.5a-c. Dirichlet boundary conditions were considered for the interstitial and capillary pressure, specifically $p_{t,\infty} = 0$ and $p_{c,\infty} = 1$ (normalized values).

Parameter influence

First, we looked at the behaviour of the solution varying the parameters k_t , L_p and L . Examples of solutions as a function of the radius are shown in Fig. 5.6. In this case, we considered the microstructure of Fig. 5.5c. Results relative to the interstitial pressure and velocity were in agreement with the ones found in [186], where the authors considered the following model:

$$\nabla \cdot (\mathbf{K} \nabla p_t) = \frac{\bar{R}_n S}{\bar{\kappa} V} (p_t - p_c), \quad (5.84)$$

where the vascular pressure p_c is assumed to be constant and S/V is the vascular area per unit volume of the tumor. Therefore, we considered this value to be equal to $|\Gamma_Y|$. The slight differences between the results obtained from the homogenized model and Baxter and Jain model (5.84) (Figure 5.6A) are due to the different rescaling of the equation, since we considered S/V to be the vascular area per unit volume of the interstitial compartment ($|\Gamma_Y|/|Y_t|$).

The interstitial fluid pressure is large and almost constant in the centre of the tumor and has a sharp drop at the periphery for increasing values of \bar{R}_n and decreasing values of $\bar{\kappa}$. As a consequence, the interstitial fluid velocity is almost zero in the centre of the tumor (since the pressure gradient is close to zero) and large at the periphery. The microvessel fluid pressure is almost constant and close to the value at the boundary. For large values of the parameter \bar{R}_n , the capillary pressure decreases and gets closer to the interstitial fluid pressure. As a consequence, also the microvessel fluid velocity is close to zero in the centre of the tumor.

Eventually, we observed the skin depth effect of $p_c - p_t$ when the permeability of the vessel walls increases (Fig 5.6B). Indeed, the pressure difference is almost zero at the centre of the tumor and increases exponentially in correspondence of the boundary.

Microstructure

We fixed the parameter values $k_t = 1.8 \cdot 10^{-12} \text{ m}^3 \cdot \text{s} \cdot \text{kg}^{-1}$, $L_p = 1.86 \cdot 10^{-10} \text{ m}^2 \cdot \text{s} \cdot \text{kg}^{-1}$ and $L = 5 \text{ mm}$ and looked at the behaviour of the solutions relative to the different microstructures. Fig. 5.7 shows the results relative to the unitary cells of Fig 5.5A-C. In all cases, the IFP shows a sharp drop at the periphery and it equates the capillary pressure in the centre of the tumor, while the capillary pressure is approximately constant in the whole tumor. The interstitial fluid velocity \mathbf{u}_t is directed outward from the domain, while the blood velocity is directed inward. The two velocities are radially homogeneous in cases 5.7A and 5.7C, while they show asymmetries in case 5.7B due to the asymmetric microscopic structure of Fig 5.5B.

We noticed that only when the capillary subdomain is smaller than the interstitial region, the

Parameter	Description	Value	Unit	Reference
μ	blood viscosity	$4 \cdot 10^{-3}$	$\text{kg} \cdot \text{m}^{-1} \cdot \text{s}^{-1}$	[227]
d	mean intercapillary distance	$50 \cdot 10^{-6}$	m	[228]
α_{BJ}	BJS constant	1	-	-
$p_{t,\infty}$	surrounding interstitial pressure	0	mmHg	-
$p_{c,\infty}$	surrounding capillary pressure	[15,80]	mmHg	[68]

Table 5.3. Fixed parameters used to simulate IFP and IFV.

Tissue	k_t [$\text{m}^3 \cdot \text{s} \cdot \text{kg}^{-1}$]	Reference
Dog squamous cell tissue	$1.8 \cdot 10^{-12}$	[229]
Mouse mammary carcinoma	$1.88 \cdot 10^{-13}$	[230]
Hepatoma 5123 in vivo	$2.9 \cdot 10^{-15}$	[231]

Table 5.4. Values of the interstitial hydraulic conductivity k_t of different tissues.

blood velocity is larger than the interstitial fluid flow (data not shown). This is biologically relevant as the capillary volume fraction is usually within the range [16%, 50%] [225] and the average blood velocity is larger than the interstitial fluid velocity [226, 65].

Boundary conditions

Eventually, we tested model (2) with different boundary conditions. In particular, Neumann boundary conditions were considered for the capillary pressure, in order to ensure the continuity of the normal velocity in the vessels at the tumor periphery:

$$-\mathbf{E}\nabla p_c \cdot \mathbf{n} = \mathbf{u}_{c,\infty} \cdot \mathbf{n},$$

where $\mathbf{u}_{c,\infty}$ is the blood velocity in the surrounding tissue. Dirichlet boundary conditions were imposed to the interstitial pressure. Well-posedness of model (2) is guaranteed with this set of boundary conditions for $(p_t, p_c) \in H_0^1(\Omega) \times H^1(\Omega)$.

We ran experiments with different boundary conditions for the capillary pressure p_c as summarized in Table 5.7. Homogeneous Dirichlet boundary conditions were considered for the interstitial fluid pressure p_t . Figure S1 shows the results at the centre of the sphere as function of the normalized radius. The interstitial pressure increases at the centre of the tumor and equates the blood pressure in the three cases. When considering the case "Neumann 2", the blood velocity is constantly high inside the domain and the capillary pressure profile is therefore due to the gradient along the x -axis.

Tissue	L_p [$\text{m}^2 \cdot \text{s} \cdot \text{kg}^{-1}$]	Reference
Mouse mammary carcinoma	$1.86 \cdot 10^{-10}$	[230]
R3230 mammary adenocarcinoma	$4.5 \cdot 10^{-11}$	[232]
Healy rat hindquarter tissue	$2.3 \cdot 10^{-12}$	[233]

Table 5.5. Values of the vessel permeability L_p of different tissues.

Characteristic length L [mm]	Tumor volume [mm^3]	$\varepsilon = d/L$
5	4.2	0.05
10	523.6	0.01
15	4200	0.005

Table 5.6. Characteristic length (diameter) of the tumor and corresponding tumor volume and value of ε .

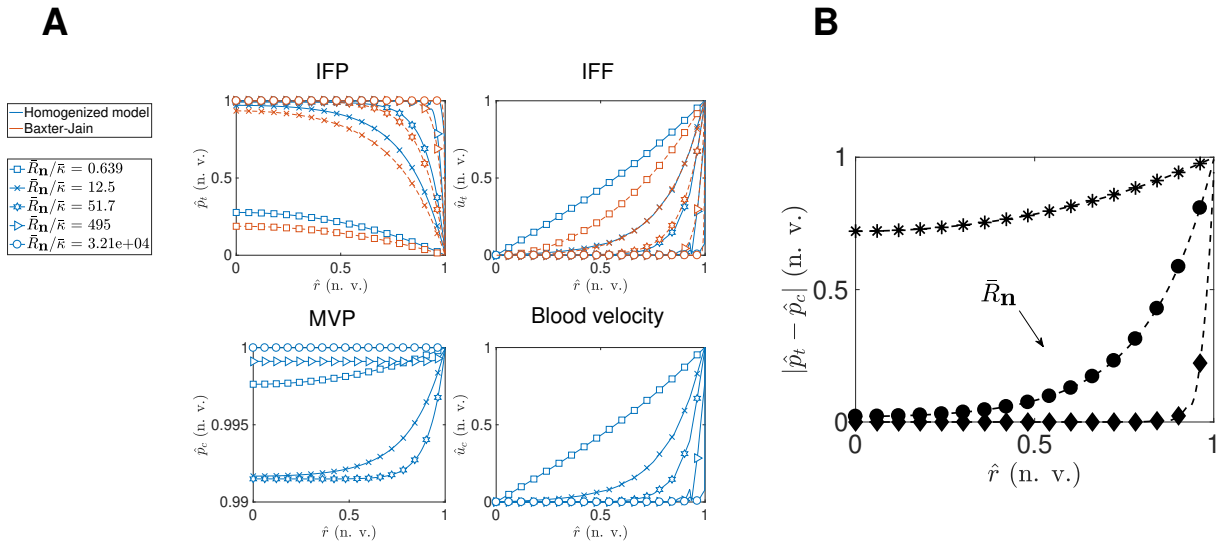


Figure 5.6. (A) Normalized values (n.v.) of interstitial fluid pressure and flow (IFP and IFF), of microvascular pressure (MVP) and of blood velocity as functions of the normalized radius \hat{r} varying the parameter $\bar{R}_n/\bar{\kappa}$. The microstructure considered in this case corresponds to Fig 5.5c. The blue lines are the simulations of the homogenized model (2) and the red lines are the results of Baxter and Jain model [186]. (B) Difference between \hat{p}_c and \hat{p}_t in normalized values (n.v.) as functions of the normalized radius \hat{r} varying the parameter \bar{R}_n and with $\bar{\kappa}$ fixed.

Experiment	Boundary condition (on $\partial\Omega$)	Parameter value (normalized)
Dirichlet	$p_c = p_{c,\infty}$	$p_{c,\infty} = 1$
Neumann 1	$-\mathbf{E}\nabla p_c \cdot \mathbf{n} = \mathbf{u}_{c,\infty} \cdot \mathbf{n}$	$\mathbf{u}_{c,\infty} = -1 \cdot 10^{-3} \mathbf{n}$
Neumann 2	$-\mathbf{E}\nabla p_c \cdot \mathbf{n} = \mathbf{u}_{c,\infty} \cdot \mathbf{n}$	$\mathbf{u}_{c,\infty} = [-1 \cdot 10^{-5}, 0, 0]^T$

Table 5.7. Different boundary conditions considered for the microvessel pressure p_c .

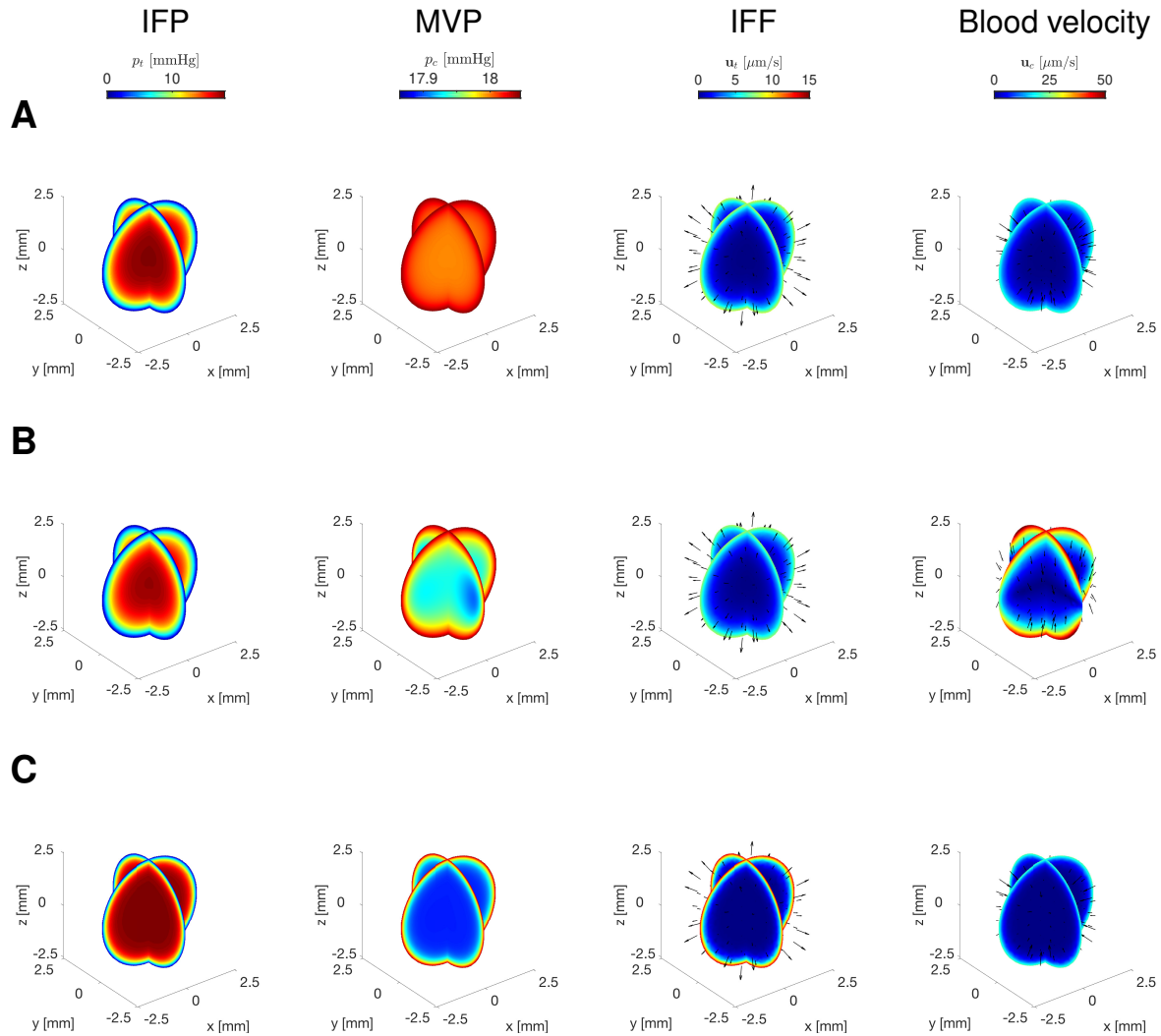


Figure 5.7. 3D slices at the centre of the sphere with the interstitial pressure (first column), the capillary pressure (second column), interstitial velocity (third column) and capillary velocity (fourth column). Results were computed using the microstructure of Fig 5.5a (A), of Fig 5.5b (B) and of Fig 5.5c (C) and setting $k_t = 1.8 \cdot 10^{-12} \text{ m}^3 \cdot \text{s} \cdot \text{kg}^{-1}$, $L_p = 1.86 \cdot 10^{-10} \text{ m}^2 \cdot \text{s} \cdot \text{kg}^{-1}$ and $L = 5 \text{ mm}$. IFP = interstitial fluid pressure, MVP = microvascular pressure, IFF = interstitial fluid flow.

5.7 Discussion

We have provided an analysis of the impact of microstructure properties of the tumor employing the homogenization theory.

First, we have described a model at the microscopic scale that couples vascular, transvascular and interstitial fluids, adopting an asymptotic expansion technique. Then, we have derived three macro-scale models according to the vessel wall permeability and the interstitial hydraulic conductivity. After having analyzed the well-posedness of the problems, we performed numerical simulations to assess some properties according to the microstructure.

Well-posedness is guaranteed when the two subdomains Y_t and Y_c are connected. When one region is not connected with respect to one axis, the fluid is not transported along this direction. For example, in Fig. 5.5e the capillary microstructure is a closed sphere, therefore there is no fluid transport in the blood vessels; in Fig. 5.5d, the vessel geometry is connected only along the x -axis that is the only direction for the capillary fluid flow. This represents a limit for the 2D simulations, as the subdomains Y_t and Y_c cannot be both connected. In this case, one among the interstitial or the vessel flow is always zero. However, tensors \mathbf{K} and \mathbf{E} can be determined by calibrating directly the homogenized models to medical imaging data.

Furthermore, we motivated the links between the various regimes and shown that model (2) covers a wide range of cases, confirming previous results [81]. In particular, we have shown that model (1) is equivalent to model (2) under certain conditions and that model (2) can be approximated to model (3) under certain assumptions on the parameters.

Eventually, we calibrated model (2) with parameters taken from the literature and analyzed their influence on the solutions. We observed that different microstructures and different sets of boundary conditions strongly impact the macroscopic dynamics of the fluids. The geometric shape of the unitary cell influences the isotropy of the capillary fluid velocity, while the vascular volume fraction affects the blood velocity. Indeed, when the capillary volume fraction $|Y_c|$ is large, the blood velocity \mathbf{u}_c is equal or lower than the interstitial fluid velocity \mathbf{u}_t . This might not be biologically relevant. On the other hand, when the capillary volume fraction is smaller the blood velocity is of higher magnitude and gets closer to the average values (around $1.62 \text{ mm} \cdot \text{s}^{-1}$ [234]). This confirms that the homogenized models are consistent with biological observations. Indeed, the vascular volume fraction lies within the values of 16% and 50%. [225, 183, 235]. Moreover, the average values of the pressures and of the velocities obtained from simulations with different sets of boundary conditions were compared against literature values. When Dirichlet-Dirichlet boundary conditions are considered, both the interstitial and the capillary pressures fit better the well-known profile of the IFP that is high at the centre of the tumor and shows a sharp drop at the periphery [186]. However, when Dirichlet-Neumann boundary conditions are considered for the interstitial and the capillary pressure, respectively, the blood velocity reaches average values closer to the literature ones. Possible improvements of our computations might be achieved by considering the correctors and by adding boundary layers, to take into account the Dirichlet boundary conditions that are imposed to

the true solution $(p_t^\varepsilon, p_c^\varepsilon)$ of the micro-scale model, but are not satisfied by the periodic solutions to the homogenized ones.

The current work focuses on the analysis of asymptotic models that describe fluid transport in tumor tissues. Fluid velocities are necessary to develop convection-diffusion models for the description of drug transport in tumor tissues. This motivated our choice of a steady-state model, as in reality, the time variation of the fluid transport is negligible with respect to the evolution of drug distribution inside the tumor. However, spatial tumor growth might be included in the model.

Further extensions might include a relaxation of the periodicity hypothesis, that might not be realistic in a biological context, as tumors are highly heterogeneous. Assuming a random distribution of the capillaries, it is possible to define properly the representative volume element to better predict the fluid flow in the tumor [236]. Moreover, rheological effects of blood should be included to model blood transport in capillaries [237].

Applications of the models include the incorporation of 3D imaging data. Images provide the microstructure of the vessel network, that is necessary to compute the correctors.

MACRO-SCALE MODEL OF NANOPARTICLE AND DRUG TRANSPORT IN THE TUMOR INTERSTITIUM

Abstract. In this chapter, we derive a time-dependent spatial model that describes nanoparticle transport in the tumor interstitium using formal two-scale asymptotic expansion. Under the hypothesis of a periodic domain, we derive a computational model that includes vascular transport, interstitial transport, and cellular uptake. Model calibration was done using drug specific parameters. Numerical simulations showed the different trends of nanoparticles (ANCs and liposomes) with respect to free drugs (docetaxel). Moreover, we provide an analysis of the impact of the tumor microenvironment on the nanoparticle and drug transport. Future applications of this model include the calibration with patient-specific data to predict nanoparticle accumulation in the tumor tissue.

Contents

6.1	Introduction	123
6.2	A microscopic model of nanoparticle transport in the tumor interstitium . . .	124
6.3	Derivation of a macroscale model of nanoparticle concentration in the tumor tissue	125
6.3.1	Two-scale asymptotic expansion of nanoparticle concentration in tumor tissues	125
6.3.2	Boundary and initial conditions	128
6.4	Numerical simulations	128
6.4.1	A 1D semi-implicit finite difference scheme	128
6.4.2	Nanoparticle and drug specific parameters	129
6.4.3	Results	133
6.5	Discussion	137

6.1 Introduction

Physiological barriers of malignant tissues, such as abnormal vasculature and dense interstitial matrix, impair a uniform distribution of nanoparticles, leading to poor efficacy of nanotherapeutics [60]. Mathematical models can describe the delivery process to the tumor to quantify nanoparticle accumulation and possibly analyze new methods to overcome the barriers.

Drug concentration in the tumor interstitium is classically modeled by a diffusion-convection-reaction equation [186]. This is the case also for nanoparticle penetration in tumors [60]. Nanoparticle penetration in tumor spheroids has been analyzed using systems of partial differential equations [52, 53] to describe the NPs transport in the tumor interstitium and the cellular uptake. Nanoparticle kinetics has been studied in more complex organisms thanks to the increasing number of available data. The impact of blood rheology and vessel permeability on the nanoparticle diffusion coefficient in blood vessels has been investigated by Gentile *et al.* [50]. Liu *et al.* [238] introduced a multi-scale model to describe the nanoparticle delivery process in the vascular environment, taking into account the probability of adhesion of nanoparticles to the vessel walls. The transvascular pathway of nanoparticles has been studied using the pore model for transcapillary exchange [239, 240, 241]. The pore size in tumor vessels is usually large enough to guarantee the extravasation of nanoparticles large up to 400 nm. However, vessel permeability might be affected by the size and by the composition of the nanoparticle or macromolecule [240]. Mathematical models have been used to investigate different properties of the nanoparticles. Shape and size affect diffusion and cellular uptake of nanoparticles [242] as well as other transport features such as margination [54, 55].

Multiple-scale approaches are often considered to take into account the complexity of tumor architecture [243, 244]. Indeed, they permit to properly describe the biological processes at the single scales and to take into account the interdependence among them, hence providing a deep analysis of the microscopic processes in a biological system. Homogenization techniques allow taking into account the microscopic features at the macroscopic dynamic, thus not requiring the discretization of the entire system that might be computationally expensive. Shipley and Chapman [81] derived different homogenized models of drug transport in tumors coupling the interstitial and blood concentrations with different transvascular exchange equations. Penta *et al.* relaxed the periodicity assumption [82].

Here, we derived a macroscale model to describe the spatial and temporal variations of the nanoparticle concentration in the tumor interstitium using two-scale asymptotic expansion. The NP concentration in the blood vessels was assumed to be saturated, hence spatial variations were neglected. Moreover, we modeled the cellular uptake of the nanoparticles. The calibration was done using drug-specific parameters. Diffusion coefficients were evaluated empirically. *In vitro* data were used to quantify the cellular uptake; *in vivo* pharmacokinetic data provided information on the permeability of the vessel walls and the nanoparticle concentration in the tumor vessels. Numerical simulations on an axisymmetric domain were performed to investigate the impact of either the tumor microscopic structure and nanoparticle properties on the NPs penetration. The results were

compared to the literature.

The qualitative analysis performed in this study is a fundamental step to prove the validity of the model. Further perspectives include the calibration of the model with individual data (such as imaging data) to predict the tumor accumulation of nanoparticles and the treatment efficacy.

6.2 A microscopic model of nanoparticle transport in the tumor interstitium

At the microscale, the domain is a medium $\Omega \in \mathbb{R}^3$ composed by the interstitium Ω_t and the capillaries Ω_c , such that $\Omega_t \cap \Omega_c = \emptyset$. The interface $\Gamma = \partial\Omega_c \cap \partial\Omega_t$ is the vascular wall.

For the microscopic model of nanoparticle transport, we assumed that the interstitial fluid velocity \mathbf{u}_t and pressure p_t as well as the microvascular pressure p_c are given functions that solve the microscopic model of fluid transport defined in section 5.2.

We assumed the nanoparticle concentration in the capillaries c_c to be saturated in Ω_c . Therefore, spatial variations of c_c were neglected and only temporal variations were considered, according to the plasma clearance rate k_c :

$$\frac{dc_c}{dt} = -k_c c_c \quad \text{in } \Omega_c \times (0, T).$$

We introduce a diffusion-convection-reaction equation for the nanoparticle concentration in the interstitium (c_t) [186, 245]. We assumed the binding between the nanoparticles and the cells to be mediated by the Her2 receptors and denoted by c_b the bounded nanoparticle concentration [53, 246].

$$\begin{aligned} \frac{\partial c_t}{\partial t} + \nabla \cdot (\mathbf{u}_t c_t) &= D_t \nabla^2 c_t - k_{\text{on}} c_t (c_r - c_b) + k_{\text{off}} c_b - k_d c_t, & \text{in } \Omega_t \times (0, T), \\ \frac{\partial c_b}{\partial t} &= k_{\text{on}} c_t (c_r - c_b) c_t - k_{\text{off}} c_b - k_{\text{int}} c_b - k_d c_b, & \text{in } \Omega_t \times (0, T). \end{aligned}$$

where D_t is the diffusion coefficient of the interstitium. The reaction coefficient depends on the binding of the nanoparticles: k_{on} is the binding rate constant, c_r is the concentration of the cell receptors. The parameter k_{off} denotes the dissociation rate constant, while k_{int} is the cell internalization rate. The rate constant of degradation of the nanoparticles is denoted by k_d .

At the interface, the transport across the tumor vessel walls can be approximated as [186, 247]

$$\begin{aligned} (c_t \mathbf{u}_t - D_t \nabla c_t) \cdot \mathbf{n} &= (c_c \mathbf{u}_c - D_c \nabla c_c) \cdot \mathbf{n} & \text{on } \Gamma \times (0, T) \\ &= L_p (p_c - p_t - \mu [(\mathbf{n} \cdot \nabla) \mathbf{u}_c] \cdot \mathbf{n}) (1 - \sigma) c_c + P (c_c - c_t), \end{aligned} \quad (6.1)$$

where σ is the filtration reflection coefficient ($0 < \sigma < 1$) and P is the diffusive vascular permeability. The first term in (6.1) accounts the convection transvascular transport, while the second term denotes the diffusive transport through the vessel walls.

Nondimensionalization

We rescaled our fields as follows:

$$\mathbf{x} = L\mathbf{x}', \quad t = \frac{L}{U}t', \quad \mathbf{u} = U\mathbf{u}', \quad p = \frac{\mu LU}{d^2}p', \quad c = Cc', \quad (6.2)$$

where L is the characteristic size of the domain, d is the vessel diameter, U is a characteristic velocity and C is a characteristic concentration. The non-dimensional nanoparticle concentration system reads as (neglecting the primes for the sake of simplicity):

$$\begin{aligned} \frac{\partial c_t}{\partial t} + \nabla \cdot (\mathbf{u}_t c_t) &= A_t \nabla^2 c_t - \lambda_t c_t (c_e - c_b) + \lambda_b c_b - \lambda_d c_t, & \text{in } \Omega_t \times (0, T), \\ \frac{\partial c_b}{\partial t} &= \lambda_t c_t (c_e - c_b) - \lambda_b c_b - \lambda_{\text{int}} c_b - \lambda_d c_b, & \text{in } \Omega_t \times (0, T), \\ (c_t \mathbf{u}_t - A_t \nabla c_t) \cdot \mathbf{n} &= (c_c \mathbf{u}_c - A_c \nabla c_c) \cdot \mathbf{n} & \text{on } \Gamma \times (0, T) \\ &= R_n (p_c - p_t - \nu [(\mathbf{n} \cdot \nabla) \mathbf{u}_c] \cdot \mathbf{n}) (1 - \sigma) c_c + \Lambda (c_c - c_t), \end{aligned}$$

where

$$A_t = \frac{D_t}{LU}, \quad c_e = \frac{c_r}{C}, \quad \lambda_t = k_{\text{on}} \frac{CL}{V_f U}, \quad \lambda_b = \frac{k_{\text{off}} L}{U}, \quad \lambda_{\text{int}} = \frac{k_{\text{int}} L}{U}, \quad \lambda_d = \frac{k_d L}{U}, \quad \Lambda = \frac{P}{U}.$$

6.3 Derivation of a macroscale model of nanoparticle concentration in the tumor tissue

6.3.1 Two-scale asymptotic expansion of nanoparticle concentration in tumor tissues

The hypotheses on the periodic domain are summarized in Section 5.3.

As for the multiscale model for fluid transport in tumor tissues, we consider $\nu = \varepsilon^2 \bar{\nu}$ and two different cases for the vessel permeability coefficient R_n according to its magnitude.

The multiscale problem associated to the nanoparticle concentration reads

$$\begin{aligned} \varepsilon^2 \frac{\partial c_t}{\partial t} + \varepsilon \nabla_y \cdot (\mathbf{u}_t c_t) + \varepsilon^2 \nabla_x \cdot (\mathbf{u}_t c_t) &= \varepsilon^2 A_t \nabla_x^2 c_t + 2A_t \varepsilon \nabla_y \cdot \nabla_x c_t + A_t \nabla_y^2 c_t \\ &\quad - \lambda_t \varepsilon^2 c_t (c_e - c_b) + \lambda_b \varepsilon^2 c_b - \lambda_d \varepsilon^2 c_t \\ &\quad \text{in } \Omega_t^\varepsilon \times Y_t \times (0, T) \end{aligned} \quad (6.3)$$

$$\begin{aligned} (\varepsilon c_t \mathbf{u}_t - \varepsilon A_t \nabla_x c_t - A_t \nabla_y c_t) \cdot \mathbf{n} &= \varepsilon^{\gamma+1} \bar{R}_n (p_c - p_t - \varepsilon^2 \bar{\nu} [(\mathbf{n} \cdot \nabla_y) \mathbf{u}_c] \cdot \mathbf{n} \\ &\quad - \varepsilon^2 \bar{\nu} [(\mathbf{n} \cdot \nabla_x) \mathbf{u}_c] \cdot \mathbf{n}) (1 - \sigma) c_c + \varepsilon^{\xi+1} \bar{\Lambda} (c_c - c_t) \\ &\quad \text{on } \Gamma^\varepsilon \times \Gamma_Y \times (0, T) \end{aligned} \quad (6.4)$$

We analyze different cases according to the value of the parameters. In particular, we derived homogenized macro-scale models according to the order of magnitude of the diffusion coefficient, the fluid velocity, the reaction term, the vessel permeability R_n and the parameter relative to the vessel permeability of the nanoparticle Λ .

Summary of the asymptotic models

We introduce the following cell problem on the Y -periodic cell variable L^i :

$$\nabla_y^2 L^i = 0, \quad \text{in } Y_t, \quad (6.5a)$$

$$\nabla_y L^i \cdot \mathbf{n} = \mathbf{e}_i \cdot \mathbf{n}, \quad \text{on } \Gamma_Y. \quad (6.5b)$$

We define the following tensor:

$$[\mathbf{D}_t]_{ij} = A_t \left(\delta_{ij} - \frac{1}{|Y_t|} \int_{Y_t} \nabla_y L^j \cdot \mathbf{e}_i \right).$$

Moreover, we define the following operator that couples the nanoparticle concentrations in the interstitium and in the capillaries, representing the transvascular transport of nanoparticles:

$$\mathcal{T}_v[c_c, c_t^{(0)}] = \bar{R}_n |\Gamma_Y| (p_c^{(0)} - p_t^{(0)}) (1 - \sigma) c_c + \bar{\Lambda} |\Gamma_Y| (c_c - c_t^{(0)})$$

We summarize here the main asymptotic models that were found:

- **Model 1:** $\gamma = \xi = 1$.

Convergence:

$$c_t^\varepsilon(\mathbf{x}, \mathbf{y}) \rightarrow c_t^{(0)}(\mathbf{x}), \quad c_b^\varepsilon(\mathbf{x}, \mathbf{y}) \rightarrow c_b^{(0)}(\mathbf{x}).$$

Equation of the leading order:

$$\begin{aligned} \frac{\partial c_t^{(0)}}{\partial t} + \left\langle \nabla \cdot (c_t^{(0)} \mathbf{u}_t^{(0)}) \right\rangle_{Y_t} &= \nabla_x \cdot (\mathbf{D}_t \nabla_x c_t^{(0)}) + \frac{1}{|Y_t|} \mathcal{T}_v[c_c, c_t^{(0)}] \\ &\quad - \lambda_t c_t^{(0)} (c_e - c_b^{(0)}) + \lambda_b c_b^{(0)} - \lambda_d c_t^{(0)}, \quad \text{in } \Omega, \\ \frac{\partial c_b^{(0)}}{\partial t} &= \lambda_t c_t^{(0)} (c_e - c_b^{(0)}) - \lambda_b c_b^{(0)} - \lambda_{\text{int}} c_b^{(0)} - \lambda_d c_b^{(0)}, \quad \text{in } \Omega. \end{aligned}$$

- **Model 2:** $\gamma = 0, \xi = 1$.

Convergence:

$$c_t^\varepsilon(\mathbf{x}, \mathbf{y}) \rightarrow c_t^{(0)}(\mathbf{x}), \quad c_b^\varepsilon(\mathbf{x}, \mathbf{y}) \rightarrow c_b^{(0)}(\mathbf{x}).$$

Equation of the leading order:

$$\begin{aligned} \frac{\partial c_t^{(0)}}{\partial t} + \left\langle \nabla \cdot (c_t^{(0)} \mathbf{u}_t^{(0)}) \right\rangle_{Y_t} &= \nabla_x \cdot (\mathbf{D}_t \nabla_x c_t^{(0)}) + (1 - \sigma) \left\langle \nabla_x \cdot (\mathbf{u}_t^{(0)} c_c) \right\rangle_{Y_t} \\ &\quad - \lambda_t c_t^{(0)} (c_e - c_b^{(0)}) + \lambda_b c_b^{(0)} - \lambda_d c_t^{(0)} \quad \text{in } \Omega \\ \frac{\partial c_b^{(0)}}{\partial t} &= \lambda_t c_t^{(0)} (c_e - c_b^{(0)}) - \lambda_b c_b^{(0)} - \lambda_{\text{int}} c_b^{(0)} - \lambda_d c_b^{(0)} \quad \text{in } \Omega \end{aligned}$$

Several other asymptotic models can be derived. For example, when $A_t = \mathcal{O}(\varepsilon)$, the resulting model includes a convection-reaction equation for the interstitial transport of nanoparticles (hence, the diffusion term can be neglected). Similarly, when $\mathbf{u}_t = \mathcal{O}(\varepsilon)$ or $\lambda_t = \mathcal{O}(\varepsilon)$, we can neglect the convective or reaction term, respectively.

Furthermore, when $\Lambda = \mathcal{O}(1)$ (i.e., $\xi = 0$), we obtain that $c_t^{(0)} = c_c$. However, this case is not

of large interest, as the diffusive permeability of the vessel walls is usually much smaller than other parameters of the model. On the other hand, it is more likely that $\Lambda = \mathcal{O}(\varepsilon^2)$ (i.e., $\xi = 2$). In this case, the term multiplying Λ can be neglected in the homogenized models.

Remark 6.3.1. We noticed that model 1 converges to model 2 under the assumption that $\bar{R}_n \rightarrow \infty$. Hence, as proved in Chapter 5, model 1 covers a wider class of equations. Hence, we'll focus on this model in the next sections.

Identifying the terms of order ε^0

Equating the terms in ε^0 in (6.3) and (6.4) we obtain

$$\begin{aligned} A_t \nabla_{\mathbf{y}}^2 c_t^{(0)} &= 0 && \text{in } Y_t \times (0, T), \\ A_t \nabla_{\mathbf{y}} c_t^{(0)} \cdot \mathbf{n} &= 0 && \text{on } \Gamma_Y \times (0, T), \end{aligned}$$

therefore $c_t^{(0)} = c_t^{(0)}(\mathbf{x})$ depends only on the macroscale variable.

Identifying the terms of order ε^1

Equating the terms in ε^1 in (6.3) and (6.4) we obtain

$$\begin{aligned} A_t \nabla_{\mathbf{y}}^2 c_t^{(1)} &= 0 && \text{in } Y_t \times (0, T), \\ A_t \nabla_{\mathbf{x}} c_t^{(0)} \cdot \mathbf{n} + A_t \nabla_{\mathbf{y}} c_t^{(0)} \cdot \mathbf{n} &= 0 && \text{on } \Gamma_Y \times (0, T). \end{aligned}$$

Therefore, we exploit the linearity of the system and propose a solution of the form

$$c_t^{(1)} = - \sum_{i=1}^N L^i \nabla_{\mathbf{x}} c_t^{(0)} \cdot \mathbf{e}_i + \bar{c}_t^{(1)}$$

where L^i depends on the fast variable \mathbf{y} and is the solution to the cell problem (6.5), while $\bar{c}_t^{(1)} = \bar{c}_t^{(1)}(\mathbf{x})$ depends on the slow variable only.

Identifying the terms of order ε^2

Equating the terms in ε^2 in (6.3) and (6.4) yields

$$\begin{aligned} \frac{\partial c_t^{(0)}}{\partial t} + \nabla_{\mathbf{x}} \cdot (c_t^{(0)} \mathbf{u}_t^{(0)}) + \nabla_{\mathbf{y}} \cdot (c_t^{(0)} \mathbf{u}_t^{(1)}) + \nabla_{\mathbf{y}} \cdot (c_t^{(1)} \mathbf{u}_t^{(0)}) &= \\ A_t \nabla_{\mathbf{x}}^2 c_t^{(0)} + 2A_t \nabla_{\mathbf{x}} \cdot \nabla_{\mathbf{y}} c_t^{(1)} + A_t \nabla_{\mathbf{y}}^2 c_t^{(2)} - \lambda_t c_t^{(0)} (c_e - c_b^{(0)}) + \lambda_b c_b^{(0)} - \lambda_d c_t^{(0)} & \text{in } Y_t \times (0, T) \\ (c_t^{(0)} \mathbf{u}_t^{(1)} + c_t^{(1)} \mathbf{u}_t^{(0)} - A_t \nabla_{\mathbf{x}} c_t^{(1)} - A_t \nabla_{\mathbf{y}} c_t^{(2)}) \cdot \mathbf{n} &= \\ \bar{R}_n (p_c^{(0)} - p_t^{(0)}) (1 - \sigma) c_c + \bar{\Lambda} (c_c - c_t^{(0)}) & \text{on } \Gamma_Y \times (0, T). \end{aligned}$$

Integrating in Y_t we obtain the following equation for the leading order

$$\begin{aligned} \frac{\partial c_t^{(0)}}{\partial t} + \left\langle \nabla \cdot (c_t^{(0)} \mathbf{u}_t^{(0)}) \right\rangle_{Y_t} &= \nabla_{\mathbf{x}} \cdot (\mathbf{D}_t \nabla_{\mathbf{x}} c_t^{(0)}) + \frac{1}{|Y_t|} \mathcal{J}_v[c_c, c_t^{(0)}] \\ &\quad - \lambda_t c_t^{(0)} (c_e - c_b^{(0)}) + \lambda_b c_b^{(0)} - \lambda_d c_t^{(0)} \quad \text{in } \Omega \end{aligned} \quad (6.6)$$

$$\frac{\partial c_b^{(0)}}{\partial t} = \lambda_t c_t^{(0)} (c_e - c_b^{(0)}) - \lambda_b c_b^{(0)} - \lambda_{\text{int}} c_b^{(0)} - \lambda_d c_b^{(0)} \quad \text{in } \Omega \quad (6.7)$$

In the following sections we will neglect the superscripts and consider c_t and c_b the leading orders $c_t^{(0)}$ and $c_b^{(0)}$, respectively.

6.3.2 Boundary and initial conditions

We assume that the boundary conditions for the nanoparticle concentration depend on their transport in the surrounding normal tissue, which is assumed to be able to absorb the fluid which comes out of the tumor [186]. Therefore, the boundary conditions read:

$$(\mathbf{D}_t \nabla c_t - \mathbf{u}_t c_t) \cdot \mathbf{n}|_{\partial\Omega^-} = (\mathbf{D}_{t,\text{ext}} \nabla c_t - \mathbf{u}_t c_t) \cdot \mathbf{n}|_{\partial\Omega^+},$$

where $\mathbf{D}_{t,\text{ext}}$ is the diffusion coefficient of the nanoparticle in the surrounding tissue.

As initial condition, we consider the concentration in the tumor interstitium to be zero:

$$c_t(\mathbf{x}, 0) = 0, \quad c_b(\mathbf{x}, 0) = 0, \quad \mathbf{x} \in \Omega.$$

6.4 Numerical simulations

6.4.1 A 1D semi-implicit finite difference scheme

The computational domain $\Omega \subset \mathbb{R}^3$ is the tumor tissue that we assumed to be a sphere. Since 3D numerical simulation were computationally expensive, we considered the formulation of equations (7.1)-(7.2) in spherical coordinates, assuming that the tumor is axisymmetric:

$$\begin{aligned} \frac{\partial(c_t)}{\partial t} + \frac{1}{r^2} \frac{\partial}{\partial r} (r^2 u_t c_t) &= \frac{1}{r^2} \frac{\partial}{\partial r} \left(\hat{D}_t \frac{\partial}{\partial r} c_t \right) + \frac{1}{|Y_t|} \mathcal{J}_v[c_c, c_t] - \lambda_t c_t (c_e - c_b) + \lambda_b c_b - \lambda_d c_t, \\ \frac{\partial c_b}{\partial t} &= \lambda_t c_t (c_e - c_b) - \lambda_b c_b - \lambda_{\text{int}} c_b - \lambda_d c_b, \end{aligned}$$

where $r \in [0, 1]$ and $t \in (0, T)$, and u_t and \hat{D}_t are respectively the interstitial fluid velocity and diffusion coefficient in spherical coordinates. Boundary conditions were set as follows:

$$\begin{aligned} u_t c_t - \hat{D}_t \frac{\partial}{\partial r} c_t \Big|_{r=0} &= 0, \\ u_t c_t - \hat{D}_t \frac{\partial}{\partial r} c_t \Big|_{r=1} &= u_t c_t - \hat{D}_{t,\text{ext}} \frac{\partial}{\partial r} c_t \Big|_{r=1}. \end{aligned}$$

A semi-implicit finite difference scheme was implemented in Matlab to run simulations. The non-dimensional radius $r \in [0, 1]$ was discretized in subintervals of dimension $h = 0.001$. The time grid was built on the interval $(0, T)$ (where $T = 48$ hours) with time step $\Delta t = 0.01$ hours. The time

variables were then normalized according to the transformation introduced in 6.2. Denoting by c_t^n and c_b^n , respectively, the interstitial and cellular concentrations at time $t = n\Delta t$, the semi-implicit scheme reads as

$$\begin{aligned}\frac{c_t^{n+1} - c_t^{*,n}}{\Delta t} &= \frac{1}{r^2} \frac{\partial}{\partial r} \left(\hat{D}_t \frac{1}{\partial r} c_t^{n+1} \right) + \frac{1}{|Y_t|} \mathcal{J}_v[c_c^n, c_t^{n+1}] - \lambda_t c_t^{n+1} (c_e - c_b^n) + \lambda_b c_b^n - \lambda_d c_t^{n+1}, \\ \frac{c_b^{n+1} - c_b^n}{\Delta t} &= \lambda_t c_t^{n+1} (c_e - c_b^{n+1}) - \lambda_b c_b^{n+1} - \lambda_{\text{int}} c_b^{n+1} - \lambda_d c_b^{n+1},\end{aligned}$$

where $c_t^{*,n}$ is the approximation of the convection term obtained with an upwind scheme. Moreover, we used a second-order central finite difference scheme to discretize the Laplacian [248, 249].

6.4.2 Nanoparticle and drug specific parameters

In this section, we estimate some parameters of the model and provide the information on the parameters that were taken from the literature. We considered three different types of drug administration: the free drugs, namely docetaxel and trastuzumab, the antibody-nanoconjugates (ANC) and the liposomal docetaxel with free trastuzumab.

6.4.2.1 Diffusion coefficient

We follow the same approach of [53] for the empirical determination of the diffusion coefficients of the liposomes and ANCs.

The Einstein-Stokes equation is generally employed to estimate the diffusion coefficient of spherical nanoparticles in an unbounded liquid medium D_0 :

$$D_0 = \frac{k_B T}{6\pi\mu_w r_p}, \quad (6.8)$$

where k_B is the Boltzmann's constant ($k_B = 1.38 \cdot 10^{-23} \text{ m}^2 \cdot \text{kg} \cdot \text{s}^{-2} \cdot \text{K}^{-1}$), T is the absolute body temperature ($T = 310 \text{ K}$), μ_w is the water viscosity at 310 K ($\mu_w = 8.18 \cdot 10^{-4} \text{ N} \cdot \text{s} \cdot \text{m}^{-2}$) and r_p is the radius of the particle. In particular, the diffusion coefficient is inversely proportional to the size of the nanoparticles.

Then, the nanoparticle diffusion in the interstitium can be modeled as a diffusion in porous gel matrices [53, 250], taking into account the presence of the matrix proteins:

$$D_t = D_0 \exp\left(-V_{t,\text{matrix}}^{-1/2} \frac{r_p}{r_f}\right), \quad (6.9)$$

where $V_{t,\text{matrix}}$ is the volume fraction of the interstitial matrix and r_f is the fiber radius ($r_f = 20 \text{ nm}$ [53, 251]). The volume fraction of the interstitial matrix is defined as the product of the interstitial collagen concentration (equal to $0.35 \text{ g} \cdot \text{cm}^{-3}$ in solid tumors and to $0.032 \text{ g} \cdot \text{cm}^{-3}$ in spheroids [53, 251, 252]) and the effective volume of collagen fibers (equal to $1.89 \text{ g}^{-1} \cdot \text{cm}^3$ [53, 251]). Therefore, $V_{t,\text{matrix}} = 0.06$ in spheroids and $V_{t,\text{matrix}} = 0.66$ in solid tumors.

Eventually, the presence of cells and other components in the tumor tissue can be modeled by

	r_p [nm]*	D_0 [m ² ·s ⁻¹]	D_t [m ² ·s ⁻¹] (spheroids)	D_t [m ² ·s ⁻¹] (solid tumors)
Liposome	60	4.62e-12	2.21e-12	4.04e-13
ANC	70	3.96e-12	1.68e-12	2.31e-13
Docetaxel	6.12	4.53e-11	4.21e-11	3.53e-11

Table 6.1. Theoretical estimation of the diffusion coefficient of the liposomes and the antibody-nanoconjugates. *Data were taken from [39, 76].

adding the interstitial porosity, that depends on the cell density. This can be addressed using imaging data [53, 52].

Table 6.1 provides the estimated diffusion coefficient of the nanoparticles (liposomes and ANCs). The difference between the liposomes and the antibody-nanoconjugates is given by trastuzumab engraftment on the surface of the ANC. Therefore, ANCs are 20 nm bigger than the liposomes in diameter (indeed, an antibody measures around 10 nm). Moreover, we calculated the empirical diffusion coefficient of docetaxel using the hydrodynamic radius r_H as r_p in (6.8),(6.9) defined as

$$r_H = \sqrt[3]{\frac{3m_p/N_A}{4\pi\rho_p}},$$

where $m_p = 807,88$ kDa is the molecular mass of docetaxel [253], $\rho = 1.4$ g/cm³ is the density of docetaxel [254] and $N_A = 6.022e23$ is the Avogadro's number. The estimated radius resulted equal to $r_H = 6.12$ nm.

6.4.2.2 Cellular uptake

To investigate cellular uptake, spheroid models have been employed [53, 52]. Cellular uptake depends on the binding rate k_{on} and the concentration of cell receptors c_e . Moreover, particles might dissociate from the cells with a rate constant k_{off} .

The concentration of Her2 receptors c_e was computed as follows. The numbers of Her2 receptor on each cell $N_{Her2,cell}$ were estimated in [3] and are reported in Table 6.2. Then, assuming that the volume of one cell is $V_c = 1e-15$ l and denoting by $N_A = 6.022e23$ the Avogadro's number, the concentration of cell surface receptors was estimated as

$$c_e = \frac{N_{Her2,cell}}{N_A V_c} k_\beta,$$

where L is the diameter of the tumor and $k_\beta = 0.01$ is a nondimensional parameter that takes into account the difference in the binding site density of cells in 2D cultures compared to cells in 3D cultures [52]. Indeed, cells implanted in spheroids or *in vivo* might have less accessible binding sites due to extracellular matrix components and cell interactions. The values of c_e are reported in Table 6.2.

We did not have any information on the exact parameter values k_{on} and k_{off} . However, we were able to estimate the dissociation constant at the equilibrium $k_D = k_{off}/k_{on}$ from the 2D *in vitro*

	SKBR3	MDA-MB-453	MDA-MB-231
$N_{\text{Her2,cell}} [\#/ \text{cell}]^*$	$1117 \cdot 10^3 \pm 17 \cdot 10^3$	$215 \cdot 10^3 \pm 34 \cdot 10^3$	$5 \cdot 10^3 \pm 0.3 \cdot 10^3$
$c_e [\text{M}]$	1.9e-08	3.57e-09	8.3e-11
$k_{\text{on}}, [10^4 \text{ M}^{-1} \cdot \text{s}^{-1}]^{**}$	ANC	2.97	5.37
	Liposomes	3.79	7.94
	Free drugs	4.64	5.35

Table 6.2. Parameters relative to the cellular uptake according to the cell line. *Values were taken from [3]. **Calculated assuming $k_{\text{off}} = 10^{-4} \text{ s}^{-1}$.

analysis in Chapter 3, defined as

$$k_D = Ec_{50}^\gamma.$$

The values of the parameter Ec_{50} and γ are provided in Table 3.1. Eventually, we assumed the dissociation rate k_{off} to be of the order of 10^{-4} s^{-1} [53, 52, 245] and derived the value of the association rate $k_{\text{on}} = k_{\text{off}}/k_D$ (that was found to be of the order of $10^4 \text{ M}^{-1} \cdot \text{s}^{-1}$).

The internalization rate k_{int} of the ANCs was fixed to $2.8 \cdot 10^{-4} \text{ s}^{-1}$, while for liposomes and free drugs we assumed it to be equal to $9.3 \cdot 10^{-5}$ [184]. Moreover, we assumed the decay rate of all drugs to be of the order of $1 \cdot 10^{-5} \text{ s}^{-1}$.

6.4.2.3 Transvascular transport

Microvascular permeability coefficient

Vascular walls in tumors are hyperpermeable and improve the extravasation of big and small molecules compared to those in normal tissues. Transvascular transport depends on the diffusive permeability ($P(c_c - c_t)$), convective flux of fluid across vessel walls ($L_p(p_c - p_t)f(c_c, c_t)$) and the solute reflection coefficient of microvessels σ [255, 256] according to the expression [257]

$$J_T = P_{\text{eff}}S(c_c - c_t),$$

where J_T is the flux of liposomes across the vessel wall and P_{eff} is the effective permeability coefficient (that takes into account the diffusive and convective contributions) and S is the vascular surface.

The effective (or apparent) microvascular permeability has been quantified using in vivo imaging techniques [257, 255]. Stealth liposomes of average diameter of 82 nm have an apparent microvascular permeability of $P_{\text{eff}} = 3.42 \cdot 10^{-9} \text{ m} \cdot \text{s}^{-1}$. The microvascular permeability coefficient P takes into account only the diffusive component of the transvascular transport. Importantly, it has been found to depend on the particle size [240]. Indeed, small molecules have larger effective microvascular permeability due to higher diffusion. We considered an effective permeability coefficient for the docetaxel to be of the order of $10^{-9} \text{ m} \cdot \text{s}^{-1}$ [240].

In Chapter 4, we introduced a two-compartment pharmacokinetic model based on the assumption that the nanoparticle exchange between the central and the tumor compartments is driven by the

product of the effective permeability and the surface of the vessel walls per unit volume $k_{c,t}$. We estimated this parameter in Table 4.2 for liposomes and ANC. Assuming that the average vascular surface area per unit volume is around 20000 m^{-1} [183, 186], we found an approximation of the effective permeability for the ANC $6.71\text{e-}11 \text{ m} \cdot \text{s}^{-1}$ and for the liposomes in the range of $[2.31, 4.63] \text{ e-}11 \text{ m} \cdot \text{s}^{-1}$.

Convection is the main driver of transvascular transport of big particles. The value of P for the nanoparticles has therefore been scaled of 1% of P_{eff} to take into account the convection contribution.

Reflection coefficient

For big particles, we estimated the reflection coefficient using the cylindrical pore theory [258, 247]. Assuming that the microvascular pore radius r_t is 200 nm, the coefficient σ was defined as

$$\sigma = \left(1 - \left(1 - \frac{r_p}{r_t} \right)^2 \right)^2,$$

where r_p is the radius of the particle which values relative to the ANC, liposome and docetaxel are reported in Table 6.1. The estimated values of σ were 0.33 for ANCs and 0.26 liposomes. For the docetaxel, we considered $\sigma = 0.82$ [186].

6.4.2.4 Plasma concentration

We assumed that the plasma concentration of nanoparticles or free drugs c_c to be homogeneous in the tumor. We considered an exponential decreasing function to model the concentration decay in time, depending on the clearance rate k_c :

$$c_c(t) = \frac{D}{V_d} \exp(-k_c t), \quad (6.10)$$

where D is the initial dose and V_d is the volume distribution.

Importantly, the clearance rates between nanoparticles and free drugs is significantly different. Indeed, small molecules tend to be eliminated more rapidly than big particles. Docetaxel has a half-time $t_{1/2}$ of 2.2 h when 6.67 mg/kg dose are injected [182] (conversion from mg/m^2 to mg/kg in mice was obtained by dividing by 3 the quantity in mg/m^2 [259]). Therefore, the clearance rate was quantified as

$$k_c = \ln(2)/t_{1/2},$$

and found to be equal to 0.32 h^{-1} for docetaxel. For the ANCs and liposomes, the clearance rate was considered as the sum of k_c and $k_{c,t}$ in Table 4.2 (i.e., 0.005 h^{-1}).

6.4.2.5 Characteristic concentration

To determine the characteristic concentration C of docetaxel, we considered pharmacokinetics-specific properties of liposomes and of free docetaxel. The concentration (expressed in M) was

Parameter	Description	Tumor tissue	Unit	Ref.
k_t	hydraulic conductivity of the interstitium	1.88e-13	$\text{m}^3 \cdot \text{s}^{-1} \cdot \text{kg}^{-1}$	[230]
L_p	hydraulic conductivity of the vessel wall	1.4e-10	$\text{m}^2 \cdot \text{s}^{-1} \cdot \text{kg}^{-1}$	[231]
μ	blood viscosity	4e-3	$\text{kg} \cdot \text{m}^{-1} \cdot \text{s}^{-1}$	[227]
d	intercapillary distance	50e-6	m	[228]

Table 6.3. Parameters relative to the fluid transport model in tumors (relative to the MDA-MB-231 breast cancer cell line).

defined as

$$C = \frac{D}{V_d},$$

where D is the injected dose of docetaxel (expressed in mol) and V_d is the volume of distribution (expressed in l). In particular, V_d depends on the pharmacokinetics of the free or encapsulated drug.

Docetaxel was administered at 5e-3 g/kg. Since the weight of a mouse is approximatively 20 g, the injected dose of docetaxel was equal to 1e-5 g. The conversion to mol was obtained by dividing the injected dose by the molar mass of docetaxel (807.88e3 g/mol [253]). Hence $D = 1.24\text{e-}10$ mol.

The volume of distribution of docetaxel in mice was estimated around 0.17 l [260] when administered free, and in the range of $[1.6\text{-}5.1] \cdot 10^{-3}$ l when encapsulated in nanoparticles of diameter 100-200 nm [260]. Therefore, we considered C equal to 7.3e-10 M and 2.41e-7 M for free docetaxel and the two liposomal formulations, respectively.

6.4.3 Results

In this first set of results, we assume that the tumor tissue is homogeneous, therefore we consider a periodic domain and neglect the porosity (setting it equal to 1 in the entire domain). We analyze the impact of the tumor microscopic properties on the global nanoparticle perfusion in the tumor tissue. We define the total concentration as the average of the sum of the interstitial and bounded concentration in the domain:

$$\bar{c}_t = \frac{\int_0^1 c_t r^2 dr}{\int_0^1 4\pi r^2 dr}, \quad \bar{c}_b = \frac{\int_0^1 c_b r^2 dr}{\int_0^1 4\pi r^2 dr}, \quad \bar{c}_{\text{tot}} = \bar{c}_t + \bar{c}_b$$

Parameter	Description	ANC	Liposomes	Docetaxel	Unit
D_t	diffusion coefficient in tumor interstitium	4.04e-13	2.31e-13	3.53e-11	$\text{m}^2 \cdot \text{s}^{-1}$
c_e	concentration of surface receptors	MDA-MB-231	8.3e-11	8.3e-11	M
		MDA-MB-453	3.57e-9	3.57e-9	M
		SKBR3	1.9e-8	1.9e-8	M
k_{on}	association rate constant	MDA-MB-231	4.44e04	5.03e04	$\text{M}^{-1} \cdot \text{s}^{-1}$
		MDA-MB-453	5.37e04	7.94e04	M
		SKBR3	2.97e04	3.79e04	M
k_{off}	dissociation rate constant	1e-04	1e-04	1e-04	s^{-1}
P_{eff}	effective microvascular permeability	6.71e-11	2.59e-11	2.82e-9	$\text{m} \cdot \text{s}^{-1}$
σ	reflection coefficient	0.33	0.26	0.82	-
k_c	plasma clearance rate	0.005	0.005	0.32	h^{-1}

Table 6.4. Parameters of the nanoparticle transport model (relative to the MDA-MB-231 breast cancer cell line).

6.4.3.1 Impact of the tumor microscopic characteristics on the global dynamic

First, we evaluated the impact of the tumor microscopic structure on the penetration of drugs in the tumor tissue, comparing immunoliposomes, liposomes, and docetaxel on the MDA-MB-231 cell line. In particular, we investigated how the tumor characteristic length L , the permeability of the vessel wall L_p and the hydraulic conductivity k_t affect the transport of nanoparticles. We used the parameters provided in Tables 6.3 and 6.4 and varied the values of L_p , L and k_t .

Results are shown in Figure 6.1. Liposomes and immunoliposomes showed a similar behaviour although having different parameter values reported in Table 6.4. The slightly higher accumulation of liposomes compared to ANCs was mainly due to the different reflection coefficient values (Figure 6.1A) that depend on the NP size. In Chapter 5, we observed that the interstitial fluid pressure p_t almost equates the microvascular pressure p_c for large values of $\bar{R}_n/\bar{k} = L_p L/k_t$. The high interstitial fluid pressure impaired a homogeneous distribution of the drug within the tumor tissue. Smaller values of \bar{R}_n/\bar{k} enhanced the penetration of nanoparticles at the center of the tumor (Figure 6.1B). Indeed, small tumors with small permeability of the vessel walls L_p show larger pressure difference $p_c - p_t$ in the entire domain. Docetaxel showed a different behavior compared with the two liposomal formulations. First, the significantly different plasma pharmacokinetic profile led to a poorer tumor accumulation. Furthermore, the tumor concentration did not vary significantly for different values of \bar{R}_n/\bar{k} (Figure 6.1C). Indeed, the vascular exchange of small particles is driven by the diffusive permeability. Moreover, the larger diffusion coefficient due to the small size of the molecule improved the drug penetration in the center of the tumor (Figure 6.1D).

6.4.3.2 Binding affinity and receptor concentration: comparison between MDA-MB-231, MDA-MB-453 and SKBR3 cell lines

We compared the treatments on the different cell lines. Simulations were run according to the binding affinity and internalization rates defined in Table 6.2 in a tumor of diameter of 2 cm. Furthermore, in our model we computed the internalization rate defined as

$$\frac{\partial c_{\text{int}}}{\partial t} = \lambda_{\text{int}} c_{\text{int}} \quad r \in (0, 1), t \in (0, T).$$

Moreover, we computed the area under the curve (AUC) of the interstitial, bounded and internalized concentrations to evaluate the total drug accumulation:

$$\text{AUC}_{c_t} = \int_0^T \bar{c}_t dt, \quad \text{AUC}_{c_b} = \int_0^T \bar{c}_b dt, \quad \text{AUC}_{\bar{c}_{\text{int}}} = \int_0^T c_{\text{int}} dt,$$

where

$$\bar{c}_{\text{int}} = \frac{\int_0^1 c_{\text{int}} r^2 dr}{\int_0^1 r^2 dr}.$$

Results are shown in Figure 6.2. The SKBR3 cell line had higher tumor accumulation of ANCs, liposomes and docetaxel due to the overexpression of Her2 receptors on the cell surface (Figure 6.2A). However, the large binding affinity prevents the penetration of the drug in the tumor center.

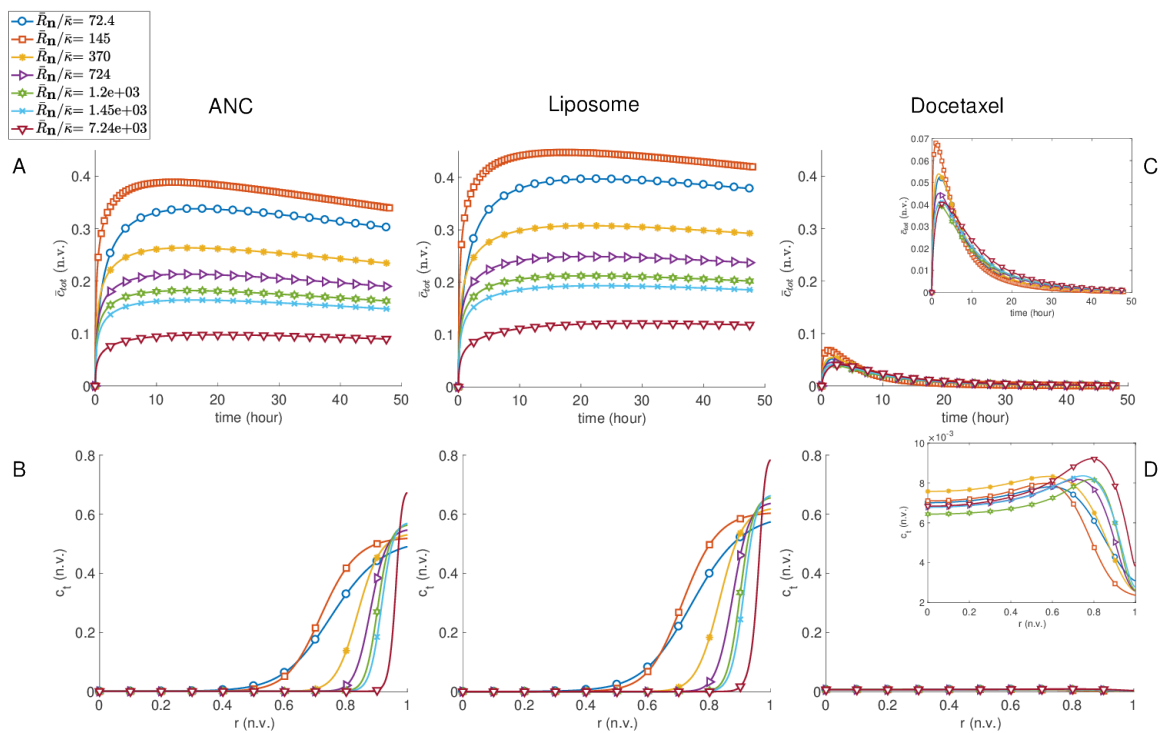


Figure 6.1. Normalized values (n.v.) of the total concentration c_{tot} as function of time (A), and average interstitial concentration c_t with respect to the normalized radius (B, $r = 0$ corresponds to the center of the tumor and $r = 1$ is the periphery of the tumor) of immunoliposomes (left), liposomes (center) and docetaxel as free drug (right), varying $\bar{R}_n/\bar{k} = L_p L/k_t$. (C) and (D) are zooms of the free docetaxel concentration trends. The concentration was normalized with respect to the initial plasma concentration C .

Indeed, the interstitial concentration of drugs was found to be larger for the MDA-MB-231 and MDA-MB-453 cell lines, that could imply a more homogeneous distribution within the tumor tissue (Figure 6.2B). ANCs showed improved cellular internalization than liposomes thanks to the antibody coated on the surface (Figure 6.2C). This was particularly evident for the SKBR3 cell line, which has a significantly larger number of cell-surface receptors. The low accumulation of docetaxel as free drug was mainly due to the plasma clearance. Moreover, the larger vascular diffusive permeability allowed a better penetration of the drug at the center of the tumor (Figure 6.2D).

6.5 Discussion

We introduced a macroscale model of nanoparticle penetration in tumor tissues that couples transvascular transport, interstitial transport and cellular uptake. The model was obtained using two-scale asymptotic expansion that allowed us to take into account the microscopic properties of the tumor microenvironment and nanoparticles (such as diffusion coefficient, vascular permeability and the structure of the capillary network) in the global dynamic. We derived two different models according to the hydraulic permeability of the vessel walls. The model obtained with weakly-permeable vessel walls was found to be a generalization of the model with large-permeable vessel walls, in agreement with the results obtained in Chapter 5. Moreover, this model was in agreement with models found in the literature [81, 82]. The main difference is that we considered a reaction term that depends on specific nanoparticle-cell interactions and a transvascular transport term that depends on the diffusive and convective phenomena.

The calibration of the model was done using drug-specific parameters, that allowed us to compare the accumulation of ANCs, liposomes (when injected with free trastuzumab) and docetaxel (when injected with free trastuzumab). The diffusion coefficient and some parameters relative to the transvascular transport were determined based on the size of the nanoparticles. Since liposomes do not have trastuzumab coated on the surface, their radius is slightly smaller than that of the ANCs, explaining the tiny improved tumor accumulation of liposomes compared to the ANCs. However, other characteristics such as the charge and composition of nanoparticles were not considered in our study and could be integrated into future works. Plasma clearance and vascular permeability of nanoparticles were determined from the pharmacokinetic modeling in Chapter 4.

The tumor microscopic structure impacts the nanoparticle accumulation. In the first set of simulations, we studied how parameters such as the interstitial hydraulic permeability k_t , hydraulic conductivity of the vessel walls L_p and tumor size L affect NP penetration. In particular, the interstitial fluid pressure gradient drives liposome transport outside the tumor tissue. Indeed, the large interstitial fluid velocity, associated with high IFP, pushes nanoparticles at the periphery of the malignant tissue. NP penetration into the tumor center increases when the interstitial fluid velocity is smaller. This occurs in small malignant tissues and tumors with small permeability of the vessel walls L_p . These results were found in agreement with previous observations [186, 247]. However, we did not take into account variations of the reflection coefficient σ that depends on the pore size

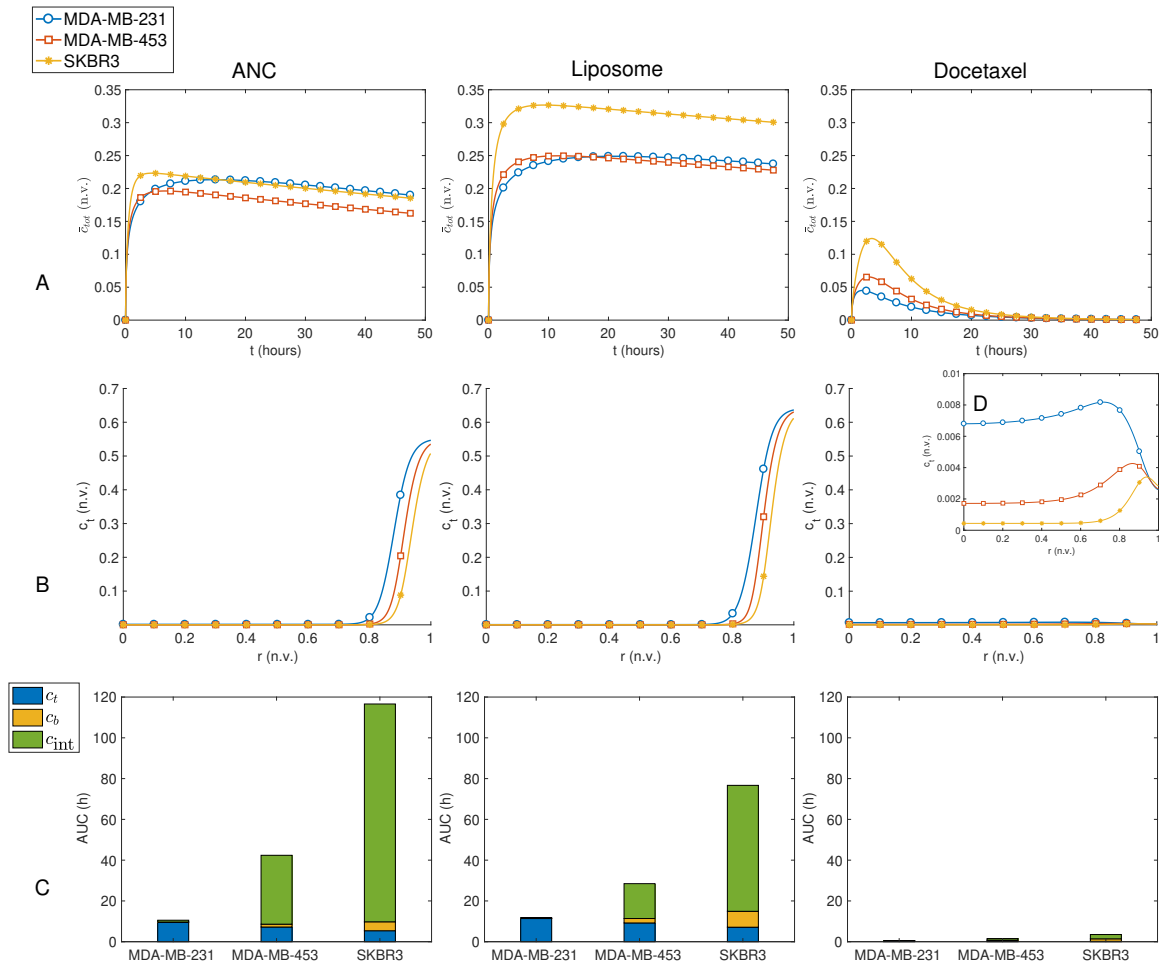


Figure 6.2. Comparison between the different cell lines (MDA-MB-231, MDA-MB-453 and SKBR3): normalized values (n.v.) of the total concentration \bar{c}_{tot} as function of time (A), and average interstitial concentration c_t with respect to the normalized radius (B, $r = 0$ corresponds to the center of the tumor and $r = 1$ is the periphery of the tumor) of immunoliposomes (left), liposomes (center) and docetaxel (right); area under the curve (AUC) of the interstitial c_t , bounded c_b and internalized c_{int} concentration of drug (third row). Zoom on the docetaxel concentration profile as function of the normalized radius (D). The concentration was normalized with respect to the initial plasma concentration C .

on the vascular endothelium. The diffusion of nanoparticles was found to be negligible compared to the convection and reaction terms. Tumor uptake was furthermore considered in our model, assuming that liposomes and immunoliposomes bind the Her2 receptors on the tumor cells. We observed that the receptor concentration plays a significant role in the tumor accumulation of nanoparticles. Indeed, a large number of Her2 receptors on the cell surface is associated with improved cellular uptake. However, the large amount of receptor might lead to the so-called "binding site barrier", a phenomenon whereby particles that are rapidly uptaken by cancer cells penetrate to a limited depth [261]. Free docetaxel showed different trends compared to the two nanoparticles. Indeed, the diffusive permeability of the vessel walls is larger for small molecules and is the main driver of transvascular transport. Moreover, the larger diffusion coefficient improved drug penetration inside the tumor tissue. However, the poorer pharmacokinetic profile (i.e., higher plasma clearance) of docetaxel compared to ANCs and liposomes affected the global drug accumulation in the tumor tissue.

Some limitations of the model and the calibration techniques must be taken into account. First, we did not consider spatial variations of the plasma concentration of NPs. In the capillaries, nanoparticle transport might be modeled with a convection equation, where the convective term is driven by the blood velocity. Furthermore, several nanoparticle properties were determined empirically, while they could be estimated experimentally. The vascular exchange of nanoparticles could be measured *in vivo* using fluorescence videomicroscopy [257] to study the plasma clearance and the interstitial accumulation. Furthermore, the probability of adhesion of the NPs to the vessel walls should be taken into account in our model. Indeed, the nanoparticle size and composition affect the interaction with the endothelial cells [262, 263]. The NP-cell interactions were modeled assuming that the nanoparticles bind Her2 receptors and might be internalized through endocytosis afterward. The association rate k_{on} was estimated using *in vitro* data and considering the dissociation rate k_{off} equal to 10^{-4} . The *in vitro* experiments analyzed in Chapter 3 did not highlight the differences in cellular uptake between the two liposomal formulations, since liposomes were administered with free trastuzumab on the monolayer culture. Hence, the binding affinity of liposomes was found to be similar to that of immunoliposomes. The difference between the two nanoparticles could reside in the internalization rate, as trastuzumab might enhance endocytosis [184]. However, the cellular uptake could be further studied with specific *in vitro* experiments to determine the number of binding sites per cell and the internalization rates of the ANCs and liposomes when injected with trastuzumab [52]. Moreover, the transport of free trastuzumab should be taken into account in the simulations of free docetaxel and liposomes.

The applications of this modeling strategy include the calibration of the mathematical model with patient-specific data. 3D imaging data could provide the information to obtain the microstructure to compute the correctors. Then, predictions of nanoparticle accumulation could be informative for treatment optimization.

A COMPUTATIONAL FRAMEWORK TO PREDICT INDIVIDUAL TUMOR NANOPARTICLE ACCUMULATION

Abstract. Quantification of nanoparticle accumulation is the first step to predict treatment response. Indeed, drugs must reach the tumor site in an optimal quantity to make the therapy successful. NPs transport in the tumor microenvironment depends on their properties, such as size, shape and chemical composition, as well as individual characteristics.

Here, we propose a methodology to integrate individual imaging data in the mathematical model. In particular, we used *ex vivo* data to recover the permeability tensors and performed individual simulations of the penetration of the nanoparticles in the tumor interstitium. These predictions were compared against results from the pharmacokinetic model calibrated from macroscopic measurements.

These results are promising for treatment personalization. The emerging technologies to acquire images permit to quantify the tumor microscopic properties *in vivo*. These data can be integrated into the model to predict nanoparticle accumulation and to schedule the optimal dose to enhance therapeutic efficacy.

Contents

7.1	Introduction	143
7.2	Ex vivo data: microscopy fluorescence imaging	144
7.3	Methods	144
7.3.1	Mathematical model	144
7.3.2	Extrapolation of volume fractions from 2D imaging data	147
7.3.3	Parameter settings	148
7.4	Results	150
7.5	Discussion	154

7.1 Introduction

Patient-specific simulations of nanoparticle and drug transport are of large interest to quantify their tumor penetration and investigate their efficacy. Indeed, they provide information on the drug distribution and permit to schedule personalized treatments based on tumor-specific parameters and individual characteristics. This potentially implies a higher efficacy at the site of action and drastically improves survival.

In the previous chapters, we investigated a spatial mathematical model that describes the drug transport in the tumor interstitium. In chapter 5, we observed that the tumor microscopic structure influences the interstitial fluid flow, which in turn drives the convective transport of particles within the tissue. In chapter 6, we investigated how the nanoparticle or molecule properties affect their penetration within the tumor tissue. Qualitative results were discussed against observations available in the literature. This was a first, fundamental step to prove the validity of the model. Here, we calibrate the model using different experimental data. *ex vivo* microscopy imaging data enabled to recover the microstructure of the tumor environment. In particular, these data were informative on the tumor vascularization and interstitial porosity.

Previously, nanoparticle accumulation and dynamics have been analyzed using imaging data and mathematical modeling [264, 51]. Van de Ven *et al.* used intravital microscopy to acquire longitudinal measurements of the dynamic of nanoparticles in animals [265]. These data were integrated into a mathematical model to quantify the accumulation of doxorubicin and treatment efficacy. Stapleton *et al.* quantified the liposomal accumulation in tumors using a mathematical model of the enhanced permeability retention (EPR) effect that was calibrated using computed tomography measurements [247]. The penetration of nanoparticles for different subtypes of triple-negative breast cancer has been investigated and discussed against imaging data of tumor histology by Goel *et al.* [266]. Importantly, the authors observed that nanoparticle properties are not sufficient to predict tumor accumulation, and tissue architecture must be taken into account to evaluate NPs kinetics. Machine learning algorithms have been also integrated into 3D microscopy imaging techniques to assess the penetration of nanoparticles in metastases [267]. Sykes *et al.* designed nanoparticles according to tumor pathophysiology [268] monitoring the degree of vascularization (CD31 for vessel), cell density and ECM content (Movat's Pentachrome staining) and nanoparticle biodistribution (fluorescence).

Here, we introduced a mathematical model for nanoparticle transport similar to Chapter 6. Moreover, we modeled the porosity of the interstitium, which is the interstitial volume fraction available to the nanoparticles. *Ex vivo* data were employed to estimate the individual vascular and interstitial volume fractions that are needed to solve the equations. Individual predictions were compared with the results of the pharmacokinetic model introduced in Chapter 4 and found in agreement.

Although our methodology has to be validated further, results are promising for treatment personalization. In future works, histological data acquired *in vivo* could be integrated into the model

to make predictions of the tumor accumulation of nanoparticles.

7.2 *Ex vivo* data: microscopy fluorescence imaging

An overview on the experiment details and image segmentation have been presented in [269]. Here, we give a concise description. Nude mice were orthotopically grafted with 80 000 human MDA-MB-231 cells. After 18 days, mice were divided in three groups: 12 control (saline), 15 liposomal docetaxel + free trastuzumab, 15 immunoliposomes. All treatments were administered by retro-orbital injection once a week over 4 consecutive weeks. Liposomal docetaxel and trastuzumab were administered at 5 and 1.9 mg/kg, respectively, either when given as free drugs or as immunoliposome. Blood vessel density and cell density of several animals (7 of the ANC group, 3 of the liposome + free trastuzumab group, and 4 of the control group) were measured *ex-vivo* using anti-CD31 antibodies and electronic microscopy at 2, 4 and 6 weeks. Several slices were sampled at the center and periphery of the tumor and different acquisitions were taken for each tumor slice. Image segmentation was done thanks to an algorithm developed in Matlab¹. Figure 7.1 shows an example of microscopy images and their segmentation of an individual treated with ANC.

7.3 Methods

To perform individual predictions of nanoparticle accumulation in the tumor interstitium, we used a spatial mathematical model based on a diffusion-convection equation. Several parameters of the model were estimated from the available *in vitro* and *in vivo* data, while the diffusion coefficient was calculated empirically, based on the properties of the nanoparticles. Individual *ex vivo* imaging data were used to simulate the interstitial nanoparticle concentration of each animal.

7.3.1 Mathematical model

In Chapters 5 and 6, we have derived a diffusion-advection-reaction model to describe nanoparticle transport in a tumor Ω . The nondimensionalization and meaning of each parameter of the model are provided in Chapters 5 and 6. In the tumor capillaries, we have assumed that the concentration is a given function that can be provided, for example, by the plasma concentration. A transvascular transport component couples the interstitial and capillary concentrations. Moreover, we have taken into account the cellular uptake of the nanoparticles. However, the two-scale homogenization requires the domain periodicity assumption that is unrealistic for tumors. Malignant tissues are indeed highly heterogeneous media characterized by avascular regions, zones with low perfusion, and dense interstitium. To take into account the inhomogeneity of the tumor tissues, we introduce the

¹We thank Florian Correard (INP, CNRS, UMR 7051, Aix Marseille University, France) for providing the segmented images.

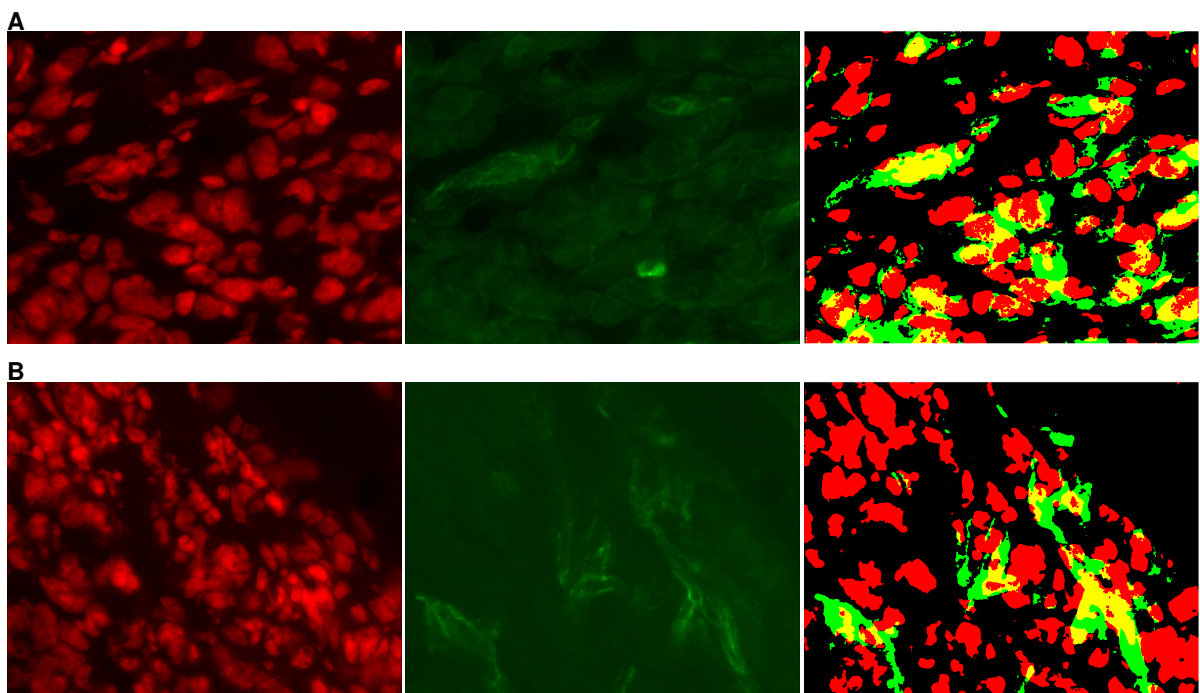


Figure 7.1. Example of microscopy fluorescence imaging. Cells (left), vasculature (center) and image segmentation (right), where the red pixels correspond to the cells, the green pixels to the vessels and the yellow ones are the regions where cells and vessels are overlapped. The tumor slice is at the center (A) and periphery (B) of the tumor of a mouse treated with ANC. Sections were observed under a microscope at 60x magnification.

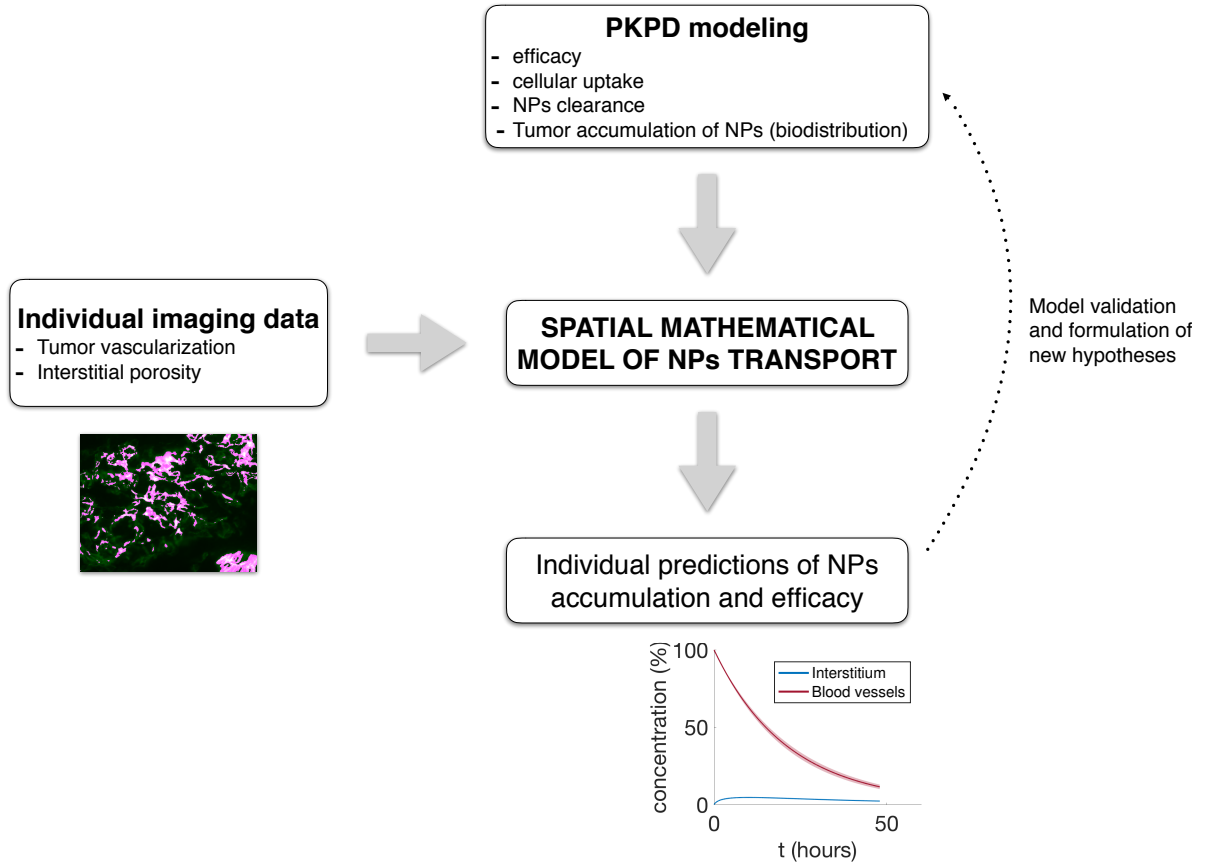


Figure 7.2. Workflow employed to quantify individual accumulation of nanoparticle in the tumor: model calibration with individual imaging data and parameter estimation using pharmacokinetics-pharmacodynamics (PKPD) modeling (in particular, from *in vitro* data and *in vivo* PK data).

porosity of the interstitial compartment ϕ_t that is the fraction of a representative elementary volume available for the interstitial fluid. Indeed, transport of particles in porous media is dominated by advection in zones of high permeability and by diffusion in regions of low permeability [270]. Previously, the poroelastic theory has been employed to investigate the interstitial fluid transport [271] and solute transport [272]. Alteration of the porosity in biological tissue after injection of an extracellular matrix degradation enzyme has been addressed with a mathematical model by [75].

The nanoparticle concentration in the interstitium reads as:

$$\frac{\partial(\phi_t c_t)}{\partial t} + \nabla \cdot (\phi_t c_t \mathbf{u}_t) = \nabla \cdot (\phi_t \mathbf{D}_t \nabla c_t) + \frac{1}{|Y_t|} \mathcal{J}_v[c_c, \phi_t c_t] - \lambda_t \phi_t c_t (c_e - c_b) + \lambda_b \phi_t c_b - \lambda_d \phi_t c_t, \quad \text{in } \Omega \times (0, T). \quad (7.1)$$

Furthermore, the concentration of bounded nanoparticles is described by:

$$\frac{\partial(\phi_t c_b)}{\partial t} = \lambda_t \phi_t c_t (c_e - c_b) - \lambda_b \phi_t c_b - \lambda_{\text{int}} \phi_t c_b - \lambda_d \phi_t c_b, \quad \text{in } \Omega \times (0, T). \quad (7.2)$$

Assuming that the tumor is a sphere and that all the variables are axisymmetric, the model is provided in the radial coordinate. The normalized radius is denoted by $r \in (0, 1)$ and the temporal

variable by $t \in (0, T)$.

Cell problems introduced in equations (5.37) and (5.38) were solved on 3D domains considering various configurations. This allowed us to recover the values of the tensors \mathbf{K} , \mathbf{E} and \mathbf{D}_t that are needed to simulate the fluid transport and the nanoparticle/drug concentration in tumors. Since we assumed that the variables are axisymmetric, we considered only the cases where the domains Y_t and Y_c are symmetric with respect to the three axes (therefore, \mathbf{K} , \mathbf{E} and \mathbf{D}_t are all proportional to the identity matrix).

Fluid transport in tumor tissue was modeled by means of a coupled system of Darcy's equations that describes the interstitial fluid pressure p_t and velocity u_t , and the microvascular pressure p_c :

$$\begin{aligned} \frac{1}{r^2} \frac{\partial}{\partial r} \left(\bar{\kappa} K \frac{\partial}{\partial r} p_t \right) &= \frac{R_n |Y_t|}{|Y_t|} (p_t - p_c), & r \in (0, 1), \\ \frac{1}{r^2} \frac{\partial}{\partial r} \left(E \frac{\partial}{\partial r} p_c \right) &= \frac{R_n |Y_t|}{|Y_c|} (p_c - p_t), & r \in (0, 1), \\ u_t &= -\bar{\kappa} K \frac{\partial}{\partial r} p_t, & r \in (0, 1), \end{aligned}$$

where $K = \mathbf{K}_{11}$ and $E = \mathbf{E}_{11}$.

Particle concentrations in the interstitium c_t and on the cell surface c_b are defined as

$$\begin{aligned} \frac{\partial(\phi_t c_t)}{\partial t} + \frac{1}{r^2} \frac{\partial}{\partial r} (r^2 u_t \phi_t c_t) &= \frac{1}{r^2} \frac{\partial}{\partial r} \left(\hat{D}_t \phi_t \frac{\partial}{\partial r} c_t \right) + \frac{1}{|Y_t|} \mathcal{J}_v[c_c, \phi_t c_t] - \lambda_t \phi_t c_t (c_e - c_b) + \\ &\quad \lambda_b \phi_t c_b - \lambda_d \phi_t c_t, & r \in (0, 1), t \in (0, T), \\ \frac{\partial \phi_t c_b}{\partial t} &= \lambda_t \phi_t c_t (c_e - c_b) - \lambda_b \phi_t c_b - \lambda_d \phi_t c_b, & r \in (0, 1), t \in (0, T), \end{aligned}$$

where $\hat{D}_t = \mathbf{D}_{t11}$.

7.3.2 Extrapolation of volume fractions from 2D imaging data

We estimated the individual vascular and cell volume fractions from imaging data. Thanks to the image segmentation, we were able to compute the capillary surface fraction S_c and the cell surface fraction S_{cell} of each tumor slice, defined as:

$$S_c = \frac{N_{p,c}}{N_{p,\text{tot}}}, \quad S_{\text{cell}} = \frac{N_{p,\text{cell}}}{N_{p,\text{tot}}},$$

where $N_{p,c}$ is the number of green pixels (that represent the vessels), $N_{p,\text{cell}}$ is the number of red pixels (of the cells) and $N_{p,\text{tot}}$ is the total number of pixel.

Assuming an isotropic, uniform and random sampling of the tumor slices, we quantified the vascular volume fraction $|Y_c|$ and cell volume fraction ϕ_{cell} as [273, 274]:

$$|Y_c| = \langle S_c \rangle \pm 2 \frac{\sigma_{S_c}}{\sqrt{n_{S_c}}}, \quad \phi_{\text{cell}} = \langle S_{\text{cell}} \rangle \pm 2 \frac{\sigma_{S_{\text{cell}}}}{\sqrt{n_{S_{\text{cell}}}}}, \quad (7.3)$$

where $\langle S_c \rangle$ and σ_{S_c} ($\langle S_{\text{cell}} \rangle$ and $\sigma_{S_{\text{cell}}}$) are, respectively, the average and standard deviation of the vascular (cell) surface fractions obtained from the different images, and n_{S_c} ($n_{S_{\text{cell}}}$) is the number of surfaces used to compute the volume fraction.

ID	Tumor volume (mm ³)	$\langle S_c \rangle \pm 2 \frac{\sigma_{S_c}}{\sqrt{n_{S_c}}}$		$\langle S_{\text{cell}} \rangle \pm 2 \frac{\sigma_{S_{\text{cell}}}}{\sqrt{n_{S_{\text{cell}}}}}$	
		periphery	center	periphery	center
A1	1357	0.44 ± 0.06	0.44 ± 0.06	0.18 ± 0.12	0.18 ± 0.12
A2	1143	0.13 ± 0.08	0.15 ± 0.04	0.14 ± 0.05	0.30 ± 0.05
A3	715	0.42 ± 0.07	0.50 ± 0.10	0.25 ± 0.05	0.19 ± 0.05
A4	1110	0.32 ± 0.07	0.32 ± 0.07	0.27 ± 0.04	0.27 ± 0.04
A5	356	0.14 ± 0.06	0.45 ± 0.08	0.30 ± 0.03	0.19 ± 0.07
A6	2062	0.09	0.17	0.28	0.28
A7	1367	0.35 ± 0.09	0.49 ± 0.04	0.28 ± 0.03	0.27 ± 0.03

Table 7.1. Individual data of animals treated with ANCs: tumor volume, vascular volume fractions ($\langle Y_c \rangle$) and cell volume fractions (ϕ_b) in the periphery and in the center of the tumor.

ID	Tumor volume (mm ³)	$\langle S_c \rangle \pm 2 \frac{\sigma_{S_c}}{\sqrt{n_{S_c}}}$		$\langle S_{\text{cell}} \rangle \pm 2 \frac{\sigma_{S_{\text{cell}}}}{\sqrt{n_{S_{\text{cell}}}}}$	
		periphery	center	periphery	center
L1	477	0.27 ± 0.12	0.38 ± 0.10	0.22 ± 0.03	0.17 ± 0.04
L2	683	0.06 ± 0.02	0.18 ± 0.09	0.22 ± 0.04	0.18 ± 0.04
L3	2406	0.41 ± 0.07	0.41 ± 0.07	0.17 ± 0.13	0.17 ± 0.13

Table 7.2. Individual data of animals treated with liposomes: tumor volume, vascular volume fractions ($\langle Y_c \rangle$) and cell volume fractions (ϕ_b) in the periphery and in the center of the tumor.

We made a distinction between the center and the periphery of the tumor. Figure 7.3 shows the vascular and cell volume fractions as function of the tumor volume. Tables 7.1 and 7.3.2 provide the values of the tumor size and volume fractions of each individual. The inferior vascular volume fraction of large tumors was probably due to the necrosis.

7.3.3 Parameter settings

We considered the model parameter values relative to the MDA-MB-231 cell line in Tables 6.3 and 6.4. The tumor characteristic length was defined as the diameter of the sphere with volume given by the last caliper measurement of the tumor. The characteristic velocity U was fixed equal to 0.12 m·s⁻¹ for all individuals.

Simulations were run on the temporal interval (0, 168) h with a time step $\Delta t = 0.003$ h using the finite difference scheme explained in Section 6.4.1. The computational domain was the normalized radius $r \in (0, 1)$ discretized in intervals of size $h = 0.002$. The domain was divided into two zones, namely the center of the tumor (for $r \in (0, 0.8)$) and the periphery (for $r \in (0.8, 1)$). The permeability tensors \mathbf{K} , \mathbf{E} and \mathbf{D}_t were computed taking into account the differences between the two regions.

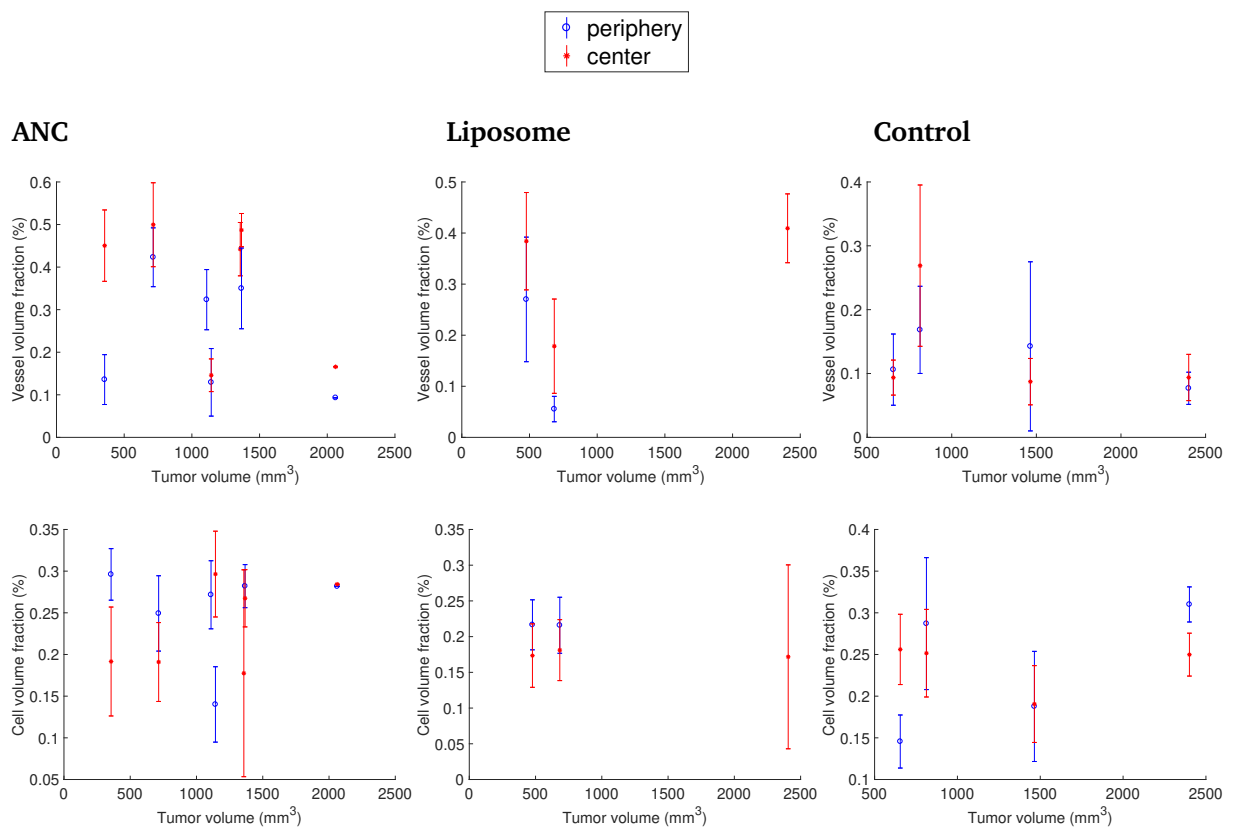


Figure 7.3. Vascular volume fraction (first row) and cell volume fraction (second row) at the tumor center (red) and at the periphery (blue) of the different groups of mice as function of the tumor volume.

Denoting by \mathbf{A} a generic permeability tensor, its definition reads as follows:

$$\mathbf{A} = \begin{cases} \mathbf{A}_{\text{center}} & 0 \leq r \leq 0.8 - \delta, \\ \frac{\mathbf{A}_{\text{periphery}} - \mathbf{A}_{\text{center}}}{\delta}(r - 0.8 + \delta) + \mathbf{A}_{\text{center}} & 0.8 - \delta < r \leq 0.8, \\ \mathbf{A}_{\text{periphery}} & 0.8 < r \leq 1. \end{cases} \quad (7.4)$$

The central and peripheric permeability tensors were obtained solving the 3D cell problems. We used the vascular volume fractions to recover the unitary cell, assuming a capillary domain of the form of Figure 5.5A and C.

For each animal, the central and peripheric vascular volume fractions were sampled from the distributions obtained from (7.3). In total, 36 simulations were performed for each animal to take into account the variability of the vascular volume fraction at the periphery and at the center of the tumor.

Let us denote by $S_{\text{cell,center}}$ and $S_{\text{cell,periphery}}$ the mean cell volume fraction at the tumor center and periphery, respectively, computed according to 7.3. The discretized interstitial porosity ϕ_t^i at $r^i = ih$ was defined as an oscillating function:

$$\phi_t^i = \begin{cases} 1 - \langle S_{\text{cell,center}} \rangle + \varepsilon_{\text{center}}^i & 0 \leq r^i \leq 0.8, \\ 1 - \langle S_{\text{cell,periphery}} \rangle + \varepsilon_{\text{periphery}}^i & 0.8 < r^i \leq 1, \end{cases} \quad (7.5)$$

where

$$\varepsilon_{\text{center}}^i \sim \mathcal{N}\left(0, 2 \frac{\sigma_{S_{\text{cell,center}}}}{\sqrt{n_{S_{\text{cell,center}}}}}\right), \quad \varepsilon_{\text{periphery}}^i \sim \mathcal{N}\left(0, 2 \frac{\sigma_{S_{\text{cell,periphery}}}}{\sqrt{n_{S_{\text{cell,periphery}}}}}\right).$$

A schematic of the methodology is highlighted in Figure 7.4.

7.4 Results

Spatio-temporal individual simulations were run based on the tumor volume and the vascular and interstitial volume fractions of each animal. To compare the results of the spatial model to the pharmacokinetic model of Chapter 4, we defined the total amount of nanoparticles in the tumor as the integral of the total concentration over the entire domain:

$$A_t(t) = 4\pi L^3 \int_0^1 \phi_t(c_t + c_b)r^2 dr,$$

where L is the radius of the tumor (in dm).

Furthermore, we analyzed the penetration of nanoparticles into the tumor by defining the following quantities:

$$A_{t,\text{center}}(t) = 4\pi L^3 \int_0^{0.8} \phi_t(c_t + c_b)r^2 dr, \quad A_{t,\text{periphery}}(t) = 4\pi L^3 \int_{0.8}^1 \phi_t(c_t + c_b)r^2 dr.$$

To quantify the nanoparticle accumulation in the interstitium, we computed the area under the

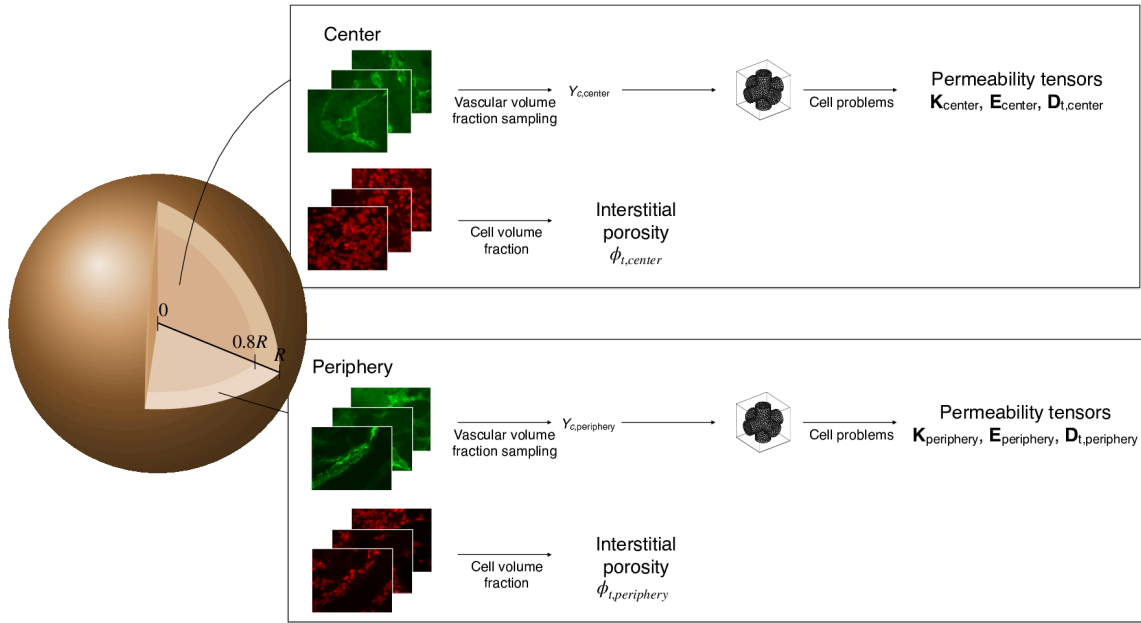


Figure 7.4. Schematic of our methodology to obtain the permeability tensors at the center and at the periphery of the tumor.

curve (AUC) of the total NP amount in the tumor:

$$\text{AUC} = \int_0^T A_t(t) dt, \quad \text{AUC}_{\text{center}} = \int_0^T A_{t,\text{center}}(t) dt, \quad \text{AUC}_{t,\text{periphery}} = \int_0^T A_{t,\text{periphery}}(t) dt.$$

Predictions of ANCs and liposomes accumulation are shown in Figures 7.5 and 7.6, respectively. Globally, results were in agreement with the pharmacokinetic (PK) model of Chapter 4. Figure 7.7A shows simulations of the PK model for the ANCs and the liposomes obtained with Simulx considering the population parameters provided in Table 4.2 (high dose). The total area under the curve of the ANCs estimated with PK model was similar to the one obtained with the spatial model, as shown in Figure 7.7B. Values of the average AUCs of the spatial model are provided in Tables 7.3 and 7.4 for ANCs and liposomes, respectively, and were found close to the mean exposures of the PK model which were 44.03 ± 0.22 mg/kg·h for the ANCs and 43.02 ± 0.11 mg/kg·h for the liposomes.

Small penetration of ANCs and liposomes into the tumor center was observed (Tables 7.3 and 7.4). Indeed, the small diffusion coefficient and permeability of the vessel walls combined with large interstitial fluid pressure impaired a homogeneous distribution of the NPs in the tumor tissue. However, we noticed an enhanced accumulation of nanoparticles in large tumors (in particular, animal A6 and L3 had the largest tumors and highest tumor accumulation), while smaller tumors showed lower NP accumulation (such as individual A5 and L1). Comparing individuals with similar tumor volumes, we observed that the vascular and interstitial volume fractions played a significant role in the ANCs penetration into the tumor. For example, individuals A2 and A4 had equal tumor size but significantly different vascular and interstitial volume fractions in the tumor center. The larger

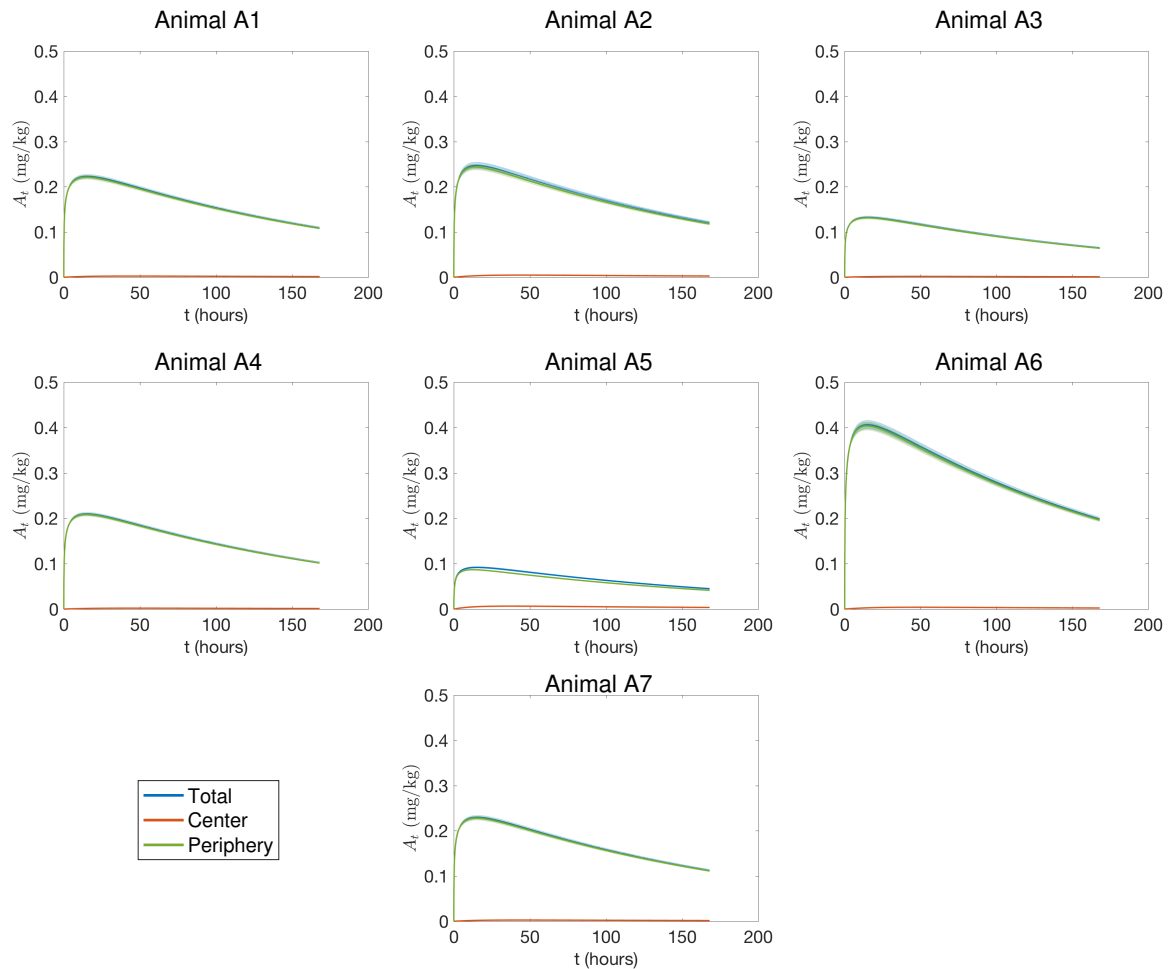


Figure 7.5. Predictions of the interstitial concentration of individuals in the ANC group as function of time: total concentration (blue), concentration in the periphery of the tumor (green) and at the center of the tumor (red).

vascularization of individual A4 led to higher interstitial fluid pressure which hindered the ANCs accumulation at the center of the tumor. Furthermore, the large difference in nanoparticle uptake by the tumor at the periphery could be motivated by the diverse interstitial volume fractions of the two individuals. The same observation held comparing animals A3 and L2. Individual L2 exhibited larger nanoparticle accumulation due to the lower interstitial fluid pressure as a consequence of the lower vascular surface compared to individual A3. Moreover, the overall improved accumulation of the liposomes compared to ANCs that resulted from our spatial model could be due to the smaller reflection coefficient of the liposomes, that was computed based on the size of the nanoparticles.

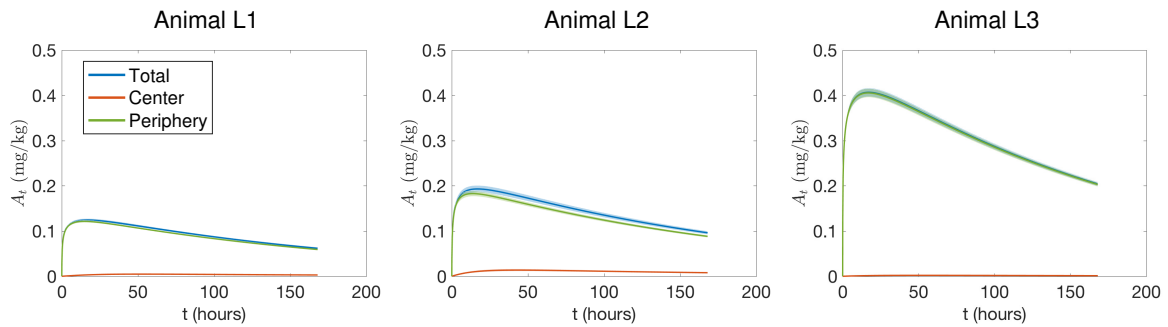


Figure 7.6. Predictions of the interstitial concentration of individuals in the liposome group as function of time: total concentration (blue), concentration in the periphery of the tumor (green) and at the center of the tumor (red).

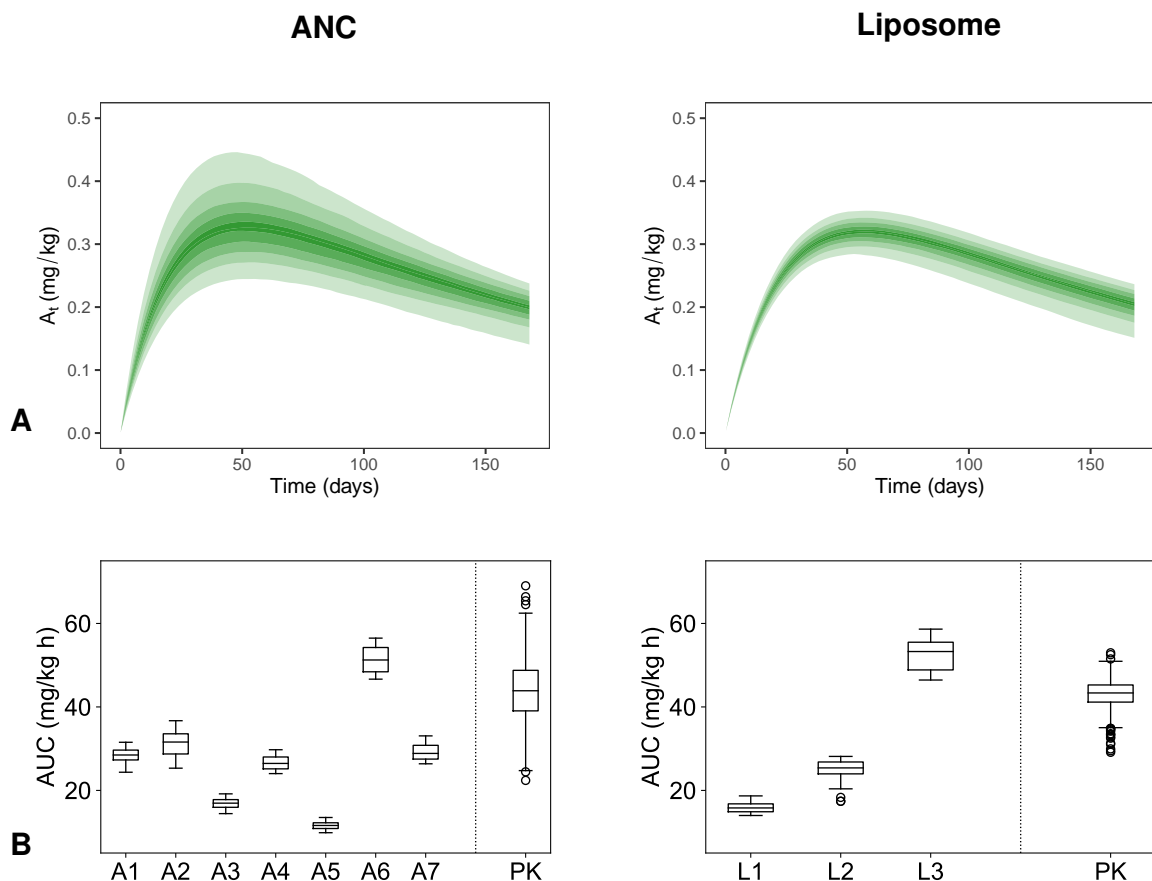


Figure 7.7. Comparison between the individual predictions of the spatial model and the population predictions obtained with the pharmacokinetic (PK) model simulation from Chapter 4: (A) PK model simulation with the population parameters estimated in Chapter 4; (B) area under the curve (AUC) of the total concentration in the tumor of each animal and of the PK model.

	A1	A2	A3	A4	A5	A6	A7
AUC	28.38±0.32	31.27±0.50	16.87±0.21	26.60±0.28	11.63±0.16	51.41±0.65	29.21±0.32
AUC _{periphery}	28.03±0.33	30.63±0.43	16.61±0.21	26.32±0.27	10.77±0.08	50.86±0.61	28.85±0.32
AUC _{center}	0.36±0.02	0.64±0.08	0.26±0.01	0.28±0.01	0.86±0.08	0.55±0.04	0.36±0.01

Table 7.3. Estimated area under the curve of each individual treated with ANCs: total accumulation (AUC), area under the curve in the periphery (AUC_{periphery}) and in the center of the tumor (AUC_{center}). The reported values are the mean ± standard error of the mean and are expressed in hours.

	L1	L2	L3
AUC	15.98±0.21	24.76±0.50	52.52±0.61
AUC _{periphery}	15.34±0.14	22.93±0.34	52.24±0.62
AUC _{center}	0.64±0.07	1.83±0.17	0.29±0.01

Table 7.4. Estimated area under the curve of each individual treated with liposomes: total accumulation (AUC), area under the curve in the periphery (AUC_{periphery}) and in the center of the tumor (AUC_{center}). The reported values are the mean ± standard error of the mean and are expressed in hours.

7.5 Discussion

We calibrated a mathematical model of nanoparticle transport in tumor tissues with *ex vivo* imaging data providing the vascular and cell volume fractions. The computational domain was divided into two regions (center and periphery) to evaluate the penetration depth of the nanoparticles. Different permeability tensors were considered in these two regions according to the respective volume fractions. Nanoparticle specific parameters were considered as explained in Chapter 5.

This methodology allowed us to make individual predictions of nanoparticle accumulation and penetration in tumors. Moreover, results were compared to the predictions of the two-compartment pharmacokinetic model introduced in Chapter 4, that were found in agreement. In the spatial model, the inter-individual variability in tumor accumulation of nanoparticles was mainly due to the differences in tumor volume. Indeed, nanoparticle uptake by the malignant tissue increased with the tumor volume, in agreement with previous observations [268]. Interestingly, we observed that the larger vascularization of the tumor tissue was not associated with an improved nanoparticle accumulation. Indeed, from the fluid transport model, the large vascular surface results in high interstitial fluid pressure, which hinders the penetration of nanoparticles. Moreover, a larger interstitial volume fraction improved the distribution of the particles.

Our methodology has some limitations. The simulations in 1D on an axisymmetric domain did not highlight the heterogeneity of the entire tumor. A 3D efficient numerical scheme with a real tumor geometry could improve the understanding of the nanoparticle distribution in the malignant tissue. Here, we divided the domain into two regions (center and periphery) but the tumor could be sampled in a higher number of zones. This procedure would allow taking into account avascular regions and necrosis. Importantly, we assumed that fixed values for the characteristic velocity U and

the hydraulic conductivities of the vessel walls L_p and of the interstitium k_t , but we expect these two parameters to be highly variable among individuals [186]. As shown in Section 6.4.3.1, the model is sensitive to changes in these parameters.

We observed an enhanced vascularization in tumors treated with ANCs, that could potentially increase the filtration of nanoparticles in malignant tissues. However, this property resulted in a lower accumulation of nanoparticles due to the high interstitial fluid pressure obtained from the fluid transport model, in agreement with previous observations [275]. Here, we assumed a homogeneous hydraulic conductivity of the vessel walls in the domain which in reality could be significantly heterogeneous according to the vasculature type. Further studies on the vascularization of the tumor could highlight the permeability properties of the walls to better describe the transvascular transport of the immunoliposomes. On the one hand, the protein corona that forms on the surface of the nanoparticles [276] might bring oxygen to the tumor, altering its permeability [277, 278]. On the other hand, trastuzumab has been proven to have indirect anti-angiogenic effects on mice that overexpress the Her2 receptors [72]. It might reduce the permeability of the vessel walls, resulting in diminished IFP.

Several strategies could be considered to reduce interstitial fluid pressure, which would enhance nanoparticle accumulation. For example, interstitial matrix normalization could significantly reduce the tumor IFP and improve the diffusion of the nanoparticles within the tumor interstitium [60].

Although our predictions were globally in agreement with the results of Chapter 4, the validation of the model with imaging data has to be done. Spatial distribution of the drug in the tumor tissue could be measured using MALDI-MSI (matrix-assisted laser desorption ionization mass spectrometry imaging) imaging [279]. *in vivo* predictions [280].

CONCLUSION AND PERSPECTIVES

In this thesis, the biodistribution and pharmacodynamic of antibody-nanoconjugates have been analyzed using mathematical modeling. The results of this work give a direct contribution to the development of the antibody-nanoconjugates in breast cancer treatment.

We derived a reduced Gompertz model in the statistical framework of the nonlinear mixed-effects models to describe untreated tumor growth. This model, which has one population-level parameter and one individual-specific parameter, showed good descriptive power (similar to the Gompertz model) and improved the predictions of the initiation time of the tumor. Moreover, thanks to the biological interpretation of the reduced Gompertz parameters, we were able to validate the model on a new dataset by estimating the parameters from independent experiments. Our model should be further tested to predict individual tumor size (i.e., for forward predictions). Indeed, a good characterization of the tumor growth is of fundamental importance to make predictions on the individual response of the treatments. Although our method remains to be extended to clinical data, these results are promising for the personalized estimation of the age of a tumor from limited measurements at diagnosis. The estimation of the age of a patient's tumor could be indeed informative for clinical practice. Indeed, an older tumor has a greater probability of having already spread than a younger one. These results could contribute to the development of personalized computational models of metastasis [118, 154, 155].

The biodistribution of the ANCs and their efficacy were evaluated using a pharmacokinetic-pharmacodynamic model. A two-compartment pharmacokinetic (PK) model based on a system of ordinary differential equations was used to describe the nanoparticle exchange between the systemic and tumor compartments. The PK model was calibrated on four different datasets, that allowed us to compare the distribution of the antibody-nanoconjugates and the liposomes (without trastuzumab engrafted on the surface) in the central and tumor compartments. A resistance pharmacodynamic (PD) model was employed to evaluate the nanoparticle efficacy. The comparison between the liposomes and the ANCs did not show significant differences in terms of cytotoxic activity, although the acquired resistance to ANCs was slightly lower than the resistance to liposomes. The mechanisms of action of liposomes and immunoliposomes should be further highlighted [281], even if the global higher efficacy of the ANCs could be due to a more efficient internalization thanks to the coated antibody on the surface [184]. Moreover, the efficacy of the two nanoparticles was higher than the free drugs thanks to the improved pharmacokinetics of the two liposomal formulations. However,

the PK of the ANCs and liposomes could be further evaluated. Measuring the plasma concentration of the drug would allow us to estimate the volume of distribution and the systemic clearance of the two liposomal formulations. Indeed, immunoliposomes might be recognized and eliminated more rapidly by the macrophage system or they could be uptaken by other organs because of the engrafted trastuzumab. As a future perspective, a mechanistic physiologically based pharmacokinetic (PBPK) model could provide insights into the phenomena involved in the absorption, distribution, metabolism and excretion processes. Moreover, the *in vivo* efficacy of the nanoparticles could be modeled taking into account docetaxel and trastuzumab in the drug-induced decay process [282]. Pharmacokinetic-pharmacodynamic modeling is fundamental in the drug development process: the PK allows to evaluate the exposure at the site of action as a function of the injected dose, while the PD describes the treatment response. New treatment schedules could be tested experimentally according to our model predictions. Importantly, PKPD modeling permits the translation of the PK to clinical applications by quantifying the initial in-human dose.

The large heterogeneity of malignant tissues and the nanodrug design impact the delivery of therapeutics at the tumor site. To understand the main factors that affect the nanoparticle distribution, we derived a spatial model of drug transport that takes into account the microscopic characteristics of the tumor on the global dynamic using the two-scale asymptotic expansion method. Tumor size, interstitial fluid pressure, vascularization and permeability of the vessel walls play a significant role in the nanoparticle penetration into the center of the tumor. Furthermore, the size of the liposomes affects significantly the drug delivery at the tumor site: big particles have lower diffusion coefficient and are more likely to encounter transvascular barriers than small particles. In our work, we focused on a simple mathematical model of fluid and nanoparticle transport in the tumor tissue. However, more complexity could be added. A coupled model of therapeutic transport and tumor growth, including angiogenesis and transport of nutrients, could be used to better investigate the interplay of the NPs with the different tumor components [202] or the combination of different drugs [73]. Moreover, model calibration could be improved. Nanoparticle uptake could be further studied with 3D *in vitro* experiments [53, 52]. This could help in understanding the internalization mechanism by the cells and might improve the calibration of the spatial model and the efficacy models. Importantly, this analysis could highlight the differences between ANCs and liposomes without trastuzumab coated on the surface and give more insights into the different efficacies of these two therapeutics [184]. Spheroids experiments could be furthermore informative on the spatial diffusion of nanoparticles in avascular tumors [53, 52, 283]. Indeed, they could give insights into the interstitial volume fraction accessible to the nanoparticles and the free macromolecules (such as trastuzumab). Indeed, it could be possible that liposomes have larger motility than macromolecules thanks to their highly lipophilic composition [39]. This analysis could be performed using our spatial model by neglecting the vascular volume fraction and the transvascular transport term in our model and adding suitable boundary conditions that take into account the drug administration on cell cultures. Moreover, the transport model could be coupled with a spheroid growth model to evaluate drug efficacy [284, 285]. In the spatial model for vascularized tumors, there is the need for the quantification of the permeability of the vessel walls to the nanoparticles with specific experiments [255]. It is also important to quantify

the interactions between the nanoparticles and the endothelial cells according to the NP composition, to evaluate the probability of adhesion of the liposomes to the vessel walls [263]. Moreover, more detailed imaging data could be informative of the vascular network and the interstitial collagen structure and could help to investigate the regions with poor nanoparticle delivery [280]. Although individual predictions were validated against the pharmacokinetic model, the model should be tested on *ex vivo* imaging data with the spatial nanoparticle distribution [279]. As a future perspective, our methodology could be used to make individual predictions of the nanoparticle accumulation *in vivo* using histological data, which provide the tumor microscopic structure.

The asymptotic model we obtained should be further studied to prove theoretically the two-scale convergence. For the fluid transport model, we proved numerically that the L^2 -error between the solutions to the microscopic model the homogenized model decreases linearly with ε . Furthermore, the periodicity assumption should be relaxed in future works to take into account the realistic geometry of malignant tissues. This could be achieved by properly defining the representative volume element [236]. Moreover, an efficient 3D numerical scheme should be implemented to simulate the nanoparticle concentration model. It would potentially allow us to take into account realistic geometries and to improve the predictions on the heterogeneity of the tumor.

Several strategies could be employed to improve the drug delivery by the nanoparticles at the tumor site. According to our analysis, the large interstitial fluid pressure is the main barrier of an inefficient penetration within the tumor tissue. To decrease the interstitial fluid pressure, vascular normalization could be a possible solution. The decrease of the vascular surface area and hydraulic conductivity of the vessel walls would reduce the fluid filtration and the interstitial fluid pressure [186]. However, it would also lead to a loss of nanoparticle filtration due to the loss of permeability of the vessel walls [60]. A second possible strategy could be the normalization of the interstitial matrix. Increasing the interstitial hydraulic conductivity would yield lower interstitial fluid pressure. Moreover, interstitial matrix normalization could enhance nanoparticle diffusion, which is affected by the collagen gels [286]. Furthermore, immunoliposomes properties could be optimized. In this work, we have observed that the size of the nanoparticles plays a significant role in their transport. Indeed, large particles are less likely to be extravasated in the tumor interstitium than small particles and their diffusion is hindered. Hence, the size reduction could enhance a homogeneous penetration within the tumor tissue. Furthermore, the trastuzumab engraftment rate might affect the binding affinity of the nanoparticles and the internalization rates. *In vitro* experiments could provide insights on this property of the immunoliposomes. Moreover, the nanoparticle encapsulated drug could be modulated to optimize the drug amount that reaches the tumor site. A recent study showed that there might be a NP number threshold dose that could improve drug delivery (namely, 1 trillion nanoparticles in mice) [287]. Moreover, in Chapter 7, we observed that the ANCs might improve vascularization. The impact of the immunoliposomes on the tumor vascularization could be further studied to assess the effects on the permeability of the vessel walls. In particular, the protein corona that forms on the surface of the nanoparticles might bring oxygen to the tumor, enhancing its permeability [277, 278]. Furthermore, the protein corona might be different according to the chemical

composition of the nanoparticle, which could highlight differences in tumor accumulation between liposomes and immunoliposomes.

APPENDICES

Contents

A	Cell doubling time	161
A.1	Mixed effects modelling	163
A.2	Fit to the average	167
A.3	Doubling time	167
B	Supplementary figures and tables to Chapter 2	169
C	Supplementary material to Chapter 3	180
C.1	Nonlinear regression	180
C.2	Python computation	184
C.3	Results on the MDA-MB-231 cell line	185
C.4	Results on the SKBR3 cell line	191
C.5	Results on the MDA-MB-453 cell line	197

A Cell doubling time

The xCELLigence system [288] is a method to monitor cell viability in real time. It measures electrical impedance across interdigitated micro-electrodes integrated on the bottom of the cell culture. The impedance measurement is displayed as *cell index*. The cell index (CI) is defined as

$$CI = \frac{R_n - R_b}{15}, \quad (9.6)$$

where R_n is the cell-electrode impedance of the well with the cells and R_b is the background impedance of the well with the medium alone [289]. The CI value directly correlates with the number of viable cells.

We consider five different cell lines relative to the breast cancer, according to variations in Her2 expression and to cell transfection:

- MDA-MB-231: triple negative breast cancer (HER2-),
- MDA-MB-231 Dt+ Luc+: transfected MDA-MB-231,

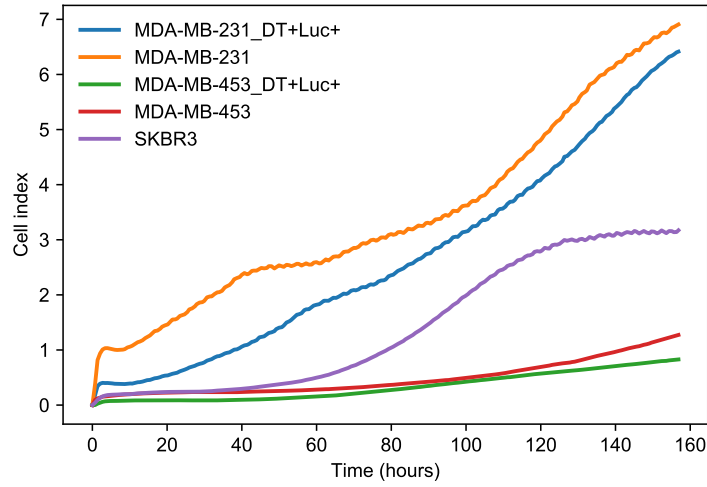


Figure A1. Mean trend of the different cell lines.

- MDA-MB-453: Her2+,
- MDA-MB-453 Dt+ Luc+: transfected MDA-MB-453,
- SKBR3: Her2++.

Figure A1 shows the mean trend of the cell index relative to the five cell lines. We want to compute the cell doubling time of each group comparing different approaches. We fit the data to two models of tumor growth (logistic and exponential) considering the time interval $(t_1, t_2) = (5, 96)$. We compare the results obtained with the individual fit, the population fit, the fit to the mean with the ones provided by the xCELLigence system. The logistic model is defined as follows:

$$\begin{cases} \frac{dV}{dt} = \rho V \left(1 - \left(\frac{V}{K}\right)\right), \\ V(t=0) = V_0, \end{cases} \quad (9.7)$$

where K is the carrying capacity and ρ depends the fraction of proliferative cells λ :

$$\lambda = \frac{K - V_0}{K} \rho$$

The exponential model is defined as

$$\begin{cases} \frac{dV}{dt} = \lambda V \\ V(t=0) = V_0, \end{cases} \quad (9.8)$$

where λ is the fraction of proliferative cells.

In both cases the cell cycle duration is defined as

$$\tau = \frac{\log 2}{\lambda} \quad (9.9)$$

We compute the cell doubling times relative to each approach and compare them to the one obtained with the xCELLigence system. In all the following analysis we consider the initial volume V_0 a free parameter that has to be estimated.

Cell line	Model	AIC	-2LL
MDA-MB-231	Exp	-109	-119
	Logistic	-1.07e+03	-1.08e+03
MDA-MB-231 Dt+Luc+	Exp	-487	-497
	Logistic	-1.62e+03	-1.63e+03
MDA-MB-453	Exp	-3.49e+03	-3.5e+03
	Logistic	-3.49e+03	-3.5e+03
MDA-MB-453 Dt+Luc+	Exp	-2.83e+03	-2.84e+03
	Logistic	-2.82e+03	-2.84e+03
SKBR3	Exp	-1.63e+03	-1.64e+03
	Logistic	-1.63e+03	-1.64e+03

Table A1. AIC and likelihood estimation obtained with the Monolix computation relative to each cell line.

A.1 Mixed effects modelling

In this section we provide the population analysis of the different cell lines. We fit the data to the exponential and to the logistic models and provide the results in Table A1. We observe that the logistic model fits better than the exponential model for the cell lines MDA-MB-231 and MDA-MB-231 Dt+ Luc+. On the other hand, the exponential model provides the best fit to the data relative to the cell lines MDA-MB-453, MDA-MB-453 Dt Luc+ and SKBR3, even if we observe that the differences between the AICs are small. However, the large standard errors associated to the estimated parameters of the logistic model (data not provided) suggest that we might encounter overfitting when fitting the data to the logistic function.

In Figure A2 we observe the visual predictive checks relative to the best fit of the different cell lines.

A.1.1 Logistic vs exponential fitting

The estimated fraction of proliferative cells computed by the logistic and the exponential fits to the data relative to the cell lines MDA-MB-453, MDA-MB-453 Dt+ Luc+ and SKBR3 don't show variability. This is due to the fact that the carrying capacity of the logistic function defined in (9.7) tends to infinite, therefore the model degenerates to an exponential one.

However, the estimated parameters relative to the cell lines MDA-MB-231 and MDA-MB-231 Dt+Luc+ show high variability from the exponential to the logistic models (see Tables A2 and A3). This is due to the fact that the estimated carrying capacity is not large. Moreover, we observe from Table A1 and Figure A3 that the best fits are given by the logistic model in both cases.

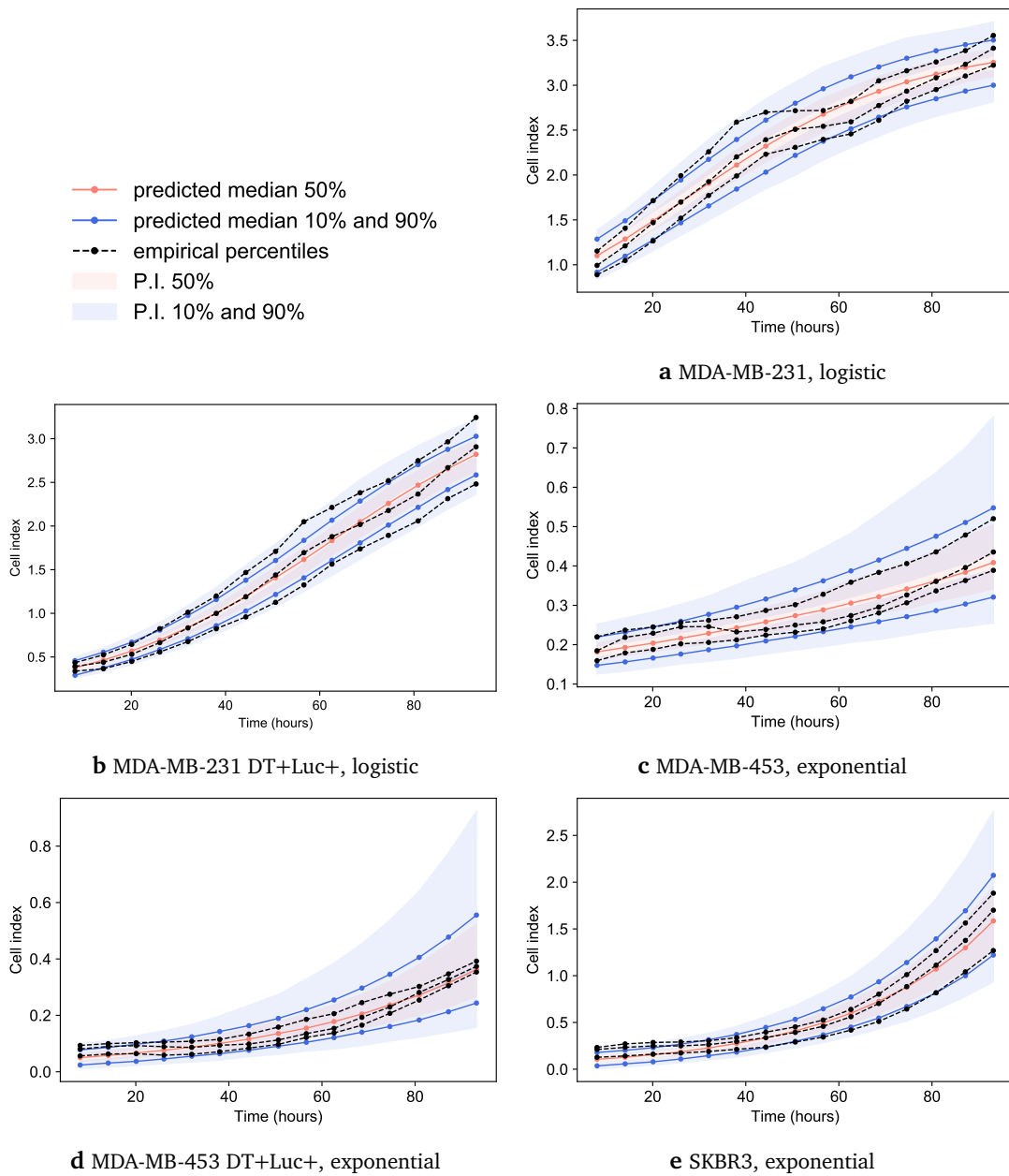


Figure A2. VPCs relative to the best fit of each cell line.

Model	Parameter	Value	St. Err.	St. Err.[%]
Logistic	$V_{0,\text{pop}}$	0.863	0.034	3.94
	ρ_{pop}	0.0406	0.00253	6.23
	K_{pop}	3.49	0.0793	2.27
	ω_{V_0}	0.0824	0.0273	33.2
	ω_{ρ}	0.133	0.0476	35.7
	ω_K	0.048	0.0176	36.7
Exp	$V_{0,\text{pop}}$	1.33	0.0574	4.33
	λ_{pop}	0.0106	0.000369	3.48
	ω_{V_0}	0.0945	0.0316	33.5
	ω_{λ}	0.0723	0.0266	36.8

Table A2. Estimated parameters relative to the cell line MDA-MB-231.

Model	Parameter	Value	St. Err.	St. Err.[%]
Logistic	$V_{0,\text{pop}}$	0.276	0.0127	4.59
	ρ_{pop}	0.0402	0.00149	3.7
	K_{pop}	3.63	0.0595	1.64
	ω_{V_0}	0.0889	0.0347	39.1
	ω_{ρ}	0.072	0.0261	36.3
	ω_K	0.0265	0.0147	55.3
Exp	$V_{0,\text{pop}}$	0.479	0.0352	7.35
	λ_{pop}	0.0198	0.00033	1.67
	ω_{V_0}	0.144	0.0538	37.3
	ω_{λ}	0.0271	0.0144	53

Table A3. Estimated parameters relative to the cell line MDA-MB-231 Dt+ Luc+.

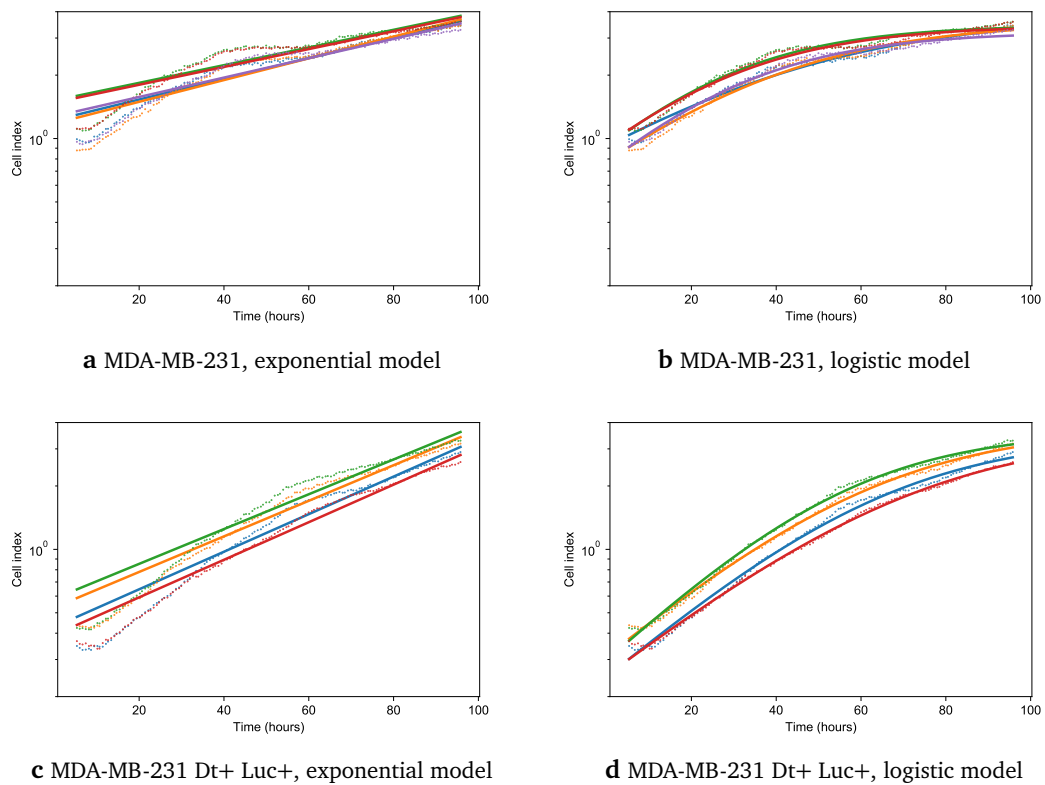


Figure A3. Individual fit to the exponential (left) and to the logistic (right) models of the cell lines MDA-MB-231 (top) and MDA-MB-231 Dt+ Luc+ (bottom).

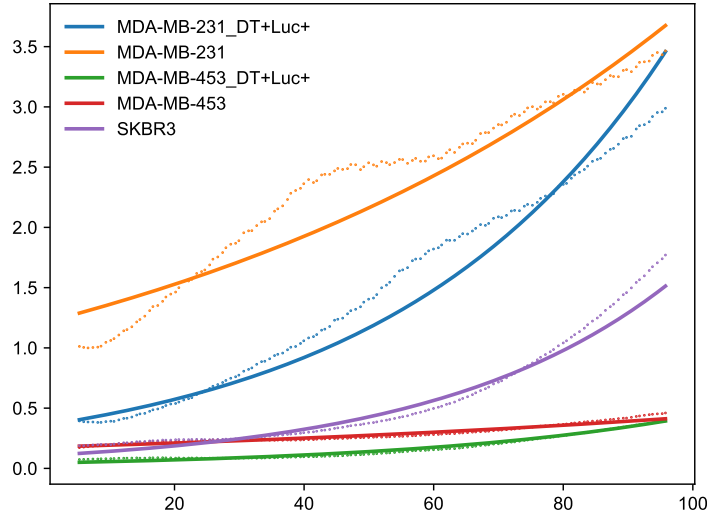


Figure A4. Exponential fit to the mean of each cell line.

A.2 Fit to the average

In this Section we analyze the exponential fit to the average. We fit the mean of the data to the following exponential function:

$$V(t) = V_0 2^{t/\tau}. \quad (9.10)$$

We apply the scipy algorithm curve fit to perform the nonlinear regression and use the standard deviation over the square root of the number of data as weight. The least squares function is then defined as follows:

$$\mathcal{L}(\tau) = \sum_{i=1}^N (w_i (\bar{y}_i - V(t_i; \tau)))^2, \quad (9.11)$$

where

$$w_i = \frac{\sigma_i}{\sqrt{n_i}} \quad (9.12)$$

are weights depending on the standard errors of the data.

Figure A4 shows the exponential fit relative to the different cell lines.

A.3 Doubling time

We now compute the cell doubling time as defined in (9.9). Table A4 provides the values of the doubling time of the different cell lines. We observe a crucial difference between the population/individual approach and the xCELLigence/mean fit for the cell lines MDA-MB-231 and MDA-MB-231 Dt+ Luc+, since the best fit of these two groups is given by the logistic model.

Cell lines	xCELLigence	Mean	Best fit	Individual	Population
MDA-MB-231	53.03 ± 0.96	59.8 ± 1.53	Logistic	17.2 ± 2.81	17.1 ± 2.27
MDA-MB-231 DT+Luc+	28.53 ± 0.26	29.2 ± 0.39	Logistic	17.3 ± 1.19	17.3 ± 1.23
MDA-MB-453	76.62 ± 0.93	78.1 ± 1.72	Exp	74.4 ± 15.8	74.2 ± 15.4
MDA-MB-453 DT+Luc+	36.72 ± 0.54	30.6 ± 0.42	Exp	29.8 ± 3.9	29.8 ± 3.76
SKBR3	28.01 ± 0.33	25.1 ± 0.48	Exp	21.6 ± 0.982	21.7 ± 0.838

Table A4. Cell doubling time of each cell line. Comparison between the xCELLigence computation, the values obtained with the fit to the mean and the results obtained with the individual and with the population approaches (we provide the values relative to the best fit only). Exp = exponential.

A.3.1 Transfected vs non-transfected cell lines

Considering the population approach, we observe a high variability in the doubling times relative to the cell line MDA-MB-453 and its transfected group MDA-MB-453 DT+ Luc+. The two groups relative to MDA-MB-231 show less diversity when the data are fitted to the logistic function. From Tables A2 and A3 indeed we observe that the parameters K_{pop} and a_{pop} are comparable, suggesting that there isn't great variability between MDA-MB-231 and its transfected.

B Supplementary figures and tables to Chapter 2

Model	-2LL	AIC	BIC
Gompertz	2232	2246	2253
Reduced Gompertz	2256	2266	2271
Logistic	2315	2327	2333
Exponential	2644	2652	2656

Table B1. Statistical indices of the tumor growth models (lung, volume). Models ranked in ascending order of AIC (Akaike information criterion). Other statistical indices are the log-likelihood estimate (-2LL) and the Bayesian information criterion (BIC).

Model	-2LL	AIC	BIC
Reduced Gompertz	2953	2961	2962
Gompertz	2953	2965	2965
Logistic	3010	3020	3020
Exponential	3097	3103	3104

Table B2. Statistical indices of the tumor growth models (breast, fluorescence). Models ranked in ascending order of AIC (Akaike information criterion). Other statistical indices are the log-likelihood estimate (-2LL) and the Bayesian information criterion (BIC).

Model	Parameter	Unit	Fixed effects	ω	R.S.E. (%)
Gompertz	α	day ⁻¹	0.718	0.166	3.87
	β	day ⁻¹	0.0742	0.239	5.82
	σ	-	[28.63, 0.078]	-	[13.71, 14.09]
Reduced Gompertz	β	day ⁻¹	0.077	0.121	2.79
	k	-	9.42	-	0.293
	σ	-	[27.32, 0.11]	-	[13.75, 10.79]
Logistic	ρ	day ⁻¹	0.476	0.123	2.84
	K	mm ³	1.65e+03	0.0895	4.04
	σ	-	[39.28, 0.11]	-	[12.63, 13.08]
Exponential	α	day ⁻¹	0.403	0.111	2.73
	σ	-	[93.69, 0.35]	-	[19.59, 15.68]

Table B3. Parameter values estimated with the SAEM algorithm (lung, volume). Fixed effects (typical values) of the parameters of the different models. ω is the standard deviation of the random effects. σ is vector of the residual error model parameters. Last column shows the relative standard errors (R.S.E.) of the estimates.

Model	Parameter	Unit	Fixed effects	ω	R.S.E. (%)
Reduced Gompertz	β	day ⁻¹	0.077	0.072	4.11
	k	-	9.85	-	0.919
	σ	-	[0,0.325]	-	[0,10.2]
Gompertz	α	day ⁻¹	0.758	0.087	4.15
	β	day ⁻¹	0.0769	0.094	5.1
	σ	-	[0,0.325]	-	[0,10.5]
Logistic	ρ	day ⁻¹	0.404	0.047	2.36
	K	mm ³	1.18e+10	0.092	8.73
	σ	-	[0,0.495]	-	[0,13.8]
Exponential	α	day ⁻¹	0.078	0.028	6.18
	σ	-	[0,589]	-	[0,17]

Table B4. Parameter values estimated with the SAEM algorithm (breast, fluorescence). Fixed effects (typical values) of the parameters of the different models. ω is the standard deviation of the random effects. σ is vector of the residual error model parameters. Last column shows the relative standard errors (R.S.E.) of the estimates.

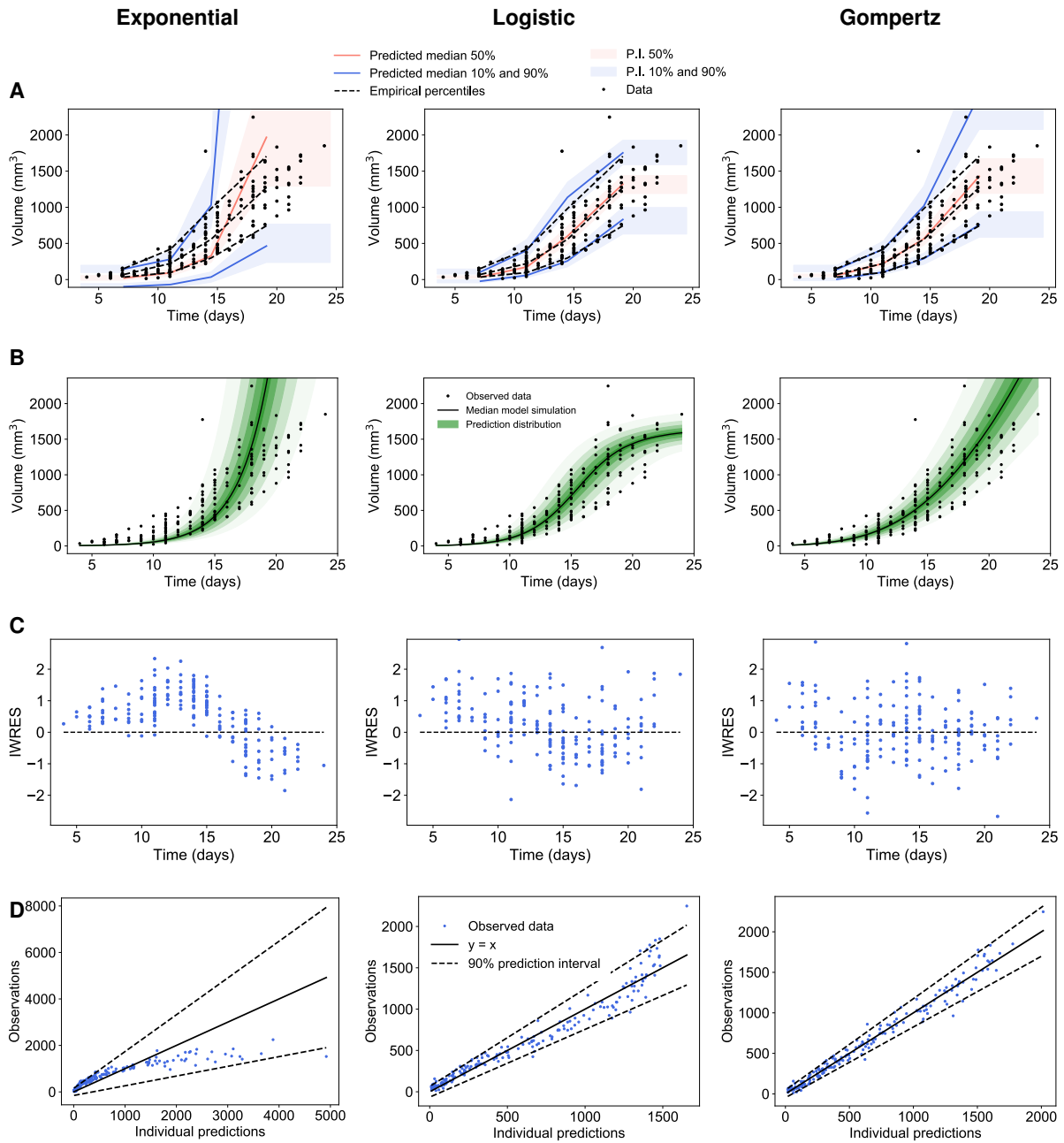


Figure B1. Diagnostic plots from population analysis (lung, volume). Population analysis of experimental tumor growth kinetics. A) Visual predictive checks assess goodness-of-fit for both structural dynamics and inter-animal variability by reporting model-predicted percentiles (together with confidence prediction intervals (PI) in comparison to empirical ones. B) Prediction distributions. C) Individual weighted residuals (IWRES) with respect to time. D) Observations vs predictions Left: exponential, Center: logistic, Right: Gompertz models.

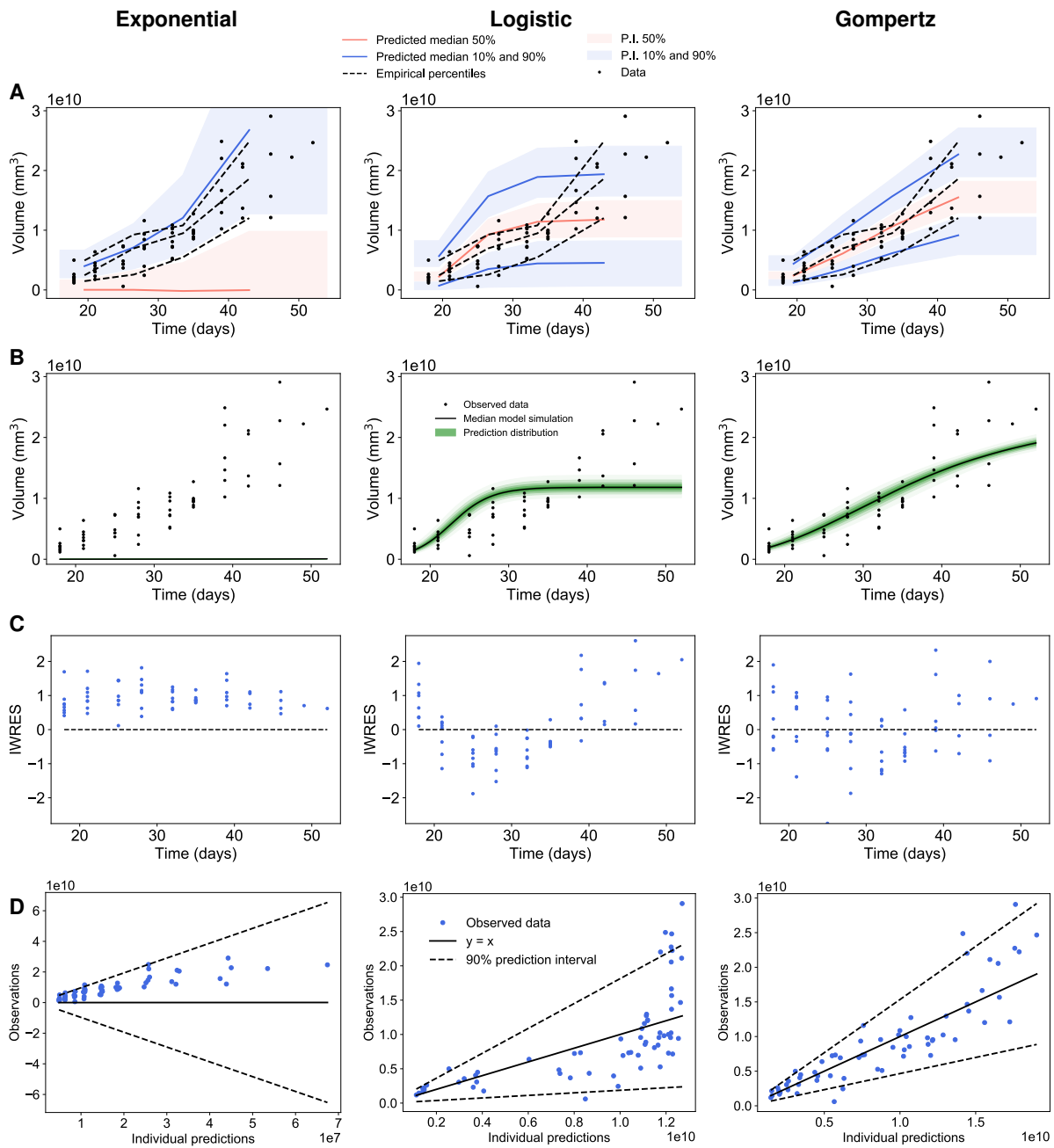


Figure B2. Diagnostic plots from population analysis (breast, fluorescence). Population analysis of experimental tumor growth kinetics. A) Visual predictive checks assess goodness-of-fit for both structural dynamics and inter-animal variability by reporting model-predicted percentiles (together with confidence prediction intervals (PI) in comparison to empirical ones. B) Prediction distributions. C) Individual weighted residuals (IWRES) with respect to time. D) Observations vs predictions Left: exponential, Center: logistic, Right: Gompertz models.

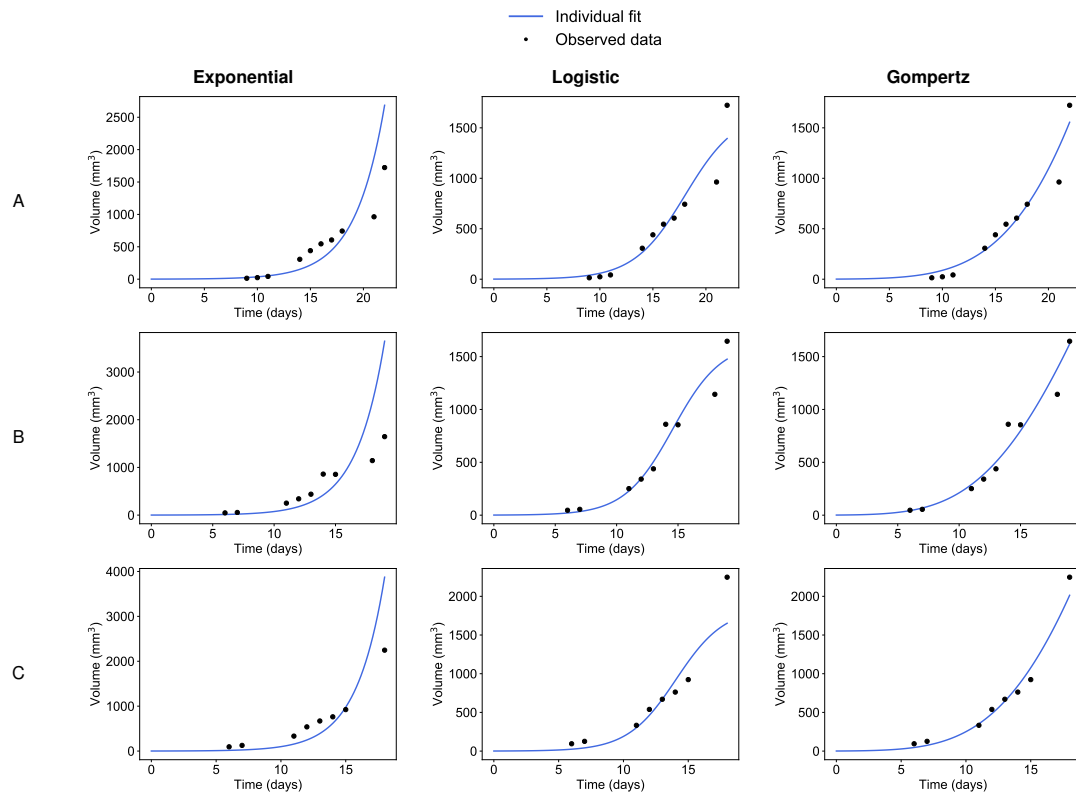


Figure B3. Individual fits from population analysis (lung, volume). Three representative examples of individual fits (animal A, animal B and animal C) computed with the population approach relative to the exponential (left), the logistic (center) and the Gompertz (right) models.

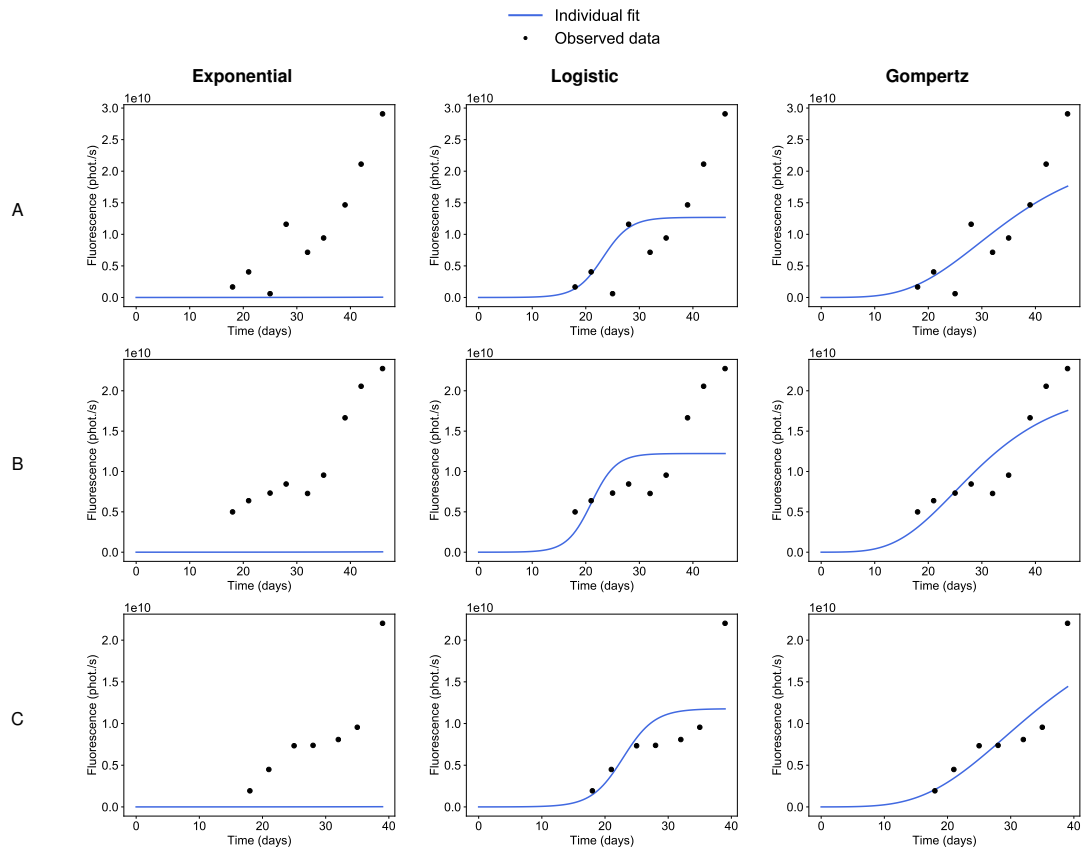


Figure B4. Individual fits from population analysis (breast, fluorescence). Three representative examples of individual fits (animal A, animal B and animal C) computed with the population approach relative to the exponential (left), the logistic (center) and the Gompertz (right) models.

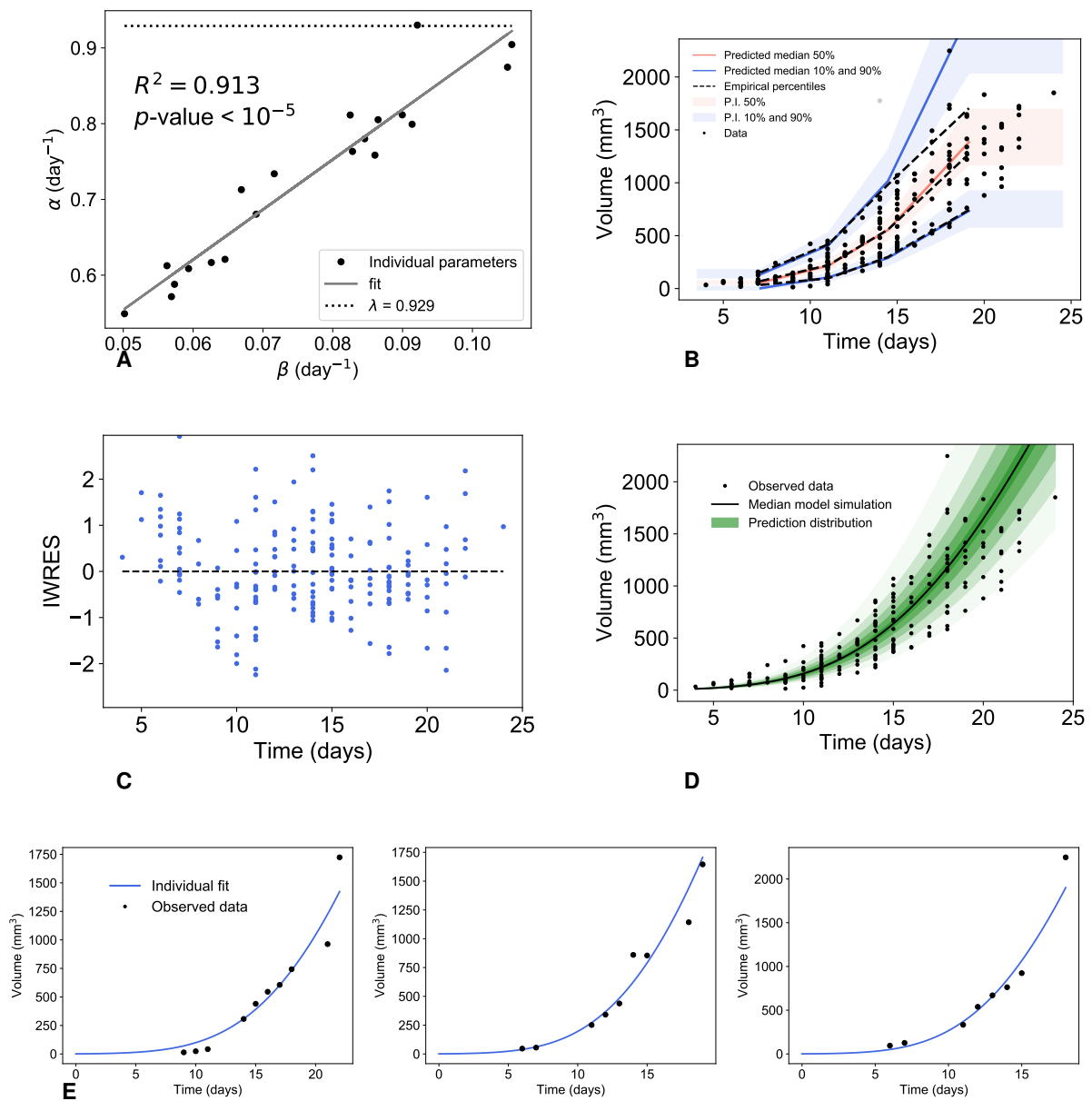


Figure B5. Correlation between the Gompertz parameters and diagnostic plots of the reduced Gompertz model with the population approach (lung, volume). Correlation between the individual parameters of the Gompertz model (A) and results of the population analysis of the reduced Gompertz model: visual predictive check (B), scatter plots of the residuals (C), prediction distribution (D) and examples of individual fits (E).

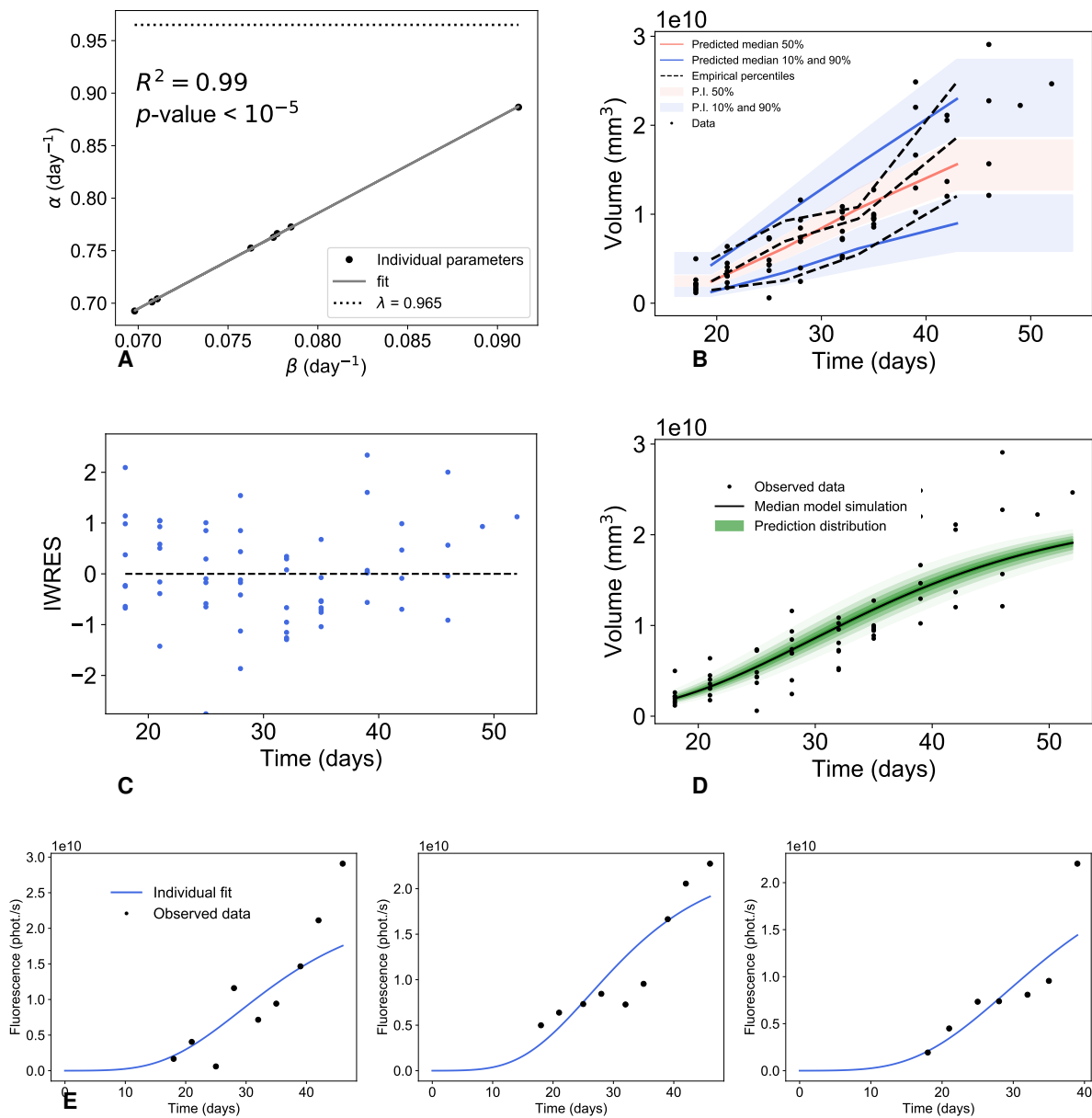


Figure B6. Correlation between the Gompertz parameters and diagnostic plots of the reduced Gompertz model with the population approach (breast, fluorescence). Correlation between the individual parameters of the Gompertz model (A) and results of the population analysis of the reduced Gompertz model: visual predictive check (B), scatter plots of the residuals (C), prediction distribution (D) and examples of individual fits (E).

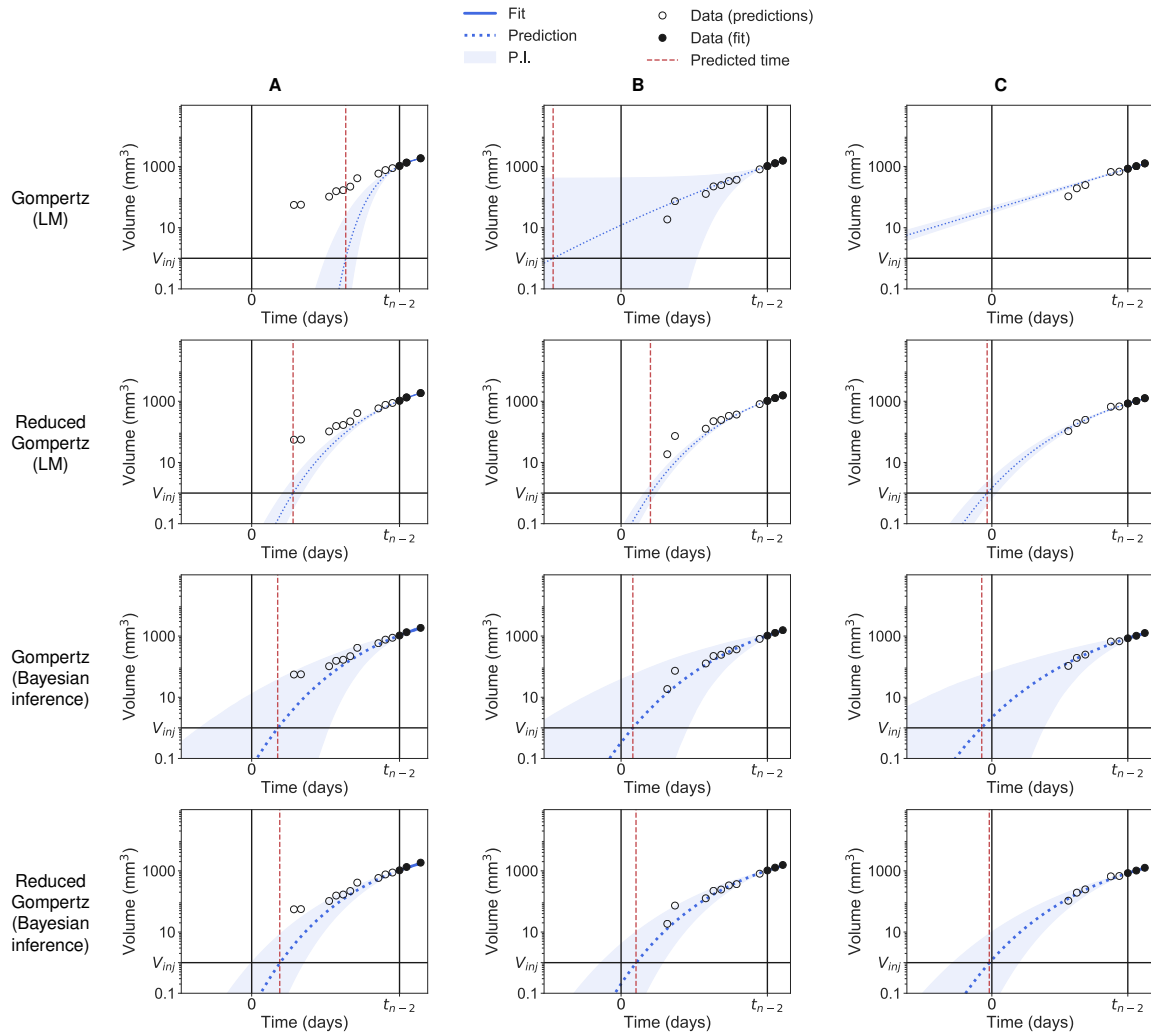


Figure B7. Backward predictions computed with likelihood maximization (LM) and with Bayesian inference (lung, volume). Three examples of backward predictions of individuals A, B and C computed with likelihood maximization (LM) and Bayesian inference: Gompertz model with likelihood maximization (first row); reduced Gompertz with likelihood maximization (second row); Gompertz with Bayesian inference (third row) and reduced Gompertz with Bayesian inference (fourth row). Only the last three points are considered to estimate the parameters. The grey area is the 95% prediction interval (P.I) and the dotted blue line is the median of the posterior predictive distribution. The red line is the predicted initiation time and the black vertical line the actual initiation time.

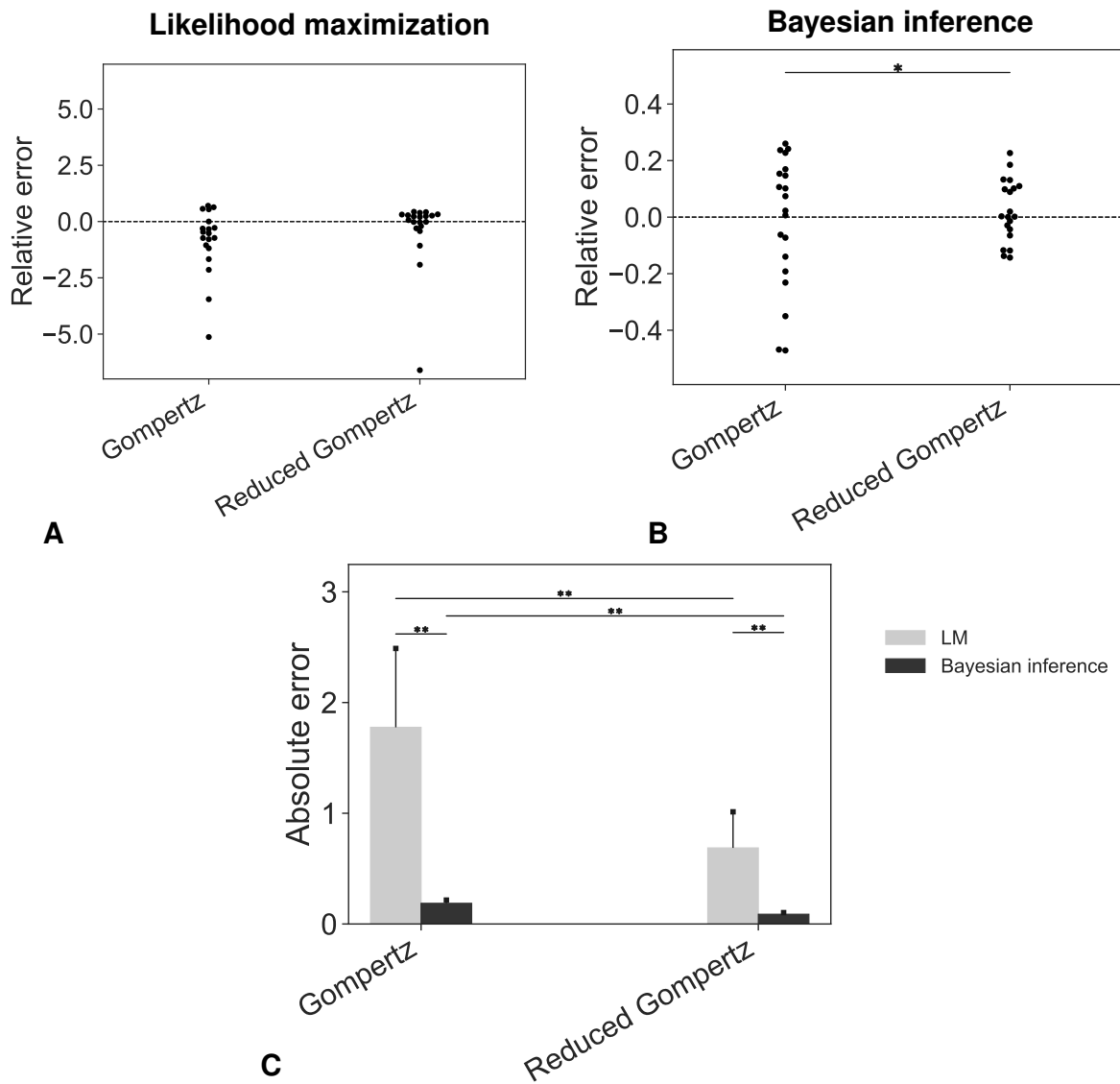


Figure B8. Error analysis of the predicted initiation time (lung, volume). Accuracy of the prediction models. Swarmplots of relative errors obtained under likelihood maximization (A) or Bayesian inference (B). (C) Absolute errors: comparison between the different distributions (* p -value < 0.05, ** p -value < 0.01).

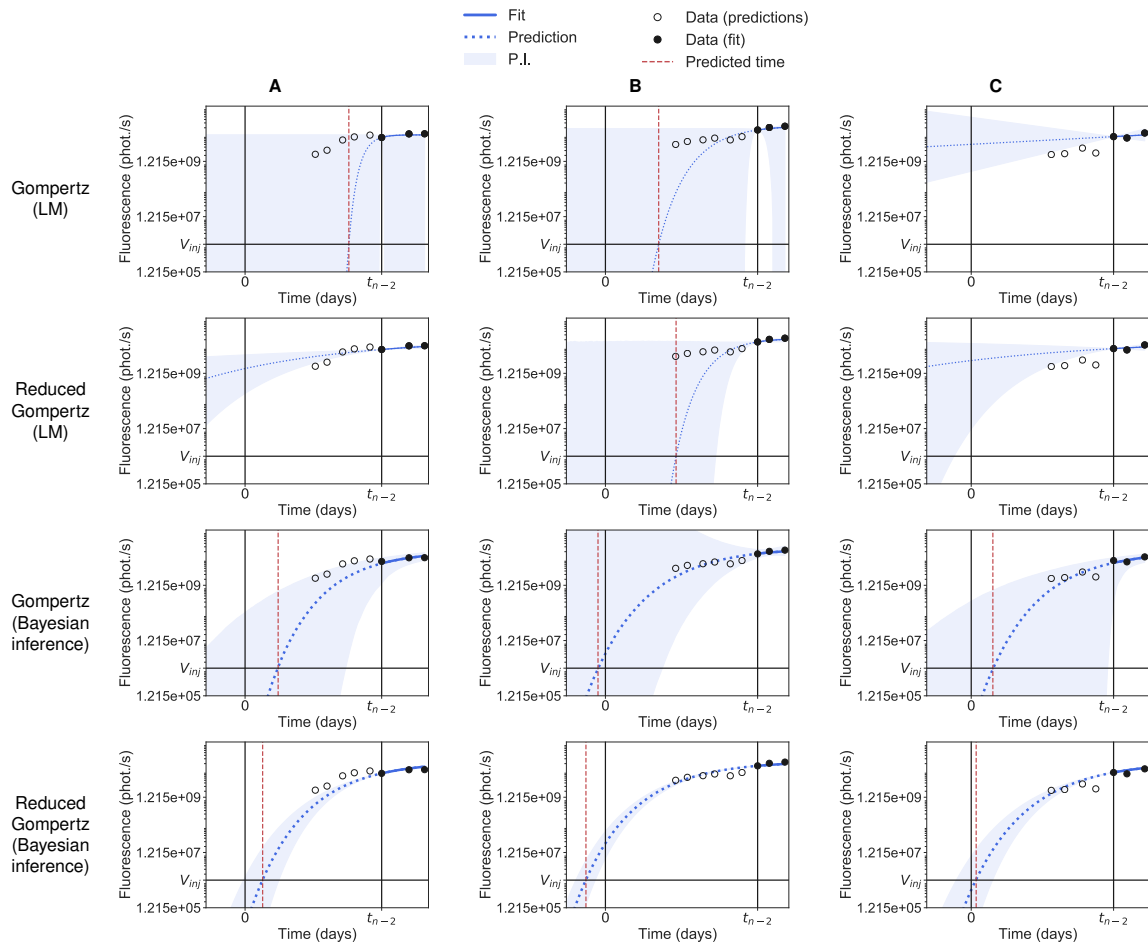


Figure B9. Backward predictions computed with likelihood maximization (LM) and with Bayesian inference (breast, fluorescence). Three examples of backward predictions of individuals A, B and C computed with likelihood maximization (LM) and Bayesian inference: Gompertz model with likelihood maximization (first row); reduced Gompertz with likelihood maximization (second row); Gompertz with Bayesian inference (third row) and reduced Gompertz with Bayesian inference (fourth row). Only the last three points are considered to estimate the parameters. The grey area is the 95% prediction interval (P.I) and the dotted blue line is the median of the posterior predictive distribution. The red line is the predicted initiation time and the black vertical line the actual initiation time.

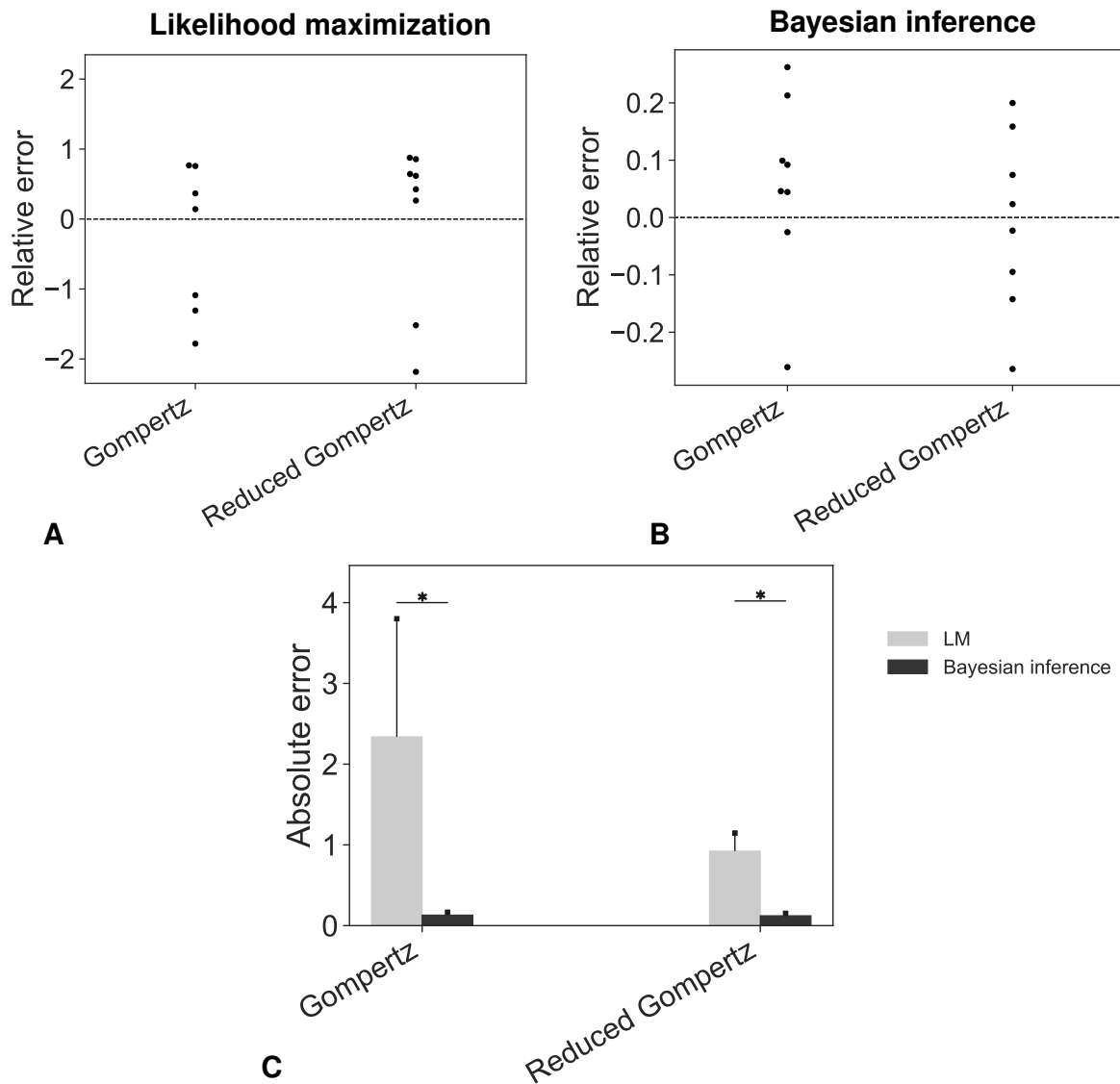


Figure B10. Error analysis of the predicted initiation time (breast, fluorescence). Accuracy of the prediction models. Swarmplots of relative errors obtained under likelihood maximization (A) or Bayesian inference (B). (C) Absolute errors: comparison between the different distributions (* p -value < 0.05 , ** p -value < 0.01).

C Supplementary material to Chapter 3

C.1 Nonlinear regression

C.1.1 Least squares and likelihood function

We now explain the nonlinear regression basic concept, with two parameters estimation methods: the least square estimation and the likelihood maximization method.

Let us suppose to have n observations $(x_i, y_i), i = 1, \dots, n$ with a known functional relationship

$f(\cdot; \theta^*)$, where $\theta^* \in \Theta \subset \mathbb{R}^p$ is the exact value defining the model:

$$y_i = f(x_i; \theta^*) + \varepsilon_i, \quad i = 1, \dots, n. \quad (9.13)$$

In (9.13) ε_i is the residual error, such that $\mathbb{E}[\varepsilon] = 0$. The **least-square estimate** of θ^* , denoted by $\bar{\theta}$, is obtained by minimizing the sum of the square residuals:

$$r(\bar{\theta}) = \sum_{i=1}^n (y_i - f(x_i; \theta))^2, \quad \theta \in \Theta. \quad (9.14)$$

We now introduce the possible numerical schemes that can be applied to find the solution to the minimization problem. We make use of the following notation:

$$\mathbf{f}(\theta) = [f(x_i, \theta)]_{i=1}^n, \quad J(\theta) = \left[\frac{\partial f(x_i, \theta)}{\partial \theta_j} \right]_{\substack{i=1, \dots, n, \\ j=1, \dots, p}}, \quad \mathbf{e}(\theta) = [\varepsilon_i]_{i=1}^n,$$

i.e. $\mathbf{f}(\theta)$ is the vector containing the evaluation of the function at points x_i , $J(\theta)$ is the Jacobian matrix and $\mathbf{e}(\theta)$ is the residual vector.

The solution to the minimization of the nonlinear least square in (9.14) is given, for example, by the following numerical schemes:

- **Gauss-Newton method.** It is an iterative algorithm to find the minimum of the least squares problem, starting from an initial guess θ^0 . We explain the derivation of the algorithm in the following. For θ close to θ^0 we have the Taylor expansion of the nonlinear function $\mathbf{f}(\theta)$

$$\mathbf{f}(\theta) \approx \mathbf{f}(\theta^0) + J(\theta^0)(\theta - \theta^0). \quad (9.15)$$

Then the residual vector is

$$\mathbf{e}(\theta) = \mathbf{y} - \mathbf{f}(\theta) \approx \mathbf{e}(\theta^0) - J(\theta^0)(\theta - \theta^0). \quad (9.16)$$

Therefore, $r(\theta) = (\mathbf{e}(\theta))^T \mathbf{e}(\theta)$ becomes

$$r(\theta) \approx (\mathbf{e}(\theta^0))^T \mathbf{e}(\theta^0) - 2(\mathbf{e}(\theta^0))^T J(\theta^0)(\theta - \theta^0) + (\theta - \theta^0)^T (J(\theta^0))^T J(\theta^0)(\theta - \theta^0). \quad (9.17)$$

The right hand side of 9.17 is minimized with respect to θ when

$$\begin{aligned} \theta - \theta^0 &= [(J(\theta^0))^T J(\theta^0)]^{-1} (J(\theta^0))^T \mathbf{e}(\theta^0) \\ &= \delta^0. \end{aligned} \quad (9.18)$$

Then, the next approximation is

$$\theta^1 = \theta^0 + \delta^0. \quad (9.19)$$

The algorithm proceeds iteratively until a certain accuracy has been reached.

- **Levenberg-Marquardt algorithm.** This method combines the Gauss-Newton algorithm with the gradient descent method. Instead of having (9.18), the Levenberg-Marquardt update is given by

$$[(J(\theta^0))^T J(\theta^0) + \lambda \text{diag}((J(\theta^0))^T J(\theta^0))](\theta - \theta^0) = (J(\theta^0))^T \mathbf{e}(\theta^0), \quad (9.20)$$

where λ is a parameter first initialized to be large, so that first updates are small steps in the steepest descent direction. If the sum of the square residuals increases, λ increases. Other-

wise, if the approximation improves, λ decreases so that the Levenberg-Marquardt method approaches to the Gauss-Newton algorithm and the solution accelerates to the local minimum.

- **Nelder-Mead algorithm.** This is a simplex method for finding a local minimum of a function of several variables. It is not based on derivatives, hence it can find minima that are not stationary points. In two dimensions, for example, a simplex is a triangle. The method is a pattern search that compares function values at three vertices of a triangle. The vertex where the function has larger value is rejected and replaced with a new vertex (for further details regarding the algorithm see [290]). In this way, the algorithm constructs a sequence of triangles where the function values at the vertices decrease. The size of the triangles reduces and finally the coordinates of the minimum point are found.

The **maximum likelihood estimator** maximizes the so called likelihood function. Let us suppose that the residuals ε_i are i.i.d. with density function $\sigma^{-1}g(\varepsilon/\sigma)$ (i.e. g is the error distribution for standardized errors). The likelihood function is the joint probability density of the observed events:

$$L(\boldsymbol{\theta}, \sigma^2) = p(\mathbf{y}|\boldsymbol{\theta}, \sigma^2) = \prod_{i=1}^n \left[\sigma^{-1} g\left(\frac{y_i - f(x_i; \boldsymbol{\theta})}{\sigma}\right) \right]. \quad (9.21)$$

If the residuals ε_i are assumed to be normally distributed (i.e. $\varepsilon_i \sim \mathcal{N}(0, \sigma^2)$, where σ^2 is assumed to be known), then the maximum likelihood estimate coincides with the least square estimate. In this case, (9.21) becomes:

$$L(\boldsymbol{\theta}, \sigma^2) = \frac{1}{(2\pi\sigma^2)^{-n/2}} \exp\left(-\frac{1}{2} \sum_{i=1}^n \frac{(y_i - f(x_i; \boldsymbol{\theta}))^2}{\sigma^2}\right). \quad (9.22)$$

Maximizing (9.22) is equivalent to minimizing the negative log-likelihood function $l(\boldsymbol{\theta}, \sigma^2)$

$$\begin{aligned} l(\boldsymbol{\theta}, \sigma^2) &= -\log L(\boldsymbol{\theta}, \sigma^2) = \frac{n}{2} \log \sigma^2 + \frac{1}{2\sigma^2} \sum_{i=1}^n (y_i - f(x_i; \boldsymbol{\theta}))^2 \\ &= -\log L(\boldsymbol{\theta}, \sigma^2) = \frac{n}{2} \log \sigma^2 + \frac{1}{2\sigma^2} r(\boldsymbol{\theta}). \end{aligned} \quad (9.23)$$

Minimizing (9.23) with respect to $\boldsymbol{\theta}$ is equivalent to minimize $r(\boldsymbol{\theta})$, i.e. to find the least-squares estimate $\bar{\boldsymbol{\theta}}$. Then, the solution to $\partial l / \partial \sigma^2$ is given by $\bar{\sigma}^2 = r(\bar{\boldsymbol{\theta}})/n$, that is a minimum of (9.23). It can be proven that the pair $(\bar{\boldsymbol{\theta}}, \bar{\sigma}^2)$ minimizes (9.23) [139].

C.1.2 Evaluation and comparison of nonlinear models

In order to evaluate and compare different nonlinear models, we compute the following quantities:

- *Standard errors.* The standard errors of the coefficients characterize the uncertainties that are generated by the random fluctuations of the data. We start from assuming that asymptotically the least squares estimator $\boldsymbol{\theta}$ is normally distributed [139]:

$$\boldsymbol{\theta} \stackrel{a}{\sim} \mathcal{N}\left(\bar{\boldsymbol{\theta}}, \frac{\text{Cov}}{n}\right),$$

where Cov is the asymptotic covariance matrix. The standard error is defined as follows

$$\text{Std}(\theta_i) = \sqrt{\text{Cov}_{i,i}}, \quad i = 1, \dots, p \quad (9.24)$$

being Cov the covariance matrix defined as

$$\text{Cov} = \text{NMSE}((J(\bar{\theta}))^T J(\bar{\theta}))^{-1}, \quad \text{where} \quad \text{NMSE} = \frac{1}{n-p} r(\bar{\theta}) \quad (9.25)$$

In (9.25), NMSE denotes the a posteriori estimate of σ^2 and J is the jacobian.

- *Akaike information criterion (AIC)*. It is an estimator of the relative quality of different models for a given set of data. It provides a measure of the quality of a statistical model, taking into account the goodness of fit and the complexity of the model. Thus, it is a criterion to compare different models rather than to evaluate the quality of a single model. It is defined as follows:

$$AIC = 2p - 2 \ln(L(\bar{\theta})). \quad (9.26)$$

The model with the lowest *AIC* is preferred.

- *Bayesian information criterion (BIC)*. As the *AIC*, it is a criterion to select a model among a finite set of parametric models with different numbers of parameters. It evaluates the overfitting of the models by introducing the penalty term for the number of parameters in the model. It is defined as follows:

$$BIC = \ln(n)p - 2 \ln(L(\bar{\theta})). \quad (9.27)$$

The model with the lowest *BIC* is preferred.

- *Likelihood ratio test (or log-likelihood ratio test)*. It is a statistical test that compares the goodness of fit of two different models. The test is based on the (log-)likelihood ratio, which compares how many times more likely the data are under a model than the other. We assume to have two statistical models \mathcal{M}_1 and \mathcal{M}_2 with different number of parameters (p_1 and p_2 , respectively) that fit a given set of data. We specify the null and the alternative hypothesis:

$$H_0 : \quad \mathcal{M}_1 \text{ fits better the data,}$$

$$H_1 : \quad \mathcal{M}_2 \text{ fits better the data.}$$

The likelihood test is based on the likelihood ratio, that is defined as follows:

$$\Lambda = \frac{L_{\mathcal{M}_1}}{L_{\mathcal{M}_2}}, \quad (9.28)$$

being $L_{\mathcal{M}_1}$ and $L_{\mathcal{M}_2}$ the computed maximum likelihood estimations of \mathcal{M}_1 and \mathcal{M}_2 , respectively. Alternatively, it is possible to substitute the maximum log-likelihood estimations in 9.28. Finally, we compute the p -value to accept or reject the null hypothesis

$$p\text{-value} = \chi_{p_2-p_1}^2(\Lambda), \quad (9.29)$$

where $\chi_{p_2-p_1}^2$ is the chi squared distribution with $p_2 - p_1$ degrees of freedom.

C.1.3 Generalized least squares

We consider now the following function to be minimized:

$$r(\boldsymbol{\theta}) = [\mathbf{y} - \mathbf{f}(\boldsymbol{\theta})]^T \mathbf{W}^{-1} [\mathbf{y} - \mathbf{f}(\boldsymbol{\theta})], \quad (9.30)$$

where \mathbf{W} is a known positive definite matrix, representing a weight matrix. This minimization criterion arises when the residual error is assumed to have variance $\sigma^2 \mathbf{W}$, i.e. $\varepsilon \sim \mathcal{N}(0, \sigma^2 \mathbf{W})$.

Let $\mathbf{W} = \mathbf{U}^T \mathbf{U}$ be the Cholesky decomposition of \mathbf{W} , where \mathbf{U} is an upper triangular matrix. Let us denote $\mathbf{R} = (\mathbf{U}^T)^{-1}$. Then (9.30) can be written as

$$r(\boldsymbol{\theta}) = [\mathbf{y} - \mathbf{f}(\boldsymbol{\theta})]^T \mathbf{R}^T \mathbf{R} [\mathbf{y} - \mathbf{f}(\boldsymbol{\theta})] \quad (9.31)$$

The numerical schemes that can be applied to solve (9.30) are the same explained in section C.1.1. As regards the derivation of the standard errors, we compute the covariance matrix as follows:

$$J(\boldsymbol{\theta}) = \left[\mathbf{R} \frac{\partial f(x_i, \boldsymbol{\theta})}{\partial \theta_j} \right]_{\substack{i=1, \dots, n, \\ j=1, \dots, p}},$$

$$\text{Cov} = \text{NMSE}((J(\boldsymbol{\theta}))^T \mathbf{W}^{-1} J(\boldsymbol{\theta}))^{-1}.$$

C.1.4 Replication

We now deal with replicated data. Suppose that a design is replicated m_i times for point x_i , so that the nonlinear model becomes

$$y_{ij} = f(x_i; \boldsymbol{\theta}^*) + \varepsilon_{ij}, \quad i = 1, \dots, n, \quad j = 1, \dots, m_i. \quad (9.32)$$

where the fluctuations ε_{ij} are assumed to be i.i.d ($\varepsilon_{ij} \sim \mathcal{N}(0, \sigma^2)$). Let us denote by $\bar{y}_i = \frac{1}{m_i} \sum_{j=1}^{m_i} y_{ij}$ the mean of the observations at point x_i . The following decomposition holds:

$$\begin{aligned} \sum_{i=1}^n \sum_{j=1}^{m_i} (y_{ij} - f(x_i; \boldsymbol{\theta}))^2 &= \sum_{i=1}^n \sum_{j=1}^{m_i} (y_{ij} - \bar{y}_i + \bar{y}_i - f(x_i; \boldsymbol{\theta}))^2 \\ &= \sum_{i=1}^n \sum_{j=1}^{m_i} (y_{ij} - \bar{y}_i)^2 + \sum_{i=1}^n m_i (\bar{y}_i - f(x_i; \boldsymbol{\theta}))^2. \end{aligned} \quad (9.33)$$

In (9.33) $\sum_{i=1}^n \sum_{j=1}^{m_i} (y_{ij} - \bar{y}_i)^2$ is usually referred to as the pure error sum of squares. Therefore, minimizing $\sum_{i=1}^n \sum_{j=1}^{m_i} (y_{ij} - f(x_i; \boldsymbol{\theta}))^2$ with respect to $\boldsymbol{\theta}$ is equivalent to minimize $\sum_{i=1}^n m_i (\bar{y}_i - f(x_i; \boldsymbol{\theta}))^2$, i.e. a weighted least-squares analysis with weights m_i [139].

C.2 Python computation

We implement the code with python to perform the nonlinear regression analysis. We use the following functions:

- `lmfit.minimize`: for the optimization problem. It takes an objective function to be minimized in the least square sense, an initial guess of the parameters and optional arguments (e.g. the name of the fitting method). The function returns the optimal parameters and the following

statistical indices:

$$\begin{aligned} AIC &= n \ln(r(\boldsymbol{\theta})/n) + 2p, \\ BIC &= n \ln(r(\boldsymbol{\theta})/n) + p \ln(n), \\ \chi^2 &= r(\boldsymbol{\theta}), \\ \text{reduced } \chi^2 &= \frac{\chi^2}{n-p}. \end{aligned}$$

In case we apply the Levenberg-Marquardt algorithm, the function returns also the covariance matrix. In order to compare different methods, we compute the covariance matrix by using other functions.

- `algopy.jacobian`: this function computes the jacobian function with the finite difference method. We apply this function in order to compute the covariance matrix to derive the standard errors of the estimated optimal parameters.

C.3 Results on the MDA-MB-231 cell line

Data fit to the Hill model were performed using the strategies introduced in the previous sections. Here, results relative to the MDA-MB-231 cell line are shown.

C.3.1 Data analysis

Figure C1 shows the *in vitro* cell viability with respect to the docetaxel concentration for each treatment group. We observed that trastuzumab only, empty ANC-1 and ANC-2 do not have any effect on the cell viability. Docetaxel only and docetaxel injected with trastuzumab showed a similar behavior. This is due to the fact that the MDA-MB-231 breast cancer is trastuzumab-resistant. Liposome-1 plus free trastuzumab and ANC-1 exhibit similar performances, as Liposome-2 plus free trastuzumab and ANC-2. In the next sections we will focus on the analysis of docetaxel, free docetaxel plus trastuzumab, ANC-1 and ANC-2.

Nonlinear regression: data fit to the Hill function

Two parameters Hill function

Let us consider the Hill function

$$f(c; Ec_{50}, \gamma) = 100 \left(1 - \frac{c^\gamma}{Ec_{50}^\gamma + c^\gamma} \right), \quad (9.34)$$

that describes the dose-response curve. We denote by Ec_{50} the half maximal inhibitory concentration, i.e. the quantity of drug (docetaxel) needed to reduce the cell viability by half, and by γ the Hill coefficient.

We fit the experimental data to the Hill function and estimate the parameters Ec_{50} and γ . We mini-

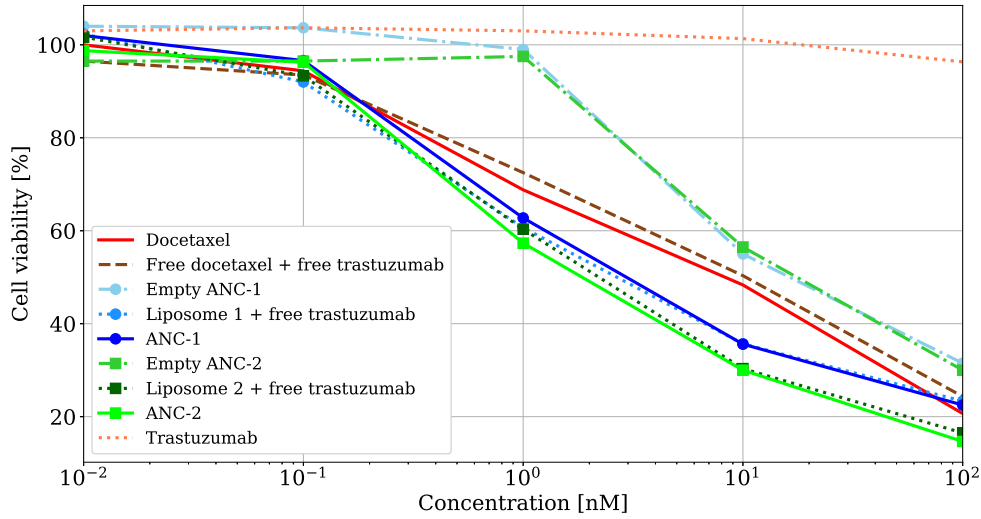


Figure C1. *In vitro* efficacy with respect to the docetaxel concentration (mean values of each group)

minimize the sum of least squares defined as follows

$$r(Ec_{50}, \gamma) = \sum_{i=1}^n \sum_{j=1}^{m_i} (y_{ij} - f(c_i; Ec_{50}, \gamma))^2, \quad (9.35)$$

where y_{ij} , $j = 1, \dots, m_i$ are the repeated observations at point c_i (for $i = 1, \dots, n$). We minimize (9.35) applying the algorithms of Levenberg-Marquardt (least squares method) and of Nelder-Mead (simplex method) and we compare the results. We denote by $(\overline{Ec}_{50}, \overline{\gamma})$ the optimal values.

Finally, we compute the standard errors as defined in (9.24): we derive first the jacobian with the algopy library and then the covariance matrix. Table C1 provides the values and the standard errors of Ec_{50} and γ , respectively, computed with the two algorithms of Levenberg-Marquardt and of Nelder-Mead. We observe that the Hill function does not describe the response of the trastuzumab only (the standard errors are indeed high), according to the biological reason that the antibody only does not have any effect on the reduction of the tumor. As regards the other groups, the two algorithms deliver the same results.

Three parameters Hill function

We now add a new parameter to equation (9.34). Therefore, we consider the following equation:

$$f(c; Ec_{50}, \gamma, E_{\max}) = 100 \left(1 - \frac{E_{\max} c^{\gamma}}{Ec_{50}^{\gamma} + c^{\gamma}} \right). \quad (9.36)$$

Note that in this case the concentration corresponding to half the effect is given by

$$\frac{Ec_{50}}{(2E_{\max} - 1)^{1/\gamma}}.$$

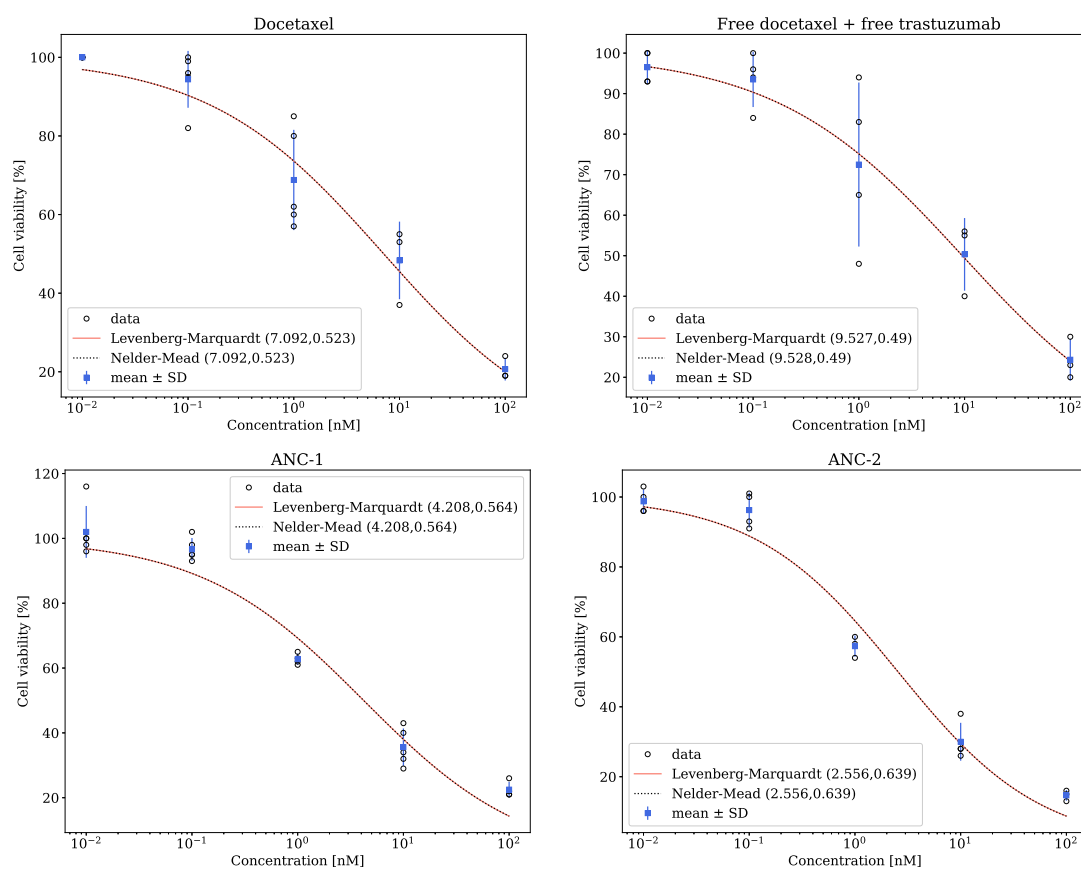


Figure C2. Data (black circles), Hill function computed with the Levenberg-Marquardt method (orange line) and with the Nelder-Mead method (black dotted line) and mean values with the standard deviations of the data (blue). The values in the brackets represent the estimated parameters EC_{50} and γ , respectively.

Drug	Parameters	Levenberg-Marquardt			Nelder-Mead		
		value	StdErr	StdErr%	value	StdErr	StdErr%
Docetaxel	Ec_{50}	7.092	1.693	23.877	7.092	1.693	23.876
	γ	0.524	0.060	11.364	0.524	0.060	11.364
Free docetaxel + trastuzumab	Ec_{50}	9.528	3.040	31.903	9.528	3.040	31.903
	γ	0.490	0.074	14.987	0.490	0.074	14.987
Empty ANC-1	Ec_{50}	22.975	7.093	30.870	22.975	7.093	30.871
	γ	0.751	0.155	20.591	0.750	0.155	20.591
Liposome 1 + free trastuzumab	Ec_{50}	3.899	0.980	25.136	3.899	0.980	25.137
	γ	0.505	0.062	12.199	0.504	0.062	12.199
ANC-1	Ec_{50}	4.208	0.788	18.727	4.208	0.788	18.727
	γ	0.565	0.056	9.974	0.565	0.056	9.974
Empty ANC-2	Ec_{50}	21.855	4.802	21.972	21.856	4.802	21.972
	γ	0.680	0.100	14.651	0.680	0.100	14.651
Liposome 2 + free trastuzumab	Ec_{50}	2.655	0.565	21.281	2.655	0.565	21.281
	γ	0.622	0.077	12.427	0.622	0.077	12.427
ANC-2	Ec_{50}	2.556	0.427	16.702	2.556	0.427	16.702
	γ	0.640	0.060	9.455	0.640	0.060	9.455
Trastuzumab	Ec_{50}	178.800	3e06	1e06	136.371	2e08	1e08
	γ	5.623	1e05	3e06	10.537	5e08	5e09

Table C1. Estimated values with the respective standard errors computed with the Lavenberg-Marquardt algorithm and with Nelder-Mead algorithm.

We proceed as explained in the previous section, applying the Nelder-Mead algorithm only to minimize

$$r(Ec_{50}, \gamma, Ec_{\max}) = \sum_{i=1}^n \sum_{j=1}^{m_i} (y_{ij} - f(c_i; Ec_{50}, \gamma, E_{\max}))^2 \quad (9.37)$$

Table C2 shows the estimated values. The large standard errors of the parameters relative to the free drugs (docetaxel and docetaxel plus trastuzumab) suggest that this model is not appropriate for these two groups. On the other hand, the parameters relative to ANC-1 and ANC-2 don't exhibit large errors.

Comparison between the two models

We now compare the two and three parameters Hill function with the indices introduced in section C.1.2. Table C3 provides the AIC , BIC , χ^2 and reduced χ^2 . For the groups docetaxel and free docetaxel plus free trastuzumab the two parameters Hill functions fits better the data, while for the two immunoliposomes (ANC-1 and ANC-2) the three parameters Hill function describes better the data.

We then perform the likelihood ratio test, where the null and the alternative hypothesis are:

$$H_0 : f(c; Ec_{50}, \gamma) \text{ fits better the data}$$

$$H_1 : f(c; Ec_{50}, \gamma, E_{\max}) \text{ fits better the data}$$

Table C4 provides the p -value for the likelihood ratio test. We reject the null hypothesis for ANC-1

Drug	Parameters	Value	StdErr	StdErr [%]
Docetaxel	Ec_{50}	4.083	2.913	71.343
	γ	0.595	0.138	23.273
	E_{max}	0.893	0.131	14.677
Free docetaxel + trastuzumab	Ec_{50}	6.848	9.232	134.817
	γ	0.524	0.176	33.591
	E_{max}	0.936	0.251	26.867
Empty ANC-1	Ec_{50}	7.414	2.370	31.963
	γ	2.134	2.087	97.810
	E_{max}	0.688	0.057	8.281
Liposome 1 + free trastuzumab	Ec_{50}	1.031	0.263	25.488
	γ	0.867	0.166	19.144
	E_{max}	0.764	0.041	5.334
ANC-1	Ec_{50}	1.188	0.219	18.456
	γ	0.983	0.153	15.585
	E_{max}	0.758	0.031	4.084
Empty ANC-2	Ec_{50}	7.535	1.077	14.295
	γ	1.602	0.534	33.362
	E_{max}	0.711	0.036	5.126
Liposome 2 + free trastuzumab	Ec_{50}	1.204	0.333	27.667
	γ	0.891	0.184	20.628
	E_{max}	0.829	0.054	6.469
ANC-2	Ec_{50}	1.132	0.208	18.405
	γ	0.948	0.136	14.327
	E_{max}	0.832	0.033	3.976
Trastuzumab	Ec_{50}	54.865	-	-
	γ	19.165	1e13	6e13
	E_{max}	0.037	-	-

Table C2. Optimal values and standard errors relative to the three parameters Hill function computed by the Nelder-Mead algorithm.

Drug	# parameters	AIC	BIC	χ^2	reduced χ^2
Docetaxel	2	91.345	93.434	1344.543	70.765
	3	92.866	95.999	1314.199	73.011
Free docetaxel + trastuzumab	2	85.876	87.657	1701.126	106.320
	3	87.817	90.488	1695.566	113.038
Empty ANC-1	2	61.801	62.931	1108.947	100.813
	3	55.546	57.241	587.666	58.767
Liposome 1 + free trastuzumab	2	64.982	66.398	874.391	67.261
	3	56.702	58.826	440.606	36.717
ANC-1	2	97.459	99.730	1338.015	63.715
	3	82.465	85.871	639.095	31.955
Empty ANC-2	2	39.793	40.398	358.496	44.812
	3	31.808	32.716	132.081	18.869
Liposome 2 + free trastuzumab	2	58.969	60.248	710.130	59.177
	3	55.519	57.436	481.114	43.738
ANC-2	2	70.262	72.043	714.501	44.656
	3	62.199	64.871	408.528	27.235
Trastuzumab	2	50.799	52.215	339.667	26.128
	3	52.799	54.923	339.667	28.306

Table C3. Comparison between the two parameters and the three parameters Hill function: Akaike information criterion, bayesian information criterion, sum of square residuals (χ^2) and reduced χ^2 .

Drug	-2 log(L), 2 parameters	-2 log(L), 3 parameters	p-value
Docetaxel	108.3450	107.8657	0.4887
Free docetaxel + free trastuzumab	99.8761	99.8172	0.8082
Empty ANC-1	70.8008	62.5457	0.0041
Liposome 1 + free trastuzumab	75.9822	65.7015	0.0013
ANC-1	116.4593	99.4648	0.0000
Empty ANC-2	45.7933	35.8083	0.0016
Liposome 2 + free trastuzumab	68.9695	63.5187	0.0196
ANC-2	84.2618	74.1994	0.0015
Trastuzumab	61.7987	61.7987	1.0000

Table C4. Likelihood ratio test: evaluation of the log-likelihood functions and *p*-value.

and ANC-2, while we accept it for docetaxel and docetaxel combined with trastuzumab. Finally, Figure C3 shows the two fitted functions for the docetaxel, docetaxel plus trastuzumab and the two nanoparticles.

C.4 Results on the SKBR3 cell line

We now consider the SKBR3 cell line, i.e. the breast cancer type that overexpresses Her2 receptor (Her2⁺⁺).

C.4.1 Data analysis

Figure C4 shows the mean values of each treatment group. As for the MDA-MB-231 cell line, we don't observe differences between the effects of ANC-1 and of liposome 1, as well as the effects of ANC-2 and liposome 2. In this case ANC-1 performs better than ANC-2. Trastuzumab only and the empty immunoliposomes do not have effects on the cell apoptosis.

C.4.2 Data fit to the Hill function

We now fit the data to the two parameters and the three parameters Hill function and finally compare the two models. In order to perform the nonlinear regression analysis, the non-weighted least squares minimization with the Nelder-Mead algorithm has been applied.

Two parameters Hill function

We proceed as explained in section C.3.1. Table C5 provides the estimated values.

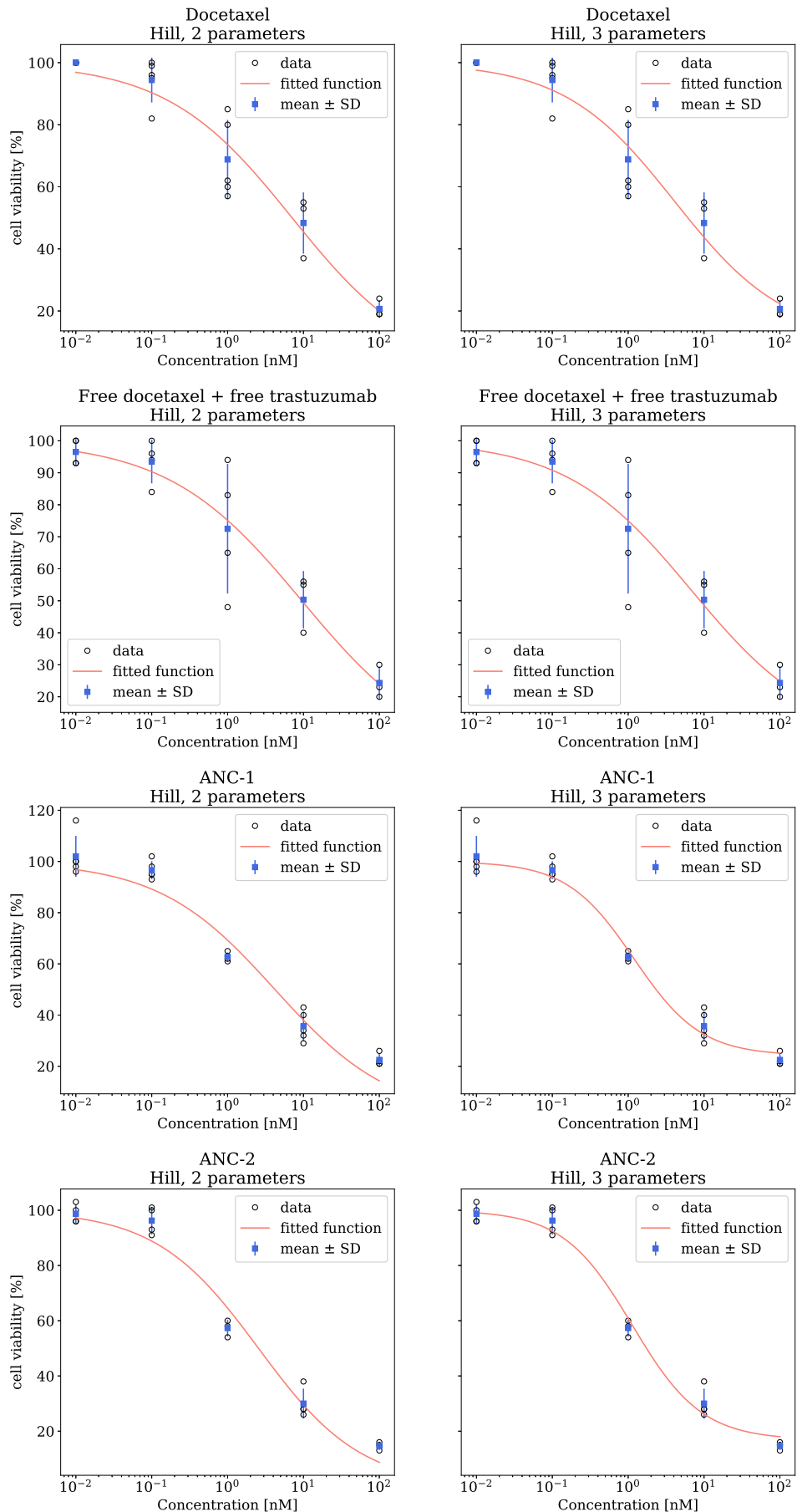


Figure C3. Comparison between the two parameters (left) and the three parameters (right) Hill functions.

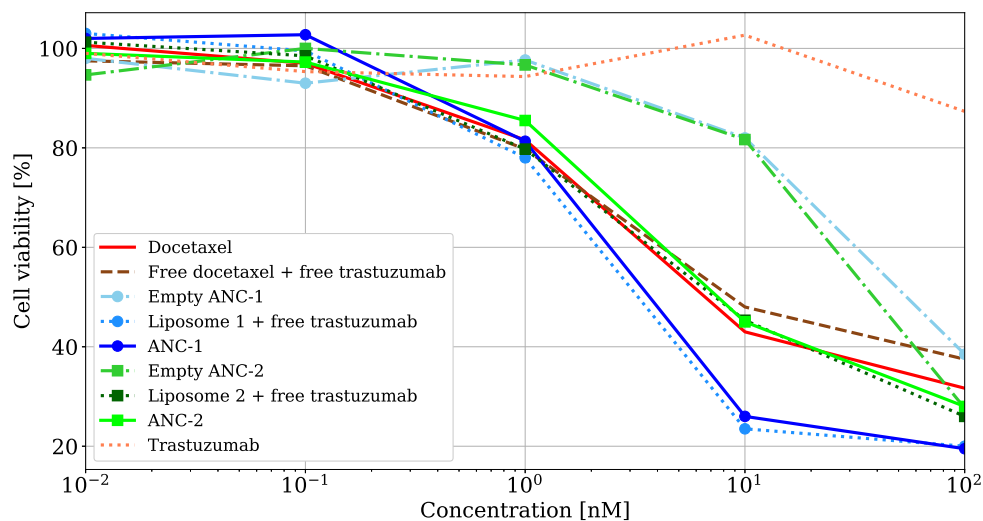


Figure C4. In vitro efficacy with respect to the docetaxel concentration relative to the SKBR3 cell line. Mean values of each treatment group.

Drug	Parameters	Value	StdErr	StdErr [%]
Docetaxel	Ec_{50}	13.758	3.890	28.274
	γ	0.543	0.070	12.835
Free drugs	Ec_{50}	17.917	5.656	31.569
	γ	0.471	0.062	13.239
Empty ANC-1	Ec_{50}	58.211	10.450	17.952
	γ	0.856	0.123	14.398
Liposome 1 + free trastuzumab	Ec_{50}	3.779	0.786	20.796
	γ	0.925	0.142	15.325
ANC-1	Ec_{50}	4.362	0.955	21.890
	γ	0.976	0.164	16.757
Empty ANC-2	Ec_{50}	40.404	4.706	11.646
	γ	1.053	0.107	10.180
Liposome 2 + free trastuzumab	Ec_{50}	9.586	2.543	26.530
	γ	0.614	0.093	15.190
ANC-2	Ec_{50}	12.359	2.613	21.145
	γ	0.625	0.070	11.118

Table C5. SKBR3 cell line: estimated values and standard errors of the two parameters Hill function computed with the Nelder-Mead algorithm.

Drug	Parameters	Value	StdErr	StdErr [%]
Docetaxel	Ec_{50}	2.576	0.896	34.805
	γ	1.068	0.281	26.305
	E_{max}	0.699	0.055	7.895
Free drugs	Ec_{50}	2.294	0.902	39.329
	γ	0.925	0.243	26.293
	E_{max}	0.647	0.061	9.494
Empty ANC-1	Ec_{50}	7e07	3e11	5e5
	γ	0.546	0.423	77.411
	E_{max}	1e3	2e6	2e5
Liposome 1 + free trastuzumab	Ec_{50}	1.734	0.464	26.757
	γ	1.763	0.722	40.958
	E_{max}	0.800	0.042	5.261
ANC-1	Ec_{50}	2.065	0.517	25.018
	γ	1.672	0.475	28.418
	E_{max}	0.800	0.041	5.154
Empty ANC-2	Ec_{50}	305.546	2041.543	668.161
	γ	0.723	0.444	61.377
	E_{max}	2.345	7.048	300.516
Liposome 2 + free trastuzumab	Ec_{50}	3.490	1.636	46.870
	γ	0.881	0.230	26.146
	E_{max}	0.773	0.094	12.182
ANC-2	Ec_{50}	3.791	0.961	25.353
	γ	1.044	0.169	16.144
	E_{max}	0.745	0.048	6.484

Table C6. SKBR3 cell line: estimated values and standard errors of the three parameters Hill function computed with the Nelder-Mead algorithm.

Three parameters Hill function

We proceed as explained in section C.3.1. Table C6 provides the estimated values. The standard errors relative to docetaxel, Free drugs and the two immunoliposomes are acceptable.

Comparison between the different models

For the SKBR3 cell line, the 3 parameters Hill function seems to fit the data better than the 2 parameters Hill function for almost all the treatment groups. Table C7 provides the statistical indices. Both the *AIC* and *BIC* of the three parameters Hill function is lower than the two parameters model or docetaxel, the Free drugs, ANC-1 and ANC-2. The goodness of fit of the model with three parameters is confirmed by the likelihood ratio test (see Table C8). Finally, Figure C5 show the comparison of the two fitted functions for each treatment group.

Drugs	# parameters	AIC	BIC	χ^2	reduced χ^2
Docetaxel	2	89.532	91.523	1439.872	79.993
	3	83.772	86.759	976.854	57.462
Free drugs	2	67.717	69.262	858.234	61.302
	3	62.583	64.901	549.505	42.270
Empty ANC-1	2	45.789	46.759	390.460	39.046
	3	47.600	49.055	384.364	42.707
Liposome 1 + free trastuzumab	2	70.517	72.063	1022.420	73.030
	3	59.234	61.552	445.725	34.287
ANC-1	2	62.453	63.731	910.722	75.893
	3	50.917	52.834	346.333	31.485
Empty ANC-2	2	52.219	53.635	373.405	28.723
	3	53.905	56.029	365.656	30.471
Liposome 2 + free trastuzumab	2	77.545	79.212	1286.137	85.742
	3	76.457	78.957	1072.523	76.609
ANC-2	2	61.983	63.528	599.768	42.841
	3	54.728	57.046	336.324	25.871

Table C7. SKBR3 cell line: comparison between the two parameters and the three parameters Hill function: Akaike information criterion, bayesian information criterion, sum of square residuals (χ^2) and reduced χ^2 .

Drug	$-2\log(L)$ 2 param- eters	$-2\log(L)$ 3 param- eters	<i>p</i> -value
Docetaxel	105.5315	97.7721	0.0053
Free drugs	79.7166	72.5829	0.0076
Empty ANC-1	53.7890	53.6002	0.6639
Liposome 1 + free trastuzumab	82.5174	69.2338	0.0003
ANC-1	72.4525	58.9168	0.0002
Empty ANC-2	63.2192	62.9047	0.5749
Liposome 2 + free trastuzumab	90.5452	87.4575	0.0789
ANC-2	73.9833	64.7278	0.0023

Table C8. SKBR3 cell line: evaluation of the log-likelihood functions and *p*-value for the likelihood ratio test.

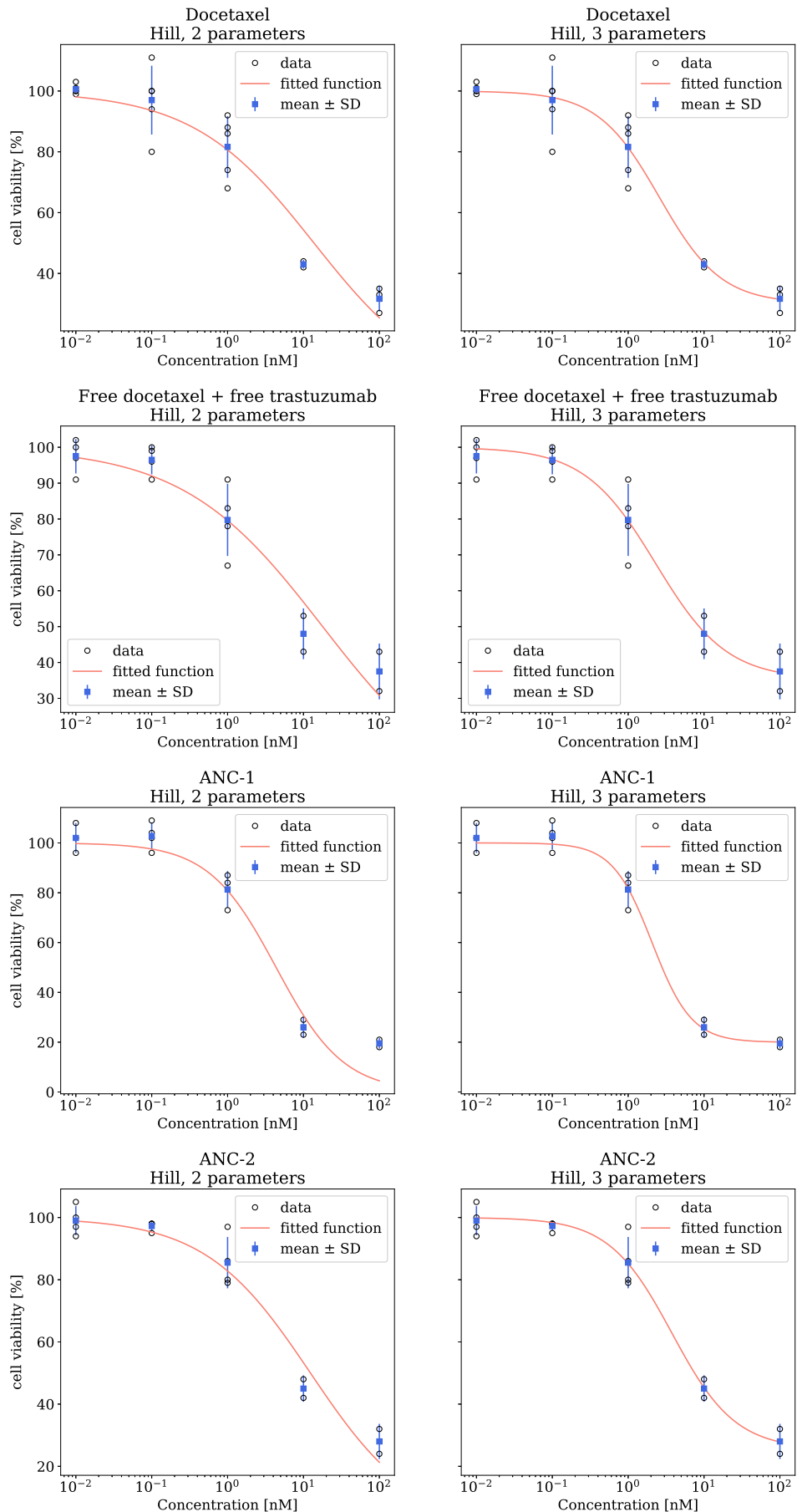


Figure C5. SKBR3 cell line: comparison between the two parameters (left) and the three parameters (right) Hill functions.

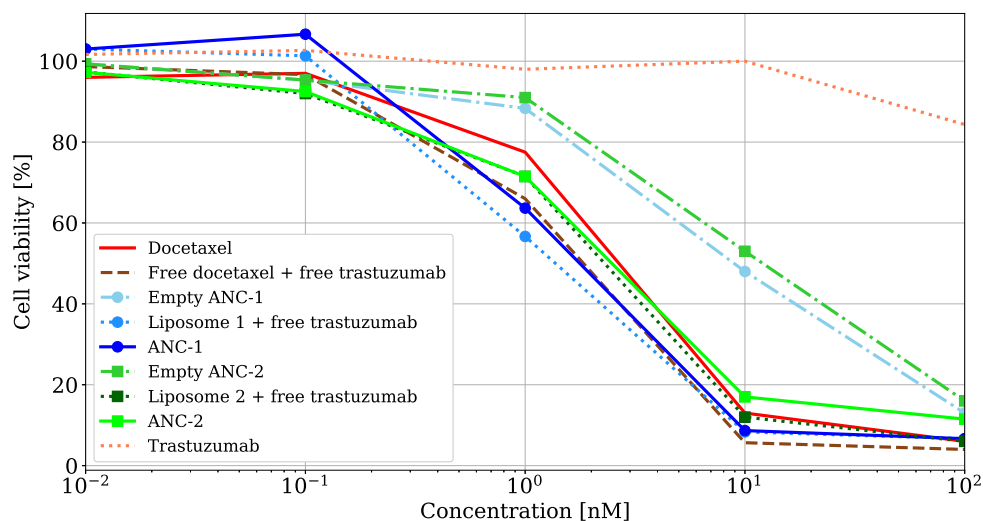


Figure C6. In vitro efficacy with respect to the docetaxel concentration relative to the MDA-MB-453 cell line. Mean values of each treatment group.

C.5 Results on the MDA-MB-453 cell line

We now consider the MDA-MB-453 cell line, that expresses the Her2 receptor (Her2+).

C.5.1 Data analysis

Figure C6 shows the mean values of each treatment group. As for the MDA-MB-231 cell line, we don't observe differences between the effects of ANC-1 and of liposome 1, as well as the effects of ANC-2 and liposome 2. As for the SKBR3 cell line, ANC-1 performs better than ANC-2. Trastuzumab only and the empty immunoliposomes do not have effects on the cell apoptosis.

C.5.2 Data fit to the Hill function

We now fit the data to the two parameters and the three parameters Hill function and finally compare the two models. In order to perform the nonlinear regression analysis, the non-weighted least squares minimization with the Nelder-Mead algorithm has been applied.

Two parameters Hill function

We proceed as explained in section C.3.1. Table C9 provides the estimated values.

Drug	Parameters	Value	StdErr	StdErr [%]
Docetaxel	Ec_{50}	2.515	0.259	10.299
	γ	1.291	0.117	9.085
Free drugs	Ec_{50}	1.547	0.168	10.830
	γ	1.433	0.165	11.504
Empty ANC-1	Ec_{50}	9.419	1.943	20.627
	γ	0.840	0.146	17.372
Liposome 1 + free trastuzumab	Ec_{50}	1.274	0.155	12.131
	γ	1.318	0.256	19.396
ANC-1	Ec_{50}	1.543	0.224	14.494
	γ	1.433	0.309	21.543
Empty ANC-2	Ec_{50}	12.156	2.031	16.706
	γ	0.832	0.116	13.970
Liposome 2 + free trastuzumab	Ec_{50}	2.062	0.380	18.426
	γ	1.102	0.179	16.211
ANC-2	Ec_{50}	2.257	0.319	14.118
	γ	0.925	0.093	10.088

Table C9. MDA-MB-453 cell line: estimated values and standard errors of the two parameters Hill function computed with the Nelder-Mead algorithm.

Three parameters Hill function

We proceed as explained in section C.3.1. Table C10 provides the estimated values. This model is not appropriate for liposome 1 + free trastuzumab and ANC-1. The covariance matrix is indeed singular, therefore the standard errors tend to infinite. For the other treatment groups, the standard errors are acceptable.

Comparison between the two models

Table C11 provides the statistical indices for the evaluation of the two models. In this case, the three parameters Hill function fits better the data relative to the groups of docetaxel and ANC-2. Regarding the Free drugs, *AIC* and *BIC* don't show big variety between the 2 parameters and the three parameters Hill function, although they lower for the three parameters model. In Table C12, the large *p*-value relative to the Free drugs suggests to accept the null hypothesis, i.e. the 2 parameters model fits better the data. Figure C7 shows the two fitted functions for each treatment group.

Drug	Parameters	Value	StdErr	StdErr [%]
Docetaxel	Ec_{50}	2.106	0.236	11.192
	γ	1.534	0.180	11.711
	E_{max}	0.945	0.020	2.099
Free drugs	Ec_{50}	1.406	0.177	12.556
	γ	1.713	0.383	22.339
	E_{max}	0.968	0.021	2.203
Empty ANC-1	Ec_{50}	8.650	4.096	47.353
	γ	0.879	0.252	28.715
	E_{max}	0.973	0.138	14.216
Liposome 1 + free trastuzumab	Ec_{50}	1.011	-	-
	γ	11.809	-	-
	E_{max}	0.925	0.023	2.532
ANC-1	Ec_{50}	1.036	-	-
	γ	12.123	-	-
	E_{max}	0.923	0.027	2.877
Empty ANC-2	Ec_{50}	10.247	4.030	39.329
	γ	0.914	0.234	25.638
	E_{max}	0.946	0.117	12.349
Liposome 2 + free trastuzumab	Ec_{50}	1.872	0.496	26.517
	γ	1.223	0.310	25.336
	E_{max}	0.965	0.058	6.051
ANC-2	Ec_{50}	1.769	0.329	18.598
	γ	1.149	0.181	15.793
	E_{max}	0.918	0.040	4.361

Table C10. MDA-MB-453 cell line: estimated values and standard errors of the three parameters Hill function computed with the Nelder-Mead algorithm.

Drugs	# parameters	AIC	BIC	χ^2	reduced χ^2
Docetaxel	2	38.150	39.280	179.805	16.346
	3	33.066	34.761	104.265	10.426
Free drugs	2	37.213	38.343	167.305	15.210
	3	36.607	38.302	136.914	13.691
Empty ANC-1	2	62.188	63.467	893.706	74.475
	3	64.147	66.064	891.035	81.003
Liposome 1 + free trastuzumab	2	59.246	60.662	596.503	45.885
	3	55.145	57.269	397.167	33.097
ANC-1	2	58.652	59.930	694.195	57.850
	3	55.072	56.989	466.000	42.364
Empty ANC-2	2	55.599	56.877	558.205	46.517
	3	57.408	59.325	550.637	50.058
Liposome 2 + free trastuzumab	2	49.036	50.006	511.802	51.180
	3	50.585	52.039	492.895	54.766
ANC-2	2	53.533	54.949	407.586	31.353
	3	51.381	53.505	309.031	25.753

Table C11. MDA-MB-453 cell line: comparison between the two parameters and the three parameters Hill function: Akaike information criterion, bayesian information criterion, sum of square residuals (χ^2) and reduced χ^2 .

Drug	$-2\log(L)$ 2 parameters	$-2\log(L)$ 3 parameters	p -value
Docetaxel	47.1500	40.0658	0.0078
Free drugs	46.2133	43.6072	0.1065
Empty ANC-1	72.1885	72.1466	0.8378
Liposome 1 + free trastuzumab	70.2455	64.1446	0.0135
ANC-1	68.6517	63.0718	0.0182
Empty ANC-2	65.5994	65.4083	0.6620
Liposome 2 + free trastuzumab	57.0364	56.5847	0.5015
ANC-2	64.5330	60.3808	0.0416

Table C12. MDA-MB-453 cell line: evaluation of the log-likelihood functions and p -value for the likelihood ratio test.

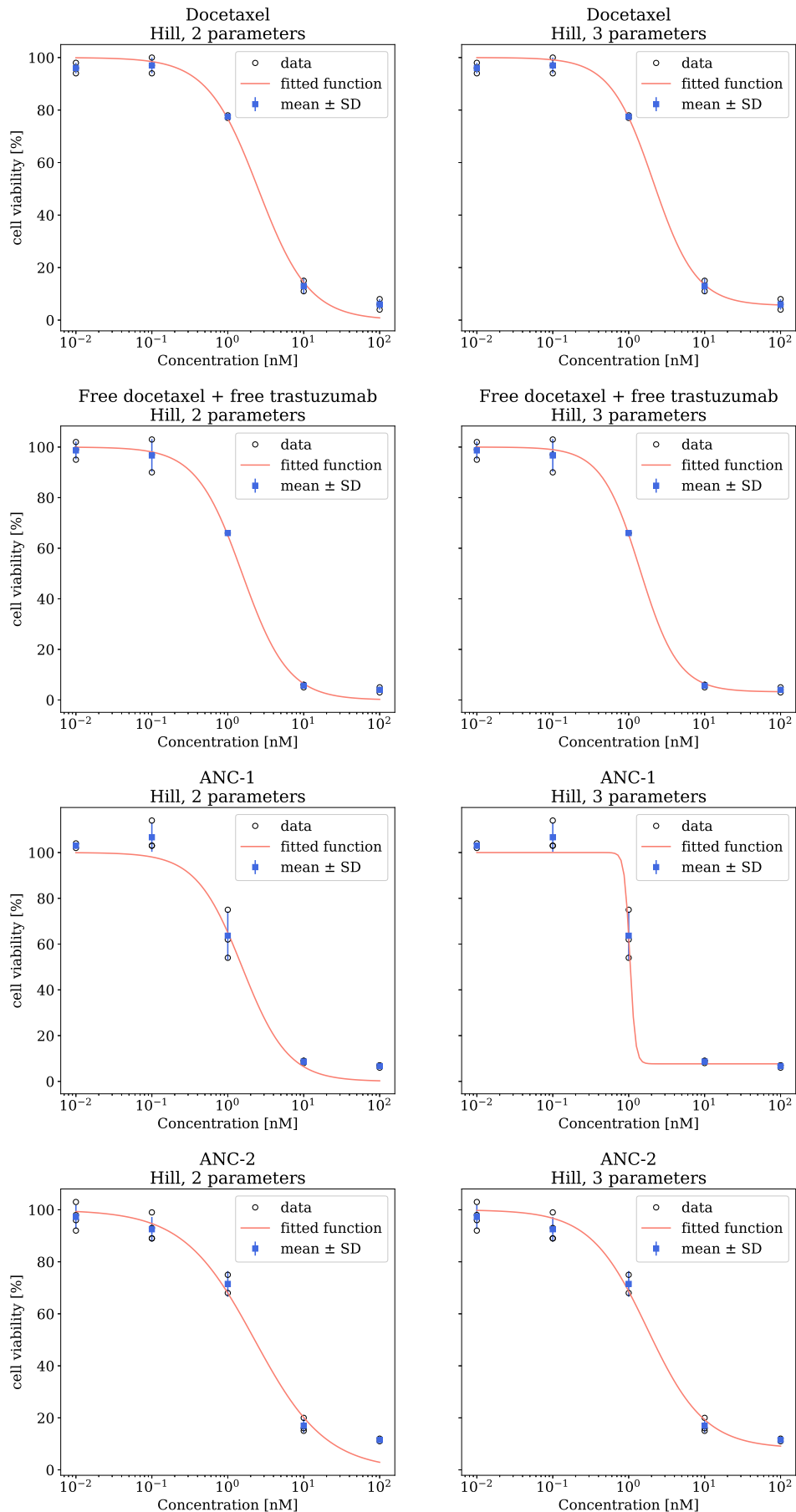


Figure C7. Comparison between the two parameters (left) and the three parameters (right) Hill functions.

BIBLIOGRAPHY

- [1] Momenimovahed Z, Salehiniya H. Epidemiological Characteristics of and Risk Factors for Breast Cancer in the World. *Breast Cancer: Targets and Therapy*. 2019 Apr;Volume 11:151–164.
- [2] Harbeck N, Penault-Llorca F, Cortes J, Gnant M, Houssami N, Poortmans P, et al. *Breast Cancer*. *Nat Rev Dis Primers*. 2019 Dec;5(1).
- [3] Rodallec A, Brunel JM, Giacometti S, Maccario H, Correard F, Mas E, et al. Docetaxel-Trastuzumab Stealth Immunoliposome: Development and in Vitro Proof of Concept Studies in Breast Cancer. *Int J Nanomedicine*. 2018 Jun;Volume 13:3451–3465.
- [4] Waks AG, Winer EP. Breast Cancer Treatment: A Review. *JAMA*. 2019 Jan;321(3):288.
- [5] Ali S, Coombes RC. Estrogen Receptor Alpha in Human Breast Cancer: Occurrence and Significance. *J Mammary Gland Biol Neoplasia*. 2000;5(3):271–281.
- [6] Loibl S, Gianni L. HER2-Positive Breast Cancer. *Lancet*. 2017 Jun;389(10087):2415–2429.
- [7] Denkert C, Liedtke C, Tutt A, von Minckwitz G. Molecular Alterations in Triple-Negative Breast Cancer—the Road to New Treatment Strategies. *Lancet*. 2017 Jun;389(10087):2430–2442.
- [8] Dhillon S. Trastuzumab Emtansine: A Review of Its Use in Patients with HER2-Positive Advanced Breast Cancer Previously Treated with Trastuzumab-Based Therapy. *Drugs*. 2014 Apr;74(6):675–686.
- [9] Saadeh Y, Leung T, Vyas A, Chaturvedi LS, Perumal O, Vyas D. Applications of Nanomedicine in Breast Cancer Detection, Imaging, and Therapy. *J Nanosci Nanotechnol*. 2014 Jan;14(1):913–923.
- [10] Wu D, Si M, Xue HY, Wong HL. Nanomedicine Applications in the Treatment of Breast Cancer: Current State of the Art. *Int J Nanomedicine*. 2017 Aug;Volume 12:5879–5892.
- [11] Howard KA, Vorup-Jensen T, Peer D, editors. *Nanomedicine. Advances in Delivery Science and Technology*. New York: Springer; 2016.

- [12] Pelaz B, Alexiou C, Alvarez-Puebla RA, Alves F, Andrews AM, Ashraf S, et al. Diverse Applications of Nanomedicine. *ACS Nano*. 2017 Mar;11(3):2313–2381.
- [13] de Jong. Drug Delivery and Nanoparticles: Applications and Hazards. *Int J Nanomedicine*. 2008 Jun;p. 133.
- [14] Jiang W, Rutherford D, Vuong T, Liu H. Nanomaterials for Treating Cardiovascular Diseases: A Review. *Bioact Mater*. 2017 Dec;2(4):185–198.
- [15] Teleanu D, Chircov C, Grumezescu A, Volceanov A, Teleanu R. Blood-Brain Delivery Methods Using Nanotechnology. *Pharmaceutics*. 2018 Dec;10(4):269.
- [16] Smith BR, Gambhir SS. Nanomaterials for In Vivo Imaging. *Chem Rev*. 2017 Feb;117(3):901–986.
- [17] Salvati E, Stellacci F, Krol S. Nanosensors for Early Cancer Detection and for Therapeutic Drug Monitoring. *Nanomedicine (Lond)*. 2015 Dec;10(23):3495–3512.
- [18] Chen F, Ehlerding EB, Cai W. Theranostic Nanoparticles. *J Nucl Med*. 2014 Dec;55(12):1919–1922.
- [19] Jun Han Z, Rider AE, Ishaq M, Kumar S, Kondyurin A, Bilek MMM, et al. Carbon Nanostructures for Hard Tissue Engineering. *RSC Adv*. 2013;3(28):11058.
- [20] Deshpande PP, Biswas S, Torchilin VP. Current Trends in the Use of Liposomes for Tumor Targeting. *Nanomedicine*. 2013 Sep;8(9):1509–1528.
- [21] Bangham AD, Standish MM, Watkins JC. Diffusion of Univalent Ions across the Lamellae of Swollen Phospholipids. *J Mol Biol*. 1965 Aug;13(1):238–IN27.
- [22] Gregoriadis G, Ryman BE. Liposomes as Carriers of Enzymes or Drugs: A New Approach to the Treatment of Storage Diseases. *Biochem J*. 1971 Oct;124(5):58P–58P.
- [23] Gregoriadis G. Drug Entrapment in Liposomes. *FEBS Lett*. 1973 Nov;36(3):292–296.
- [24] Allen TM, Cullis PR. Liposomal Drug Delivery Systems: From Concept to Clinical Applications. *Adv Drug Deliv Rev*. 2013 Jan;65(1):36–48.
- [25] Allen TM, Chonn A. Large Unilamellar Liposomes with Low Uptake into the Reticuloendothelial System. *FEBS Lett*. 1987 Oct;223(1):42–46.
- [26] Allen TM. Stealth Liposomes: Avoiding Reticuloendothelial Uptake. In: Lopez-Berestein G, Fidler I, editors. *Liposomes in the Therapy of Infectious Disease and Cancer*, UCLA Symposium in Molecular and Cellular Biology, CRC Press, Boca Raton, FL; 1989. p. 405–415.
- [27] Maeda H. The Enhanced Permeability and Retention (EPR) Effect in Tumor Vasculature: The Key Role of Tumor-Selective Macromolecular Drug Targeting. *Adv Enzyme Regul*. 2001;41:189–207.

- [28] Maruyama K, Takizawa T, Yuda T, Kennel SJ, Huang L, Iwatsuru M. Targetability of Novel Immunoliposomes Modified with Amphipathic Poly(Ethylene Glycol)s Conjugated at Their Distal Terminals to Monoclonal Antibodies. *Biochim Biophys Acta Biomembr.* 1995 Mar;1234(1):74–80.
- [29] Park JW, Kirpotin DB, Hong K, Shalaby R, Shao Y, Nielsen UB, et al. Tumor Targeting Using Anti-Her2 Immunoliposomes. *J Control Release.* 2001 Jul;74(1-3):95–113.
- [30] Torchilin VP. Recent Advances with Liposomes as Pharmaceutical Carriers. *Nat Rev Drug Discov.* 2005 Feb;4(2):145–160.
- [31] Barenholz YC. Doxil[®] — The First FDA-Approved Nano-Drug: Lessons Learned. *J Control Release.* 2012 Jun;160(2):117–134.
- [32] Perrault SD, Walkey C, Jennings T, Fischer HC, Chan WCW. Mediating Tumor Targeting Efficiency of Nanoparticles Through Design. *Nano Lett.* 2009 May;9(5):1909–1915.
- [33] Yameen B, Choi WI, Vilos C, Swami A, Shi J, Farokhzad OC. Insight into Nanoparticle Cellular Uptake and Intracellular Targeting. *J Control Release.* 2014 Sep;190:485–499.
- [34] Bazak R, Hourri M, El Achy S, Kamel S, Refaat T. Cancer Active Targeting by Nanoparticles: A Comprehensive Review of Literature. *J Cancer Res Clin Oncol.* 2015 May;141(5):769–784.
- [35] Wilhelm S, Tavares AJ, Dai Q, Ohta S, Audet J, Dvorak HF, et al. Analysis of Nanoparticle Delivery to Tumours. *Nat Rev Mater.* 2016 Apr;1(5):16014.
- [36] Kirpotin DB, Drummond DC, Shao Y, Shalaby MR, Hong K, Nielsen UB, et al. Antibody Targeting of Long-Circulating Lipidic Nanoparticles Does Not Increase Tumor Localization but Does Increase Internalization in Animal Models. *Cancer Res.* 2006 Jul;66(13):6732–6740.
- [37] Rodallec A, Benzekry S, Lacarelle B, Ciccolini J, Fanciullino R. Pharmacokinetics Variability: Why Nanoparticles Are Not Just Magic-Bullets in Oncology. *Crit Rev Oncol Hematol.* 2018 Sep;129:1–12.
- [38] Gianni L, Eiermann W, Semiglazov V, Lluch A, Tjulandin S, Zambetti M, et al. Neoadjuvant and Adjuvant Trastuzumab in Patients with HER2-Positive Locally Advanced Breast Cancer (NOAH): Follow-up of a Randomised Controlled Superiority Trial with a Parallel HER2-Negative Cohort. *Lancet Oncol.* 2014 May;15(6):640–647.
- [39] Rodallec A, Brunel JM, Giacometti S, Maccario H, Correard F, Mas E, et al. Development of a Docetaxel-Trastuzumab stealth immunoliposome in breast cancer: characterization and in vivo proof of concept studies. 2017;.
- [40] Moghimi SM, Parhamifar L, Ahmadvand D, Wibroe PP, Andresen TL, Farhangrazi ZS, et al. Particulate Systems for Targeting of Macrophages: Basic and Therapeutic Concepts. *J Innate Immun.* 2012;4(5-6):509–528.

- [41] Mitchell MJ, Jain RK, Langer R. Engineering and Physical Sciences in Oncology: Challenges and Opportunities. *Nat Rev Cancer*. 2017 Oct;17(11):659–675.
- [42] Decuzzi P. Facilitating the Clinical Integration of Nanomedicines: The Roles of Theoretical and Computational Scientists. *ACS Nano*. 2016 Sep;10(9):8133–8138.
- [43] Dogra P, Butner JD, Chuang YI, Caserta S, Goel S, Brinker CJ, et al. Mathematical Modeling in Cancer Nanomedicine: A Review. *Biomed Microdevices*. 2019 Jun;21(2).
- [44] Luo Z, Jiang J. pH-Sensitive Drug Loading/Releasing in Amphiphilic Copolymer PAE-PEG: Integrating Molecular Dynamics and Dissipative Particle Dynamics Simulations. *J Control Release*. 2012 Aug;162(1):185–193.
- [45] Jämbeck JPM, Eriksson ESE, Laaksonen A, Lyubartsev AP, Eriksson LA. Molecular Dynamics Studies of Liposomes as Carriers for Photosensitizing Drugs: Development, Validation, and Simulations with a Coarse-Grained Model. *J Chem Theory Comput*. 2014 Jan;10(1):5–13.
- [46] Ding Hm, Ma Yq. Design Strategy of Surface Decoration for Efficient Delivery of Nanoparticles by Computer Simulation. *Sci Rep*. 2016 Jul;6(1).
- [47] Dell’Orco D, Lundqvist M, Oslakovic C, Cedervall T, Linse S. Modeling the Time Evolution of the Nanoparticle-Protein Corona in a Body Fluid. *PLoS ONE*. 2010 Jun;5(6):e10949.
- [48] Gao H, Shi W, Freund LB. Mechanics of Receptor-Mediated Endocytosis. *Proc Natl Acad Sci USA*. 2005 Jul;102(27):9469–9474.
- [49] Decuzzi P, Ferrari M. The Receptor-Mediated Endocytosis of Nonspherical Particles. *Biophys J*. 2008 May;94(10):3790–3797.
- [50] Gentile F, Ferrari M, Decuzzi P. The Transport of Nanoparticles in Blood Vessels: The Effect of Vessel Permeability and Blood Rheology. *Ann Biomed Eng*. 2008 Feb;36(2):254–261.
- [51] Ng TSC, Garlin MA, Weissleder R, Miller MA. Improving Nanotherapy Delivery and Action through Image-Guided Systems Pharmacology. *Theranostics*. 2020;10(3):968–997.
- [52] Goodman TT, Chen J, Matveev K, Pun SH. Spatio-Temporal Modeling of Nanoparticle Delivery to Multicellular Tumor Spheroids. *Biotechnol Bioeng*. 2008 Oct;101(2):388–399.
- [53] Gao Y, Li M, Chen B, Shen Z, Guo P, Wientjes MG, et al. Predictive Models of Diffusive Nanoparticle Transport in 3-Dimensional Tumor Cell Spheroids. *AAPS J*. 2013 Jul;15(3):816–831.
- [54] Toy R, Hayden E, Shoup C, Baskaran H, Karathanasis E. The Effects of Particle Size, Density and Shape on Margination of Nanoparticles in Microcirculation. *Nanotechnology*. 2011 Mar;22(11):115101.
- [55] Toy R, Peiris PM, Ghaghada KB, Karathanasis E. Shaping Cancer Nanomedicine: The Effect of Particle Shape on the *in Vivo* Journey of Nanoparticles. *Nanomedicine (Lond)*. 2014 Jan;9(1):121–134.

- [56] Miller MA, Gadde S, Pfirschke C, Engblom C, Sprachman MM, Kohler RH, et al. Predicting Therapeutic Nanomedicine Efficacy Using a Companion Magnetic Resonance Imaging Nanoparticle. *Sci Transl Med*. 2015 Nov;7(314):314ra183–314ra183.
- [57] Fedosov DA, Noguchi H, Gompper G. Multiscale Modeling of Blood Flow: From Single Cells to Blood Rheology. *Biomech Model Mechanobiol*. 2014 Apr;13(2):239–258.
- [58] Jain RK. Transport of Molecules in the Tumor Interstitium: A Review. *Cancer Res*. 1987 Jun;47(12):3039–3051.
- [59] Chauhan VP, Stylianopoulos T, Boucher Y, Jain RK. Delivery of Molecular and Nanoscale Medicine to Tumors: Transport Barriers and Strategies. *Annu Rev Chem Biomol Eng*. 2011 Jul;2(1):281–298.
- [60] Jain RK, Stylianopoulos T. Delivering Nanomedicine to Solid Tumors. *Nat Rev Clin Oncol*. 2010 Nov;7(11):653–664.
- [61] Jain RK. Barriers to Drug Delivery in Solid Tumors. *Sci Am*. 1994 Jul;271(1):58–65.
- [62] Nagy J, Chang SH, Shih SC, Dvorak A, Dvorak H. Heterogeneity of the Tumor Vasculature. *Semin Thromb*. 2010 Apr;36(03):321–331.
- [63] Jain RK. Determinants of Tumor Blood Flow: A Review. *Cancer Res*. 1988 May;48(10):2641–2658.
- [64] Leunig M, Yuan F, Menger MD, Boucher Y, Goetz AE, Messmer K, et al. Angiogenesis, Microvascular Architecture, Microhemodynamics, and Interstitial Fluid Pressure during Early Growth of Human Adenocarcinoma LS174T in SCID Mice. *Cancer Res*. 1992 Dec;52(23):6553–6560.
- [65] Kamoun WS, Chae SS, Lacorre DA, Tyrrell JA, Mitre M, Gillissen MA, et al. Simultaneous Measurement of RBC Velocity, Flux, Hematocrit and Shear Rate in Vascular Networks. *Nat Methods*. 2010 Aug;7(8):655–660.
- [66] Vakoc BJ, Lanning RM, Tyrrell JA, Padera TP, Bartlett LA, Stylianopoulos T, et al. Three-Dimensional Microscopy of the Tumor Microenvironment in Vivo Using Optical Frequency Domain Imaging. *Nat Med*. 2009 Oct;15(10):1219–1223.
- [67] Young JS, Lumsden CE, Stalker AL. The Significance of the Tissue Pressure of Normal Testicular and of Neoplastic (Brown-Pearce Carcinoma) Tissue in the Rabbit. *J Pathol Bacteriol*. 1950 Jul;62(3):313–333.
- [68] Boucher Y, Jain RK. Microvascular Pressure Is the Principal Driving Force for Interstitial Hypertension in Solid Tumors: Implications for Vascular Collapse. *Cancer Res*. 1992 Sep;52(18):5110–5114.

- [69] Jain RK, Baxter LT. Mechanisms of Heterogeneous Distribution of Monoclonal Antibodies and Other Macromolecules in Tumors: Significance of Elevated Interstitial Pressure. *Cancer Res.* 1988 Dec;48(24 Pt 1):7022–7032.
- [70] Yuan H, Li J, Bao G, Zhang S. Variable Nanoparticle-Cell Adhesion Strength Regulates Cellular Uptake. *Phys Rev Lett.* 2010 Sep;105(13):138101.
- [71] Chithrani BD, Chan WCW. Elucidating the Mechanism of Cellular Uptake and Removal of Protein-Coated Gold Nanoparticles of Different Sizes and Shapes. *Nano Lett.* 2007 Jun;7(6):1542–1550.
- [72] Izumi Y, Xu L, di Tomaso E, Fukumura D, Jain RK. Herceptin Acts as an Anti-Angiogenic Cocktail. *Nature.* 2002 Mar;416(6878):279–280.
- [73] Yonucu S, Yılmaz D, Phipps C, Unlu MB, Kohandel M. Quantifying the Effects of Antiangiogenic and Chemotherapy Drug Combinations on Drug Delivery and Treatment Efficacy. *PLoS Comput Biol.* 2017 Sep;13(9):e1005724.
- [74] Wong C, Stylianopoulos T, Cui J, Martin J, Chauhan VP, Jiang W, et al. Multistage Nanoparticle Delivery System for Deep Penetration into Tumor Tissue. *Proc Natl Acad Sci USA.* 2011 Feb;108(6):2426–2431.
- [75] Deville M, Natalini R, Pognard C. A Continuum Mechanics Model of Enzyme-Based Tissue Degradation in Cancer Therapies. *Bull Math Biol.* 2018 Dec;80(12):3184–3226.
- [76] Rodallec A, Sicard G, Giacometti S, Carré M, Pourroy B, Bouquet F, et al. From 3D Spheroids to Tumor Bearing Mice: Efficacy and Distribution Studies of Trastuzumab-Docetaxel Immunoliposome in Breast Cancer. *Int J Nanomedicine.* 2018 Oct;Volume 13:6677–6688.
- [77] Choy G, O'Connor S, Diehn FE, Costouros N, Alexander HR, Choyke P, et al. Comparison of Noninvasive Fluorescent and Bioluminescent Small Animal Optical Imaging. *BioTechniques.* 2003 Nov;35(5):1022–1026, 1028–1030.
- [78] Vaghi C, Rodallec A, Fanciullino R, Ciccolini J, Mochel J, Mastri M, et al. Population Modeling of Tumor Growth Curves, the Reduced Gompertz Model and Prediction of the Age of a Tumor. In: *Bebis G, Benos T, Chen K, Jahn K, Lima E, editors. Mathematical and Computational Oncology.* vol. 11826. Cham: Springer International Publishing; 2019. p. 87–97.
- [79] Vaghi C, Rodallec A, Fanciullino R, Ciccolini J, Mochel JP, Mastri M, et al. Population Modeling of Tumor Growth Curves and the Reduced Gompertz Model Improve Prediction of the Age of Experimental Tumors. *PLoS Comput Biol.* 2020 Feb;16(2):e1007178.
- [80] Vaghi C, Fanciullino R, Benzekry S, Pognard C. Macro-Scale Models for Fluid Flow in Tumour Tissues: Impact of Microstructure Properties. *Cancer Biology*; 2020.

- [81] Shipley RJ, Chapman SJ. Multiscale Modelling of Fluid and Drug Transport in Vascular Tumours. *Bull Math Biol.* 2010 Aug;72(6):1464–1491.
- [82] Penta R, Ambrosi D, Quarteroni A. Multiscale Homogenization for Fluid and Drug Transport in Vascularized Malignant Tissues. *Math Models Methods Appl Sci.* 2015 Jan;25(01):79–108.
- [83] Monolix Version 2018R2. Antony, France; 2018. Lixoft SAS.
- [84] Carpenter B, Gelman A, Hoffman MD, Lee D, Goodrich B, Betancourt M, et al. *Stan* : A Probabilistic Programming Language. *J Stat Softw.* 2017;76(1).
- [85] Kramer A, Calderhead B, Radde N. Hamiltonian Monte Carlo Methods for Efficient Parameter Estimation in Steady State Dynamical Systems. *BMC Bioinformatics.* 2014;15(1):253.
- [86] Hecht F. New Development in FreeFem++. *J Numer Math.* 2012;20:251–265.
- [87] Geuzaine C, Remacle JF. Gmsh: A 3-D Finite Element Mesh Generator with Built-in Pre- and Post-Processing Facilities: THE GMSH PAPER. *Int J Numer Meth Eng.* 2009 Sep;79(11):1309–1331.
- [88] Cooper GM. *The Cell: A Molecular Approach.* 2nd ed. Washington, DC: ASM Press [u.a.]; 2000.
- [89] Adair TH, Montani JP. *Angiogenesis. Integrated Systems Physiology: From Molecule to Function to Disease.* San Rafael (CA): Morgan & Claypool Life Sciences; 2010.
- [90] Loizzi V, Del Vecchio V, Gargano G, De Liso M, Kardashi A, Naglieri E, et al. Biological Pathways Involved in Tumor Angiogenesis and Bevacizumab Based Anti-Angiogenic Therapy with Special References to Ovarian Cancer. *Int J Mol Sci.* 2017 Sep;18(9):1967.
- [91] Puaux AL, Ong LC, Jin Y, Teh I, Hong M, Chow PKH, et al. A Comparison of Imaging Techniques to Monitor Tumor Growth and Cancer Progression in Living Animals. *Int J Mol Imaging.* 2011;2011:1–12.
- [92] Rehemtulla A, Stegman LD, Cardozo SJ, Gupta S, Hall DE, Contag CH, et al. Rapid and Quantitative Assessment of Cancer Treatment Response Using In Vivo Bioluminescence Imaging. *Neoplasia.* 2000 Nov;2(6):491–495.
- [93] Hoffman RM, Yang M. Whole-Body Imaging with Fluorescent Proteins. *Nat Protoc.* 2006 Nov;1(3):1429–1438.
- [94] Mollard S, Fanciullino R, Giacometti S, Serdjebi C, Benzekry S, Ciccolini J. In Vivo Bioluminescence Tomography for Monitoring Breast Tumor Growth and Metastatic Spreading: Comparative Study and Mathematical Modeling. *Sci Rep.* 2016 Dec;6(1).
- [95] Barbolosi D, Ciccolini J, Lacarelle B, Barlesi F, André N. Computational oncology–mathematical modelling of drug regimens for precision medicine. *Nat Rev Clin Oncol.* 2016 Apr;13(4):242–254.

- [96] Altrock PM, Liu LL, Michor F. The mathematics of cancer: integrating quantitative models. *Nat Rev Cancer*. 2015 Nov;15(12):730–745.
- [97] Meille C, Barbolosi D, Ciccolini J, Freyer G, Iliadis A. Revisiting Dosing Regimen Using Pharmacokinetic/Pharmacodynamic Mathematical Modeling: Densification and Intensification of Combination Cancer Therapy. *Clin Pharmacokinet*. 2016 Aug;55(8):1015–1025.
- [98] Collins VP, Loeffler RK, Tivey H. Observations on growth rates of human tumors. *Am J Roentgenol Radium Ther Nucl Med*. 1956;76(5).
- [99] Steel GG. Growth kinetics of tumours: cell population kinetics in relation to the growth and treatment of cancer. Clarendon Press; 1977.
- [100] Laird AK. Dynamics of tumor growth. *Br J Cancer*. 1964 Sep;13:490–502.
- [101] Winsor CP. The Gompertz curve as a growth curve. *Proc Natl Acad Sci U S A*. 1932;18(1):1–8.
- [102] Norton L. A Gompertzian model of human breast cancer growth. *Cancer Res*. 1988 Dec;48(24):7067–7071.
- [103] Frenzen CL, Murray JD. A Cell Kinetics Justification for Gompertz' Equation. *SIAM J Appl Math*. 1986 Aug;46(4):614–629.
- [104] Norton L, Simon R, Brereton HD, Bogden AE. Predicting the Course of Gompertzian Growth. *Nature*. 1976 Dec;264(5586):542–545.
- [105] Brunton GF, Wheldon TE. Characteristic Species Dependent Growth Patterns of Mammalian Neoplasms. *Cell Tissue Kinet*. 1978 Mar;11(2):161–175.
- [106] Demicheli R. Growth of testicular neoplasm lung metastases: Tumor-specific relation between two Gompertzian parameters. *Eur J Cancer*. 1980 Dec;16(12):1603–1608.
- [107] Parfitt AM, Fyhrie DP. Gompertzian growth curves in parathyroid tumours: further evidence for the set-point hypothesis. *Cell Prolif*. 1997;30(8-9):341–349.
- [108] Steel GG. Species-dependent growth patterns for mammalian neoplasms. *Cell Tissue Kinet*. 1980 Jul;13(4):451–453.
- [109] Benzekry S, Lamont C, Beheshti A, Tracz A, Ebos JML, Hlatky L, et al. Classical Mathematical Models for Description and Prediction of Experimental Tumor Growth. *PLoS Comput Biol*. 2014 Aug;10(8):e1003800.
- [110] Vaidya VG, Alexandro FJ. Evaluation of some mathematical models for tumor growth. *Int J Biomed Comput*. 1982 Jan;13(1):19–36.
- [111] Lavielle M. Mixed Effects Models for the Population Approach: Models, Tasks, Methods and Tools. Chapman & Hall/CRC Biostatistics Series. Boca Raton: Taylor & Francis; 2014.

- [112] Parra-Guillen ZP, Mangas-Sanjuan V, Garcia-Cremades M, Troconiz IF, Mo G, Pitou C, et al. Systematic Modeling and Design Evaluation of Unperturbed Tumor Dynamics in Xenografts. *J Pharmacol Exp Ther*. 2018 Jul;366(1):96–104.
- [113] Karaman E, Narinc D, Firat MZ, Aksoy T. Nonlinear Mixed Effects Modeling of Growth in Japanese Quail. *Poult Sci J*. 2013 Jul;92(7):1942–1948.
- [114] Wang Z, Zuidhof MJ. Estimation of Growth Parameters Using a Nonlinear Mixed Gompertz Model. *Poult Sci J*. 2004 Jun;83(6):847–852.
- [115] Claret L, Girard P, Hoff PM, Van Cutsem E, Zuideveld KP, Jorga K, et al. Model-based prediction of phase III overall survival in colorectal cancer on the basis of phase II tumor dynamics. *J Clin Oncol*. 2009 Sep;27(25):4103–4108.
- [116] Ribba B, Holford NH, Magni P, Trocóniz I, Gueorguieva I, Girard P, et al. A Review of Mixed-Effects Models of Tumor Growth and Effects of Anticancer Drug Treatment Used in Population Analysis. *CPT Pharmacometrics Syst Pharmacol*. 2014 May;3(5):1–10.
- [117] Hartung N, Mollard S, Barbolosi D, Benabdallah A, Chapuisat G, Henry G, et al. Mathematical modeling of tumor growth and metastatic spreading: validation in tumor-bearing mice. *Cancer Res*. 2014 Nov;74(22):6397–6407.
- [118] Benzekry S, Tracz A, Mastri M, Corbelli R, Barbolosi D, Ebos JML. Modeling Spontaneous Metastasis Following Surgery: An In Vivo-In Silico Approach. *Cancer Res*. 2016 Feb;76(3):535–547.
- [119] Simeoni M, Magni P, Cammia C, De Nicolao G, Croci V, Pesenti E, et al. Predictive pharmacokinetic-pharmacodynamic modeling of tumor growth kinetics in xenograft models after administration of anticancer agents. *Cancer Res*. 2004 Feb;64(3):1094–1101.
- [120] Frieboes HB, Smith BR, Chuang YL, Ito K, Roettgers AM, Gambhir SS, et al. An Integrated Computational/Experimental Model of Lymphoma Growth. *PLoS Comput Biol*. 2013 Mar;9(3):e1003008.
- [121] Finley SD, Popel AS. Effect of Tumor Microenvironment on Tumor VEGF During Anti-VEGF Treatment: Systems Biology Predictions. *J Natl Cancer Inst*. 2013 Jun;105(11):802–811.
- [122] Stylianopoulos T, Martin JD, Snuderl M, Mpekris F, Jain SR, Jain RK. Coevolution of solid stress and interstitial fluid pressure in tumors during progression: implications for vascular collapse. *Cancer Res*. 2013 Jul;73(13):3833–3841.
- [123] Kronik N, Kogan Y, Elishmereni M, Halevi-Tobias K, Vuk-Pavlović S, Agur Z. Predicting Outcomes of Prostate Cancer Immunotherapy by Personalized Mathematical Models. *PLoS ONE*. 2010 Dec;5(12):e15482.

- [124] Kogan Y, Halevi-Tobias K, Elishmereni M, Vuk-Pavlovic S, Agur Z. Reconsidering the Paradigm of Cancer Immunotherapy by Computationally Aided Real-Time Personalization. *Cancer Res.* 2012 May;72(9):2218–2227.
- [125] Claret L, Girard P, Hoff PM, Van Cutsem E, Zuideveld KP, Jorga K, et al. Model-Based Prediction of Phase III Overall Survival in Colorectal Cancer on the Basis of Phase II Tumor Dynamics. *J Clin Oncol.* 2009 Sep;27(25):4103–4108.
- [126] Ribba B, Kaloshi G, Peyre M, Ricard D, Calvez V, Tod M, et al. A Tumor Growth Inhibition Model for Low-Grade Glioma Treated with Chemotherapy or Radiotherapy. *Clin Cancer Res.* 2012 Sep;18(18):5071–5080.
- [127] Colin T, Iollo A, Lombardi D, Saut O. Prediction of the Evolution of Thyroidal Lung Nodules Using a Mathematical Model. *ERCIM News.* 2010;.
- [128] Konukoglu E, Clatz O, Menze BH, Stieltjes B, Weber MA, Mandonnet E, et al. Image Guided Personalization of Reaction-Diffusion Type Tumor Growth Models Using Modified Anisotropic Eikonal Equations. *IEEE Trans Med Imaging.* 2010 Jan;29(1):77–95.
- [129] Baldock AL, Yagle K, Born DE, Ahn S, Trister AD, Neal M, et al. Invasion and proliferation kinetics in enhancing gliomas predict IDH1 mutation status. *Neuro-Oncology.* 2014 Jun;16(6):779–786.
- [130] Gelman A. *Bayesian Data Analysis.* Third edition ed. Chapman & Hall/CRC Texts in Statistical Science. Boca Raton: CRC Press; 2014.
- [131] Patrone MV, Hubbs JL, Bailey JE, Marks LB. How long have I had my cancer, doctor? Estimating tumor age via Collins' law. *Oncology (Williston Park, NY).* 2011 Jan;25(1):38–43–46.
- [132] Cardoso F, van't Veer LJ, Bogaerts J, Slaets L, Viale G, Delaloge S, et al. 70-Gene Signature as an Aid to Treatment Decisions in Early-Stage Breast Cancer. *N Engl J Med.* 2016 Aug;375(8):717–729.
- [133] Mastri M, Tracz A, Ebos JML. Tumor Growth Kinetics of Human LM2-4LUC+ Triple Negative Breast Carcinoma Cells. <https://zenodo.org/record/3574531>. Zenodo; 2019.
- [134] Ebos JML, Lee CR, Bogdanovic E, Alami J, Van Slyke P, Francia G, et al. Vascular Endothelial Growth Factor-Mediated Decrease in Plasma Soluble Vascular Endothelial Growth Factor Receptor-2 Levels as a Surrogate Biomarker for Tumor Growth. *Cancer Res.* 2008 Jan;68(2):521–529.
- [135] Rodallec A, Giacometti S, Ciccolini J, Fanciullino R. Tumor Growth Kinetics of Human MDA-MB-231 Cells Transfected with dTomato Lentivirus. <https://zenodo.org/record/3593919>. Zenodo; 2019.

- [136] Benzekry S, Lamont C, Weremowicz J, Beheshti A, Hlatky L, Hahnfeldt P. Tumor Growth Kinetics of Subcutaneously Implanted Lewis Lung Carcinoma Cells. <https://zenodo.org/record/3572401>. Zenodo; 2019.
- [137] Bertram JS, Janik P. Establishment of a Cloned Line of Lewis Lung Carcinoma Cells Adapted to Cell Culture. *Cancer Lett.* 1980 Nov;11(1):63–73.
- [138] Deylon B, Lavielle M, Moulines E. Convergence of a Stochastic Approximation Version of the EM Algorithm. *Ann Statist.* 1999;27(1):94–128.
- [139] Seber GAF, Wild CJ. *Nonlinear Regression*. Wiley Series in Probability and Statistics. Hoboken, N.J.: Wiley-Interscience; 2003.
- [140] Brunton GF, Wheldon TE. Prediction of the Complete Growth Pattern of Human Multiple Myeloma from Restricted Initial Measurements. *Cell Tissue Kinet.* 1977 Nov;10(6):591–594.
- [141] Brunton GF, Wheldon TE. The Gompertz Equation and the Construction of Tumour Growth Curves. *Cell Tissue Kinet.* 1980 Jul;13(4):455–460.
- [142] D’Onofrio A, Gandolfi A. A Family of Models of Angiogenesis and Anti-Angiogenesis Anti-Cancer Therapy. *Math Med Biol.* 2008 Nov;26(1):63–95.
- [143] Sarapata EA, de Pillis LG. A comparison and catalog of intrinsic tumor growth models. *Bulletin of Mathematical Biology.* 2014 Aug;76(8):2010–2024.
- [144] Hart D, Shochat E, Agur Z. The growth law of primary breast cancer as inferred from mammography screening trials data. *Br J Cancer.* 1998 Aug;78(3):382–7.
- [145] Sullivan PW, Salmon SE. Kinetics of tumor growth and regression in IgG multiple myeloma. *J Clin Invest.* 1972 Jul;51(7):1697–1708.
- [146] Spratt JA, von Fournier D, Spratt JS, Weber EE. Decelerating growth and human breast cancer. *Cancer.* 1993 Mar;71(6):2013–2019.
- [147] Marusić M, Bajzer Z, Vuk-Pavlović S, Freyer JP. Tumor growth in vivo and as multicellular spheroids compared by mathematical models. *Bull Math Biol.* 1994 Jul;56(4):617–631.
- [148] d’Onofrio A. Fractal Growth of Tumors and Other Cellular Populations: Linking the Mechanistic to the Phenomenological Modeling and Vice Versa. *Chaos Soliton Fract.* 2009 Jul;41(2):875–880.
- [149] Marusić M, Bajzer Z, Freyer JP, Vuk-Pavlović S. Analysis of growth of multicellular tumour spheroids by mathematical models. *Cell Prolif.* 1994 Feb;27(2):73–94.
- [150] Casey AE. The Experimental Alteration of Malignancy with an Homologous Mammalian Tumor Material : I . Results with Intratesticular Inoculation. *Am J Cancer.* 1934;21:760–775.

- [151] Michelson S, Glicksman aS, Leith JT. Growth in solid heterogeneous human colon adenocarcinomas: comparison of simple logistical models. *Cell Prolif.* 1987 May;20(3):343–355.
- [152] Rofstad EK, Fodstad O, Lindmo T. Growth characteristics of human melanoma xenografts. *Cell Tissue Kinet.* 1982 Sep;15(5):545–554.
- [153] Wheldon TE. *Mathematical models in cancer research.* Bristol: Hilger; 1988.
- [154] Bilous M, Serdjebi C, Boyer A, Tomasini P, Pouypoudat C, Barbolosi D, et al. Quantitative Mathematical Modeling of Clinical Brain Metastasis Dynamics in Non-Small Cell Lung Cancer. *Sci Rep.* 2019 Dec;9(1).
- [155] Nicolò C, Périer C, Prague M, Bellera C, MacGrogan G, Saut O, et al. Machine Learning and Mechanistic Modeling for Prediction of Metastatic Relapse in Early-Stage Breast Cancer. *JCO Clin Cancer Inform.* 2020 Sep;(4):259–274.
- [156] Monolix Version 2019R2. Antony, France; 2019. Lixoft SAS.
- [157] Lavielle M, Ilinca E, Kuate R. *mlxR: Simulation of Longitudinal Data;* 2019.
- [158] Hill AV. The Combinations of Haemoglobin with Oxygen and with Carbon Monoxide. I. *Biochem J.* 1913 Oct;7(5):471–480.
- [159] Goutelle S, Maurin M, Rougier F, Barbaut X, Bourguignon L, Ducher M, et al. The Hill Equation: A Review of Its Capabilities in Pharmacological Modelling. *Fundam Clin Pharmacol.* 2008 Dec;22(6):633–648.
- [160] Michaelis L, Menten ML, Johnson KA, Goody RS. The Original Michaelis Constant: Translation of the 1913 Michaelis-Menten Paper. *Biochemistry.* 2011 Oct;50(39):8264–8269.
- [161] Wagner JG. Kinetics of Pharmacologic Response I. Proposed Relationships between Response and Drug Concentration in the Intact Animal and Man. *J Theor Biol.* 1968 Aug;20(2):173–201.
- [162] Mager DE, Wyska E, Jusko WJ. Diversity of Mechanism-Based Pharmacodynamic Models. *Drug Metab Dispos.* 2003 May;31(5):510–518.
- [163] Csajka C, Verotta D. Pharmacokinetic–Pharmacodynamic Modelling: History and Perspectives. *J Pharmacokinet Pharmacodyn.* 2006 Jun;33(3):227–279.
- [164] Holford NHG, Sheiner LB. Understanding the Dose-Effect Relationship: Clinical Application of Pharmacokinetic-Pharmacodynamic Models. *Clin Pharmacokinet.* 1981;6(6):429–453.
- [165] Murray JD. *Mathematical Biology: I. An Introduction.* New York, NY: Springer-Verlag Berlin Heidelberg.; 2004.

- [166] Macheras P, Iliadis A. Modeling in Biopharmaceutics, Pharmacokinetics and Pharmacodynamics: Homogeneous and Heterogeneous Approaches. Second edition ed. No. 30 in Interdisciplinary Applied Mathematics. Cham Heidelberg New York Dordrecht London: Springer; 2016.
- [167] Zou H, Banerjee P, Leung SSY, Yan X. Application of Pharmacokinetic-Pharmacodynamic Modeling in Drug Delivery: Development and Challenges. *Front Pharmacol.* 2020;11:997.
- [168] Danhof M, Alvan G, Dahl SG, Kuhlmann J, Paintaud G. Mechanism-Based Pharmacokinetic-Pharmacodynamic Modeling—A New Classification of Biomarkers. *Pharm Res.* 2005 Sep;22(9):1432–1437.
- [169] Sykes EA, Chen J, Zheng G, Chan WCW. Investigating the Impact of Nanoparticle Size on Active and Passive Tumor Targeting Efficiency. *ACS Nano.* 2014 Jun;8(6):5696–5706.
- [170] Yu T, Hubbard D, Ray A, Ghandehari H. In Vivo Biodistribution and Pharmacokinetics of Silica Nanoparticles as a Function of Geometry, Porosity and Surface Characteristics. *J Control Release.* 2012 Oct;163(1):46–54.
- [171] Schlupe T, Hwang J, Hildebrandt IJ, Czernin J, Choi CHJ, Alabi CA, et al. Pharmacokinetics and Tumor Dynamics of the Nanoparticle IT-101 from PET Imaging and Tumor Histological Measurements. *Proc Natl Acad Sci USA.* 2009 Jul;106(27):11394–11399.
- [172] Baker SD, Rudek MA. Pharmacokinetic Modeling. In: Figg WD, McLeod HL, editors. *Handbook of Anticancer Pharmacokinetics and Pharmacodynamics.* Totowa, NJ: Humana Press; 2004. p. 129–137.
- [173] Li M, Al-Jamal KT, Kostarelos K, Reineke J. Physiologically Based Pharmacokinetic Modeling of Nanoparticles. *ACS Nano.* 2010 Nov;4(11):6303–6317.
- [174] von Goetz, Bachler G, Hungerbühler K. A Physiologically Based Pharmacokinetic Model for Ionic Silver and Silver Nanoparticles. *Int J Nanomedicine.* 2013 Sep;p. 3365.
- [175] Dogra P, Butner JD, Ruiz Ramírez J, Chuang YI, Nouredine A, Jeffrey Brinker C, et al. A Mathematical Model to Predict Nanomedicine Pharmacokinetics and Tumor Delivery. *Comput Struct Biotechnol J.* 2020;18:518–531.
- [176] Singh AP, Shah DK. Application of a PK-PD Modeling and Simulation-Based Strategy for Clinical Translation of Antibody-Drug Conjugates: A Case Study with Trastuzumab Emtansine (T-DM1). *AAPS J.* 2017 Jul;19(4):1054–1070.
- [177] Cilliers C, Guo H, Liao J, Christodolu N, Thurber GM. Multiscale Modeling of Antibody-Drug Conjugates: Connecting Tissue and Cellular Distribution to Whole Animal Pharmacokinetics and Potential Implications for Efficacy. *AAPS J.* 2016 Sep;18(5):1117–1130.

- [178] Kumar R, Roy I, Ohulchanskyy TY, Vathy LA, Bergey EJ, Sajjad M, et al. *In Vivo* Biodistribution and Clearance Studies Using Multimodal Organically Modified Silica Nanoparticles. *ACS Nano*. 2010 Feb;4(2):699–708.
- [179] Chou LYT, Chan WCW. Fluorescence-Tagged Gold Nanoparticles for Rapidly Characterizing the Size-Dependent Biodistribution in Tumor Models. *Adv Healthc Mater*. 2012 Nov;1(6):714–721.
- [180] Ribba B, Holford NH, Magni P, Trocóniz I, Gueorguieva I, Girard P, et al. A Review of Mixed-Effects Models of Tumor Growth and Effects of Anticancer Drug Treatment Used in Population Analysis. *CPT Pharmacometrics Syst Pharmacol*. 2014 May;3(5):e113.
- [181] He H, Yuan D, Wu Y, Cao Y. Pharmacokinetics and Pharmacodynamics Modeling and Simulation Systems to Support the Development and Regulation of Liposomal Drugs. *Pharmaceutics*. 2019 Mar;11(3):110.
- [182] Extra JM, Rousseau F, Bruno R, Clavel M, Le Bail N, Marty M. Phase I and Pharmacokinetic Study of Taxotere (RP 56976; NSC 628503) Given as a Short Intravenous Infusion. *Cancer Res*. 1993 Mar;53:1037–1042.
- [183] Hilmas DE, Gillette EL. Morphometric Analyses of the Microvasculature of Tumors during Growth and after X-Irradiation. *Cancer*. 1974 Jan;33(1):103–110.
- [184] Nielsen UB, Kirpotin DB, Pickering EM, Hong K, Park JW, Refaat Shalaby M, et al. Therapeutic Efficacy of Anti-ErbB2 Immunoliposomes Targeted by a Phage Antibody Selected for Cellular Endocytosis. *Biochim Biophys Acta Mol Cell Res*. 2002 Aug;1591(1-3):109–118.
- [185] Simeoni M, Magni P, Cammia C, De Nicolao G, Croci V, Pesenti E, et al. Predictive Pharmacokinetic-Pharmacodynamic Modeling of Tumor Growth Kinetics in Xenograft Models after Administration of Anticancer Agents. *Cancer Res*. 2004 Feb;64(3):1094–1101.
- [186] Baxter LT, Jain RK. Transport of Fluid and Macromolecules in Tumors. I. Role of Interstitial Pressure and Convection. *Microvasc Res*. 1989 Jan;37(1):77–104.
- [187] Baish JW, Gazit Y, Berk DA, Nozue M, Baxter LT, Jain RK. Role of Tumor Vascular Architecture in Nutrient and Drug Delivery: An Invasion Percolation-Based Network Model. *Microvasc Res*. 1996 May;51(3):327–346.
- [188] Helmlinger G, Netti PA, Lichtenbeld HC, Melder RJ, Jain RK. Solid Stress Inhibits the Growth of Multicellular Tumor Spheroids. *Nat Biotechnol*. 1997 Aug;15(8):778–783.
- [189] Sevick EM, Jain RK. Viscous Resistance to Blood Flow in Solid Tumors: Effect of Hematocrit on Intratumor Blood Viscosity. *Cancer Res*. 1989 Jul;49(13):3513–3519.
- [190] Netti PA, Berk DA, Swartz MA, Grodzinsky AJ, Jain RK. Role of Extracellular Matrix Assembly in Interstitial Transport in Solid Tumors. *Cancer Res*. 2000 May;60(9):2497–2503.

- [191] Dvorak HF, Brown LF, Detmar M, Dvorak AM. Vascular Permeability Factor/Vascular Endothelial Growth Factor, Microvascular Hyperpermeability, and Angiogenesis. *Am J Pathol.* 1995 May;146(5):1029–1039.
- [192] Boucher Y, Baxter LT, Jain RK. Interstitial Pressure Gradients in Tissue-Isolated and Subcutaneous Tumors: Implications for Therapy. *Cancer Res.* 1990 Aug;50(15):4478–4484.
- [193] Netti PA, Baxter LT, Boucher Y, Skalak R, Jain RK. Time-Dependent Behavior of Interstitial Fluid Pressure in Solid Tumors: Implications for Drug Delivery. *Cancer Res.* 1995 Nov;55(22):5451–5458.
- [194] Starling EH. On the Absorption of Fluids from the Connective Tissue Spaces. *J Physiol.* 1896 May;19(4):312–326.
- [195] Krogh A. *The Anatomy and Physiology of Capillaries.* New Haven, Yale Univ. Press; 1922.
- [196] Apelblat A, Katzir-Katchalsky A, Silberberg A. A Mathematical Analysis of Capillary-Tissue Fluid Exchange. *Biorheology.* 1974 Feb;11(1):1–49.
- [197] Blake TR, Gross JF. Analysis of Coupled Intra- and Extraluminal Flows for Single and Multiple Capillaries. *Math Biosci.* 1982 Jun;59(2):173–206.
- [198] Baish JW, Netti PA, Jain RK. Transmural Coupling of Fluid Flow in Microcirculatory Network and Interstitium in Tumors. *Microvasc Res.* 1997 Mar;53(2):128–141.
- [199] Pozrikidis C, Farrow DA. A Model of Fluid Flow in Solid Tumors. *Ann Biomed Eng.* 2003 Feb;31(2):181–194.
- [200] Soltani M, Chen P. Numerical Modeling of Fluid Flow in Solid Tumors. *PLoS ONE.* 2011 Jun;6(6):e20344.
- [201] Bartha K, Rieger H. Vascular Network Remodeling via Vessel Cooption, Regression and Growth in Tumors. *J Theor Biol.* 2006 Aug;241(4):903–918.
- [202] Welter M, Rieger H. Interstitial Fluid Flow and Drug Delivery in Vascularized Tumors: A Computational Model. *PLoS ONE.* 2013;8(8):e70395.
- [203] Schuff MM, Gore JP, Nauman EA. A Mixture Theory Model of Fluid and Solute Transport in the Microvasculature of Normal and Malignant Tissues. I. Theory. *J Math Biol.* 2013 May;66(6):1179–1207.
- [204] Owen MR, Alarcón T, Maini PK, Byrne HM. Angiogenesis and Vascular Remodelling in Normal and Cancerous Tissues. *J Math Biol.* 2009 Apr;58(4-5):689–721.
- [205] Wijeratne PA, Hipwell JH, Hawkes DJ, Stylianopoulos T, Vavourakis V. Multiscale Biphasic Modelling of Peritumoural Collagen Microstructure: The Effect of Tumour Growth on Permeability and Fluid Flow. *PLoS ONE.* 2017 Sep;12(9):e0184511.

- [206] Zhao J, Salmon H, Sarntinoranont M. Effect of Heterogeneous Vasculature on Interstitial Transport within a Solid Tumor. *Microvasc Res.* 2007 May;73(3):224–236.
- [207] Sweeney PW, d’Esposito A, Walker-Samuel S, Shipley RJ. Modelling the Transport of Fluid through Heterogeneous, Whole Tumours in Silico. *PLoS Comput Biol.* 2019 Jun;15(6):e1006751.
- [208] Penta R, Ambrosi D, Shipley RJ. Effective Governing Equations for Poroelastic Growing Media. *Q J Mech Appl Math.* 2014 Feb;67(1):69–91.
- [209] Penta R, Merodio J. Homogenized Modeling for Vascularized Poroelastic Materials. *Meccanica.* 2017 Nov;52(14):3321–3343.
- [210] Shipley RJ, Sweeney PW, Chapman SJ, Roose T. A Four-compartment Multiscale Model of Fluid and Drug Distribution in Vascular Tumours. *Int J Numer Method Biomed Eng.* 2020 Feb;.
- [211] Amar M, Andreucci D, Bisegna P, Gianni R. On a Hierarchy of Models for Electrical Conduction in Biological Tissues. *Math Meth Appl Sci.* 2006 May;29(7):767–787.
- [212] Perrussel R, Poignard C. Asymptotic Expansion of Steady-State Potential in a High Contrast Medium with a Thin Resistive Layer. *Appl Math Comput.* 2013 Sep;221:48–65.
- [213] Allaire G. Homogenization and Two-Scale Convergence. *SIAM J Math Anal.* 1992 Nov;23(6):1482–1518.
- [214] Beavers GS, Joseph DD. Boundary Conditions at a Naturally Permeable Wall. *J Fluid Mech.* 1967 Oct;30(1):197–207.
- [215] Discacciati M, Quarteroni A. Navier-Stokes/Darcy Coupling: Modeling, Analysis, and Numerical Approximation. *Rev Mat Complut.* 2009 Jul;22(2).
- [216] Layton WJ, Schieweck F, Yotov I. Coupling Fluid Flow with Porous Media Flow. *SIAM J Numer Anal.* 2002 Jan;40(6):2195–2218.
- [217] Saffman PG. On the Boundary Condition at the Surface of a Porous Medium. *Stud Appl Math.* 1971 Jun;50(2):93–101.
- [218] Voutouri C, Stylianopoulos T. Evolution of Osmotic Pressure in Solid Tumors. *J Biomech.* 2014 Nov;47(14):3441–3447.
- [219] Arbogast T, Lehr HL. Homogenization of a Darcy–Stokes System Modeling Vuggy Porous Media. *Comput Geosci.* 2006 Sep;10(3):291–302.
- [220] Conca C. On the Application of the Homogenization Theory to a Class of Problems Arising in Fluid Mechanics. *J Math Pures Appl.* 1985;64:31–75.

- [221] Kato T. *Perturbation Theory for Linear Operators*. vol. 132 of *Classics in Mathematics*. Berlin, Heidelberg: Springer Berlin Heidelberg; 1995.
- [222] Vaghi C, Benzekry S, Poinard C. *Asymptotic Analysis of a Tumor Fluid Flow Model*. To be submitted;
- [223] Balanis CA. *Advanced Engineering Electromagnetics*. 2nd ed. Hoboken, N.J: John Wiley & Sons; 2012.
- [224] Discacciati M, Quarteroni A. *Analysis of a Domain Decomposition Method for the Coupling of Stokes and Darcy Equations*. In: Brezzi F, Buffa A, Corsaro S, Murli A, editors. *Numerical Mathematics and Advanced Applications*. Milano: Springer Milan; 2003. p. 3–20.
- [225] Forster JC, Harriss-Phillips WM, Douglass MJ, Bezak E. *A Review of the Development of Tumor Vasculature and Its Effects on the Tumor Microenvironment*. *Hypoxia (Auckl)*. 2017;5:21–32.
- [226] Walker-Samuel S, Roberts TA, Ramasawmy R, Burrell JS, Johnson SP, Siow BM, et al. *Investigating Low-Velocity Fluid Flow in Tumors with Convection-MRI*. *Cancer Res*. 2018 Apr;78(7):1859–1872.
- [227] Rand PW, Lacombe E, Hunt HE, Austin WH. *Viscosity of Normal Human Blood under Normothermic and Hypothermic Conditions*. *J Appl Physiol*. 1964 Jan;19(1):117–122.
- [228] Less JR, Skalak TC, Sevick EM, Jain RK. *Microvascular Architecture in a Mammary Carcinoma: Branching Patterns and Vessel Dimensions*. *Cancer Res*. 1991 Jan;51(1):265–273.
- [229] Guyton AC, Granger HJ, Taylor AE. *Interstitial Fluid Pressure*. *Physiol Rev*. 1971 Jul;51(3):527–563.
- [230] Jain RK, Tong RT, Munn LL. *Effect of Vascular Normalization by Antiangiogenic Therapy on Interstitial Hypertension, Peritumor Edema, and Lymphatic Metastasis: Insights from a Mathematical Model*. *Cancer Res*. 2007 Mar;67(6):2729–2735.
- [231] Swabb EA, Wei J, Gullino PM. *Diffusion and Convection in Normal and Neoplastic Tissues*. *Cancer Res*. 1974 Oct;34(10):2814–2822.
- [232] Sevick EM, Jain RK. *Measurement of Capillary Filtration Coefficient in a Solid Tumor*. *Cancer Res*. 1991 Feb;51(4):1352–1355.
- [233] Rippe B, Kamiya A, Folkow B. *Simultaneous Measurements of Capillary Diffusion and Filtration Exchange during Shifts in Filtration-Absorption and at Graded Alterations in the Capillary Permeability Surface Area Product (PS)*. *Acta Physiol Scand*. 1978 Nov;104(3):318–336.
- [234] Stamatelos SK, Kim E, Pathak AP, Popel AS. *A Bioimage Informatics Based Reconstruction of Breast Tumor Microvasculature with Computational Blood Flow Predictions*. *Microvasc Res*. 2014 Jan;91:8–21.

- [235] Vogel AW. Intratumoral Vascular Changes With Increased Size of a Mammary Adenocarcinoma: New Method and Results. *J Natl Cancer Inst.* 1965 May;34:571–578.
- [236] Kanit T, Forest S, Galliet I, Mounoury V, Jeulin D. Determination of the Size of the Representative Volume Element for Random Composites: Statistical and Numerical Approach. *Int J Solids Struct.* 2003 Jun;40(13-14):3647–3679.
- [237] Pries AR, Secomb TW, Gessner T, Sperandio MB, Gross JF, Gaehtgens P. Resistance to Blood Flow in Microvessels in Vivo. *Circ Res.* 1994 Nov;75(5):904–915.
- [238] Liu Y, Shah S, Tan J. Computational Modeling of Nanoparticle Targeted Drug Delivery. *Rev Nanosci Nanotechnol.* 2012 Mar;1(1):66–83.
- [239] Deen WM. Hindered Transport of Large Molecules in Liquid-Filled Pores. *AIChE J.* 1987 Sep;33(9):1409–1425.
- [240] Yuan F, Dellian M, Fukumura D, Leunig M, Berk DA, Torchilin VP, et al. Vascular Permeability in a Human Tumor Xenograft: Molecular Size Dependence and Cutoff Size. *Cancer Res.* 1995 Sep;55(17):3752–3756.
- [241] Hobbs SK, Monsky WL, Yuan F, Roberts WG, Griffith L, Torchilin VP, et al. Regulation of Transport Pathways in Tumor Vessels: Role of Tumor Type and Microenvironment. *Proc Natl Acad Sci USA.* 1998 Apr;95(8):4607–4612.
- [242] Shi W, Wang J, Fan X, Gao H. Size and Shape Effects on Diffusion and Absorption of Colloidal Particles near a Partially Absorbing Sphere: Implications for Uptake of Nanoparticles in Animal Cells. *Phys Rev.* 2008 Dec;78(6).
- [243] Ozcelikkale A, Ghosh S, Han B. Multifaceted Transport Characteristics of Nanomedicine: Needs for Characterization in Dynamic Environment. *Mol Pharm.* 2013 Jun;10(6):2111–2126.
- [244] Taffetani M, de Falco C, Penta R, Ambrosi D, Ciarletta P. Biomechanical Modelling in Nanomedicine: Multiscale Approaches and Future Challenges. *Arch Appl Mech.* 2014 Oct;84(9-11):1627–1645.
- [245] Stylianopoulos T, Jain RK. Combining Two Strategies to Improve Perfusion and Drug Delivery in Solid Tumors. *Proc Natl Acad Sci USA.* 2013 Nov;110(46):18632–18637.
- [246] Mok W, Stylianopoulos T, Boucher Y, Jain RK. Mathematical Modeling of Herpes Simplex Virus Distribution in Solid Tumors: Implications for Cancer Gene Therapy. *Clin Cancer Res.* 2009 Mar;15(7):2352–2360.
- [247] Stapleton S, Milosevic M, Allen C, Zheng J, Dunne M, Yeung I, et al. A Mathematical Model of the Enhanced Permeability and Retention Effect for Liposome Transport in Solid Tumors. *PLoS ONE.* 2013 Dec;8(12):e81157.

- [248] Ford Versypt AN, Braatz RD. Analysis of Finite Difference Discretization Schemes for Diffusion in Spheres with Variable Diffusivity. *Comput Chem Eng.* 2014 Dec;71:241–252.
- [249] Mitchell AR, Griffiths DE. *The Finite Difference Method in Partial Differential Equations*. Chichester [Eng.] ; New York: Wiley; 1980.
- [250] Pluen A, Netti PA, Jain RK, Berk DA. Diffusion of Macromolecules in Agarose Gels: Comparison of Linear and Globular Configurations. *Biophys J.* 1999 Jul;77(1):542–552.
- [251] Levick JR. Flow through Interstitium and Other Fibrous Matrices. *Q J Exp Physiol.* 1987 Oct;72(4):409–437.
- [252] Davies CdL, Berk DA, Pluen A, Jain RK. Comparison of IgG Diffusion and Extracellular Matrix Composition in Rhabdomyosarcomas Grown in Mice versus in Vitro as Spheroids Reveals the Role of Host Stromal Cells. *Br J Cancer.* 2002 May;86(10):1639–1644.
- [253] National Center for Biotechnology Information. PubChem Compound Summary for CID 148124, Docetaxel. <https://pubchem.ncbi.nlm.nih.gov/compound/Docetaxel;>
- [254] [http://www.chemspider.com/Chemical-Structure.130581.html;](http://www.chemspider.com/Chemical-Structure.130581.html)
- [255] Yuan F, Leunig M, Huang SK, Berk DA, Papahadjopoulos D, Jain RK. Microvascular Permeability and Interstitial Penetration of Sterically Stabilized (Stealth) Liposomes in a Human Tumor Xenograft. *Cancer Res.* 1994 Jul;54(13):3352–3356.
- [256] Renkin EM, Crone C. Microcirculation and Capillary Exchange. In: Greger R, Windhorst U, editors. *Comprehensive Human Physiology*. Berlin, Heidelberg: Springer Berlin Heidelberg; 1996. p. 1965–1979.
- [257] Wu NZ, Da D, Rudoll TL, Needham D, Whorton AR, Dewhirst MW. Increased Microvascular Permeability Contributes to Preferential Accumulation of Stealth Liposomes in Tumor Tissue. *Cancer Res.* 1993 Aug;53(16):3765–3770.
- [258] Anderson JL, Malone DM. Mechanism of Osmotic Flow in Porous Membranes. *Biophys J.* 1974 Dec;14(12):957–982.
- [259] Nair A, Jacob S. A Simple Practice Guide for Dose Conversion between Animals and Human. *J Basic Clin Pharm.* 2016;7(2):27.
- [260] Chu KS, Hasan W, Rawal S, Walsh MD, Enlow EM, Luft JC, et al. Plasma, Tumor and Tissue Pharmacokinetics of Docetaxel Delivered via Nanoparticles of Different Sizes and Shapes in Mice Bearing SKOV-3 Human Ovarian Carcinoma Xenograft. *Nanomedicine: NBM.* 2013 Jul;9(5):686–693.
- [261] Graff CP, Wittrup KD. Theoretical Analysis of Antibody Targeting of Tumor Spheroids: Importance of Dosage for Penetration, and Affinity for Retention. *Cancer Res.* 2003 Mar;63(6):1288–1296.

- [262] Frieboes HB, Wu M, Lowengrub J, Decuzzi P, Cristini V. A Computational Model for Predicting Nanoparticle Accumulation in Tumor Vasculature. *PLoS ONE*. 2013 Feb;8(2):e56876.
- [263] Decuzzi P, Ferrari M. The Adhesive Strength of Non-Spherical Particles Mediated by Specific Interactions. *Biomaterials*. 2006 Oct;27(30):5307–5314.
- [264] Dogra P, Butner JD, Nizzero S, Ruiz Ramírez J, Noureddine A, Peláez MJ, et al. Image-guided Mathematical Modeling for Pharmacological Evaluation of Nanomaterials and Monoclonal Antibodies. *WIREs Nanomed Nanobiotechnol*. 2020 Sep;12(5).
- [265] van de Ven AL, Wu M, Lowengrub J, McDougall SR, Chaplain MAJ, Cristini V, et al. Integrated Intravital Microscopy and Mathematical Modeling to Optimize Nanotherapeutics Delivery to Tumors. *AIP Adv*. 2012 Mar;2(1):011208.
- [266] Goel S, Ferreira CA, Dogra P, Yu B, Kuttyreff CJ, Siamof CM, et al. Size-Optimized Ultrasmall Porous Silica Nanoparticles Depict Vasculature-Based Differential Targeting in Triple Negative Breast Cancer. *Small*. 2019 Nov;15(46):1903747.
- [267] Kingston BR, Syed AM, Ngai J, Sindhvani S, Chan WCW. Assessing Micrometastases as a Target for Nanoparticles Using 3D Microscopy and Machine Learning. *Proc Natl Acad Sci USA*. 2019 Jul;116(30):14937–14946.
- [268] Sykes EA, Dai Q, Sarsons CD, Chen J, Rocheleau JV, Hwang DM, et al. Tailoring Nanoparticle Designs to Target Cancer Based on Tumor Pathophysiology. *Proc Natl Acad Sci USA*. 2016 Mar;113(9):E1142–E1151.
- [269] Sicard G, Rodallec A, Correard F, Vaghi C, Poignard C, Ciccolini J, et al. Abstract 6244: Turning Poorly Vascularized Tumors into Highly Vascularized Tumors with Nanoparticles: Proof of Concept and Pharmacometric Analysis. In: *Experimental and Molecular Therapeutics*. American Association for Cancer Research; 2020. p. 6244–6244.
- [270] Shen L, Chen Z. Critical Review of the Impact of Tortuosity on Diffusion. *Chem Eng Sci*. 2007 Jul;62(14):3748–3755.
- [271] Netti PA, Baxter LT, Boucher Y, Skalak R, Jain RK. Macro- and Microscopic Fluid Transport in Living Tissues: Application to Solid Tumors. *AIChE J*. 1997 Mar;43(3):818–834.
- [272] Pishko GL, Astarly GW, Mareci TH, Sarntinoranont M. Sensitivity Analysis of an Image-Based Solid Tumor Computational Model with Heterogeneous Vasculature and Porosity. *Ann Biomed Eng*. 2011 Sep;39(9):2360–2373.
- [273] Russ JC. *Practical Stereology*. Springer; 2013.
- [274] Ledru Y. *Etude de La Porosité Dans Les Matériaux Composites Stratifiés Aéronautiques*. Institut National Polytechnique de Toulouse; 2009.

- [275] Boucher Y, Leunig M, Jain RK. Tumor Angiogenesis and Interstitial Hypertension. *Cancer Res.* 1996 Sep;56(18):4264–4266.
- [276] Ma Z, Bai J, Jiang X. Monitoring of the Enzymatic Degradation of Protein Corona and Evaluating the Accompanying Cytotoxicity of Nanoparticles. *ACS Appl Mater Interfaces.* 2015 Aug;7(32):17614–17622.
- [277] Liou GY, Storz P. Reactive Oxygen Species in Cancer. *Free Radic Res.* 2010 Jan;44(5):479–496.
- [278] Sandra F, Khaliq NU, Sunna A, Care A. Developing Protein-Based Nanoparticles as Versatile Delivery Systems for Cancer Therapy and Imaging. *Nanomaterials.* 2019 Sep;9(9):1329.
- [279] Ryu S, Ohuchi M, Yagishita S, Shimoi T, Yonemori K, Tamura K, et al. Visualization of the Distribution of Nanoparticle-Formulated AZD2811 in Mouse Tumor Model Using Matrix-Assisted Laser Desorption Ionization Mass Spectrometry Imaging. *Sci Rep.* 2020 Dec;10(1).
- [280] d’Esposito A, Sweeney PW, Ali M, Saleh M, Ramasawmy R, Roberts TA, et al. Computational Fluid Dynamics with Imaging of Cleared Tissue and of in Vivo Perfusion Predicts Drug Uptake and Treatment Responses in Tumours. *Nat Biomed Eng.* 2018 Oct;2(10):773–787.
- [281] Fehling-Kaschek M, Peckys DB, Kaschek D, Timmer J, de Jonge N. Mathematical Modeling of Drug-Induced Receptor Internalization in the HER2-Positive SKBR3 Breast Cancer Cell-Line. *Sci Rep.* 2019 Dec;9(1).
- [282] Jarrett AM, Shah A, Bloom MJ, McKenna MT, Hormuth DA, Yankeelov TE, et al. Experimentally-Driven Mathematical Modeling to Improve Combination Targeted and Cytotoxic Therapy for HER2+ Breast Cancer. *Scientific Reports.* 2019 Dec;9(1).
- [283] Wientjes MG, Yeung BZ, Lu Z, Wientjes MG, Au JLS. Predicting Diffusive Transport of Cationic Liposomes in 3-Dimensional Tumor Spheroids. *J Control Release.* 2014 Oct;192:10–18.
- [284] Michel T, Fehrenbach J, Lobjois V, Laurent J, Gomes A, Colin T, et al. Mathematical Modeling of the Proliferation Gradient in Multicellular Tumor Spheroids. *J Theor Biol.* 2018 Dec;458:133–147.
- [285] Ward JP, King JR. Mathematical Modelling of Drug Transport in Tumour Multicell Spheroids and Monolayer Cultures. *Math Biosci.* 2003 Feb;181(2):177–207.
- [286] Ramanujan S, Pluen A, McKee TD, Brown EB, Boucher Y, Jain RK. Diffusion and Convection in Collagen Gels: Implications for Transport in the Tumor Interstitium. *Biophys J.* 2002 Sep;83(3):1650–1660.
- [287] Ouyang B, Poon W, Zhang YN, Lin ZP, Kingston BR, Tavares AJ, et al. The Dose Threshold for Nanoparticle Tumour Delivery. *Nat Mater.* 2020 Aug;
- [288] Real-Time and Dynamic Monitoring of Cell Proliferation and Viability for Adherent Cells. ACEA Biosciences, Inc.; 2011.

- [289] Ke N, Wang X, Xu X, Abassi YA. The xCELLigence System for Real-Time and Label-Free Monitoring of Cell Viability. In: Stoddart MJ, editor. *Mammalian Cell Viability*. vol. 740. Totowa, NJ: Humana Press; 2011. p. 33–43.
- [290] Mathews JH, Fink KD. *Numerical Methods Using MATLAB*. 4th ed. Upper Saddle River, N.J: Pearson; 2004.

